Materials Science
Poland

Contents

Crystallization kinetics of
SiO$_2$–MgO–3CaO–P$_2$O$_5$–Al$_2$O$_3$–ZrO$_2$ glass

S. Y$_{ILMAZ}$[1]*, V. G$_{UNAY}$[2]

[1]Sakarya University, Engineering Faculty, Department of Metallurgy and Material Engeneering,
Esentepe Campus, 54187 Sakarya, Turkey

[2]TUBITAK, MRC, Materials Institute, P.O Box 21, 41470 Gebze-Kocaeli, Turkey

The crystallization behaviour of SiO$_2$–MgO–3CaO–P$_2$O$_5$–Al$_2$O$_3$–ZrO$_2$ glass was studied using glass samples prepared by melting reagent grade SiO$_2$, MgO, Ca$_5$(PO$_4$)$_3$OH, P$_2$O$_5$, Al$_2$O$_3$ and ZrO$_2$. DTA and XRD analysis revealed the crystallization of whitlockite, anorthite and baddeleyite phases. The crystallization kinetics was studied by applying the DTA measurements carried out at various heating rates. The activation energies of crystallization and viscous flow were measured as 209 kJ·mol^{-1} and 356 kJ·mol^{-1}, respectively. The resultant SiO$_2$–MgO–3CaO–P$_2$O$_5$–Al$_2$O$_3$–ZrO$_2$ glass-ceramics revealed very fine and homogenous microstructure.

Key words: *bioceramics; bioglass; heat treatment; crystallization; kinetics*

1. Introduction

Ceramics used for the repair and reconstruction of diseased or damaged parts of the muscular-skelatal system, termed bioceramics, may be bioinert (alumina, zirconia), resorbable (tricalcium phosphate), bioactive (hydroxyapatite, bioactive glasses and glass-ceramics), or porous for tissue ingrowth (hydroxyapatite-coated metals, alumina). Bioceramics are needed to alleviate pain and restore function to diseased or damaged parts of the body [1, 2].

Ceramics and glasses are frequently used as biomaterials for the repair of bone tissue. They are popular because of their biocompatibility and the ability of firm composition into established bone. This latter property is described as bioactivity or osteoconductivity [3]. Natural bone and teeth are multiphase materials; their combination of properties probably can be simulated only by multiphase materials. Crystallization of glasses seems to be a very effective way to simulate hard tissues for those applications where elastic modulus mismatch and toughness are not important [4].

_____

*Corresponding author, e-mail: symaz@sakarya.edu.tr

The first studies on glass-ceramics of the SiO_2–CaO–P_2O_5–MgO system were made by Kokubo and co-workers [5, 6]. Glass-ceramics can form a tight chemical bond with bones resulting in a high mechanical strength [7]. Moreover, after heat treatment, fine crystals such as apatite, wollastonite, whitlockite and Mg silicates precipitate from the glass matrix [7, 8] and they were found to have potential as biomaterials [8]. The crystals can enhance the mechanical strength and even promote the bioactivity of the glass-ceramics. Owing to such properties, the glass-ceramics in the SiO_2–CaO–P_2O_5–MgO system is used in clinic, either in the powder form as bone filler or in a bulk material for prosthetic application. The types of crystals formed in the glass matrix are determined by heat treatment and analyses of glass composition [8].

Kokubo, Lacerda, Salinas et al. [4–8] studied glass-ceramics of the SiO_2–CaO–P_2O_5 –MgO system based on comprehensive consideration of biological and medical properties. In this study, we studied the crystallization kinetics of SiO_2–MgO–CaO–P_2O_5–Al_2O_3– ZrO_2 glass system. Al_2O_3 and ZrO_2 were added to glass composition to improve some properties such as strength and chemical resistance of the glass-ceramic system [9, 10].

2. Experimental

The SiO_2–MgO–$3CaO$–P_2O_5–Al_2O_3–ZrO_2 glass was melted from reagent grade SiO_2, MgO, $Ca_5(PO_4)_3OH$, P_2O_5, Al_2O_3 and ZrO_2. The composition of the bioglass sample is given in Table 1.

Table 1. Glass composition

Compound	Content [wt. %]
SiO_2	40.00
CaO	14.00
MgO	10.00
P_2O_5	18.00
Al_2O_3	12.00
ZrO_2	6.00

The calculated batch was melted in platinum–2% rhodium crucible at 1500 °C for 2 h using an electric furnace (HERAEUS). To ensure homogeneity, the melt was poured into water. The cast was crushed, pulverised and remelted at the same temperature for 2 h and rotated several times in 30 min intervals to achieve homogeneity. The refined and homogenized melt was cast into a preheated stainless steel rectangular mould with the dimensions ($1\times3\times0.5$ cm^3). In order to remove thermal residual stress of the glass sample, it was annealed in a regulated muffle furnace at about 600 °C for 1 h. The muffle furnace was left to cool to room temperature at the rate of 30 °C·h^{-1}. Glass-ceramic samples were prepared by applying suitable heat treatments planned

according to the results of differential thermal analysis (DTA) of the amorphous glass. Heat treatments were carried out at temperatures of 800, 900 and 1000 °C for 1 h in a Lenton tube furnace to promote internal crystallization. The crystallization temperatures were selected from the DTA curve depending on the endothermic and exothermic reaction temperatures (Table 1). The crystallization kinetics was studied by the differential thermal analysis (DTA) to determine the activation energies for the crystallization and the viscous flow. The crystalline phase in the heat treated glass samples was determined by X-ray diffraction (XRD) analysis using a RIGAKU D/MAX-2200/PC diffractometer using CuK_α radiation (1.5418 Å). The kinetics of crystallization of glass was determined by the DTA experiments performed in a Netzch STA 429 thermoanalyser using 200 mg powdered samples and employing heating rates of 5, 10, 15 and 20 $°C·min^{-1}$ in open atmosphere with Al_2O_3 powder as a reference material. Some of the crystallized glass specimens were mounted in conductive resin, ground with 600, 1200 and 2500 grit of silicon carbide and finally polished with 1 μm diamond slurry to observe microstructure using a JEOL 6060 LV scanning electron microscope (SEM).

3. Results and discussion

3.1. Differential thermal analysis and crystalline phases

The DTA curves of the glasses are presented in Fig. 1. Endothermic reactions at the temperature range of 665–691 °C have been identified. These endothermic peaks are attributed to the glass transition (T_g), at which the sample changes from solid to liquid behaviour. Various exothermic effects such as that at 734–762 °C indicating reaction of crystallization in the glasses are also recorded.
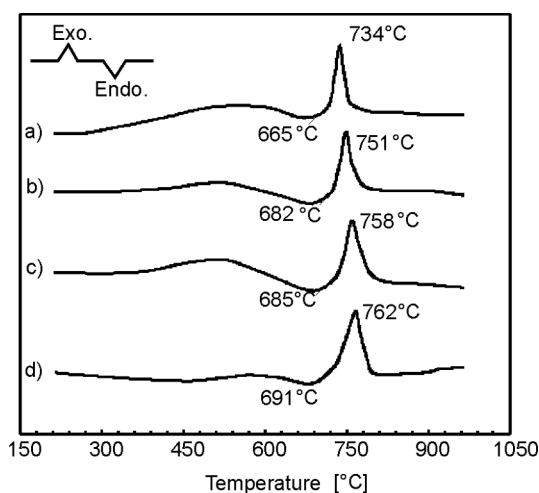
Fig. 1. DTA diagrams of the SiO₂–MgO–3CaO–P₂O₅–Al₂O₃–ZrO₂ glass at the heating rates of: a) 5 °C/min, b) 10 °C/min, c) 15 °C/min and d) 20 °C/min

The appearance of a crystallization peak on the DTA curve implies that at least a different crystal phase is formed during the heat treatment. This was also confirmed by XRD results (Fig. 2). This agrees with previous studies [11, 12].
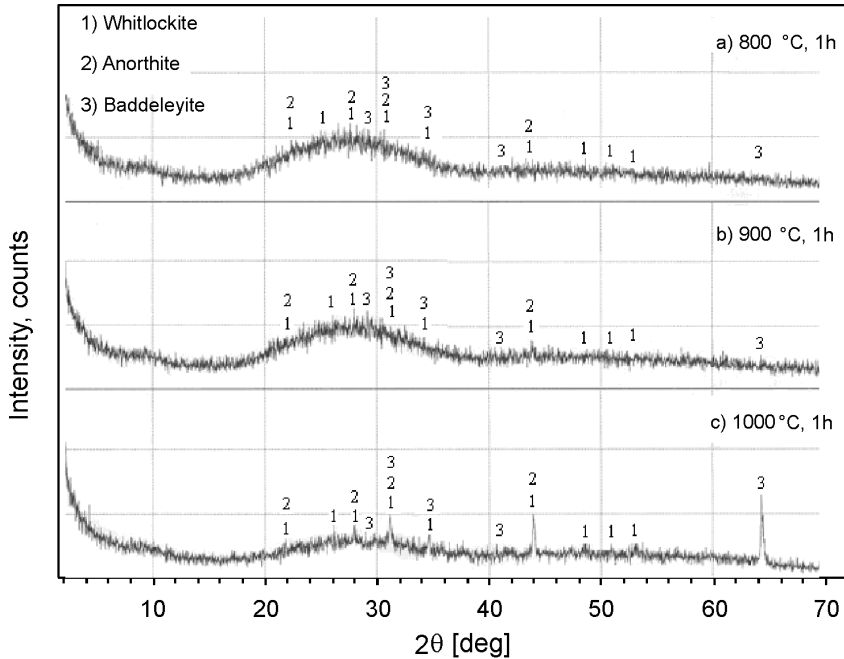
Fig. 2. X-ray diffraction patterns of the SiO_2–MgO–$3CaO$–P_2O_5–Al_2O_3–ZrO_2 glass-ceramics heat treated at 800, 900 and 1000 °C for 1 h

The XRD analysis of bioglass sample showed no crystalline peaks. The cast and annealed glass structure was amorphous and so the spontaneous cooling obtained by glass melt in the furnace ensures glass formation. Figure 2 shows the resulys of XRD analysis of glass samples heat treated at 800, 900 and 1000 °C for 1 h. The determined crystal phase was whitlockite ($Ca_3(PO_4)_2$) (card number: PDF 09-0169), anorthite ($2CaAl_2Si_2O_8$) (card number: PDF 01-070-0287) and baddeleyite (ZrO_2) (card number: PDF 01-072-1669). The degree of crystallization is low in the bioglass-ceramics heat treated at 800 and 900 °C for 1 h (Fig. 2a, b), peaks are not visible clearly and the sample seems to be nearly amorphous. The bioglass system started to crystallize but the ratio of crystallization was not high enough for complete transformation of glass-ceramics. This may be due to high Al_2O_3 content in glass composition leading to inhibition of crystallization [13]. The maximum crystallization was observed in the bioglass-ceramics heat treated at 1000 °C for 1 h (Fig. 2c). XRD analysis showed that the higher is the crystallization temperature the higher the whitlockite peak. Increase in treatment temperature leads to the formation of higher amounts of crystalline phase [11, 12].

3.2. Microstructure

SEM micrograph of the polished surface of the glass-ceramics is shown in Fig. 3.
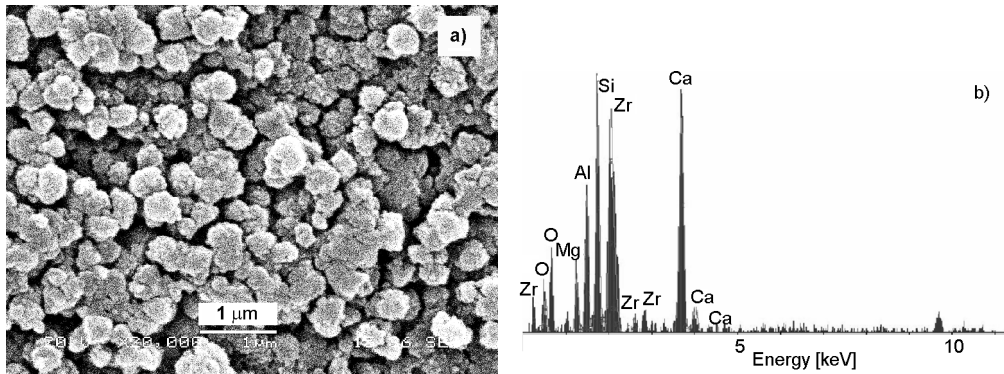
Fig. 3. SEM micrograph (a) and EDAX spectrum (b) of the surface of the glass-ceramic
specimen heat treated at 1000 °C for 1 h and etched using 2.5 % HF in ethanol for 30 s
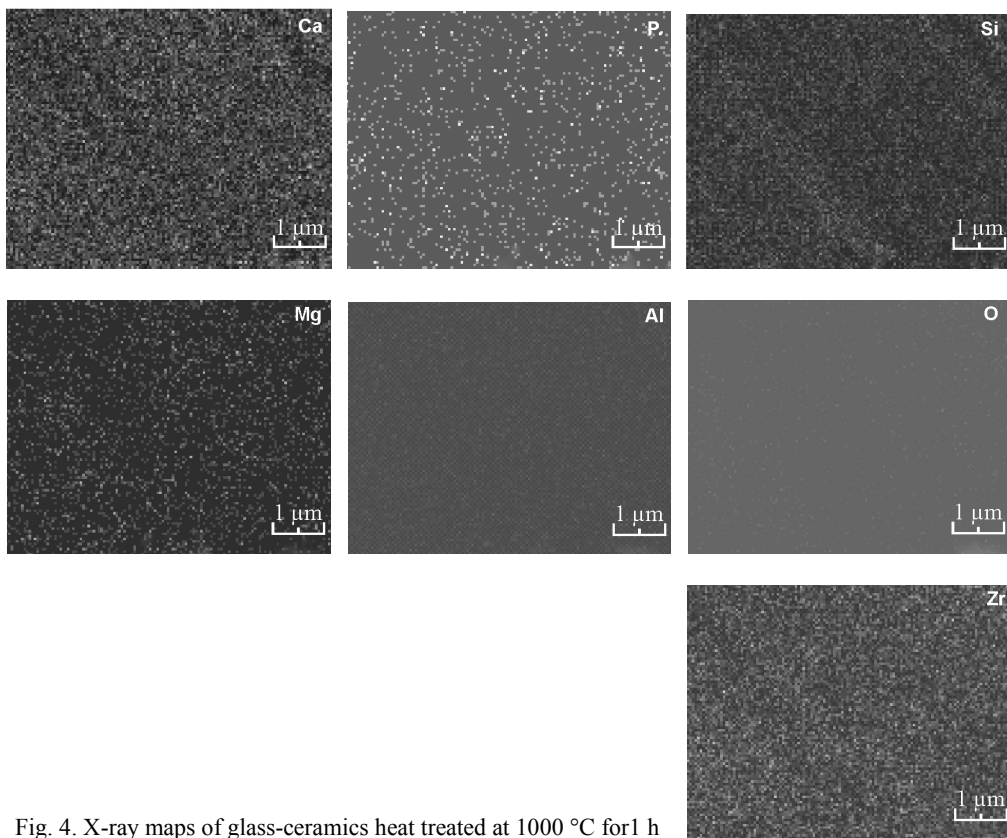
Fig. 4. X-ray maps of glass-ceramics heat treated at 1000 °C for 1 h

Glass microstructure of samples heat treated at 1000 °C is not clear: whitlockite, anorthite and baddeleyite crystals detected by XRD are very small (< 1 μm). The highest peak belongs to Si and Ca in the EDAX analysis (Fig. 3b); whitlockite, anorthite and baddeleyite crystals are present in the glassy matrix. From the amorhous glassy matrix, Ca, P, Al, Si and Zr leave to crystallize in whitlockite, anorthite and baddeleyite phases. This was also confirmed by XRD results (Fig. 2). In Figure 4, X-ray maps of the glass-ceramics heat treated at 1000 °C 1 h are shown. All elements are homogenously distributed in the sample.

3.2. The kinetics of crystallization

Solid state reactions such as crystallization of glass can be described by the phenomenological Johnson–Mehl–Avrami (JMA) equation [11, 12, 14].

$$X = 1 - \exp\left[-(kt)^n\right] \tag{1}$$

Taking natural logarithms and rearranging Eq. (1), we obtain

$$\ln(1 - X) = n\ln k + n\ln t \tag{2}$$

where X is the volume fraction crystallized after time t [11, 12, 14], n is the Avrami parameter which depends on the growth direction number and the mechanism of nucleation and crystal growth [11, 12, 15] shown in Table 2, and k is the reaction rate constant [s^{-1}] whose temperature dependence being expressed by the Arrhenius equation:

$$k = V\exp\left(-E_a/RT\right) \tag{3}$$

where V is the frequency factor [s^{-1}], E_a – the activation energy for crystallization [J·mol^{-1}], R – the gas constant and T – the absolute temperature [K] [11, 12].

Table 2. Values of the parameter n
for various crystallization mechanisms [11, 12]

Mechanism	n
Bulk nucleation	
Three-dimensional growth	4
Two-dimensional growth	3
One-dimensional growth	2
Surface nucleation	1

From the value of the activation energy E_a, the Avrami parameter n can be calculate by the DTA results [11, 12, 16]:

$$n = \frac{2.5}{\Delta T} \frac{T_p^2}{(E_a/R)} \tag{4}$$

where ΔT is the full width of the exotermic peak at the half maximum intensity from DTA crystallization peak. The value of the activation energy for crystallization of glasses was determined using a method based on JMA equation which was first introduced by Kissenger and modified by others. This method is based on the dependence of the crystallization peak temperature (T_p) on the DTA heating rate (β) [10, 12, 15–17]:

$$\ln \frac{T_p^2}{\beta} = \ln \frac{E_a}{R} - \ln V_a + \frac{E_a}{RT_p} \tag{5}$$

likewise, Eq. (5) can also be used to predict the viscous energy [11, 12]:

$$\ln \frac{T_g^2}{\beta} = \ln \frac{E_c}{R} - \ln V_c + \frac{E_c}{RT_g} \tag{6}$$

where E_c is the corresponding activation energy for viscous flow, T_g is the glass transformation temperature, V_a is the frequency factor for crystallization and V_c is the frequency factor for viscous flow.

Plots of $\ln(T_p^2/\beta)$ vs. $1/T_p$ and $\ln(T_g^2/\beta)$ vs. $1/T_g$ obtained at various heating rates should be linear with the slopes E_a/R and the intercepts $\ln(E_a/R) - \ln V_a$ and $\ln(E_c/R) - \ln V_c$. Therefore, if E_a/R and E_c/R are estimated from the slope, the frequency factors can be calculated from the intercepts [11, 12]. The peak temperatures (T_g and T_p) changing with heating rates and T values for calculating n are given in Table 3. The same data are plotted in Figs. 5 and 6.

Table 3. The results of DTA
for SiO$_2$–MgO–3CaO–P$_2$O$_5$–Al$_2$O$_3$–ZrO$_2$ glass

Heating rate, β [K·min^{-1}]	Peak temperature [°C]		ΔT [°C]
	T_g	T_p	
5	665	734	17
10	682	751	25
15	685	758	26
20	691	762	28
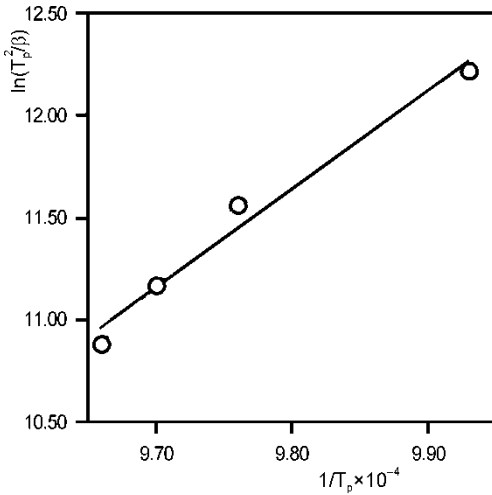
Fig. 5. Plot of ln T_p^2/β vs. 1/T_p for the determination   Fig. 6. Plot of ln T_g^2/β versus 1/T_g for the determination
of the activation energy for the crystallization   of the activation energy for the viscous flow
of SiO_2–MgO–$3CaO$–P_2O_5–Al_2O_3–ZrO_2 glass   of SiO_2–MgO–$3CaO$–P_2O_5–Al_2O_3–ZrO_2 glass

In accordance with the literature data, the temperature corresponding to the crystallization peak is higher at faster heating rates [11]. The calculated values of E_a, E_c and V_a,V_c (Figs. 6 and 7) are as follows: $E_a = 209$ kJ·mol^{-1}, $E_c = 356$ kJ·mol^{-1}, $V_a = 2.37 \times 10^{10}$ s^{-1}, $V_c = 3.91 \times 10^{10}$ s^{-1}.

Table 4. The n values of SiO_2–MgO–$3CaO$–P_2O_5–Al_2O_3–ZrO_2 glasses

Heating rate, β [K·min^{-1}]	5	10	15	20
n	4.0	4.1	4.0	3.7

The n values, calculated from Eq. (4), are given in Table 4. It can be seen that $n \cong 4$ and $n > 4$, which indicates that the crystallization of the SiO_2–MgO–$3CaO$ –P_2O_5–Al_2O_3–ZrO_2 glass at all heating rates is caused by bulk nucleation with three-dimensional crystal growth.

4. Conclusions

In the crystallization of the SiO_2–MgO–$3CaO$–P_2O_5–Al_2O_3–ZrO_2 glass, whitlockite ($Ca_3(PO_4)_2$) crystallizes. The Johnson–Mehl–Avrami, Kissenger and Mahadevan equations were used to calculate the activation energies of crystallization and of viscous flow. The dimensionless parameter n, related to the reaction mechanism was determined by using T values obtained from DTA measurements at various heating rates. Depending on the heating rate, the n values varied between 3.7 and 4.1, indicating the

bulk nucleation in the SiO_2–MgO–$3CaO$–P_2O_5–Al_2O_3–ZrO_2 glass by three-dimensional crystal growth. The activation energies of the crystallization and of viscous flow were calculated as 209 kJ mol^{-1} and 356 kJ mol^{-1}, respectively.

References

 [1] HENCH L.L., J. Amer. Cer. Soc., 74 (1991), 1487.
 [2] HENCH L.L., J. Amer. Cer. Soc., 81 (1998), 1705.
 [3] SALAM S.N., DARWISH H., ABO-MOSALLAM H.A., Ceramics Int., 32 (2006), 357.
 [4] SALINAS A.J., ROMAN J., VALLET-REGI M., OLIVEIRA J.M., CORREIA R.N., FERNANDES M.H., Biomater., 21 (2000), 251.
 [5] KOKUBO T., Biomater., 12 (1991), 155.
 [6] KOKUBO T., ITO S., SAKKA S., YAMAMURO T., J. Mater. Sci., 21 (1986), 536.
 [7] CHANG C.K., MAO D.L., WU J.S., Ceramics Int., 26 (2000), 779.
 [8] LACERDA S.R., OLIVEIRA J.M., CORRIERA R.N., FERNANDES M.H., J. Non-Cryst. Sol., 221 (1997) 255.
 [9] DEMIRKESEN E., MAYTALMAN E., Ceramics Int., 27 (2001), 99.
[10] DEMIRKESEN E, GOLLER G., Ceramics Int., 29 (2003), 463.
[11] YILMAZ S., OZKAN O.T., GUNAY V., Ceramics Int., 22 (1996), 477.
[12] BAYRAK G., YILMAZ S., Ceramics Int., 32 (2006), 441.
[13] MCMILLAN P.W., *Glass-ceramics*, 2nd Ed., Academic Press, London, 1979.
[14] BALAYA P., SUNANDANA C.S., J. Non-Cryst. Sol., 162 (1993), 253.
[15] KARAMANOV A., PELINO M., J. Non-Cryst. Sol., 281 (2001), 139.
[16] PARK J., HEO J., Ceramics Int., 28 (2002), 669.
[17] EROL M., KUCUKBAYRAK S., MERICBOYU A.E., OVECOGLU M.L., J. Europ. Cer. Soc., 21 (2001), 2835.

Elastic properties of double layered manganite La$_{1.2}$Sr$_{1.8-x}$Ca$_x$Mn$_2$O$_7$ (*x* = 0.0–0.4)

Y.S. REDDY[1], M.V. RAMANA REDDY[1],
P. VEERASOMAIAH[2], C. VISHNUVARDHAN REDDY[1*]

[1]Department of Physics, Osmania University, Hyderabad, India-500 007

[2]Department of Chemistry, Nizam College, Osmania University, Hyderabad, India-500 001

Polycrystalline bulk samples of double layered manganite system La$_{1.2}$Sr$_{1.8-x}$Ca$_x$Mn$_2$O$_7$ (*x* = 0.0–0.4) have been synthesized by the sol-gel method. Based on powder X-ray diffraction, it has been found that their lattice parameters decrease with increasing Ca content. The elastic behaviour of the system has been investigated at ~300 K employing ultrasonic pulse transmission technique at 1 MHz. The values of elastic moduli and acoustic Debye temperatures have been computed from the longitudinal and shear wave velocities. The measured values of elastic moduli have been corrected to zero porosity using various correction methods. The variation of elastic moduli with Ca content is interpreted in terms of the strength of interatomic bonding.

Key words: *manganite; CMR; elastic properties; porosity*

1. Introduction

During the past decade, there has been upsurge in the study of various manganites due to colossal magnetoresistance (CMR) phenomenon exhibited by these compounds. Recently, CMR effect has been observed in the *n* = 2 member of the Ruddlesden–Popper (RP) series of manganites La$_{1.2}$Sr$_{1.8-x}$Ca$_x$Mn$_2$O$_7$ [1, 2]. From the fundamental research point of view, the elastic constants are important to elucidate the nature of binding forces and to understand thermal properties like the specific heat or Debye temperature of a solid. When one thinks about the application of any polycrystalline material, although much attention is paid to the 'primary' material property for a given application, mechanical properties are of critical importance in the incorporation of the material into a functional device. On the other hand, it is known that elastic modulus is

---

*Corresponding author, e-mail: reddycvv@osmania.ac.in

a function of temperature, thus room temperature measurements give an idea about the minimum strength of the material.

Until now, the measurements of mechanical properties of manganites have not received much attention. In the past five years, a few reports have been available on some measurements of these properties [3–7]. Of course, these reports deal with La-based cubic perovskites. To our knowledge, no work has been reported on elastic behaviour of double layered manganites.

In this paper, we report on the values of elastic constants and acoustic Debye temperatures of $La_{1.2}Sr_{1.8-x}Ca_xMn_2O_7$ ($x = 0.0$–0.4) system determined by ultrasonic pulse transmission technique at ~300 K. Obtaining information about the elastic behaviour of such compounds may greatly help in further studies of temperature dependences of the elastic constants of present and other double layered manganites and of their interplay with the magnetoresistance effect.

2. Experimental

$La_{1.2}Sr_{1.8-x}Ca_xMn_2O_7$ ($x = 0.0$–0.4) powders have been prepared by the sol-gel method [8]. High purity powders of La_2O_3, $MnCO_3$, $Sr(NO_3)_2$ and $Ca(NO_3)_2.4H_2O$, weighted in appropriate proportions, were used to obtain the nominal compositions of $La_{1.2}Sr_{1.8-x}Ca_xMn_2O_7$ ($x = 0.0$–0.4). La_2O_3 and $MnCO_3$ were converted into nitrates prior to use. All the nitrates were dissolved in citric acid solutions and then the pH was adjusted to ~6 with ammonia solution. After getting the water evaporated, ethylene glycol was added and heated at about 90 ºC until a gel-type solution was formed. The gel was dried at 150 ºC and then decomposed at 250 ºC in air for 2 h to decompose nitrates and all organic materials. The resultant ash was ground to get a fine homogeneous powder. The powder was calcined in air at 1100 ºC for 10 h and then pressed into circular pellets. The pellets were finally sintered in air at 1400 ºC for 6 h.

The structural characterization has been carried out by the powder X-ray diffraction technique employing X-pert pro system, M/S Panalytical, using CuK_α radiation. The X-ray density (ρ_x) values have been calculated from the corresponding lattice constants and the values of bulk densities (ρ) of the samples have been determined by the immersion method. Using the values of ρ_x and ρ, pore fraction (C) has been determined using the formula $C = 1 - \rho/\rho_x$.

The ultrasonic measurements have been carried out by the ultrasonic pulse transmission (UPT) technique at ~ 300 K, with a variation of ± 2 K [9]. X- and Y-cut quartz transducers, with a fundamental frequency of 1 MHz, have been used to transmit and receive the longitudinal and shear waves, respectively. The r.f. pulses generated by the pulse oscillator have been applied to the transmitting transducer, which converted them into acoustic pulses. The acoustic pulses, after propagating through the test sample, have been converted back into electrical signals by the receiving transducers. The amplified output signal has been displayed on a 100 MHz digital storage oscilloscope

(Tektronix model No.2221). The difference in time (ΔT) between two overlapping received pulse trains has been recorded using a timer. The velocity of sound has been measured using the equation $V = t/\Delta T$, where t is the thickness of the sample. The overall accuracy of these measurements was ± 10 m·s^{-1} which is about 1% in sound velocity and 2% in elastic moduli.

3. Results and discussion

The XRD patterns of $La_{1.2}Sr_{1.8-x}Ca_xMn_2O_7$ ($x = 0.0$–0.4), shown in Fig. 1, confirm the single phase formation of the samples. The samples have been indexed to the $Sr_3Ti_2O_7$ type structure with a tetragonal unit cell (space group: $I4/mmm$). It can be seen that the lattice constants (a and c) and cell volume (V) decrease as Ca content increases, which is due to the substitution of smaller Ca^{2+} ions (1.18 Å for the coordination number 9) for larger Sr^{2+} sites (1.31 Å for the coordination number 9) [10] (see Fig. 2).

Elastic constants and acoustic Debye temperatures (Table 1) have been calculated using the longitudinal (V_L) and shear (V_S) wave velocities (at ~300 K) obtained from UPT technique. For a polycrystalline ceramic sample, a standard isotropic elastic medium approximation applies. In the approximation, shear modulus $G = \rho V_S^2$, where ρ is the bulk density of the sample, bulk modulus $B = \rho V_L^2 - 4G/3$, Poisson's ratio $\sigma = (3B - 2G)/(6B + 2G)$ and Young's modulus $E = (1+\sigma)2G$ [9, 11]. The acoustic Debye temperature (θ_D) has been determined using the Anderson formula [12].

$$\theta_D = \frac{h}{k_B}\left(\frac{3\rho N_A q}{4\pi M}\right) V_m$$

where h is the Planck constant, k_B is the Boltzmann constant, ρ is the bulk density of the sample, N_A is the Avogadro number, q is the number of atoms in the unit formula (in the present case, $q = 12$), M is the molecular weight and V_m is the mean sound velocity given by

$$V_m = \left[\frac{1}{3}\left(\frac{1}{V_L^3} + \frac{2}{V_S^3}\right)\right]^{-1/3}$$

In general, the perovskite materials are porous and it is well known fact that porosity plays a key role in governing the elastic properties of materials. Hence, the measured elastic moduli have been corrected to zero porosity using the Hasselman –Fulrath (HF) [13] and Ledbetter–Datta (LD) formulae [14] (Table 2). The values of elastic moduli corrected to zero porosity using the two models are in good agreement and increase with increasing Ca concentration.
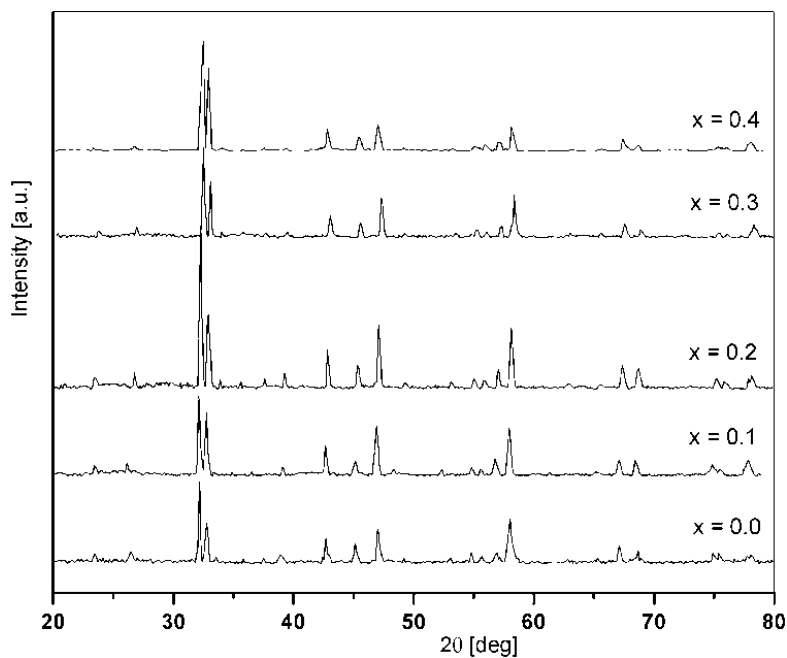
Fig. 1. XRD patterns of $La_{1.2}Sr_{1.8-x}Ca_xMn_2O_7$ ($x = 0.0–0.4$)
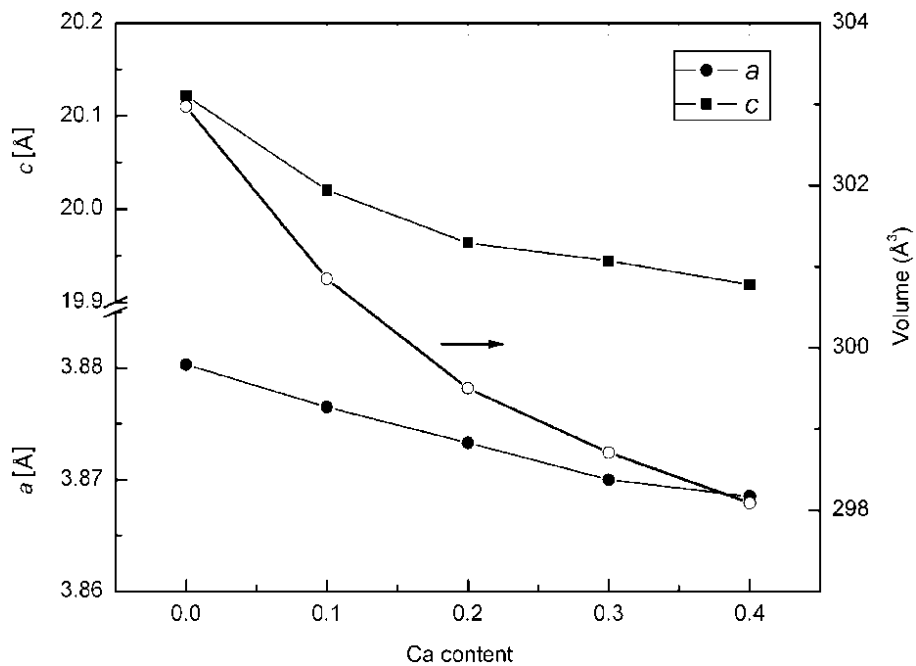
Fig. 2. Variation of lattice constants and cell volume with Ca content

Table 1. X-ray density (ρ_x), bulk density (ρ), pore fraction (*C*), longitudinal velocity (V_L), shear velocity (V_S), mean velocity (V_m), shear modulus (*G*), bulk modulus (*B*), Young's modulus (*E*), Poisson's ratio (σ) and acoustic Debye temperature(θ_D) of $La_{1.2}Sr_{1.8-x}Ca_xMn_2O_7$ (*x* = 0.0–0.4) system

x	ρ_x	ρ	*C*	V_L	V_S	V_m	*G*	*B*	*E*	σ	θ_D [K]
	[$\times 10^3$ kg/m^3]			[m/s]			[GPa]				
0.0	5.987	5.618	0.062	3860	2245	2491	28.31	45.97	70.47	0.244	311.7
0.1	5.977	5.599	0.063	3913	2275	2524	28.99	47.10	72.16	0.245	316.5
0.2	5.951	5.565	0.065	3967	2310	2562	29.69	48.00	73.84	0.244	321.55
0.3	5.914	5.490	0.072	4022	2345	2601	30.20	48.56	75.04	0.242	325.9
0.4	5.873	5.442	0.073	4079	2382	2642	30.88	49.39	76.66	0.241	331.0

Table 2. Elastic moduli corrected to zero porosity using HF and LD models
and elastic moduli and acoustic Debye temperatures obtained from the MMM rule

x	Model	G_0 [GPa]	B_0 [GPa]	E_0 [GPa]	σ_0	θ_D [K]
0.0	HF	32.20	53.24	80.40	0.248	–
	LD	31.95	52.72	79.75	–	–
	MMMR	36.19	47.92	77.24	–	251.02
0.1	HF	33.09	54.78	82.62	0.249	–
	LD	32.81	54.21	81.92	–	–
	MMMR	36.21	47.99	77.44	–	252.66
0.2	HF	34.02	56.05	84.88	0.248	254.32
	LD	33.72	55.43	84.12	–	–
	MMMR	36.24	48.06	77.64	–	–
0.3	HF	35.14	57.67	87.62	0.247	–
	LD	34.76	56.90	86.65	–	–
	MMMR	36.26	48.13	77.84	–	255.98
0.4	HF	36.08	58.90	89.89	0.246	–
	LD	35.68	58.80	88.84	–	–
	MMMR	36.29	48.21	78.04	–	257.64

Recently, Modi et al. have developed a model, known as Modi's heterogeneous metal mixture rule (MMMR), to estimate the elastic constants of spinel ferrites [15], garnets [16], superconductors [17, 18] and La-based perovskites [9]. According to this model, the value of elastic constant or acoustic Debye temperature can be calculated from the following formula:

$$K^*_{pm} = \frac{1}{n} \sum_{i>0,\ n=1}^{\infty} C_{in} K_n$$

where K^*_{pm} is either the elastic modulus or acoustic Debye temperature of the composition to be estimated, *n* is the total number of metallic cations in the unit chemical formula (*n* = 5 in the present case), c_{in} is the concentration of the *n*th cation in the for-

mula unit, while K_n is the corresponding modulus or acoustic Debye temperature of the metallic element present in the system. The elastic moduli and acoustic Debye temperatures of the metallic elements are taken from the literature [19, 20] to estimate K_{pm}^*. The estimated values of elastic moduli and acoustic Debye temperatures using the MMM rule given in Table 2 are in good agreement with the values obtained from the UPT measurements.

The variation of elastic moduli with Ca content can be interpreted on the basis of the strength of interatomic bonding [21]. When larger Sr^{2+} ions (ionic radius – 1.31 Å) are replaced by smaller Ca^{2+} (ionic radius – 1.18 Å) ions, the length of the interatomic bonding decreases resulting in the increase of the strength of interatomic bonding, which in turn increases the magnitude of elastic moduli. The values of elastic moduli corrected to zero porosity and of porous materials show similar dependences on Ca concentration, which confirms the quality of the test samples and the validity of the method employed.
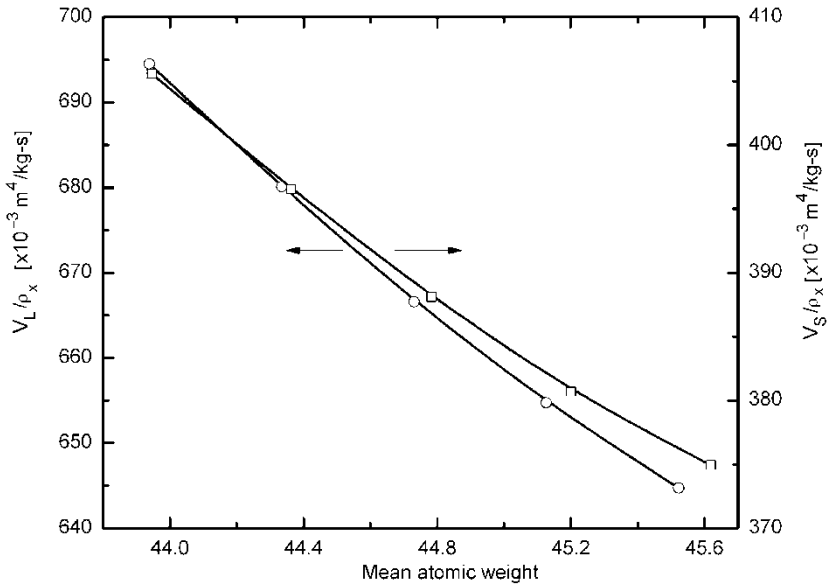
Fig. 3. Variation of V_L/ρ_x and V_S/ρ_x with the mean atomic weight (M/q)

The measured and corrected values of Poisson's ratios have been found to be in good agreement (Tables 1 and 2) and lie in the theoretical range from -1 to 0.5. Increasing Ca concentration results in the increase of the acoustic Debye temperature (Table 1) which suggests a hindrance in lattice vibrations with Ca substitution. This can be attributed to the increasing strength of interatomic bonding with increasing Ca content.

In the case of oxides having the same mean atomic weights (M/q) (M – molecular weight, q – number of atoms in a formula unit), it is proved that longitudinal and shear

wave velocities vary linearly with X-ray density [22, 23]. Hence, the variation in the mean atomic weight corresponds to the variation in the values of V_L/ρ_x and V_S/ρ_x because the product of M/q with V_L/ρ_x and V_S/ρ_x should be a constant [24, 25]. A similar behaviour can be seen from Fig. 3, thus establishing the fact that these materials behave like any other oxide materials described in the literature.

4. Conclusions

Based on the elastic constants determined by ultrasonic pulse transmission technique supported by heterogeneous metal mixture rule for $La_{1.2}Sr_{1-8-x}Ca_xMn_2O_7$ ($x = 0.0–0.4$), it is concluded that the observed increase of elastic constants and acoustic Debye temperature with Ca substitution suggests the strengthening of interatomic bonding and this may be due to the decrease in bond length by replacement of larger Sr^{2+} ions by smaller Ca^{2+} ions in the system. The elastic moduli, corrected to zero porosity with two different models, are in good agreement with each other and to those determined by metal mixture rule, confirming the consistency in the methods employed.

References

[1] SHEN C.H., LIU R.S., HU S.F., HUANG C.Y., SHEU H.S., J. Appl. Phys., 86 (1999), 2178.
[2] TAKEMOTO M., KATADA A., OGAWA T., IKAWA H., J. Eur. Ceram. Soc., 19 (1999), 1511.
[3] ORLOVSKAYA N., KLEVEHAND K., GRANDE T., EINARSURD M., J. Eur. Ceram. Soc., 20 (2000), 51.
[4] CUTLER R.A., L.MEXINER D., Solid State Ionics, 59 (2003), 9.
[5] CHOU Y.S., STEVEN J.W., ARMSTRONG T.R., PEDERSON L.R., J. Amer.Ceram. Soc. 83 (2000), 1457.
[6] MAXINER D.L., CUTLER R.A., Solid State Ionics, 146 (2002), 273.
[7] GHIVELDER G., ABREGO CASTILLO I., GUSMÃO M.A., ALONSO J.A., COHEN L.F., Phys. Rev. B, 60 (1999), 12184.
[8] REDDY Y.S., KISTAIAH P., VISHNUVARDHAN REDDY C., Mater. Chem. Phys., 102 (2007), 171 .
[9] REDDY Y.S., PRASHANTH KUMAR V., KISTAIAH P., VISHNUVARDHAN REDDY C., J. Alloys. Comp. 424 (2006), 46.
[10] SHANNON R.D., Acta Cryst., A32 (1976), 751.
[11] BALDEV RAJ V., RAJENDRAN P., PALANICHAMY, Science and Technology of Ultrasonics, Narosa Publishing House, New Delhi, 2004.
[12] ANDERSON Q.L., J. Phys. Chem. Sol., 24 (1963), 909.
[13] HASSELMAN D.P.H., FULRATH R.M., J. Amer. Ceram. Soc., 47 (1964), 52.
[14] LEDBETTER H., DATTA S, J. Acoust. Soc. Amer., 79 (1986), 239.
[15] MODI K.B., CHHANTBAR M.C., JOSHI H.H., Ceram. Inter., 32 (2006), 111.
[16] MODI K.B., CHHANTBAR M.C., SHARMA P.U., JOSHI H.H., J. Mater. Sci., 40 (2005), 1247.
[17] SOLUNKE M.B., SHARMA P.U., LAKHANI V.K., PANDYA M.P., MODI K.B., REDDY P.V., SHAH S.S., Ceram. Int., 33 (2007), 21.
[18] SOLUNKE M.B., SHARMA P.U., LAKHANI V.K., PANDYA M.P., MODI K.B., REDDY P.V., SHAH S.S., Pramana - J. Phys., 65 (2005), 481.
[19] www.webelements.com.

[20] RAGHAVAN V., *Materials Science and Engineering*, 4th Ed., Prentice-Hall of India Pvt. Ltd., India, 2004.

[21] WOOSTER W.A., Rep. Prog. Phys. 16 (1953), 62.

[22] BIRCH F., J. Geophys. Res., 66 (1961), 2199.

[23] SIMMONS J., J. Geophys. Res. 69 (1964), 1117.

[24] ANDERSON O.L, [in:] W.P. Mason (Ed.), *Physical Acoustics*, Vol. 3B, Academic Press, New York 1965.

[25] NITENDAR KUMAR, PURUSHOTHAM Y., VENUGOPAL REDDY P., ZAIDI Z.H, PRAN KISHAN, J. Magn. Magn. Mater. 192 (1999), 116.

Peculiarities of hydration of
cement paste with addition of hydrosodalite

G. Skripkiūnas[1], V. Sasnauskas[1], M. Daukšys[1], D. Palubinskaite[2*]

[1]Department of Building Materials, Kaunas University of Technology,
Studentų g. 48, LT-51367 Kaunas, Lithuania

[2]Department of Silikate Technology, Kaunas University of Technology,
Radvilenų str. 19, LT-50254 Kaunas, Lithuania

A synthetic zeolite – hydrosodalite was used as a hydraulic additive for hardened cement paste, and the influence of this additive on the hydration and other properties of the system was determined. Hydraulic activity of zeolite has been examined, X-ray diffraction, DTA and IR analysis of the hardened cement paste with zeolite additive have been carried out. The results have shown that the additive has a high hydraulic activity (the content of bound CaO – 370 mg/g). The addition of hydrosodalite reduces the content of $Ca(OH)_2$ in hardened cement paste which transforms into calcium zeolite – gismundite. The density of the hardened cement paste with the addition of hydrosodalite after 3, 7 and 28 days of curing decreases by about 11%. This predetermines a decrease in the compressive strength of the hardened cement paste. The compressive strength after 3 days of curing decreases by about 70%, after 7 days of curing – by 66%, and after 28 days of curing – by about 65%.

Key words: *hydrosodalite; hydraulic activity; hardened cement paste*

1. Introduction

Puzzolanic additives, micro silica, fly ash and other substances have been used in Portland cement mortars and concretes for a long time. Micro silica and fly ash similar to other puzzolanic substances can improve the strength of concrete when $Ca(OH)_2$ reacts with puzzolans. Zeolites are alkaline and ground alkaline metal hydroaliumosilicates and contain large amounts of active SiO_2 and Al_2O_3. This investigation was carried out to estimate the influence of zeolites on the hydration process and the properties of hardened cement paste.

Investigations of Canpolat, Yilmaz and Köse show that natural zeolites behave like other puzzolanic substances in cement paste and improve concrete strength. Zeo-

_____

*Corresponding author, e-mail: danute.palubinskaite@ktu.lt

lites also encourage the origination of such undesirable compounds as alkalis and other complex compounds [1].

The influence of mineral admixture on the compressive strength of concrete containing natural zeolite and powdered inorganic substances were investigated by Feng, Yang and Zu [2]. Upon blending 450 kg/m^3 of Portland cement with 50 kg/m^3 of this mineral additive, the concrete showed a compressive strength of 80 MPa and upon addition of 500 kg/m^3 of Portland cement – 70 MPa. Using such mineral additive (5–10% of cement content) together with superplasticizer at W/C = 0.31–0.35, the concrete strength increased by 10–15%. Super-high-strength concrete can be obtained by adding some zeolites to cement, by shortening the time of hydration of cement, so that the concrete shows higher initial compressive strength. Zeolites and cement can undergo the Puzzolanic reaction which results in less void content and higher final compressive strength, so a super high strength concrete is obtained [3]. Antimicrobial cement compositions have many dental applications, including fillers, adhesives, and medical applications such as bone cements, implant components and substitutes. A particularly preferred cement is an antimicrobial glass ionomer cement composition for dental use, comprising a polyelectrolyte, glass ionomer particles, and antimicrobial zeolite particles [4]. The acidic resistance of mortars made from blended cement with 35% by weight of zeolite and zeolite sand as well as Portland cement mortar attacked for 365 days by 0.5%, 1.0% and 1.5% solution of hydrochloridic acid was studied by Janotka. The result shows that zeolite increases acid resistance of cement. Zeolite sand neutralizes HCl solutions, thus contributing to the increased acidic resistance of zeolite mortar [5, 6]. Addition of zeolite to Portland cement contributes to the significant decrease of the arising solids volume and evident elimination of damaging expansion relative to that of alone Portland cement when exposed to the sulphate solution [7].

Zeolites have low bulk densities and high porosities. Natural zeolites can be used to prepare lightweight concrete for construction. Natural zeolite has a high ion exchange capacity and a particular affinity of cations. It can absorb, e.g., strontium 90, cesium 137, and other isotopes from solution, and hold them in the crystal frame. The adsorption, cation exchange, biotechnical properties of zeolitic materials can be used for new materials with special properties [8]. Hydrosodalite, as a hydraulic admixture to Portland cement, was used in our investigation. The basic formula of hydrosodalite is $Na_{6+x}(SiAlO_4)_6(OH)_x \cdot nH_2O$. This synthetic zeolite was obtained through low-temperature synthesis (under 100 ºC). The aim of the work was to determine the influence of addition of hydrosodalite on hydration processes and microstructures of hardened cement paste.

2. Materials and methods

Pure reagents have been used for analysis of hydrosodalite synthesis: silicagel $SiO_2 \cdot nH_2O$ (loss on ignition – 23.5%, SiO_2 – 76.5%); $Al(OH)_3$; $NaOH$ and water. Port-

land cement CEM I 42.5 R and superplasticizer Rebaflow 202 (FM) on the basis of polycarboxylate resins were used for the preparation of cement pastes. *W*/*C* ratio of cement paste was 0.38 in all mixtures. The addition of superplasticizer into cement paste accounted for 2.0% of the cement mass in all mixtures. Cement was blended with powdered hydrosodalite (5–15% of the cement mass) and mixed with an appropriate amount of water to obtain a paste. The X-ray diffraction analysis was conducted using DRON-6 diffractometer (2Θ angle 4–60º, Ni-filtered CuK_α radiation). The degree of hydration was determined based on specimen mass losses on ignition and the ratio of the water requirement for fully hydrated hardened cement paste. Thermographic investigations have been carried out using a differential scanning calorimeter STA 409 PC (Netzsch). Maximum temperature was 1500 ºC, and the rate of temperature increase was 10 ºC/min. The products of hydration were investigated with the scanning electronic microscope JSM–5600 (JEOL). The electron emitter of the microscope (cathode) was made of wolfram, the resolution power was 3.5 nm, enlargement 18–300000×, voltage accelerating electron flux was 0.5–30 kV.

The consistency of the paste was determined using Suttard viscometer. The density and compressive strength of cubes of hardened cement paste ($20\times20\times20$ mm^3) were tested 3, 7 and 28 days after preparation.

3. Results and discussions

The consistency of cement pastes is presented in Table 1. With the increasing content of hydrosodalite, the fluidity of cement paste decreases which may be explained by high surface area and porosity of the hydrosodalite additive.

Table 1. The consistency of cement pastes
with various contents of hydrosodalite

Content of hydrosodalite [%]	Consistency of cement paste [mm]
0	28
5	24
10	15
15	9

The X-ray diffraction patterns of hydrosodalite are given in Fig. 1 (lower curve). First, hydraulic activity of hydrosodalite was determined. X-ray diffraction patterns of hydrosodalite after chemisorption of CaO from saturated $Ca(OH)_2$ solution are also shown in Fig. 1 (upper curve).
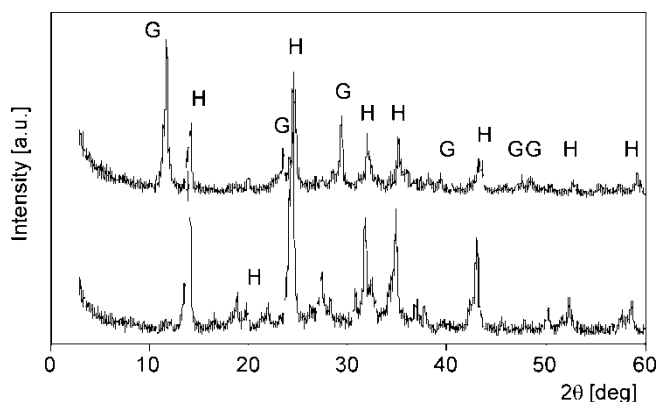
Fig. 1. X-ray diffraction patterns of hydrosodalite: lower curve – pure hydrosodalite;
upper curve – after hydraulic activity test; G – gismundite, H – hydrosodalite

After 28-day chemisorption, a part of hydrosodalite reacted with the $Ca(OH)_2$ contained in water and was transformed into calcium zeolite – gismundite ($CaAl_2Si_2O_8 \cdot 4H_2O$), which formed hydrosodalite upon replacement of Na with Ca. In this case, an ion exchange typical of zeolites takes place [9]. It was also established that during chemisorption the volume of the solid phase (volume of deposits) increases nearly 4 times. Volume expansion may have a negative effect on the strength of the hardened cement paste. Volume expansion was also noticed when zeolites were formed in cement hardened paste [9]. Hydrosodalite under investigation has a fairly high hydraulic activity (370 mg/g), higher than that of opoca (281 mg/g) and microsilica (352 mg/g) but lower than that of tripolite (401 mg/g) [10] rather due to the presence of SiO_2 and Al_2O_3 than the content of SiO_2 or specific surface.

The investigation of X-ray diffraction patterns of hardened cement paste with hydrosodalite admixture shows that when the content of hydrosodalite increases from 0 to 15%, the content of $Ca(OH)_2$ in the mineralogical composition of hardened cement paste decreases. $Ca(OH)_2$ peaks of 0.493 nm interplane distances in Fig. 2 are more intensive without hydrosodalite admixture, and when hydrosodalite is added (5, 10 or 15%), lower intensities of the peaks are observed (Fig. 2b).

Upon increasing duration of curing (Fig. 2, curves 1 and 2), the content of $Ca(OH)_2$ rises, and more $3CaO \cdot SiO_2$ and $2CaO \cdot SiO_2$ converts into calcium hydrosilicate and calcium hydroxide. This tendency is still more distinct when the specimens are steam-cured in a steam-curing chamber (Fig. 2a, curve 3).

When 5 and 10% of hydrosodalite was added to the hardened cement paste, the X-ray diffraction patterns of the hydration products did not reveal the presence of the mentioned additive but part of the non-reacted hydrosodalite remains after 3, 7 and 28 days of curing when using 15% of hydrosodalite. After steam-curing, hydrosodalite reacted and the X-ray diffraction patterns did not show any peaks of hydrosodalite (Fig. 2b, curve 3).
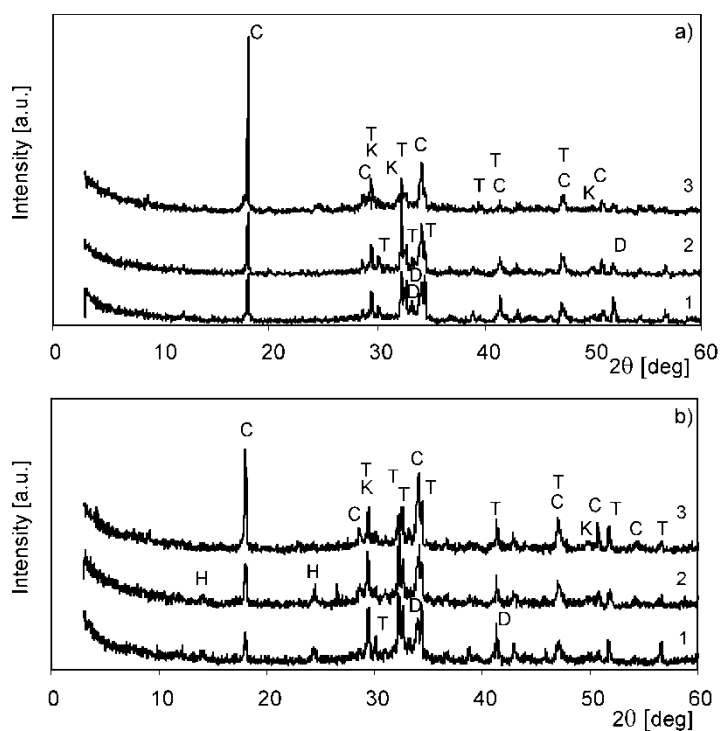
Fig. 2. X-ray diffraction patterns of hardened cement paste with 0% (a) and 15% (b)
of hydrosodalite: 1 – after 3 days; 2 – after 28 days; 3 – after steam curing at 90 ºC for 24h;
C – Ca(OH)$_2$; T – 3CaO·SiO$_2$; K – C–S–H(II); D – 2CaO·SiO$_2$; H – hydrosodalite

The secondary processes take place among the clinker hydration products and hy-
draulic admixtures. First of all this is the reaction between Ca(OH)$_2$ and hydrosodalite.
Hydrosodalite reacts with Ca(OH)$_2$ and passes into gismundite. In the X-ray diffraction
patterns, it is difficult to identify the peaks typical of gismundite because hydrosoda-
lite was blended into the mix as admixture (up to 15% of cement mass) and the peaks
of other main compounds cover the peaks characteristic of this mineral. At typical
conditions and a typical temperature, the C–S–H(I) type compound (0.8-1.5)CaO–SiO$_2$
–(0.5-2.5)H$_2$O is formed and its basicity depends on the concentration of Ca(OH)$_2$ in
the liquid medium. After hydrosodalite reacts with Ca(OH)$_2$, NaOH is released and
alkali, which reduce the concentration of Ca(OH)$_2$, emerge in the liquid phase. The
most frequent compound is 3CaO·2SiO$_2$·3H$_2$O (C$_3$S$_2$H$_3$) which depends on
C-S-H(II) type for calcium hydrosilicates. Taking into consideration the fact that
the structures of calcium hydrosilicates are similar to the structure of natural to-
bermorite 5CaO·6SiO$_2$·5H$_2$O (C$_5$S$_6$H$_5$), they are called minerals of the tobermo-
rite group.
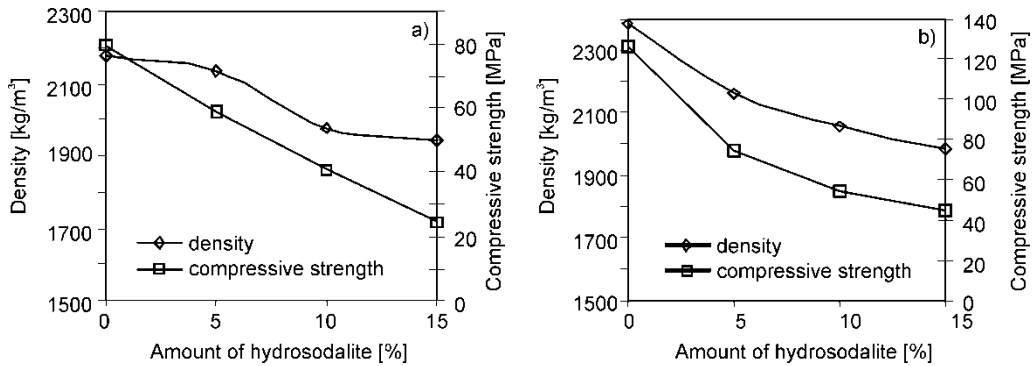
Fig. 3. Dependence of density and compressive strength of hardened
cement paste on the additive amount after 3 days (a) and after 28 days (b)

The density and compressive strength of hardened cement paste decreases with increasing hydrosodalite amount (Fig. 3). The density of hardened cement paste after 3–7 days of curing decreases from 2160–2180 kg/m^3 to 1920–1950 kg/m^3, i.e. by about 11% (Fig. 3a). The density decreases proportionally to the content of hydrosodalite. This determines a decrease in the compressive strength of the hardened cement paste. After 3 days of curing it decreases by about 70%; after 7 days of curing – 66% and after 28 days of curing – about 65% (Fig. 3b).
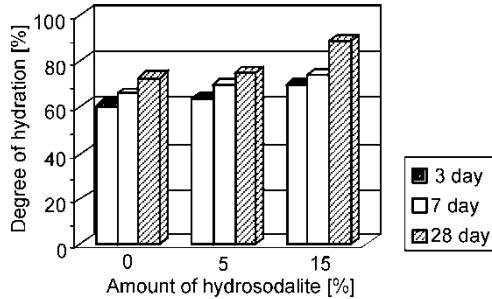
Fig. 4. Influence of additive amount on the hydration
degree of hardened cement paste

The degree of cement hydration increases when the content of hydrosodalite increases (Fig. 4) but the strength of hardened cement paste decreases (Fig. 3b). The reduction of the strength of hardened cement paste is caused by different microstructure of the hardened cement paste but not by the retardation of cement hydration process.

Microscope inspection of the hardened cement paste was carried out, revealing large hexagonal crystals of calcium hydroxide and their adhesions in hardened cement paste without hydrosodalite (Fig. 5a). Upon the addition of 15% of hydrosodalite, smaller hexagonal crystals of calcium hydroxide, which are more distant from one another, as well as larger amount of amorphous mass, are obtained (Fig. 5b). Multi-

mineral products of cement hydration are nearly amorphous compounds forming from C–S–H needles and their network, and the gaps are filled with the substance of undefined structure as well as with $Ca(OH)_2$ crystals and non-hydrated cement phases. A disordered arrangement of these structures is observed.
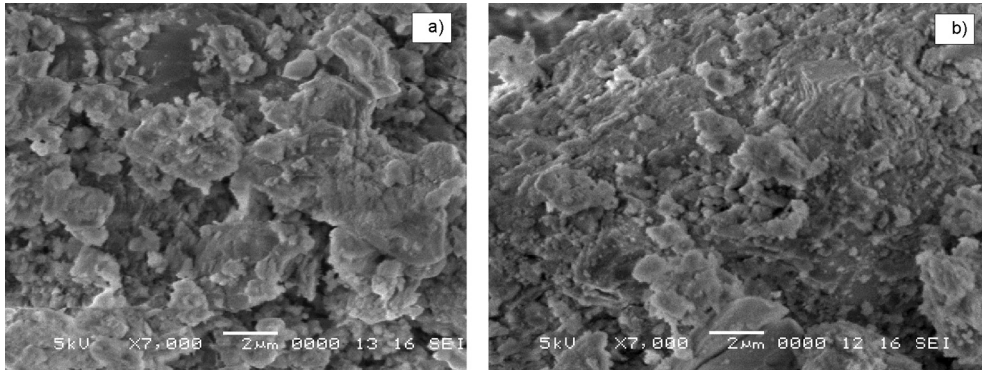
Fig. 5. Microscope photos: hardened cement paste without hydrosodalite (a)
and hardened cement paste with 15% of hydrosodalite (b)
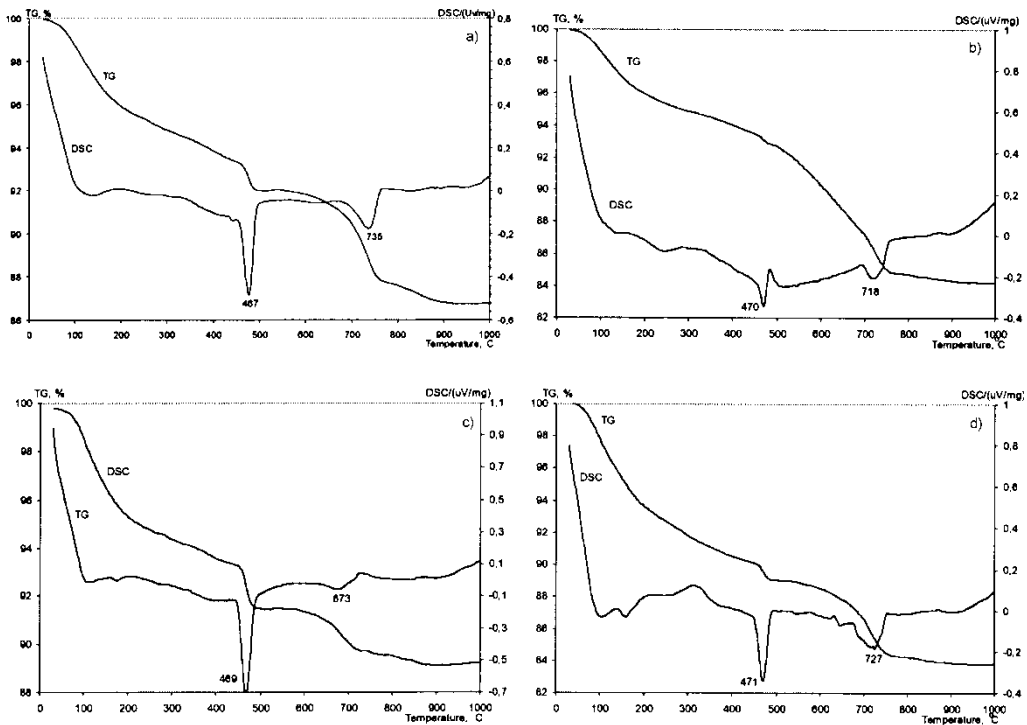
Fig. 6. DTA curves: hardened cement paste without hydrosodalite after 3 days (a); hardened cement paste with 15% hydrosodalite after 3 days (b); hardened cement paste without hydrosodalite after 28 days (c) and hardened cement paste with 15% hydrosodalite after 28 days (d)

In order to supplement the results of X-ray diffraction analysis, thermal analysis of the tested hardened cement paste specimens was performed. It is considered that endothermal peaks in the 100–200 ºC temperature range display water loss from the tobermorite gel phase. Another intense endothermal peak, visible in all the DSC curves (Fig. 6), within the temperature range of 467–481 ºC corresponds to the de-composition of $Ca(OH)_2$. Peaks within the temperature range of 718–735 ºC are linked with water loss from calcium hydrosilicate $(1.5–2.0)CaO·SiO_2·nH_2O$ similar to tober-morite. Belite $2CaO·SiO_2$ forms at this temperature [11].

Based on TG curves, it can be stated that the content of $Ca(OH)_2$ in the hardened cement paste with hydrosodalite admixture decreases upon increasing amount of the hydrosodalite. In Figure 6, TG curves a) and c) show a higher calcination loss than b) and d) curves (1.33 and 1.82%, vs. 0.68 and 1.10%). As the duration of specimen curing increases, the content of $Ca(OH)_2$ also increases because calcination loss related to $Ca(OH)_2$ increases from 1.33% to 1.82%, without using hydrosodalite admixture, and increases from 0.68 to 1.10%, when applying 15% of the admixture. The thermal analysis results confirm those of X-ray diffraction analysis.

4. Conclusions

• The additive of hydrosodalite can be used as a puzzolanic admixture for Portland cement due to its high hydraulic activity.

• The additive of hydrosodalite reduces the content of $Ca(OH)_2$ in the hardened cement paste when it forms some amount of calcium zeolite gismundite, and NaOH, as it is demonstrated by X–ray diffraction and thermal analysis results.

• Reduction of $Ca(OH)_2$ content influences the formation of hydrosilicates $3CaO·2SiO_2·3H_2O$ of lower alkalinity in the hardened cement paste with hydro-sodalite.

• The density of the hardened cement paste containing hydrosodalite after 3, 7 and 28 days of curing decreases by about 11%. This determines a decrease in the compres-sive strength of the hardened cement paste. The compressive strength after 3 days of curing decreases by about 70%, after 7 days of curing – by 66%, and after 28 days of curing – by about 65%.

References

[1] Canpolat F., Yilmaz K., Köse M. M., Sümer M., Yurdusev M.A., Cement Concr. Res., 34 (2004), 731.

[2] Feng N. Q., Yang H.M., Zu L.H., Cement Concr. Res., 18 (1988), 464.

[3] Ku R., *Super High Strength Concrete*. US Patent Application: 20020117090, Law Office of Liauh & Assoc (2002).

[4] Santerre J., Friedman S., *Antimicrobial Cement Compositions*, International application published under the patent cooperation: WO 99/07326, Riches McKenzie and Herbert (1999).

[5] JANOTKA I., Ceramics-Silikaty 43 (1999), 61.

[6] JANOTKA I., KRAJCI L., DZIVAK M., Clays Clay Miner., 51 (2003), 616.

[7] JANOTKA I., MOJUMDAR S., *Hydration of Portland cement – natural zeolite mortar in water and sulphate solution*, [in:] Proc. 5th Solid State Chemistry, Bratislava, Slovak Republic (2002).

[8] MUMPTON F.A., *La roca magica: Uses of natural zeolites in agriculture and industry*, The National Academy of Sciences. Proc. Natl. Acad. Sci., USA 96 (1999), 3463.

[9] KOMARNENI S., ROY D. M., ROY R., Cement Concr. Res., 12 (1982), 773.

[10] BULOTAITE J., *The investigation of binding materials with puzzolans admixture*, MSci Thesis, KTU Kaunas (1999), p. 58 (in Lithuanian).

[11] GORSHKOV V.S., *The physical and chemical methods of binding materials analysis*, Vyzshaja Shkola. Moscow, 1981, p. 335 (in Russian).

The influence of Al containing component on synthesis of analcime of various crystallographic systems

A. BALANDIS[*], A. TRAIDARAITE

Department of Silicate Technology, Faculty of Chemical Technology,
Kaunas University of Technology, Radvilenu st. 19, 50254 Kaunas, Lithuania

The influence of the form of the Al-containing component, molar ratio of Na_2O:Al_2O_3:SiO_2, and the duration of isothermal curing under saturated steam at 180 °C have been examined. The results obtained experimentally show that the form of the Al-containing component ($Al(OH)_3$ or γ-Al_2O_3) significantly affects the formation of crystal system of analcime. Pure analcime of the tetragonal crystallographic system forms under saturated steam at 180 °C after 7 h of isothermal curing, in the presence of considerable excess of NaOH, only when $Al(OH)_3$ is used in the initial mixture. Pure analcime of the cubic crystallographic system forms when γ-Al_2O_3 is used in the initial mixture of hydrothermal synthesis.

Key words: *analcime; zeolite; $Al(OH)_3$; γ-Al_2O_3; hydrothermal synthesis*

1. Introduction

Analcime $NaAl(Si_2O_6)\cdot(H_2O)$ belongs to minerals of tectosilicate group with zeolitic structure [1]. Due to the similarity of structure, under natural conditions it often crystallizes in magmatic vein rocks with a low SiO_2 content, as well as in metamorphic and hydrothermal vein rocks in paragenetic associations together with pollucite, wairakite, faujasite, paulingite, viseite and other zeolites [2]. New examinations have shown that natural analcime, depending on the conditions of its formation and impurities, may belong to the cubic, tetragonal, orthorhombic, monoclinic or triclinic crystallographic systems. At room temperature, differences between the crystal lattice parameters *a*, *b*, and *c* normally do not exceed a few hundred or even thousand nanometers, and deviations of the angles α, β, and γ from 90° are also minor and do not exceed 0.2–0.4°. These facts explain certain difficulties in identifying analcime modifications belonging to various crystallographic systems in the products of the synthesis.

_____

[*]Corresponding author, e-mail: alfredas.balandis@ktu.lt

Analcime, like other minerals of zeolitic structure, boasts a variety of application possibilities in technologies. Recently, analcime has received increased attention from electronics specialists who have started research on synthetic pure fine-dispersive minerals of the zeolitic structure due to their specific interaction with magnetic fields. The centres of positive and negative charges in the crystal lattice of analcime with the orthorhombic crystal system do not coincide, resulting in formation of a polar lattice. Another field of analcime application is stomatology. Cubic analcime can be used for obtaining cubic leucite (through ion exchange under hydrothermal conditions), which is a very important component of dental porcelain [3–6].

Despite the fact that natural zeolites are cheaper than their synthetic counterparts, their use is limited by contamination with impurities. Such important fields as energy economy control of environment pollution, hydrocarbon separation, bifunctional catalysis, production of dental porcelain and other normally use pure synthetic zeolites.

Synthetic analcimes, as a rule, belong to tetragonal, orthorhombic or cubic crystallographic systems. It has been established [2] that during heating of the orthorhombic analcime from room temperature to 150 °C, the a parameter of its crystal lattice slightly increases from 1.3720 to 1.3728 nm. However, it unevenly declines with a further increase of temperature from 150 °C to 400 °C and at 800 °C it slumps to 1.3640 nm. Consequently, at 400 °C, the crystal lattice of the orthorhombic analcime greatly differs from the cubic one. If, under change of temperature, such uneven changes in the size of the crystal analcime lattice take place within a crystal, they cause internal tensions in the crystal along with significant decrease in the material strength leading to its cracking, for instance, in dental porcelain veneers. With regard to temperature impact, cubic analcime and cubic leucite are more preferable in ceramic composites because increasing temperature does not change the type of their crystal lattice.

The syngonic type of an analcime forming during the synthesis has a great practical importance. However, the conditions influencing the syngonic type of analcime have not been sufficiently examined. The changes in the crystallographic system of analcime synthesized from amorphous melts under hydrothermal conditions, the impact of high temperatures and high pressures have been analysed [7]. It has been established that analcimes of low category crystallographic systems, i.e. triclinic and monoclinic form at low temperature (80–160 °C) under the pressure of 100 MPa. When the temperature of synthesis rises, the number of symmetry elements grows and analcimes of orthorhombic, tetragonal and cubic crystal systems are formed.

Various authors [8–10] report on very different conditions of synthesis of analcime. Some authors [7] claim that the crystal system of analcime synthesized depends on the temperature and pressure of the hydrothermal synthesis. Under the pressure from 100 MPa to 200 MPa and within the temperature range of 160–400 °C, the analcime of cubic crystal system is the final product of the synthesis. But other authors [11], having examined the synthesis of analcime under 100 MPa, stated that the sym-

metry of the formed analcime depends on the initial materials and on the temperature of hydrothermal synthesis.

The synthesis of analcime under hydrothermal conditions and at comparatively low pressures, which could also be maintained in industrial equipment, has not been explored much. All the papers state that the synthesis of analcime has to be carried out in the presence of NaOH excess but there are different opinions on the minimal ratio of $Na_2O:Al_2O_3$ in initial mixtures.

So far too little attention has been paid to the Al containing component being one of the most important initial components of analcime synthesis. Taking into consideration the fact that the synthesis of analcime occurs in aqueous suspensions, in our opinion, the Al containing component is very important in the processes of analcime formation with regard to the amphoteric properties of aluminium compounds (Al_2O_3 or $Al(OH)_3$) and the formation of an isoelectric point in the suspensions of synthesis.

Analcime belongs to zeolites whose crystal structures do not change during the dehydration when they are heated up to 900–1000 °C. However, parameters of the crystalline lattice of analcimes of different crystal system change nonuniformly upon changing temperature. The parameters of the crystal lattice of analcime of cubic crystal system change most evenly when the temperature is increasing. This stipulates the importance of the analcime of cubic crystal system in the processes of sorption, catalysis and production of technical ceramics. However, the factors determining the crystal system type of analcime which is formed during hydrothermal synthesis have been investigated very poorly.

The aim of this paper was to analyze the influence of chemical properties of Al containing component and preparation conditions of γ-Al_2O_3 on the crystal system of analcime, forming under hydrothermal conditions.

2. Experimental

Amorphous $SiO_2 \cdot n H_2O$ was milled in a porcelain grinder for 1 h and sieved through a sieve with a mesh width of 80 μm (specific surface area S_a = 1301 m^2/kg by Blaine, ignition losses – 23.84%). The following Al containing components were used: $Al(OH)_3$ pure – gibbsite (S_a = 104.9 m^2/kg by Blaine) and two types of γ-Al_2O_3 γ-Al_2O_3 (I) (S_a = 273,9 m^2/kg by Blaine) was obtained by heating $Al(OH)_3$ at 550 ºC for 3 h while γ-Al_2O_3 (II) (S_a = 179,6 m^2/kg by Blaine) was obtained by heating $Al(OH)_3$ at 475 ºC for 4 h. NaOH solution (c = 11%) was obtained by dissolving NaOH in distilled water.

Analcime was synthesized from the mixtures $Na_2O:Al_2O_3:SiO_2$ in stainless steel and/or fluoroplastic vessels in an autoclave *Lampart* using the compositions of initial mixtures given in Table 1.

NaOH was added as an aqueous solution. An addition of NaOH corresponded to 11% of Na_2O in the dry materials, so that the water/solid ratio of the suspension was equal to 5.0.

Table 1. Compositions of initial mixtures used for synthesis of analcime

No.	Molar content in mixture			Percentage content in mixture		
	Na_2O	Al_2O_3	SiO_2	Na_2O	Al_2O_3	SiO_2
1	2	1	3	30.54	25.12	44.34
2	2	1	4	26.61	21.89	51.50
3	2	1	5	23.57	19.39	57.04
4	2	1	6	21.16	17.41	61.43
5	4	1	3	46.79	19.25	33.96
6	4	1	4	42.03	17.29	40.68
7	4	1	5	38.15	15.69	46.15
8	4	1	6	34.93	14.37	50.70

Hydrothermal synthesis of analcime in unstirred suspensions has been carried out under the saturated steam pressure at a temperature of 180 ºC; the duration of isothermal curing was 5 or 7 h. The products were filtrated, rinsed with ethyl alcohol to prevent carbonization of the material, dried at 30±5 ºC and sieved through a sieve with a mesh width of 80 μm. The X-ray powder diffraction data were collected with DRON–6 X-ray diffractometer with the Bragg–Brentano geometry using Ni-filtered Cu K_α radiation and graphite monochromator, operating with the voltage of 30 kV and emission current of 20 mA. The step-scan covered the angular range 2–60º (2θ) in steps of $2\theta = 0.02^o$. Differential scanning calorimetry (DSC) was employed for measuring the thermal stability and phase transformation of the synthesized products at the heating rate of 15 ºC/min, the temperature ranged from 30 ºC up to 1000 ºC under ambient atmosphere. The test was carried out on a Netzsch instrument STA 409 PC Luxx. The ceramic sample handlers and crucibles of Pt-Rh were used. The specific surface area was determined by Blaine's method with air permeability apparatus (Model 7201, Toni Technik Baustoffprufsysteme GmbH).

3. Results and discussion

A series of analcime syntheses with the molar $Na_2O:Al_2O_3:SiO_2$ ratios of 2:1:3, 2:1:4, 2:1:5, 2:1:6 were performed with the aim to investigate the possibility of analcime synthesis under a minimal excess of NaOH (2 mole Na_2O). The use of Al_2O_3 in the synthesis as an Al containing component is related to certain peculiarities of chemical processes. Al_2O_3 reacts with sodium hydroxide and sodium aluminate $NaAl(OH)_4$, well dissolving in water, forms. However, when the molar ratio of $Na_2O:Al_2O_3$ is around 1.7, $Al(OH)_3$ crystals precipitate from sodium aluminate solutions. To prevent the precipitation, the solution should be heated at 150–200 ºC for 4–6 h [13]:

$$Al(OH)_3 + NaOH + H_2O \rightarrow NaAl(OH)_4 + H_2O$$

The decomposition of sodium aluminate accelerates when the solution contains large amounts of $Al(OH)_3$. When NaOH solution contains soluble SiO_2, the reaction between Na_2SiO_3 and $NaAl(OH)_4$ results in formation of sodium aluminium silicates, including analcime. However, the lower the concentration of sodium aluminium silicate, the more energetic is formation of sodium aluminium silicate. Thus, to avoid decomposition of sodium aluminate and formation of less soluble crystals of $Al(OH)_3$, the molar ratio of $Na_2O:Al_2O_3$ in initial mixtures should be higher than 2.0. Another important factor in is the dissolving rate of Al_2O_3 that depends on both the modification of Al_2O_3 and the size of its crystals.

The Al containing component for the synthesis was prepared by heating pure $Al(OH)_3$ at 550; 525; 500; 475 and 450 ºC for 1–6 h in order to avoid formation of high-temperature, less soluble, and chemically less active α-Al_2O_3, and, on the other hand, to reduce the energy used to prepare the Al containing component. Basing on the results of X-ray diffraction analysis, it has been established that an active γ-Al_2O_3 forms when $Al(OH)_3$ is heated at 550 ºC for 1 h. Therefore, the formation processes of γ-Al_2O_3 were analyzed at lower temperatures (525, 500, 475 and 450 ºC). The characteristic curves of X-ray diffraction analysis of the obtained products are shown in Fig. 1.
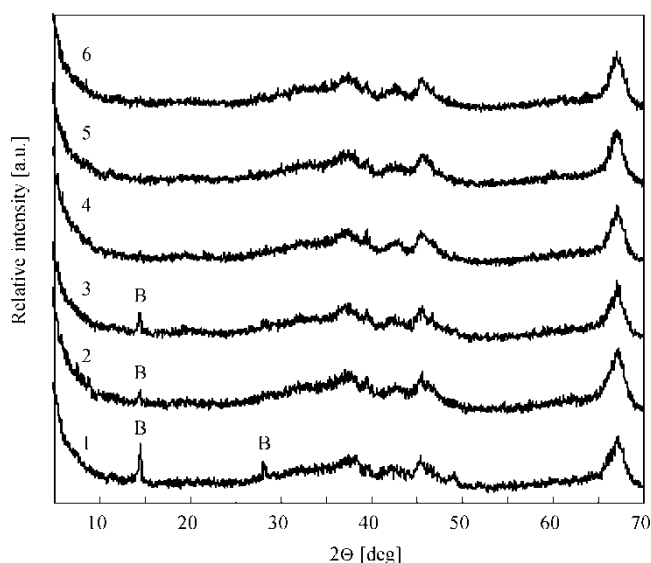
Fig. 1. X-ray diffraction patterns of the Al containing component – γ-Al_2O_3
obtained from pure $Al(OH)_3$ at various conditions: 1 – 450 ºC, 5 h; 2 – 450 ºC, 8 h;
3 – 475 ºC, 3 h; 4 – 475 ºC, 4 h; 5 – 550 ºC, 1 h; 6 – 550 ºC, 3 h; B – boehmite

The X-ray diffraction analysis of the obtained products has shown that even after 8 h of isothermal curing at 450 ºC, not only γ-Al_2O_3, but also hydrated Al_2O_3 – boehmite – forms during decomposition of $Al(OH)_3$. At a higher decomposition tempera-

ture of Al(OH)$_3$ – 475 ºC, γ-Al$_2$O$_3$ can be obtained after 4 h of isothermal curing. But the specific surface of the obtained crystals is 179.6 m^2/kg, whereas that of γ-Al$_2$O$_3$ obtained at 550 ºC amounts to 273.9 m^2/kg. These data confirm formation of bigger γ-Al$_2$O$_3$ crystals at 475 ºC, which, in turn, might have a negative influence on the dissolution processes of the Al containing component during the synthesis of analcime.

Having evaluated the modification activity, purity and dispersity of forming Al$_2$O$_3$, γ-Al$_2$O$_3$ (I) and γ-Al$_2$O$_3$ (II) were used for the synthesis of analcime. Another series of analcime syntheses was performed by using pure Al(OH)$_3$ as the Al containing component.

In the first stage of this research, analcime was synthesized from initial mixtures with the following component ratios after recalculation into molar oxide ratios: Na$_2$O:Al$_2$O$_3$:SiO$_2$ = 2:1:3; 2:1:4; 2:1:5; 2:1:6. Hydrothermal synthesis was performed at 180 ºC with isothermal curing of 5 h. After filtering and rinsing the products of synthesis, the amount of NaOH in the filtrate was established, and the reaction degree of NaOH was determined. The mineral composition of the solid phase was analyzed using X-ray diffraction and differential scanning calorimetry. The filtrate analysis data are given in Table 2.

Table 2. NaOH reaction degree [%] at 180 ºC after 5 h of isothermal curing

Al containing component	Molar ratio Na$_2$O:Al$_2$O$_3$:SiO$_2$			
	2:1:3 (44.34% SiO$_2$)	2:1:4 (51.50% SiO$_2$)	2:1:5 (57.04% SiO$_2$)	2:1:6 (61.43% SiO$_2$)
Al(OH)$_3$	94.04	94.87	93.36	90.07
γ-Al$_2$O$_3$ (I)	95.33	94.38	93.69	91.36
γ-Al$_2$O$_3$ (II)	92.19	96.62	95.99	90.77

At the Na$_2$O:Al$_2$O$_3$ molar ratio equal to 2.0, nearly all sodium hydrate contained in the initial mixture reacts (94–97%) under the conditions of synthesis. The degree of sodium hydrate reaction is noticeably lower at the presence of an excess of SiO$_2$ (molar ratio of SiO$_2$:Al$_2$O$_3$ equal to 6:1). The highest NaOH reaction degree was obtained for the initial mixture Na$_2$O:Al$_2$O$_3$:SiO$_2$ = 2:1:4. Since the obtained products had grey colour, the synthesis was repeated by synthesizing analcime not only in stainless steel, but also in small white fluoroplastic vessels. The products obtained in fluoroplastic vessels had clear white colour, and, in addition, for all Al containing components, the NaOH reaction degree was higher: in stainless steel vessels it was 91.85–93.21%, while in fluoroplastic vessels it amounted to 94.38–96.62%. This makes us suppose that during the synthesis of analcime, the sodium solution interacts even with stainless steel, slowing down the processes of analcime synthesis.

The X-ray diffraction analysis of dried reaction products (Fig. 2) has shown that during 5 h of isothermal curing at 180 ºC, pure analcime did not form in the initial

mixtures with the molar ratios of 2:1:(3–6), neither using $Al(OH)_3$ nor γ-Al_2O_3, obtained under various conditions as the Al containing component.

Fig. 2. X-ray diffraction patterns of the products formed after 5 h of hydrothermal synthesis at 180 ºC. The molar ratios of the initial mixtures $Na_2O:Al_2O_3:SiO_2$ are: 2:1:4 (curves 1–3) and 2:1:6 (curves 4–6). Al containing components: 1, 4 – $Al(OH)_3$; 2, 5 – γ-Al_2O_3 (I); 3, 6 – γ-Al_2O_3 (II); A_C – cubic analcime, A_T – tetragonal analcime, B – boehmite, P2 – zeolite P2, S – sodium aluminium silicate, M – mordenite

Apart from analcime $Na(AlSi_2O_6)\cdot(H_2O)$, also sodium aluminium silicate $Na_6(AlSiO_4)_6$ and zeolite P2 – $Na_4(Al_4Si_{12}O_{32})(H_2O)_{14}$ have been identified in the products of reaction. The mixtures prepared with $Al(OH)_3$ as an Al containing component produced analcime of the tetragonal crystallographic system (diffraction reflections established with 100% reliability: 5.6124; 4.8587; 3.4307; 2.9253 nm, etc). At

the same time, the synthesis of initial mixtures prepared with γ-Al$_2$O$_3$ as an Al containing component produced analcime of the cubic crystallographic system (diffraction reflections established with 100% reliability: 5.6072; 3.4294; 2.9235; 2.2230 nm etc.).

DSC curves of products of the synthesis showed (Fig. 3) that pure analcime did not form during this synthesis. Curve 1 shows that not only the "broadened" endothermic effect at 342 ºC of the main product is present but also the endothermic effect of zeolite P2 and the effect of unreacted Al(OH)$_3$ at 139 ºC and 570 ºC, respectively, are observed. The exothermic effect at 954 ºC is not related to weight loss at this temperature, i.e. the sample does not contain water, and therefore it shows the change of structural zeolite frame. When γ-Al$_2$O$_3$ (I) was used for the synthesis (curve 2), it was observed that less byproducts were formed and the obtained product was more stable. Changes of the structure of analcime are not observed even between 900 ºC and 1000 ºC, when all forms of water have been removed.
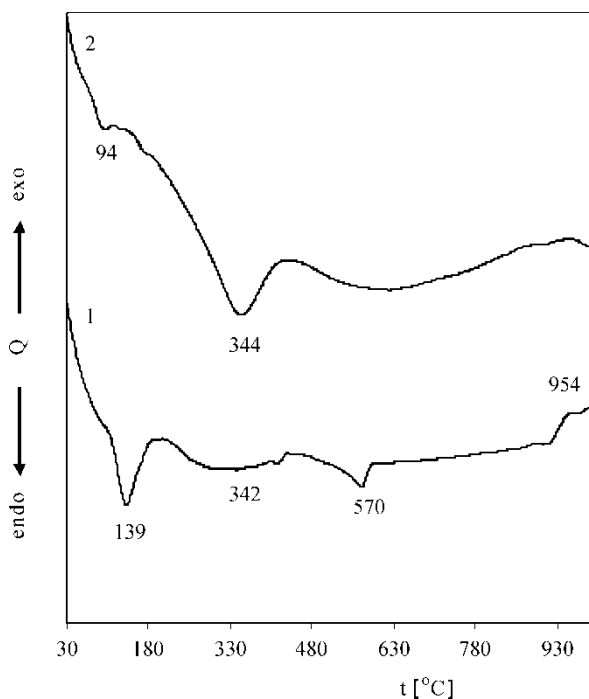
Fig. 3. DSC curves of the products formed after 5 h of hydrothermal
synthesis at 180 ºC. The molar ratio of the initial mixture Na$_2$O:Al$_2$O$_3$:SiO$_2$ – 2:1:4.
The Al containing components: 1 – Al(OH)$_3$; 2 – γ-Al$_2$O$_3$ (I)

Upon prolongation of the synthesis time at 180 ºC to 7 h, the trends of NaOH reaction practically did not change both in stainless steel and in fluoroplastic vessels. The composition the products also remained the same but, apart from analcime of the cubic and tetragonal crystallographic system, less hydrated sodium aluminium silicates, such as mordenite, formed.
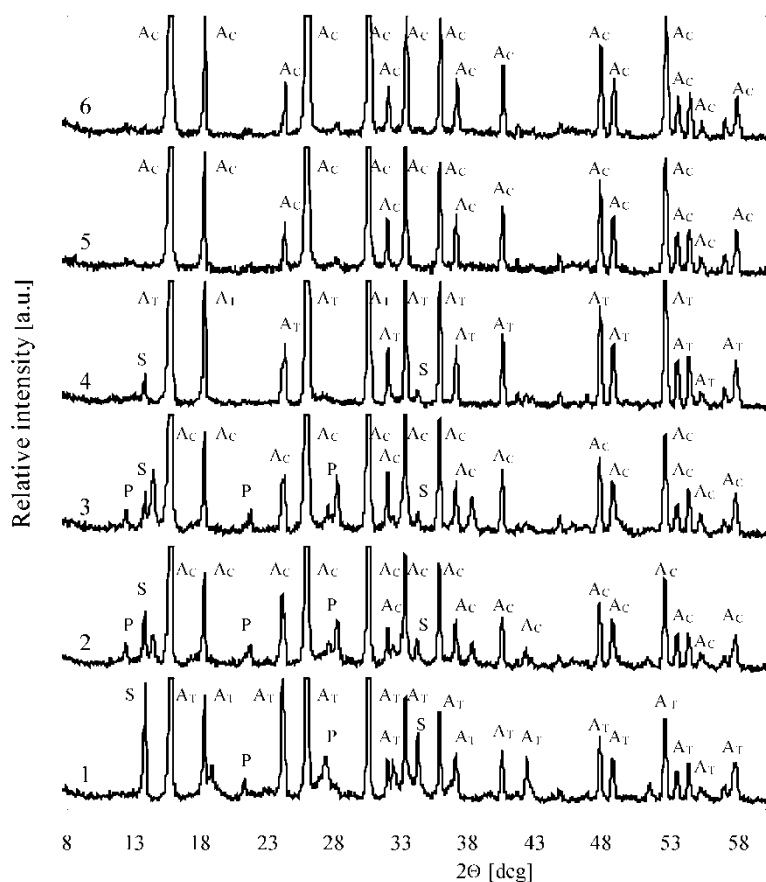
Fig. 4. X-ray diffraction patterns of the products formed after 7 h of hydrothermal synthesis at 180 ºC.
The molar ratios of the initial mixtures $Na_2O:Al_2O_3:SiO_2$: 4:1:4 (curves 1–3) and 4:1:6 (curves 4–6).
The Al containing components were: 1, 4 – $Al(OH)_3$; 2, 5 – γ-Al_2O_3 (I); 3, 6 – γ-Al_2O_3 (II);
A_C – cubic analcime, A_T – tetragonal analcime, P – zeolite P, S – sodium aluminium silicate

Taking into consideration the results of these syntheses and the influence of sodium hydroxide on the solubility and stability of sodium aluminates, in the next stages analcime was synthesized from the mixtures $Na_2O:Al_2O_3:SiO_2$ of molar ratios 4:1:(3–6). Hydrothermal synthesis was performed at 180 ºC, the period of isothermal curing was 5 h and 7 h. According to expectations, the products of synthesis after reaction contained a higher amount of unreacted NaOH, thus ensuring a sufficient excess of sodium hydroxide within the entire period of the synthesis of analcime. Based on the results of X-ray diffraction analysis and DSC methods, it has been established that pure analcime also did not form at 180 ºC after 5 h of isothermal curing. Sodium aluminium silicates and zeolite P have been identified in the products of reaction. However, on extending the duration of isothermal curing to 7 h (Fig. 4), the mixture $Na_2O:Al_2O_3:SiO_2$ with the molar ratio 4:1:6, produced pure analcime: the tetragonal crystallographic system analcime when using $Al(OH)_3$ as an Al containing component

(curve 4), and the cubic crystal system analcime when using γ-Al_2O_3 as an Al containing component (curves 5, 6).

DSC curves (Fig. 5) of the products of synthesis of analcime confirm that an increase of the amount of NaOH in the initial mixtures influences the formation of analcime and making it easier even when $Al(OH)_3$ is used as an initial Al source, (curve 1). In addition, the amount of zeolite P decreased in the products obtained if compared with analcime, when the mixture of Na_2O and Al_2O_3 with the molar ratio of 2:1 was used for the synthesis. If the amount of SiO_2 was increased in the initial mixtures, no byproducts, i.e. other zeolites, were observed during the DSC experiments (curves 3, 4). Although the DSC behaviour of analcime crystals belonging to tetragonal and cubic crystallographic systems during the DSC experiment is similar, still some differences could be observed and probably it could be related to higher stability of cubic crystal system analcime crystals during dehydration process. The endothermic effect for both analcimes was observed in the temperature range of 350–360 ºC in the DSC experiment and this effect is due to dehydration process but the area under the DSC curve in the same temperature range is 20% smaller in the case of cubic analcime.
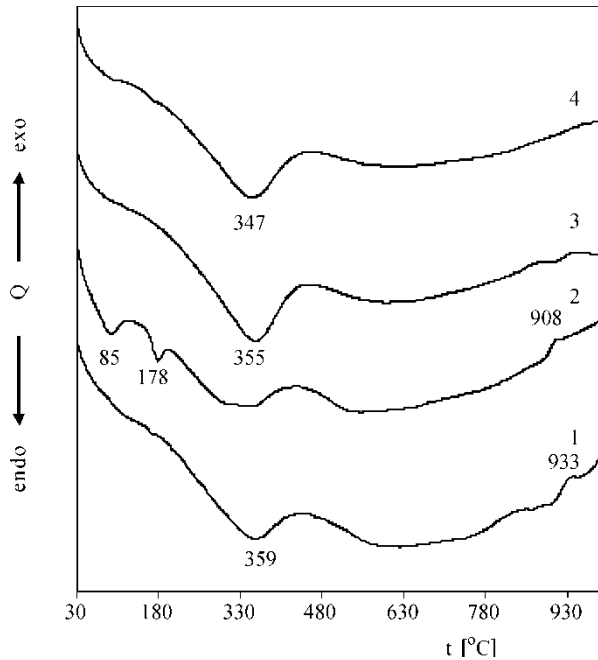
Fig. 5. DSC curves of the products formed after 7 h of hydrothermal synthesis at 180 ºC. The molar ratios of the initial mixtures are: Na_2O:Al_2O_3:SiO_2 – 4:1:4 (curves 1, 2) and 4:1:6 (curves 3, 4); Al containing components: 1, 3 – $Al(OH)_3$; 2, 4 – γ-Al_2O_3 (I)

When the excess of NaOH was greater, a larger amount of SiO_2 also reacted during the formation of analcimes. For other molar ratios of initial components sodium

aluminium silicates and zeolite P have been identified in the products of reaction. In addition, it has been noticed that the reaction degree of sodium hydroxide was slightly higher (by ca. 1.0–1.5%) when using pure $Al(OH)_3$ as an Al containing component and performing synthesis in fluoroplastic vessels.

4. Conclusions

• Chemical nature of Al containing components is very important for the course of synthesis of analcime and its crystal structure. Tetragonal analcime formed only when using $Al(OH)_3$ in the initial mixtures, while cubic analcime – when using γ-Al_2O_3.

• Pure tetragonal and cubic analcimes formed at 180 ºC after 7 h of isothermal curing only in the presence of considerable excess of NaOH in the initial mixtures when the molar ratio of the components $Na_2O:Al_2O_3:SiO_2$ was 4:1:6.

• The conditions of γ-Al_2O_3 formation from pure $Al(OH)_3$ affect the course of analcime synthesis. If pure $Al(OH)_3$ is heated at 475 ºC, larger γ-Al_2O_3 crystals of smaller specific surface have formed compared to the product heated at 550 ºC; therefore, the synthesis of analcime at 180 ºC is impeded and the NaOH reaction degree decreases.

• The synthesis of analcime is a little more efficient when using $Al(OH)_3$ as an Al containing component.

References

[1] FRYE K., *The Encyclopedia of Mineralogy*, Nedra, Leningrad, 1985 (in Russian).
[2] CRUCIANI G., GUALTIERI A., Amer. Mineral., 84 (1999), 112.
[3] PRASAD A., VAIDYANATHAN T.K., J. Dental Res., 69 (1990), 2.
[4] DENRY I.L., MACKERT J.R., HOLLOWAY J.A., ROSENSTIEL S.F., J. Dental Res., 75 (1996), 1928.
[5] RASMUSSEN S.T., GROH C.L., O'BRIEN W.J., Dental Mater., 14 (1998), 202.
[6] SATAVA V., KLOUZKOVA A., LEZAL D., NOVOTNA M., Ceramics-Silikaty, 46 (2002), 37.
[7] GHOBARKAR H., SCHAF O., Mater. Sci. Eng. B, 60 (1999), 163.
[8] PALUBINSKAITE D., SIAUCIUNAS R., SINKEVICIENE I., SADUNAS A., Mater. Sci., 6 (2000), 36.
[9] SINKEVICIENE I., BALANDIS A., Mater. Sci. Appl. Chem., 3 (2001), 55.
[10] NOVOTNA M., SATAVA V., MAIXNER J., KLOUZKOVA A., KOSTKA P., LEZAL D., J. Optoelectr., Adv. Mater., 5 (2003), 1405.
[11] PECHAR F., Cryst. Res. Technol., 24 (1989), 971.
[12] BRIAN S., MITCHELL A., *An Introduction to Materials Engineering and Science for Chemical and Materials Engineers*, Wiley, Hoboken, 2004.
[13] KNUNIANC A., *The Encyclopedia of Chemistry*, Vol. 1, Soviet Encyclopedia, Moscow, 1988 (in Russian).

Effect of annealing and γ irradiation
on tin phthalocyanine thin films

C. C. REGIMOL[*], C. S. MENON

School of Pure and Applied Physics, Mahatma Gandhi University,
Priyadarshini Hills P.O., Kottayam-686560, Kerala, India

Metal phthalocyanines are important among organic dyes because of their chemical and thermal stability. Thin film samples of tin phthalocyanine (SnPc) have been prepared for examination by thermal evaporation technique. Some optical and electrical properties of the samples were studied as a function of annealing temperature and γ radiation doses. Optical transition is found to be of direct type and optical band gaps are determined by analyzing the absorption spectrum. The activation energy of the dark conductivity is found to be highly dependent on both annealing and γ radiation doses.

Key words: *phthalocyanine; thin film; optical band gap; activation energy*

1. Introduction

Phthalocyanines (Pcs) receive great interest nowadays due to their variety of applications such as gas sensors, organic thin film transistors, and various optoelectronic applications [1–4]. Metal phthalocyanines [MPc] are highly coloured, p-type organic semiconducting compounds which exhibit high chemical and thermal stability and thus can be sublimed without decomposition to form high quality thin films by the thermal evaporation technique. The stability of these films, however, at high temperature and high radiation environment is still a matter of research. Physical properties of Pcs are strongly influenced by the growth parameters and the post-deposition treatments such as annealing [5]. Irradiation of thin films with high energy radiations like γ rays, is expected to affect their physical properties. The study of irradiated samples enhances the efficiency improvement in its applicability in a radiation environment and is also important in obtaining basic information on vacancies, defects and their interaction with impurities [6, 7]. In this work, we have made a detailed in-

---

[*]Corresponding author, e-mail: regijose2004@yahoo.co.in

vestigation on the effect of vacuum annealing and γ ray irradiation on the electrical and optical properties of vacuum deposited Tin Phthalocyanine (SnPc) thin films.

2. Experimental

Spectroscopically pure SnPc powder (Sigma-Aldrich Company, USA) was used as the source material for the preparation of thin films. The purity of the powder has been counter-checked by CHN analysis (C – 61.26%, H – 2.471%, N – 18%). Thin films of suitable thickness have been prepared by vacuum sublimation from a resistively heated molybdenum boat using a "Hind Hi-Vac" coating unit. The films were deposited onto thoroughly cleaned rectangular glass substrate at room temperature under the pressure of 10^{-5} Torr. The thickness of the films was crosschecked with the Tolansky multiple beam interference technique [8]. Thin films prepared at room temperature were annealed at various temperatures for one hour in a vacuum chamber. A programmable temperature controller (cam recorder) was used to control the temperature. UV-Visible absorption spectra in the wavelength range from 300 nm to 900 nm were recorded using a Shimadzu 160A UV-Vis spectrophotometer.

Electrical conductivity measurements were performed using a programmable Keithley electrometer (model No. 617). Electrical conductivity was studied in the temperature range 300–473 K under the pressure of 10^{-3} Torr to avoid possible contamination. The temperature was monitored using a chromel–alumel thermocouple. SnPc thin films were irradiated with ^{60}Co γ source. Radiation doses were controlled through the exposure time.

3. Results and discussion

3.1. Optical studies

The optical absorption spectra of as-deposited and γ irradiated SnPc thin films for various radiation doses are shown in Fig. 1. As the γ radiation dose increases, the absorbance decreases. The spectra originate from the orbital within the aromatic 18π electron system and from overlapping crystals on the central metal atom. The electronic $\pi \rightarrow \pi^*$ transition in the energy range 300–400 nm corresponds to an intense B band (Soret band) which gives the fundamental absorption edge, while the band in the energy range 700–800 nm (Q band) gives the onset energy [9, 10]. B band consists of a peak at 3.58 eV and Q band consists of two peaks at 1.43 eV and 1.76 eV. The interaction between molecules strongly influences the absorption spectrum leading to splitting of Q band into two distinct peaks. The fundamental absorption edge is analyzed within the framework of one electron theory of Bardeen et al. [11]. The absorption coefficient α is related to the energy band gap E_g and the photon energy $h\nu$:

$$\alpha = \alpha_0 \left(h\nu - E_g \right)^n \qquad (1)$$

where *n* is 1/2, 3/2, 2 or 3 for direct allowed, direct forbidden, indirect allowed and indirect forbidden transitions, respectively.
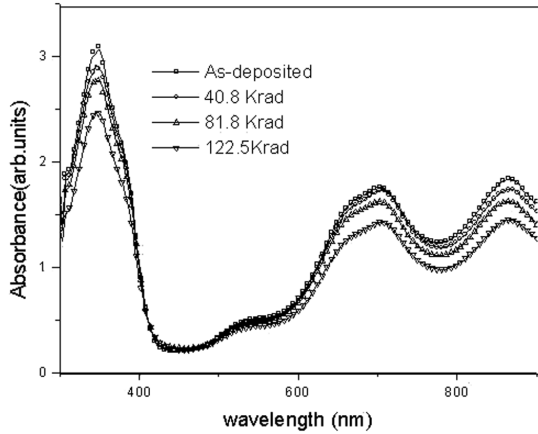
Fig. 1. Optical absorption spectrum of SnPc thin films
irradiated with various doses of γ radiation

A satisfactory linear fit is obtained for α^2 vs. hν, indicating the presence of direct allowed transition for SnPc thin films. The intercept on the energy axis, as shown in Fig. 2, gives the band gap E_g of the material.
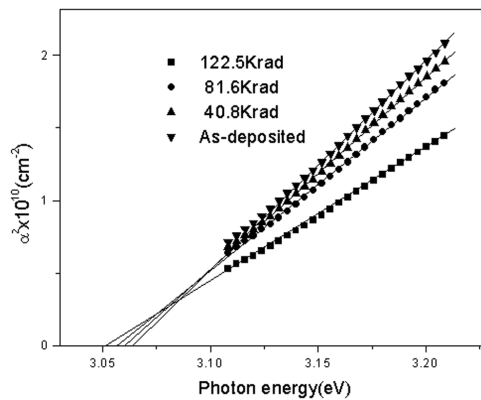
Fig. 2. Plot of α^2 versus $h\nu$ for as deposited
and irradiated SnPc thin films with different dosage

The investigation of optical properties was also extended to samples annealed at various temperatures. The optical absorption spectra of annealed samples are shown in Fig. 3. Plots of α^2 vs. $h\nu$ for the as-deposited and annealed SnPc thin films are shown in Fig. 4.
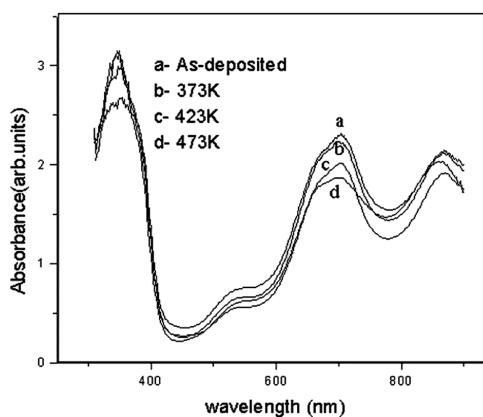
Fig. 3. Optical absorption spectra of SnPc thin films
annealed under vacuum at various temperatures
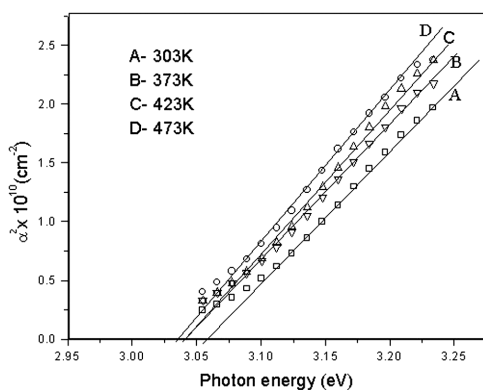
Fig. 4. Plots of α^2 versus $h\nu$
for vacuum annealed samples of SnPc

In the both cases, the fundamental and onset energy gaps amount to 3.06±0.01 eV and 1.55±0.01 eV, respectively. There is no appreciable variation in band gap and excitonic energy with annealing and γ irradiation. This shows that the optical band gaps of the material are stable upon high-energy irradiation and temperature.

3.2. Electrical studies

Electrical properties of organic semiconductor thin films strongly depend on the conditions of deposition and the post deposition treatments. For Pc thin films, the electrical conductivity σ fulfils the Arrhenius equation:

$$\sigma = \sigma_0 \exp\left(-E/k_B T\right) \qquad (2)$$

where σ is the conductivity at the temperature T [K], E is the thermal activation energy, k_B is the Boltzmann constant and σ_0 is the pre-exponential factor. The Arrhenius plot ($\ln\sigma$ vs. $1000/T$) yields a straight line, with the slope corresponding to the value of thermal activation energy. In Figure 5, $\ln\sigma$ vs. $1000/T$ is plotted for SnPc thin films 400 ± 5 nm thick before and after irradiation. According to Davis and Mott [12], in this type of material the conductivity exhibits different behaviour in various regions of the Arrhenius plot. There are two linear regions for each graph, which give two activation energies E_1 and E_2.
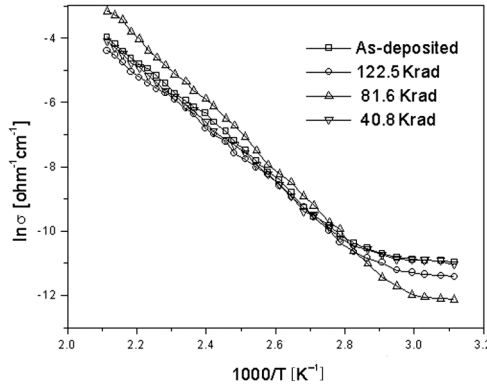
Fig. 5. Plot of $\ln\sigma$ vs. $1000/T$ for as deposited
and irradiated SnPc thin films for various doses of radiation

The activation energy E_1 is related to the intrinsic generation process and E_2 to the impurity scattering [9]. The conduction mechanism at lower temperatures is explained in terms of hopping through a band of localized states and at higher temperatures – in terms of thermal excitation of carriers to the band edges. The change in the slope, and hence the change in activation energy, reflects a change from intrinsic conduction to the extrinsic one [13]. The activation energies determined for non-irradiated and irradiated samples are listed in Table 1.

Table 1. Variation of activation energy in the intrinsic
and extrinsic region as a function of irradiation dosage

γ radiation dosage [Krad]	Activation energy [eV]	
	E_1	E_2
As deposited	0.65±0.01	0.06±0.01
40.8	0.76±0.01	0.16±0.01
81.6	0.90±0.01	0.20±0.01
122.5	0.75±0.01	0.17±0.01

The activation energy increases with exposure up to 81.6 Krad and then decreases. In the case of vacuum-annealed samples, the activation energy is found to increase with annealing temperature up to 423 K and then reduces as shown in Fig. 6. The activation energies of the samples annealed at various temperatures are given in Table 2. The reduction in activation energy at 473 K and for radiation dose of 122.5 Krad may be attributed to the instability of the material due to heavy vibrations of the atoms.
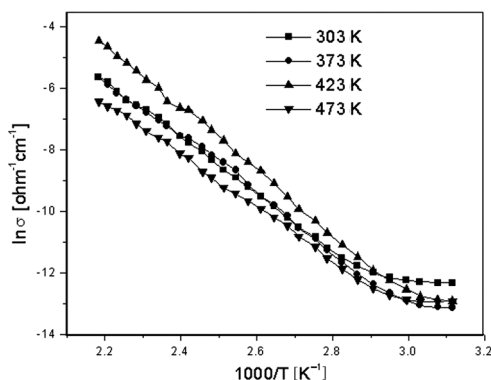
Fig. 6. Plot of $\ln\sigma$ versus $1000/T$ for SnPc thin film
annealed under vacuum at various temperatures

Table. 2. Variation of activation energy in the intrinsic
and extrinsic region as a function of annealing temperature

Temperature of annealing [K]	Activation energy [eV]	
	E_1	E_2
303	0.80±0.01	0.09±0.01
373	0.86±0.01	0.16±0.01
423	0.95±0.01	0.16±0.01
473	0.77±0.01	0.07±0.01

The charge carriers in Pc are thermally generated holes and the presence of traps plays a dominant role in the conduction of these materials [14, 15]. Presence of trap levels is attributed to defects generated by ambient nitrogen, hydrogen, and oxygen affecting electrical conductivity, mobility and trap density. Structural defects may also affect the conductivity. This, in turn, affects the position of the Fermi level [13]. During annealing in vacuum oxygen may be desorbed, which reduces the conductivity of the samples. On the other hand, irradiation of samples with high-energy radiation creates structural defects which act as trapping centres. This is indicated by the increase in activation energy and thus the reduction in the conductivity of SnPc thin films.

4. Conclusion

Thin films of SnPc have been prepared using vacuum deposition technique. Effect of post-deposition annealing and the effect of γ ray irradiation on the optical and electrical properties have been investigated. As the intensity of irradiation dose increases, the absorption intensity decreases. It is also found that the band gap remains constant but the conductivity is affected by irradiation and annealing. The activation energy varies with both annealing and irradiation.

References

[1] RADHAKRISHNAN S., DESHPANDE S.D., Sensors, 2 (2002), 185.
[2] ARSHAK A., ZLEETNI S., ARSHAK K., Sensors, 2 (2002), 174.
[3] FOREST S.R., CHEM. REV., 97 (1997), 1793.
[4] DIMITRAKOPOULOS C. D., MASCARO D.J., IBM J. Res. Dev., 45 (2001), 11.
[5] AMBILY S., MENON C.S., Thin Sold Films*,* 347(1999), 284.
[6] ARSHAK K., KOROSTYNSKA O., FAHIM F., Sensors, 3 (2003), 176.
[7] ABU EL-FADL A., EL-MAGHRABY E. M., MOHAMAD G. A., Cryst. Res. Technol., 39 (2004), 143.
[8] MAISSEL L.I., GLANG R., *Handbook of Thin Film Technology*, McGraw Hill, New York, 1985.
[9] COLLINS R.A., KRIER A., ABASS A.K., Thin Solid Films, 229 (1993), 113.
[10] EL-NAHASS M.M., ABD-EL- RAHMAN K.F., AL-GHAMDI A.A., ASIRI A.M., Physica B, 344 (2004), 398.
[11] BARDEEN J., SLATT F.L., HALL L.T., *Photoconductivity Conf*., Wiley, New York, 1965.
[12] MOTT N.F., DAVIS E.A., *Electronic Processes in Non-crystalline Materials*, Oxford University Press, Oxford, 1979.
[13] HASSAN A.K., GOULD R.D., J. Phys: Condens. Matter., 1 (1989), 6679.
[14] SUSSMAN A., J. Appl. Phys., 38 (1967), 2738.
[15] MAMMEN S., MENON C.S., UNNIKRISHNAN N.V., Mater. Sci-Poland, 23 (2005), 707.

The effect of spin coating rate on the microstructure, grain size, surface roughness and thickness of $Ba_{0.6}Sr_{0.4}TiO_3$ thin film prepared by the sol-gel process

R. Dewi[*], N. I. Baa'yah, I. A. Talib

School of Applied Physics, Faculty of Science and Technology,
University Kebangsaan Malaysia, 43600, Bangi, Selangor, Malaysia

The paper reports on the effect of spin coating rate during the sol-gel process on the microstructure, grain size, surface roughness and thickness of barium strontium titanate ($Ba_{0.6}Sr_{0.4}TiO_3$) thin films. Variable coating rates do not influence the microstructure of the films. All films are polycrystalline and single phase, as was found from X-ray diffraction analysis. Changing the spin rates also does not influence the grain sizes of the films. All films have nanometer particle size ranging from 37.2 nm to 30.7 nm. However, roughness and thickness of the film depend on the spin coating rates. The highest spin rates produce the thinnest film with the roughest surface, while the lowest spin rate produced the thickest films with the smoothest surface.

Key words: *barium strontium titanate; sol-gel method; spin coating*

1. Introduction

The sol-gel process allows one to synthesize ceramic materials of high purity and homogeneity. The sol is made of solid particles of diameter of few hundred nm suspended in a liquid phase. Then the particles are condensed in a new phase (gel), in which the solid macromolecule is immersed in a liquid phase (solvent) [1].

$Ba_{1-x}Sr_xTiO_3$ (BST) is currently one of the most interesting ferroelectric materials due to its high dielectric constant and the composition-dependent Curie temperature. The dielectric and ferroelectric properties of the sol-gel derived BST thin films are strongly dependent on the Sr content and the grain size [2]. At room temperature BST is ferroelectric when the Ba content x does not exceed 0.3 and paraelectric when it is in the range $0.3 > x > 1$ [3]. Ferroelectric BST thin films have been widely investigated as potential materials for application in microelectronic devices such as dynamic

---

[*]Corresponding author, e-mail: drahmi2002@yahoo.com

random access memories, infrared detectors, microwave devices, and hydrogen gas sensors [4–7]. In particular, dielectric nonlinearity is one of the most important factors for tunable microwave applications. It is found that tenabilities depend on the microstructures of the thin films, such as the phase, grain size, composition, defects, strain, etc. [8]. BST thin films have been prepared by various methods, such as radio-frequency (r-f) sputtering, ion-beam sputtering, laser ablation, metal-organic chemical, vapour deposition and sol-gel technique. However, sol-gel processing has advantages over other methods in homogeneity, cost, and process control [9, 10].

In this work, $Ba_{0.6}$ $Sr_{0.4}$ TiO_3 thin films have been prepared using the sol-gel method. The as-prepared films were annealed at 700 ºC in order to crystallize the films. The effect of different spin coating rates on the microstructure, grain size, surface roughness and thickness of the film was investigated.

2. Experimental

Barium acetate $Ba(CH_3CO_2)_2$, strontium acetate $Sr(CH_3CO_2)_2$ and titanium(IV) isopropyloxide, $(Ti(OCH(CH_3)_2)_4)$ 99.999% were used as starting materials for the synthesis of precursors for BST thin films. Barium acetate (0.6 mole) and strontium acetate (0.4 mole) were first dissolved in acetic acid containing 20 vol. % of deionized water at room temperature. A clear and transparent solution was obtained. Titanium(IV) isopropyloxide was then added to this solution. In order to improve the stability of the solution, a few drops of acetylacetone were added to the solution precursor during constant stirring. A transparent yellowish solution formed at room temperature. Using a spin coater, the solution was transformed into thin film form. Silicon (boron p-type with impedances 16–24 $\Omega\cdot$cm (625 μm thick) wafers were used as substrates. The coating rates were 3000, 3500 and 4000 r.p.m (hereinafter, the samples will be denoted as A, B and C films, respectively) and the coating time was 30 s for all films. The films were dried at 150 ºC in air for 15 min to evaporate the solvent and heated at 350 ºC in air for 15 min to burn off residual organics. This would form an SiO_2 layer on the substrate surface. Previous papers indicated that BST thin films annealed at temperatures lower than 600 ºC had an amorphous nature, the films annealed at 600 ºC showed inferior crystallinity, suggesting an incomplete perovskite phase formation [11], while those annealed at 700 ºC crystallized [6, 12, 13]. Hence all the investigated films were annealed at 700 ºC for 60 min in oxygen atmosphere. Figure 1 shows the flow chart of the preparation procedure.

The microstructure and grain size of the films were studied using X-ray diffractometer (XRD) model D-5000 Siemens and scanning electron microscope (SEM) model LEO VPSEM 1450, respectively. The surface roughness and thickness of the films were studied using atomic force microscopy (AFM) Burleigh personal model ARIS 3300 and Ellipsometer Rudolf model Auto E1-111, respectively.
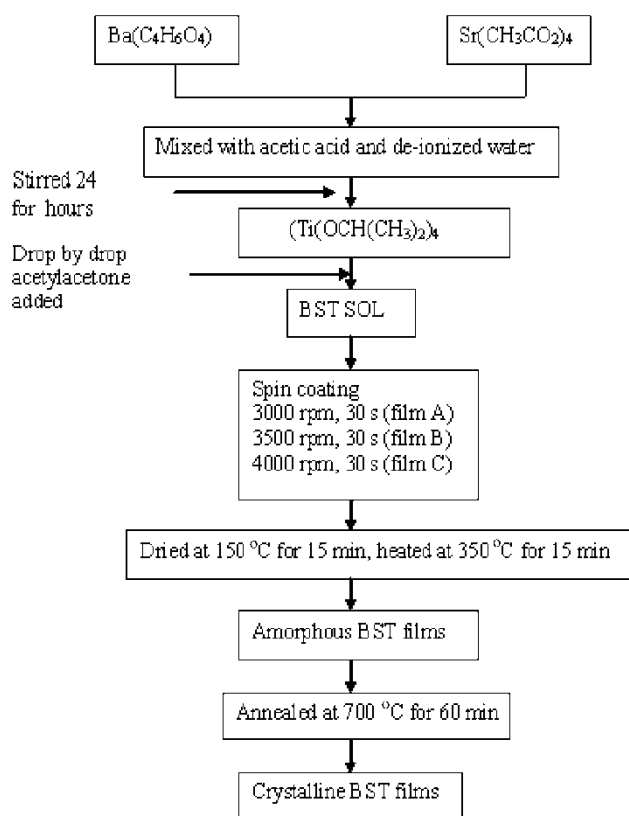
Fig. 1. Flow chart of the procedure of the film preparation

3. Results and discussion

Figure 2 shows the XRD spectra of a bare silicon wafer (a), a silicon wafer with SiO$_2$ layer produced by heating at 350 ºC (b), and films prepared at various spin coating rates (c–d). After annealing, the intensities of the diffracted peaks further increased showing an increase in the crystallinities of the films. However, different coating rates do not influence the microstructure of the films. The structure was found to be cubic with the lattice constant $a = 3.965$ Å.

Figure 3 shows the surface morphologies of the films obtained using the AFM. The scan area was 3500 nm×3500 nm. The root mean square (RMS) roughness was 7.85, 15.21 and 23.65 nm for films A, B and C, respectively. This shows that the RMS roughness increased as the spin coating rate increased. Yang et al. [14] and Shim et al. [15] have also reported that the RMS roughness increased as the film thickness decreased.
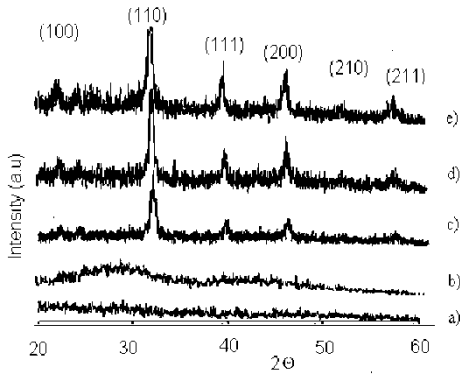
Fig. 2. The XRD patterns of: a) bare silicon wafer, b) silicon wafer with SiO_2 layer on its surface, c) film A, d) film B, e) film C
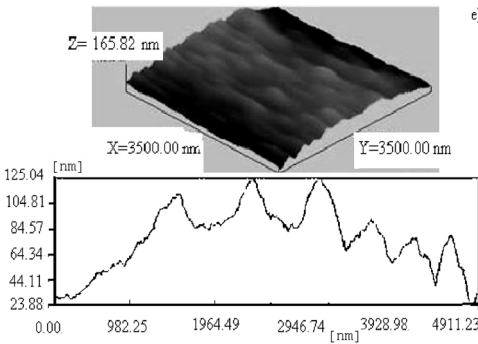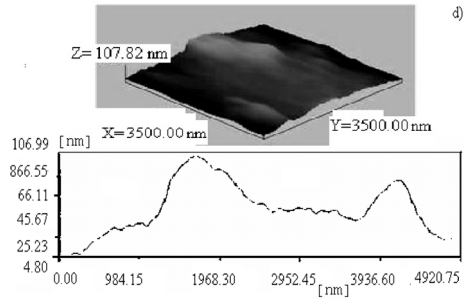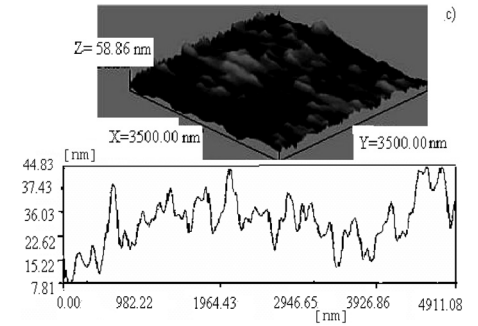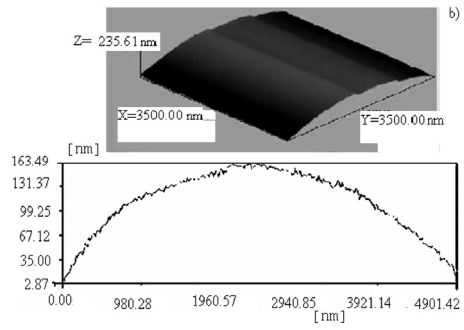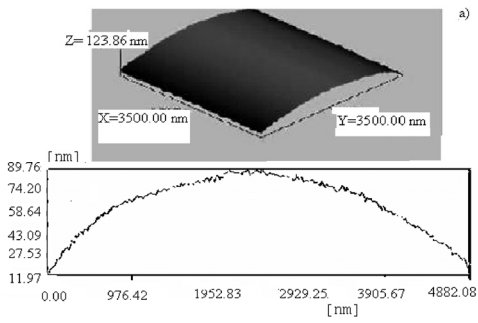
Fig. 3. The AFM images of: a) silicon (bare substrate), b) SiO_2, c) film A, d) film B, e) film C

Figure 4 shows SEM images of all films. The images indicated that the films were in orderly form, fine and homogeneous. The average grain sizes were approximately 37.2 nm for film A, 33.5 nm for film B, and 30.7 nm for film C. All of the films have nanometer size particles and, in general, changing the spin rates does not influence the grain size of the films. The larger particles that can be seen in the micrographs are actually clusters of small particles. Heywang and Thoman (1991) have also reported similar combination of small particles due to high annealing process [16].
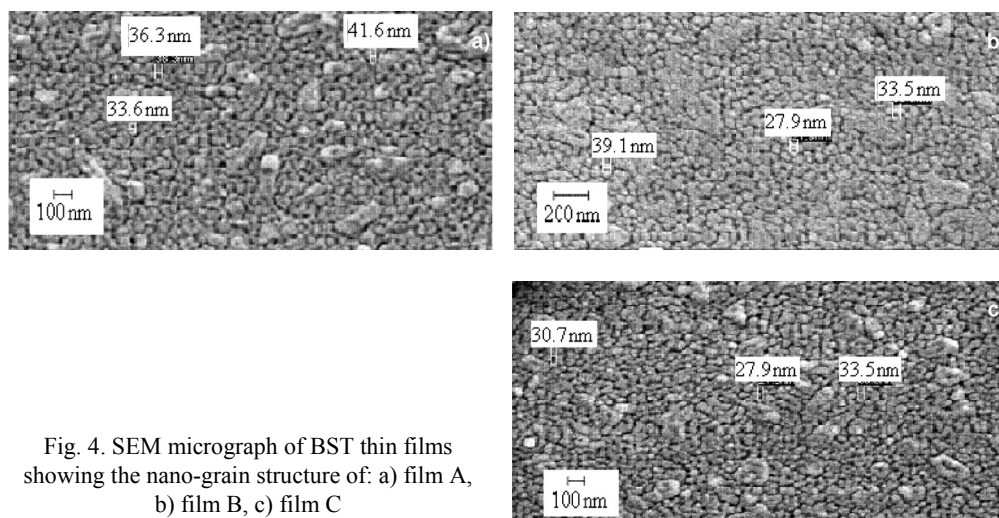
Fig. 4. SEM micrograph of BST thin films showing the nano-grain structure of: a) film A, b) film B, c) film C

The average thicknesses of the films measured using the ellipsometer are 153.5 nm, 96.02 nm and 80.39 nm, for spinning rates of 3000, 3500, and 4000 r.p.m., respectively. The film thickness versus spinning speed is plotted in Fig. 5. As appears in the figure, the higher the spinning speed, the thinner the film. This shows that increasing the spinning speed decreased the film thickness. The relation between film thickness, h, and spin rate, ω, obeys the power law relation of the form $h \propto \omega^{-3/2}$ [1].
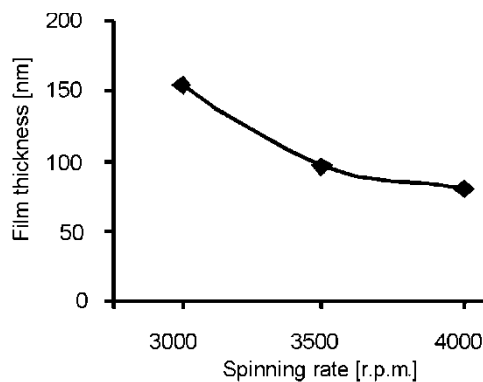
Fig. 5. Film thickness as a function of spinning rate

4. Conclusions

The effects of spin coating rates on the microstructure, grain size, surface roughness and thickness of $Ba_{0.6}Sr_{0.4}TiO_3$ sol-gel films have been investigated. The microstructure and grain sizes of the films are not affected by the coating rates. However, they do influence the roughness and thickness of the film. The highest spin rates produced the thinnest films with the roughest surfaces, while the lowest spin rates produced the thickest films with the smoothest surfaces.

References

[1] BRINKER C.J., SCHERER G.W., *Sol-Gel Science. The Physics and Chemistry of Sol-Gel Processing*, Academic Press, New York,1990.
[2] ADIKARY S.U., CHAN H.L.W., Thin Solid Films., 424 (2003), 70.
[3] MAJED S.M., NAIK R., J. Mater. Res., 10 (1996), 2588.
[4] CHENG J.G., MENG X.J., TANG I., GUO S.L., CHU J.H., Appl. Phys. A., 70 (2000), 411.
[5] YANG X., YAO X., ZHANG L., J. Ceram. Inter., 30 (2004), 1525.
[6] ZHANG T.J., NI H., J. Mater. Sci., 37 (2002), 4155.
[7] ZHU W., TAN O.K., DING J., J. Mater.Res., 15 (2000), 1291.
[8] FU C., YANG C., CHEN H., HU L., WANG Y., J. Mater. Lett., 59 (2005)**,** 330.
[9] TSUZUKI A., KATO K., KUSUMOTO K.,TORH Y., J. Mater. Sci.,33 (1998), 3055.
[10] WU D., LI A., LING H., YIN X., GE C., WANG M., MING N., J. Appl. Surface Sci., 165 (2000), 309.
[11] HU W., YANG C., ZHANG W., QIU Y., J. Sol-Gel Sci. Tech., 36 (2005), 249.
[12] PAIK D.S., RAO A.V.P., KOMARNENI S., J. Sol-Gel Sci. Tech.,10 (1997), 213.
[13] ZHU H., MIAO J., NODA M., OKUYAMA M., Sensors Act. A, 110 (2004), 371.
[14] YANG.W., LAMBETH D.E., TANG.L., LAUGHLIN D.N., J. Appl. Phys., 81 (1997), 4370.
[15] SHIM J.B., YOSHIMOTO N., YOSHIZAWA M., YOON D.H., J. Cryst. Res. Technol., 36 (2001), 1209.
[16] HEYWANG W., THOMAN H., *Positive temperature coefficient resistors*, [in:] B.C.H. Steele (Ed.), *Electronic Ceramics*, Elsevier, London, 1991, p. 29.

Influence of modification of SiO_2 on the formation of calcium silicate hydrate

K. BALTAKYS[1*], R. JAUBERTHIE[2], R. SIAUCIUNAS[1], R. KAMINSKAS[1]

[1]Department of Silicate Technology, Kaunas University of Technology, Radvilenu 19, LT – 50270 Kaunas, Lithuania

[2]Department of Civil Engineering, INSA, 20 Av. des Buttes de Coësmes, CS 14315, 35043 Rennes, France

Interactions of $Ca(OH)_2$ with various modifications of SiO_2: amorphous (Hi-Sil, TSD) or crystalline (quartz) silica were established. The molar ratio of primary mixtures CaO/SiO_2 was 0.5. The samples were cured in a vapour chamber (20 ℃, 100% humidity) for 7 and 28 days. The products were characterized by X–ray diffraction, thermogravimetry, differential scanning calorimetry, Fourier-transform infrared and scanning electron microscopy analysis. SiO_2 modification used had a decisive influence on the processes of formation of calcium silicate hydrates. In the mixture with amorphous SiO_2, $Ca(OH)_2$ reacted completely during 7 days of synthesis, while large quantity of $Ca(OH)_2$ remained unreacted even after 28 days when quartz was used. It was found that in the $Ca(OH)_2$–amorphous SiO_2–H_2O system, after a 28-day exposure, the surface of SiO_2 globules was totally covered with well-crystalline C-S-H(I) plates. Moreover, in the samples with quartz, only the gaps between quartz crystals were filled with C-S-H(I).

Key words: *calcium silicate hydrate; crystalline SiO₂; silica fume; Portland cement; X-ray diffraction*

1. Introduction

In recent times, the term pozzolan has been extended to cover all siliceous /aluminous materials which in finely dispersed form and in the presence of water, react with calcium hydroxide (CH) to form compounds with cementitious properties. This generalized definition covers waste products such as fly ash, rice husk ash, silica fume (SF) [1–4].

Silica fume is a by-product of silicon and ferro-silicon industries. It is formed by condensation of SiO_2 from the vapour phase. SF occurs as near-perfect spheres with diameters ranging from 20 to 500 nm. Typically, 85–95% of SF has the form of amor-

---

phous silica [5–7] with various impurities, such as an ultra fine by-product of the silicon metal refining industry.

As a pozzolana, SF reacts with calcium hydroxide liberated by the hydrolysis of C_3S and C_2S of Portland cement in the following reactions [8]:

$$2C_3S + 6H \rightarrow C_3S_2H_3 + 3CH \qquad (1)$$

$$2C_2S + 4H \rightarrow C_3S_2H_3 + CH \qquad (2)$$

$$3CH + 2S \rightarrow C_3S_2H_3 \qquad (3)$$

However, there are still a lot of questions concerning the role of pozzolans. The most commonly discussed mechanisms are the following [9]: (a) pozzolans reduce permeability, thereby preventing the ingress of water and transport of alkali and hydroxyl ions; (b) pozzolans increase strength and stiffness, resulting in better resistance to cracking and less expansion; (c) replacing a portion of cement with a less-alkaline pozzolanic material decreases the total amount of alkali present; and (d) pozzolans react with calcium hydroxide to form calcium silicate hydrate (CSH) with a low CaO/SiO_2 ratio. Formation of CSH depletes CH and the low C/S ratio enables the entrapment of alkalis, both of which reducing the amount of hydroxyl ions available to participate in the alkali–silica reaction.

The addition of SF to cement paste has been shown to give rise to high early strengths, although the mechanisms by which SF operates are unclear. Three principal types of interactions have been suggested:

1. SF particles cause pore blockage in the hydrating cement, which makes the hydrating gel structure more dense [6].

2. Pozzolanic reactions occur between the silica-rich SF particles and the portlandite, which is a by-product of Portland cement hydration [10].

3. SF particles act as nucleation sites for cement hydration, accelerating the process [11].

Addition of SF enhances the rate of cement hydration and accelerates both C_3S and C_3A hydration during the first few hours [12].

Calcium silicate hydrates have a vital influence on the characteristics of cement paste. Due to their morphology, CH are relatively weak, brittle and not cementitious. Moreover, the CSH phase formed by a pozzolanic reaction has a microscopic morphology similar to that developed by the hydration of the C_3S and C_2S found in Portland cement [13]. When silica fume is added to fresh concrete, it chemically reacts with the CH to produce additional CSH. The benefit of this reaction is two-fold: increased compressive strength and chemical resistance [14].

According to the collected reference data, the properties of hardening concrete with SF additive depends on CH reaction and SF kinetics parameters (the rate of reaction, advancement of reaction, etc.).

In this work, the presented data were obtained by performing syntheses of portlandite with various modifications of SiO_2: amorphous (Hi-Sil, TSD) or crystalline (quartz) silica under normal conditions.

2. Materials and methods

The following materials were used in this work: calcium hydroxide $Ca(OH)_2$ (Industrial lime: loss of ignition 23%, Manufacturer Pigeon Chaux, Saint Pierre La Cour, France); two different silica fumes (Hi-Sil 255C-D obtained from PPG (amorphous silica > 87%, crystalline silica < 0.01%, Na_2SO_4 < 2%, pH = 6.3, surface area – 180 m^2/g) and thermal silica densified – TSD (amorphous silica > 86%, carbon content < 5.4%, pH = 6.3, surface area – 120 m^2/g); quartz (from Millisil Sifraco).

Two series of samples, each being made with different SiO_2 and $Ca(OH)_2$, were used. The molar ratio of primary mixtures of CaO/SiO_2 was 0.5. The samples were cured in a vapour chamber (20 ºC, 100% humidity) for 7 and 28 days. Then, they were removed from the teflon cells and transferred into an air-conditioned chamber with relative humidity of 55% at 20 ºC, and sieved through the sieve No. 008. The products of the synthesis were characterized by X-ray powder diffraction (XRD), differential scanning calorimetry (DSC), thermogravimetry (TG), Fourier transform infrared spectroscopy (FT-IR) and scanning electron microscopy (SEM) methods.

The XRD data were collected with a Philips PW 3710 X-ray diffractometer with the Bragg–Brentano geometry using Ni-filtered CuK_α radiation, operating with the voltage of 30 kV and emission current of 20 mA. The step-scan covered the angular range 2–60º (2θ) in steps of 2θ = 0.02º.

Simultaneous thermal analysis (STA: differential scanning calorimetry – DSC and thermogravimetry – TG) was also employed for measuring the thermal stability and phase transformations of the synthesized products at a heating rate of 15 ºC/min, the temperature ranged from 30 ºC up to 1000 ºC under the ambient atmosphere. The test was carried out on a Netzsch instrument STA 409 PC Luxx with ceramic sample handlers and crucibles of Pt-Rh. SEM (JEOL-JSM-6301F) analysis of the samples was performed using an accelerating voltage of 9 kV and a working distance of 15 mm.

FT-IR spectra analysis was carried out with a spectrometer Perkin Elmer FT–IR system Spectrum X. The specimens were prepared by mixing 1 mg of the sample with 200 mg of KBr. The spectral analysis was performed in the range of 4000–400 cm^{-1} with spectral resolution of 1 cm^{-1}.

3. Results and discussion

FT-IR studies were conducted to identify differences of interaction of $Ca(OH)_2$ with various modifications of SiO_2: amorphous (Hi-Sil, TSD) or crystalline (quartz)

silica. The infrared spectra of the products after 7 and 28 days of hydrothermal curing at 20 ºC are shown in Fig. 1.
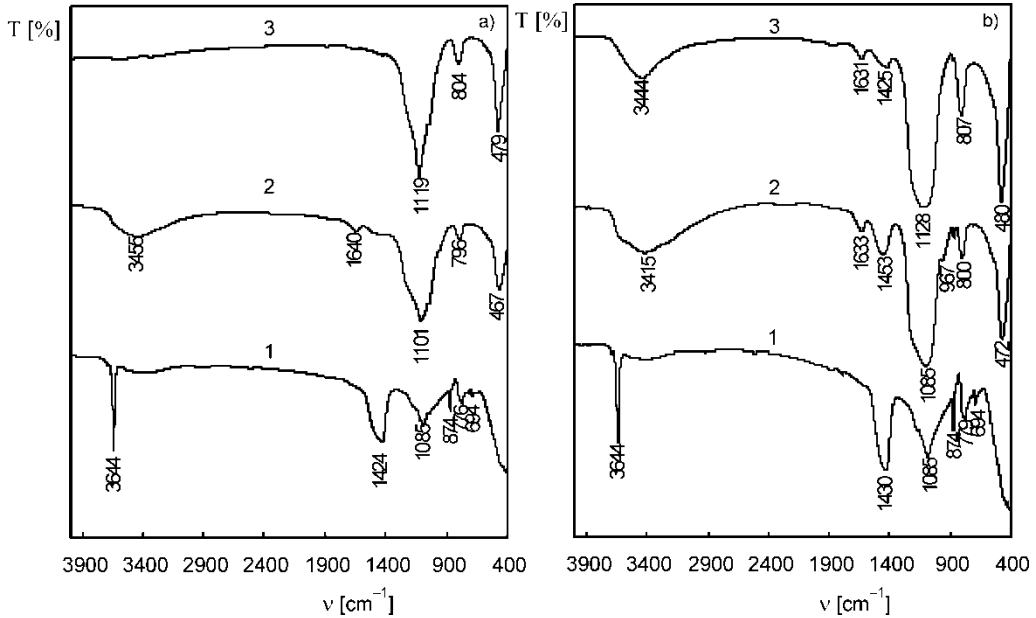
Fig. 1. IR spectra of products of the synthesis; duration of hydrothermal curing at 20 ºC:
a) 7 days, b) 28 days; SiO_2 modifications: 1 – quartz, 2 – Hi-Sil, 3 – TSD

In the $Ca(OH)_2$–quartz–H_2O system, a broad absorption band at 3644 cm^{-1} characteristic of portlandite [15, 16] was observed. The band was clearly visible in both reactions products after 7 and 28 days of exposure (Fig. 1a, b, curve 1). Also, the presence of calcite ($CaCO_3$) impurities was identified with IR absorption bands at 874 and 1424 cm^{-1}.

In the mixtures with amorphous SiO_2 (Hi-Sil or TSD), just after 7 days of exposure the portlandite was not observed (Fig. 1a, curves 2, 3). This is the result of the reaction between CH and SiO_2 when calcium silicate hydrates are formed. The most significant infrared spectra of C-S-H contain a characteristic set of bands in the range 400–1200 cm^{-1}. The broad band centred at 1101 cm^{-1} is attributed to asymmetric stretching frequency of Si–O–Si, the band centred at 796 cm^{-1} is due to symmetric stretching of Si–O–Si, and the band at 467 cm^{-1} is due to the bending frequency of O–Si–O. The frequencies of the Si–O–Si bands are an indication of the overall degree of polymerization of the silica network. In general, a lower frequency corresponds to a lower degree of polymerization. Thus, one can speculate that the degree of polymerization of reaction products using Hi-Sil is lower compared to TSD because in the latter material corresponding absorption bands are located at 1119, 804, 479 cm^{-1}. As in the previous spectra, these bands become sharper and more intense with increasing reaction time (Fig. 1b). After 28 days of synthesis, only in the samples with Hi-Sil the band (ν_3 SiO_4) characteristic of C-S-H at 967 cm^{-1} [15, 16] was observed (Fig. 1b,

curve 2). A broad band, present in each spectrum around 1630 cm^{-1}, is associated with deformation vibrations δ(OH) and together with ν(OH) stretching vibrations at 3435 cm^{-1}, the presence of water in the samples can be concluded due to humidity. This assumption could be proved by DSC-TG measurement.
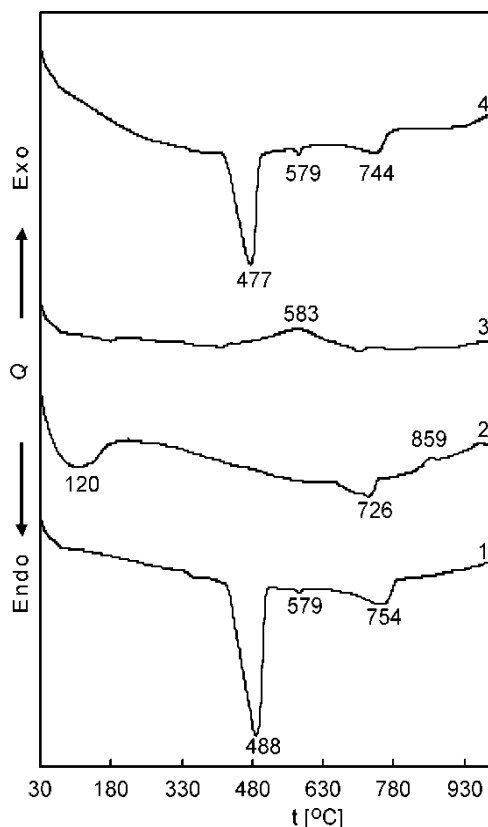
Fig. 2. DSC-TG curves for the following SiO₂ modifications and durations of hydrothermal curing at 20 ºC: 1 – quartz, 7 days; 2 – Hi-Sil, 7 days; 3 – TSD, 7 days; 4 – quartz, 28 days

The results of thermal analyses confirm the IR data. The endothermic peak in the range 475–485 ºC corresponds to the decomposition of Ca(OH)₂. This peak is clearly visible in the curves of the samples with quartz after 7 and 28 days of syntheses (Fig. 2, curves 1, 4). Moreover, this endothermic peak is not observed in any DSC curves of the samples with amorphous SiO₂ (Fig. 2, curves 2, 3).

X-ray diffraction analysis confirms that prolonging the duration of synthesis increases the quantity of semi-crystalline C-S-H(I) phase in the products and shows that the reaction proceeds more intensively in the Ca(OH)₂–Hi-Sil–H₂O mixture. The XRD data showed the presence of amorphous silica after 7 days of exposure (Fig. 3a, curves 1, 2) or quartz (Fig. 3a, curve 1) and only in the Ca(OH)₂–Hi-Sil–H₂O mixture semi-crystalline calcium silicate hydrate – C-S-H(I) can be seen (Fig. 3a, curve 2).

In the mixture with quartz, both after 7 days and 28 days, the main peak of Ca(OH)₂ was clearly visible (Fig. 3a, curve 1, *d*-spacing – 0.493, 0.262, 0.179 nm). At

the same time, this compound was not found in the mixture with amorphous silica (Hi-Sil, TSD) (Fig. 3a, curves 2, 3). After 28 days, the distinctly apparent peaks characteristic of C-S-H(I) were found in all samples. The most intensive peak was found in the mixture with Hi-Sil (Fig. 3b, curve 2).
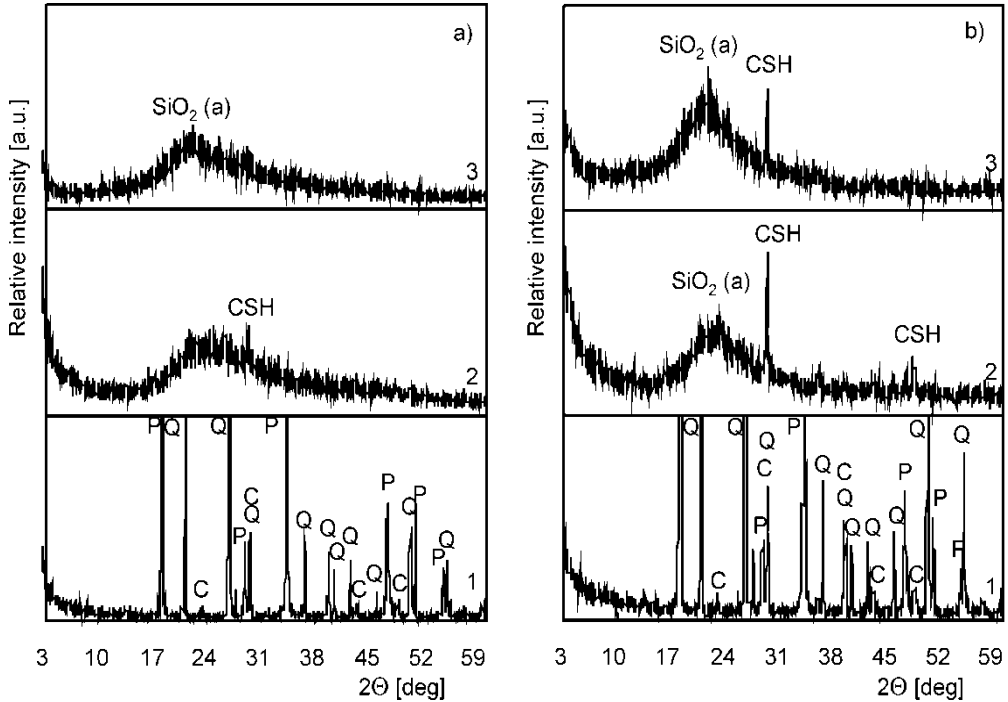
Fig. 3. X-ray diffraction patterns of the products of the synthesis; the duration of hydrothermal curing at 20 ºC: a) 7 days, b) 28 days; SiO_2 modifications: 1 – quartz, 2 – Hi-Sil, 3 – TSD; CSH – calcium silicate hydrates, P – portlandite, C – calcite, Q – quartz, SiO_2 (a) – amorphous silica

The same sequence of reactions was proved by SEM analyses. The SEM data show that the overall morphology of C-S-H can actually vary from the common fibrous type to irregular grains forming a reticular network [16].

In the mixture with amorphous SiO_2, after 7 days of synthesis, agglomerates of calcium silicate hydrates under the surface of silica globules were identified (Fig. 4a, b). $Ca(OH)_2$ reacts more quickly with Hi-Sil because the particles of this compound are significantly smaller than TSD (Fig. 4a). After prolonging the synthesis time to 28 days, well-crystalline CSH plates in the samples with Hi-Sil could be seen (Fig. 5a). The surface of SiO_2 globules was totally covered with these compounds.

At the same time, in the quartz samples only rudiments of CSH were observed after 7 days (Fig. 4c) and even after 28 days of synthesis only the gaps between quartz crystals were filled with CSH (Fig. 5b).
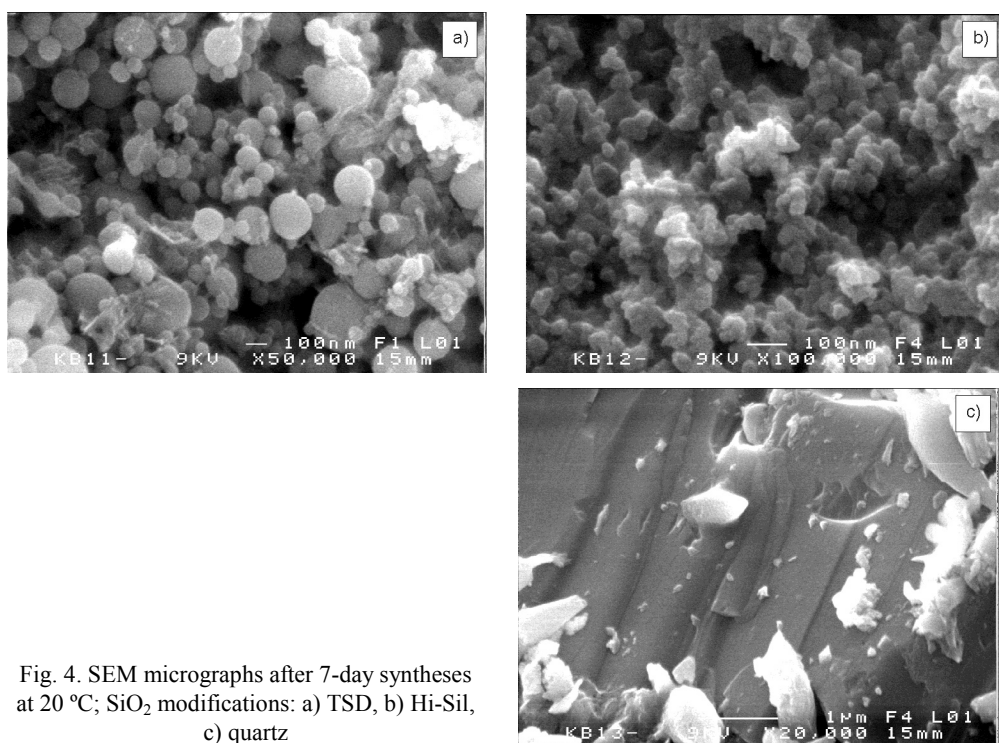
Fig. 4. SEM micrographs after 7-day syntheses at 20 ºC; SiO$_2$ modifications: a) TSD, b) Hi-Sil, c) quartz
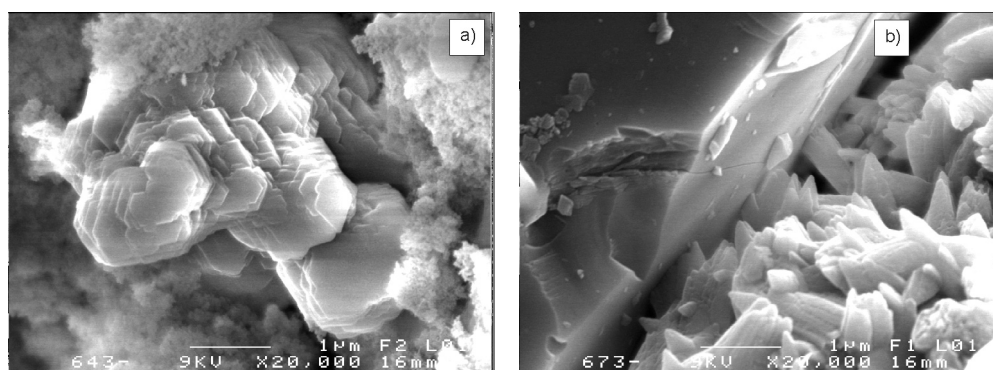
Fig. 5. SEM micrographs after 28-day syntheses at 20 ºC; SiO$_2$ modifications: a) Hi-Sil, b) quartz

4. Conclusions

• The phase compositions and properties of calcium silicate hydrates are strongly affected by crystallinity of SiO$_2$. In the mixture with amorphous SiO$_2$ (Hi-Sil or TSD), when primary mixture molar ratio CaO/SiO$_2$ was equal to 0.5, Ca(OH)$_2$ completely reacted during 7 days of synthesis at 20 ºC. When using quartz, a crystalline SiO$_2$ modification, large quantities of Ca(OH)$_2$ remained unreacted even after 28 days.

• In the Ca(OH)$_2$–amorphous SiO$_2$–H$_2$O system, after 7 days of synthesis, agglomerates of calcium silicate hydrates were formed covered by silica on the surface. After prolonging the synthesis to 28 days, the surface of SiO$_2$ globules was totally covered with well-crystalline C-S-H(I) plates.

• It was determined that, in the quartz samples, after 7 days only rudiments of C-S-H(I) were observed and even after 28 days of synthesis only the gaps between quartz crystals were filled with C-S-H(I).

References

[1] BEZERRA E.M., JOAQUIM A.P., SAVASTANO H., JOHN V.M., AGOPYAN V., Cem. Concr. Compos., 28 (2006), 555.

[2] KOHNO K., *Relative durability properties and strengths of materials containing finely ground silica and silica fume*, [in:] Proc. Third Int. Conf. *Use of Fly Ash, Silica Fume, Slag and Natural Pozzolans in Concrete*, Vol. 2, American Concrete Institute, SP-114 (1989), p. 815.

[3] MARUSIN S.L., *The influence of length of moist curing time on the weight change behaviour and chloride permeability of concrete containing silica fume*, [in:] Proc. Third Int. Conf. *Use of Fly Ash, Silica Fume, Slag and Natural Pozzolans in Concrete*, American Concrete Institute, SP-114 (1989), p. 924.

[4] MEHTA P.K., GJORV O.E., Cem. Concr. Res., 12 (1982), 587.

[5] RALPH K.I., *The Chemistry of Silica*, Wiley, New York (1979) pp. 21–29.

[6] BONEN D., KHAYAT K.H. Cem. Concr. Res., 25 (1995), 395.

[7] BABU K.G., PRAKASH P.V.S., Cem. Concr. Res., 25 (1995), 1273.

[8] APPA RAO G., Cem. Concr. Res., 33 (2003), 1765.

[9] DUCHESNE J., BÉRUBÉ M.A., Cem. Concr. Res., 24 (1994), 73.

[10] MITCHELL D.R.G., HINCZAK I., DAY R.A., Cem. Concr. Res., 28 (1998), 1571.

[11] KIRKBRIDGE T.W., *Condensed Silica Fume in Concrete*, FIP State of Art Report, [in:] FIP Commission Thomas Telford, London (1988).

[12] LARBI J.J., FRAAY A.L.A., BIJEN J.M., Cem. Concr. Res., 20 (1990), 506.

[13] CHENG YI-H., FELDMAN R.F., Cem. Concr. Res., 15 (1985), 585.

[14] MAROPOLOU A., CAKMAK A., LABROPOULOS K.C., VAN GRIEKEN R., TORFS K., Cem. Concr. Res., 34 (2004), 1.

[15] RAMACHANDRAN V.S., BEAUDOIN J.J., *Handbook of Analytical Techniques in Concrete Science and Technology*, William Andrew Publishing/Noyes, New York, 2001.

[16] TAYLOR H.F.W., *Cement Chemistry*, 2nd Ed., Thomas Thelford, London, 1997.

Atomic force microscopy investigations of gadolinia doped ceria thin films prepared by pulsed laser deposition technique

K. MUTHUKKUMARAN[1*], P. KUPPUSAMI[2],
T. MATHEWS[3], E. MOHANDAS[2], S.SELLADURAI[1]

[1]Department of Physics, Anna University, Chennai-600 025, Tamilnadu, India

[2]Material Characterization Group, Indira Gandhi Centre for Atomic Research,
Kalpakkam-603 102,Tamilnadu, India

[3]Materials Science Division, Indira Gandhi Centre for Atomic Research,
Kalpakkam-603102, Tamilnadu, India

The growth of gadolinia doped ceria films with controlled surface structure for optimum device performance often presents a significant technological problem for experimental investigation. In the present investigation, gadolinium doped ceria (GDC) thin films were prepared by pulsed laser deposition (PLD) and were studied for their surface structure evolution in relation to various growth parameters. The deposition was made with gadolinia concentrations 5, 10, 15, and 20 mol % to ceria pellets. The dependence of laser energy on 10 mol % GDC thin film was studied. The effect of substrate and substrate temperature on 20 mol % GDC thin film was also investigated. The base pressure was kept at 3.5×10^{-5} mbar during all the studies. The films were characterized using atomic force microscopy (AFM). The AFM results gave a consistent picture of the evolution of GDC film surface morphologies and microstructures in terms of growth behaviour, shape, and particle distribution.

Key words: *pulsed laser deposition; atomic force microscopy; gadolinia doped ceria*

1. Introduction

CeO_2-based materials have been intensively studied as catalyst supports and promoters for heterogeneous catalytic reactions. They have found application as oxide ion-conducting materials in electrochemical devices [1]. These applications require preparation of fine powders to be used as precursors for manufacturing bulk ceramics, coatings, films, and composites [2, 3]. The doped ceria electrolytes have increased ionic conductivity compared to the conventional yttrium-stabilized zirconia (YSZ) and

_____

*Corresponding author, email: muthuk24@yahoo.co.in

they may operate at lower temperatures (below 900 K). Various synthesis approaches using solid route, often called the "solid state reaction route," can provide a good homogeneity of the raw materials due to reagent mixing occurring at molecular level. The resulting oxide powders have a high specific surface area and, consequently, a high beneficial reactivity.

The pulsed-laser deposition (PLD) grown GDC films have been demonstrated to exhibit enhanced performance when compared to films obtained by other conventional deposition techniques. However, detailed investigations on the fundamental understanding of the growth behaviour and surface quality of these pulsed-laser deposited GDC films have not been made. Understanding the growth and morphological evolution of pulsed-laser deposited GDC films in relation to the growth conditions would improve our ability not only to explore the possible technological applications of GDC films [4, 5] but also to further tune the growth conditions to obtain films with the desired characteristics [6]. In this paper, we report on the results of our investigation focused both on understanding the growth mechanism and surface-structure evolution in pulsed-laser ablated GDC thin films. During thin-film processing, the removal of oxygen from the gadolinia doped ceria (GDC) lattice occurs when heated above a certain limiting temperature in vacuum or in a reducing atmosphere [7, 8] and this results in the formation of defects or reduced phases. The phase instability along with morphological disorder usually result in the fading or poor electrochromic/electrochemical device performance when the films are integrated in multicomponent device structures. Recently, extensive and successful efforts have been undertaken to carry out thin-film processing of GDC using PLD since it is an attractive choice for the preparation of stoichiometric and high quality metal oxide thin films for various applications [9, 10].

In the present work, the surface features of pulsed-laser deposited GDC films have been examined using atomic force microscopy (AFM) in order to understand the material characteristics on the microstructure level. The atomic force microscope is a powerful and versatile tool for measuring the surface features of thin films. The surface structure can be studied without any special preparation of the surface even for non-conducting samples. Therefore, detailed surface analysis of pulsed-laser deposited GDC films using AFM could provide guidance for the fabrication of these oxide films with controlled microstructure which is an important prerequisite for their enhanced performance in device structures. Using AFM, we have shown that the GDC films of various Gd concentration (5, 10, 15 and 20 mol %) influence the growth behaviour of the films. The size and distribution characteristics of the particles making up the films are determined by the growth parameters. An attempt has been made to establish the growth kinetics and to make a qualitative analysis of the growth mechanism.

2. Experimental

Samples of GDC were prepared from ceria and gadolinia by the conventional solid-state reaction technique. CeO_2 (99.99% pure) mixed with an appropriate quantity

of Gd_2O_3 (99.99% pure) was ground with a pestle in a mortar for 18 hours. About 5 g of the powder was uniaxially pressed into pellets of 20 mm in diameter and 6 mm thick at 4 tons/cm^2. These pellets were sintered at 1823 K for 6 h in air [11]. The densities of the sintered specimens were determined by the Archimedes method using dibutylthalate as the medium. All the samples used in the present study had the densities of about 90% of the theoretical value. The target was examined with X-ray diffraction and confirmed for its composition and structure before being put into the chamber for laser ablation to produce GDC thin films [4].

Thin films of GDC were prepared by varying the concentration (5, 10,15, and 20 mol %) of gadolinia, the 10 mol % GDC thin films were prepared by varying the laser energy, and finally the 20 mol % GDC thin films were prepared varying the substrates and their temperatures. A KrF excimer laser (Compex 205 from Lambda Physik) with the wavelength of 248 nm was used to ablate the GDC target. The UV laser beam focused by the lens passed through a quartz window to scan the target surface. The angle between the incident laser beam and the laser beam normal to the target surface was 45°. The energy of the laser pulse varied from 200 mJ to 600 mJ and the pulse repetition rate was set at 10 Hz. During the ablation, the target was rotated at the rate of six rotations per minute to avoid the depletion of the material at the same spot continuously and to obtain uniform thin films. Well-cleaned Si (100), and $LaAlO_3$ (100) substrates were employed for the deposition of GDC thin films. The substrates were heated and maintained at a constant temperature using a thermocouple and temperature controller. The target to the substrate distance was 4.5 cm.

The deposition chamber was emptied to a base pressure of 3×10^{-5} mbar prior to film deposition. For reactive deposition, pure oxygen gas was introduced (using flow controller) into the chamber during deposition. The thickness of all the pulsed-laser deposited GDC thin films in the present investigation was about 0.3 μm. The thickness of the film was measured using a Dektak-3010 surface profilometer. An atomic force microscope (DFM mode using SPA400, Seiko Instruments Inc) was used to study the surface morphology of GDC thin films in a tapping mode of operation.

3. Results and discussion

3.1. GDC films with different dopant concentrations

To study the influence of dopant concentration on the microstructure of GDC films, the films with various dopant concentrations (5, 10, 15, and 20 mol %) were examined. Figure 1 represents AFM 3D microstructure of GDC films deposited on Si (100) substrates at 873 K, 0.2 mbar oxygen partial pressure. The film was composed of spherical particles varying in size from 63.1 to ca. 100 nm. The root mean square value of the surface roughness (rms roughness) calculated from the AFM images, increases with the increasing dopant concentration (from 5 to 20 mol %) from 1.92 to 9.78 nm. The results have been shown in Table 1.
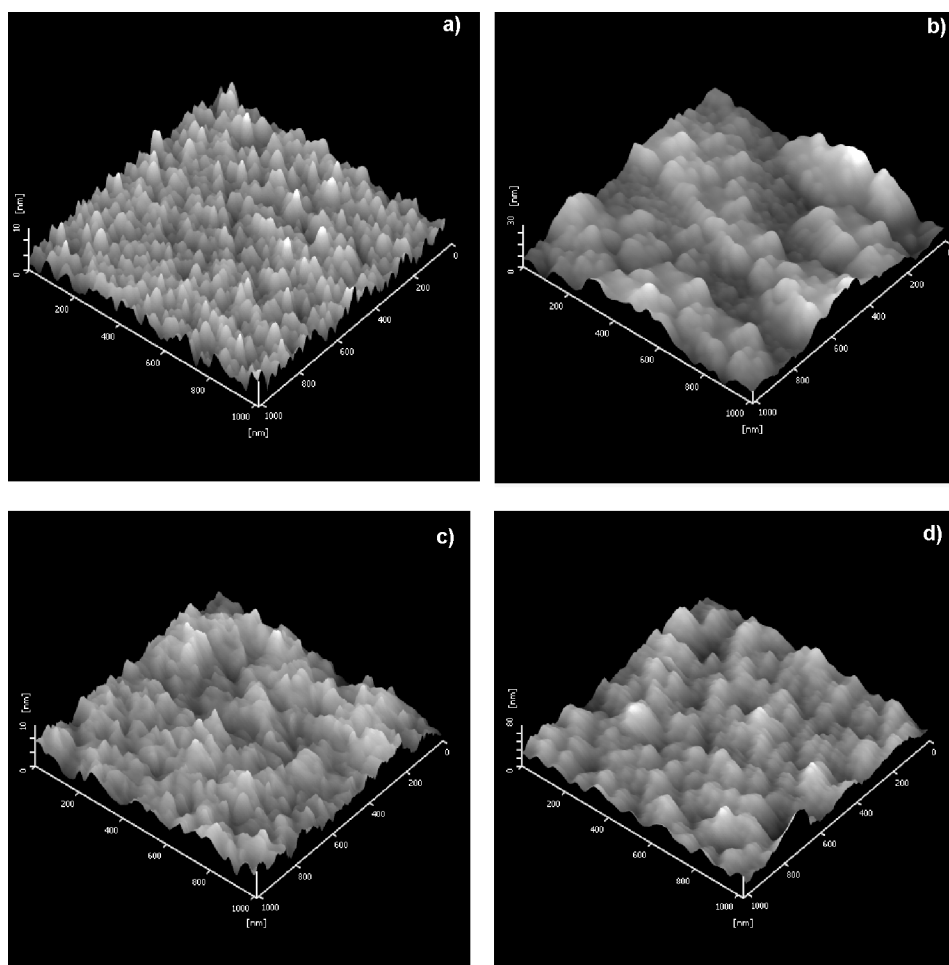
Fig. 1. 3D AFM images of GDC thin films with various dopant concentrations prepared on Si (100)
at 873 K, 0.2 mbar: a) 5 mol % GDC, b) 10 mol % GDC, c) 15 mol % GDC, d) 20 mol % GDC

Table 1. The RMS roughness and mean diameter of grains of GDC thin films
coated on Si (100) at 873 K and oxygen partial pressure of 0.2 mbar

Sample	RMS roughness [nm]	Mean diameter of grains [nm]
GDC – 5 mol % gadolinia	1.92	63.1
GDC – 10 mol % gadolinia	3.59	103.1
GDC – 15 mol % gadolinia	4.98	100.9
GDC – 20 mol % gadolinia	9.78	100.6

The increase in roughness may be due to the different kinetics of the dopant atoms
and the host atoms on the film surface at a particular temperature. Though all the films
were deposited under identical conditions at 873 K, there seems to be a significant

modification in their surface topographies. It is believed that the increasing content of Gd has been found to increase the crystallite size and hence in the increase in the roughness of the films.

3.2. 10 mol % gadolinia doped ceria films prepared at various laser energies

The AFM images of the 10 mol % GDC films prepared at various laser energies from 200 to 600 mJ/pulse at 873 K are shown in Fig. 2. At low energies, the grains are distributed uniformly, their size is small, and the film seems to be smooth. As the energy increases, the grain size and roughness also increase (Table 2).
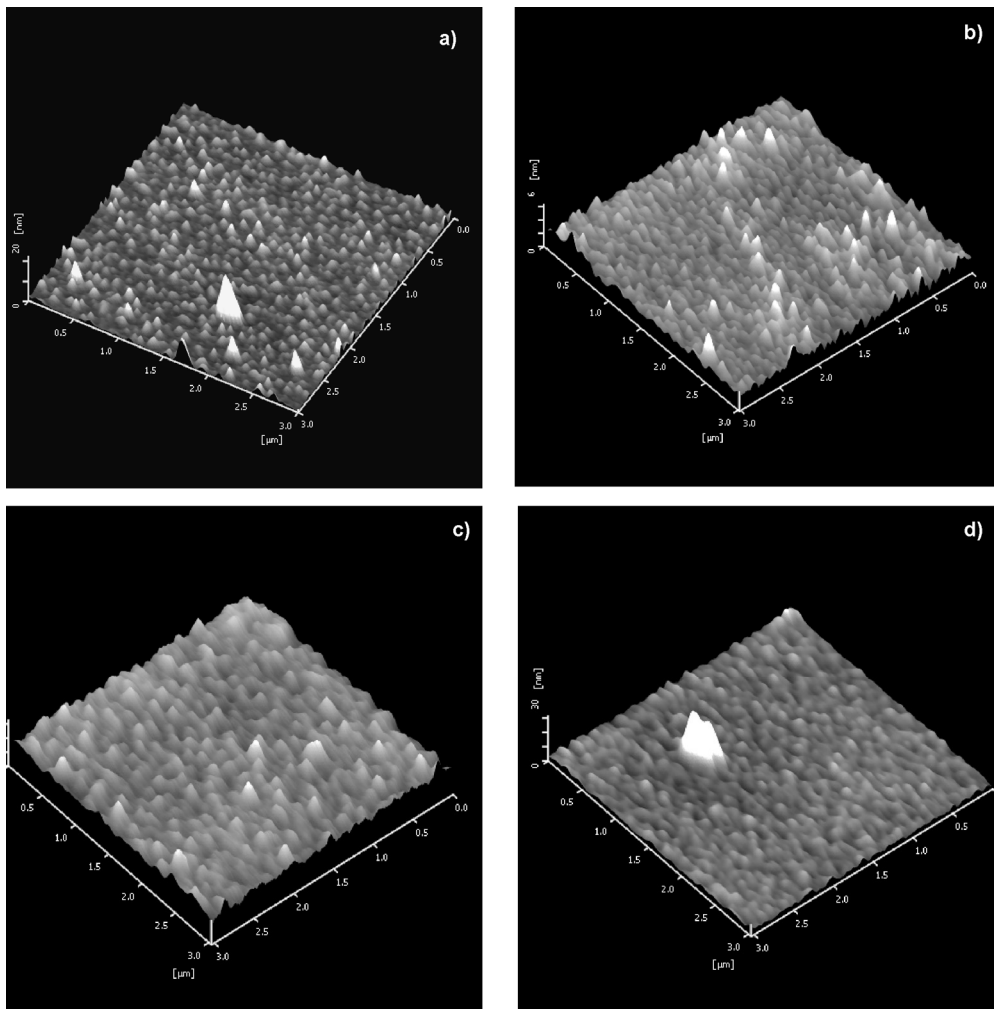
Fig. 2. 3D AFM images of GDC thin films with various laser energies
prepared on Si (100) at 873 K: a) 200 mJ, b) 400 mJ, c) 500 mJ, d) 600 mJ

Table 2. The RMS roughness and mean diameter of grains
of 10 mol % GDC thin films coated on Si (100) at 873K

Sample	RMS roughness [nm]	Mean diameter of grains [nm]
200 mJ	0.18	22.1
400 mJ	0.57	46.2
500 mJ	0.56	66.6
600 mJ	1.73	162.4

It is evident from Figs. 2a, b that the increase in grain growth with increasing laser energy is due to increased ablation rate of the target by incident laser energy which deposits larger amounts of ablated species on the substrate. Though AFM shows an increased grain growth with increasing laser energy, it is seen that each grain comprises several small crystallites appearing as grains on the surfaces of the films shown in Figs. 2c, d.

3.3. Effect of substrate and substrate temperature on 20 mol % GDC films

The AFM results of 20 mol % GDC thin films deposited on various single crystal substrate materials as a function of substrate temperature showed interesting features. The AFM images of GDC thin films were grown on Si (100) and $LaAlO_3$ (100) substrates, respectively. It can be seen in the images that the 20 mol % GDC thin films deposited on all substrate materials have finer microstructures with nano-sized grains spreading on the substrate surfaces uniformly [12, 13].

Another characteristic feature revealed in the present study is the change in the surface morphology of GDC thin films with increasing substrate temperature. Interestingly, it was also noticed that the surface morphological changes are different for 20 mol % GDC thin films grown on various substrate materials. The grain size of 20 mol % GDC thin films increased with the increasing substrate temperature. However, the shape, as well as the arrangement of the grains, were found to be different. It seems that the influence of substrate material characteristics is coming into play to show the effect with the increasing temperature [14, 15]. Figure 3 shows the AFM micrographs of laser-ablated 20 mol % GDC thin films grown on Si (100) (Figs. 3a, c) and $LaAlO_3$ (100) (Figs. 3b, d), at 873 and 973 K. The films grown at 873 K on both substrates showed mostly a cauliflower-like structure. This morphology shown in 2D images indicates several particles embedded in each grain. On the other hand, the films grown on $LaAlO_3$ (100) showed coarsened globular particles instead of a cauliflower-like structure at 973 K. It appears that the characteristics of the substrate material also influence the growth morphology of the deposited thin films.
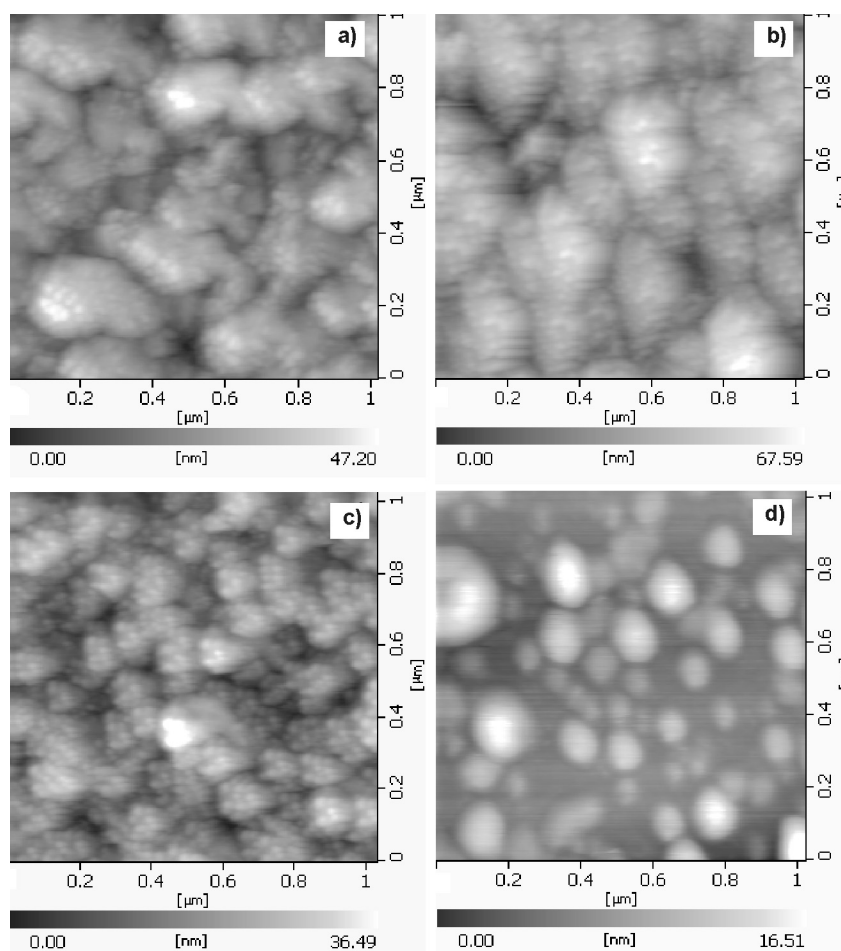
Fig. 3. 2D AFM images of 20 mol % GDC coated on: a) Si (100) at 873 K,
b) LaAlO$_3$ (100) at 873 K, c) Si (100) at 973 K, d) LaAlO$_3$ (100) at 973 K

4. Conclusions

Thin films with various dopant concentrations were fabricated and examined using the atomic force microscopy (AFM). For the thin film deposited on Si (100) substrate at 873 K and 0.2 mbar of oxygen partial pressure, the RMS value of roughness increased with the increasing dopant concentration. The increase in roughness may be related to various kinetics of dopant and host atoms on the film surface at a particular energy and temperature.

For the 10 mol % GDC films prepared at various laser energies, at low energy the grain size was small and the film was smooth. With the increase of energy, grain size

and roughness increased, which may be attributed to the increased ablation rate of the target with the increasing laser energy.

20 mol % GDC films deposited on Si (100) and LaAlO$_3$ (100) substrates have finer microstructure with nano-sized grains. The films grown at 873 K on both substrates showed mostly a cauliflower-like structure. On the other hand, the films grown on LaAlO$_3$ (100) showed coarsened globular particles instead of a cauliflower-like structure at 973 K. It appears that the characteristics of the substrate material also influence the growth morphology of the deposited thin films.

References

[1] Zhu B., Yang X.T., Xu J., Zhu Z.G., Ji S.J., Sun M.T., Sun J.C., J. Power Sourc., 118 (2003), 47.

[2] Taniguchi I., Van Landschoot R.C., Schoonman J., Solid State Ionics, 160 (2003), 271.

[3] Yashiro K., Onuma S., Kaimai A., Nigara Y., Kawada T., Mizusaki J., Kawamura K., Horita T., Yokokawa H., Solid State Ionics, 152–153 (2002), 493.

[4] Kuppusami P., Padhi S.N., Muthukkumaran K., Mohandas E., Raghunathan V.S., Surf. Eng., 21 (2005), 172.

[5] Shao Z.P., Dong H., Xiong G.X., Gong Y., Yang W.S., J. Membr. Sci., 183 (2001), 181.

[6] Ishihara T., Tsuruta Y., Todaka T., Nishiguchi H., Takita Y., Solid State Ionics, 152 (2002), 709.

[7] Julien C., Haro-Poniatowski E., Hussain O.M., Ramana C.V., Ionics , 7 (2001), 165.

[8] Zhang J.G., Mcgraw J.M., Ginley D.J., Electrochem. Soc., 144 (1997), 1630.

[9] *Pulsed laser deposition of thin films*, D.B. Chrisey, G.K. Hubler (Eds.), Wiley, New York, 1994.

[10] Mathews T., Rabu N., Sellar J.R., Muddle B.C., Solid State Ionics, 128 (2000), 111.

[11] Muthukkumaran K., Kuppusami P., Mohandas E., Raghunathan V.S., Selladurai S., Proc. Int. Symp. Res. Stud. Materials Science and Engineering, 20–22 December, Chennai, India

[12] Kah-Yoong Chan, Bee-San Teo, Microelectronics J., 37 (2006), 1064

[13] Chu K., Liu Z.-J., Lu Y.H., Shen Y.G., Appl. Surf. Sci., 252 (2006), 8091.

[14] Gerhazi L.E., Geretovszky Z., Csako T., Szorenyi T., Appl. Surf. Sci., 252 (2006), 4661.

[15] Sakama H., Osada G., Tsukamoto M., Tanokura A., Ichikawa N., Thin Solid Films, 515 (2006), 535.

Simulated geometry of open-end single-wall carbon nanotubes with adsorbed long-chain normal alkanes and resulting implications

L. STOBIŃSKI[1*], J. MAZURKIEWICZ[2], P. TOMASIK[3, 4], J. PESZKE[5], H.M. LIN[6**]

[1]Institute of Physical Chemistry, Polish Academy of Sciences,
ul. Kasprzaka 44/52, 01-224 Warsaw, Poland

[2] Department of Physics, University of Agriculture, al. Mickiewicza 21, 31-120 Cracow, Poland

[3]Department of Chemistry, Agricultural University, ul. Balicka 122, 30-149 Cracow, Poland

[4]School of Biotechnology, Agricultural University, al. 29 Listopada, 54, 31-452 Cracow, Poland

[5]Institute of Chemistry, Jan Długosz Academy, ul. Armii Krajowej 13/15, 42-201, Częstochowa, Poland

[6]Department of Materials Engineering, Tatung University, Taipei 104, Taiwan, ROC

Successful designing and computation of optimized, large (up to 10 000 atoms), complex structures of isomeric zigzag, armchair, and chiral open-end single-wall carbon nanotubes (SWCNTs) with normal-chain C_8, C_{16}, C_{40}, C_{80}, and C_{96} hydrocarbons was performed by means of HyperChem 7.0 (Molecular Dynamics and Molecular Mechanics MM+) and Gaussian 03 (Molecular Mechanics UFF) programs. The diameter of the nanotubes was around 0.4, 0.7, 0.9, 1.1, 1.3, and 1.7 nm. Octane and hexadecane positioned themselves on the nanotube surfaces in the manner influenced by the pattern of the carbon atoms in the tubes, i.e., in the manner dependent on the isomerism of the nanotubes. Longer-chain hydrocarbons usually coiled around the nanotubes, unless they were 0.4 nm in diameter. In such cases a kind of clip-shape arrangement of the hydrocarbons on the nanotube surface was noted instead of coiling. The numbers of carbon atoms in one full turn of the hydrocarbon chain coiling around the SWCNT increased with the diameter of the nanotubes, corresponding to 35, 46, 52, and 64 carbon atoms for 0.7, 1.1, 1.3 and 1.7 nm diameter nanotubes, respectively. However, the comparison of the energy of complexation calculated per one carbon atom of the alkane chain adsorbed on the nanotube surface suggests that in some cases, complexation of long-chain normal hydrocarbons to the carbon nanotube could result in the separation of those nanotubes according to their diameter.

Key words: *carbon nanotube; normal hydrocarbon; computer simulations*

---

*Corresponding author, e-mail: lstob@ichf.edu.pl
**Corresponding author, e-mail: hmlin@ttu.edu.tw

1. Introduction

There are three isomeric forms of single-wall nanotubes (SWCNTs): zigzag, armchair, and chiral nanotubes. As far as we know, none of the developed methods of synthesis of such nanotubes provides pure, isomerically uniform products. Thus far, the proposed methods available for separation of isomers [1] were based on their selective chemical functionalization. In our preliminary opinion, the separation of isomeric nanotubes could be possible by the formation of complexes with long-chain normal hydrocarbons. This view is based on results available in the literature [2–17].

Hydrocarbons have been shown to adsorb on single and bundled carbon nanotubes. Preliminary modelling studies [2, 3] suggested that methane did not adsorb on the surface of bundled SWCNTs and further investigations [4, 5] led to the conclusion that methane diffused inside the nanotubes. Based on the changes of the SWCNTs electrical resistivity caused by the adsorption of methane, a corresponding gas sensor was proposed [6]. Computational simulations suggested that a mixture of C_1–C_8 n-and i-alkanes could be separated on the carbon nanotubes. The results depended on the length of the SWCNTs. The adsorption improved with the increasing hydrocarbon chain length and it was obscured, to a certain extent, by chain branching. The diameter of a carbon nanotube is another crucial factor [7–12]. Also cycloalkanes and cycloalkenes adsorb on the surface of the SWCNTs although their adsorption is worse than that of n-alkanes of the same number of carbon atoms in the chain [13, 14]. As the chain of alkanes became longer, their surface adsorption on the SWCNTs was faster and predominated over the inclusion inside channels. This was found in the case of n-decane [15]. Such a tendency was also observed for the sorption of alkanes on multi-walled carbon nanotubes (MWCNTs) [16]. In general, sorption of alkanes on the surface of MWCNTs has a priority over their condensation inside the channels. Again, the nanotube diameter was a factor [17].

A formal curvature of graphene plane into a single-walled carbon nanotube changed the properties of the molecular orbitals on both sides of the wall of the system to an extent depending on the degree of the curvature, that is, the diameter of the resulting nanotubes [18]. Originally, sp^2 hybridized carbon atoms of graphene structure changed their hybridization slightly towards sp^3. Hence, the electrical, emissive, and other properties of the nanotubes were modified. Obviously, the possibilities of interaction of the resulting outer molecular orbital with a sorbate were also perturbed. Additionally, three types of localizations of the carbon atoms of the nanotube walls in a manner providing isomerism might have subtly influenced the mode and energy of surface–sorbate interactions.

Thus, in this paper, the energy and structure of surface complexes of single-wall zigzag, armchair, and chiral carbon nanotubes of varying length and diameter with n-octane (C_8) and selected higher n-alkanes, C_{16}, C_{40}, C_{80}, and C_{96}, were simulated to either prove or disprove this concept.

2. Computations

First, the HyperChem 7.0 program using PC IV with double CPU optimized the complex geometries. Energy minima were found by molecular dynamics (MD) calculations at 300 K (run time was 100 ps at step size of 0.001) and then by molecular mechanics (MM+) with RMS gradient of 0.001. Original parameters of the program were applied.

The Gaussian 03 computations, using molecular mechanics (UFF) with four default convergence criteria set in the program, were additionally performed with the SGI 2800 grizzly computer in the Academic Computer Centre Cyfronet in Cracow, Poland.

In every case, computations were started using the HyperChem program (MD) with an initially optimized individual structure of SWCNT and linear alkane. This procedure was initiated by situating straight hydrocarbon chains close to the nanotube surface but perpendicularly or at an angle to their long CNT axes. MD was applied for the first optimization run. During optimization, straight alkane could coil tightly around (and/or adhere along) CNT and the CNT–alkane complex was transferred through many local energetic minima, finally approaching the global minimum energy. Then the molecular mechanics MM+ method was used and a stationary point on the potential surface was found. Afterwards, the Gaussian 03 program (molecular mechanics UFF) was used to enhance the precision of the complex optimization process. This kind of computations was performed for zigzag, armchair, and chiral open-end single wall carbon nanotubes of the structure and the atomic composition specified in Table 1.

After a proper optimization of the CNT/alkane system geometry, the whole alkane chain should tightly adhere to the CNT surface independently of the alkane location on the CNT surface (coil and/or clip shape). Also, no part of the alkane chain could protrude from the CNT structure (as well as along the CNT axis and also perpendicular or at an angle to the CNT axis). In an optimized complex structure, the alkane chain could not self-cross. If one of those coincidences took place, optimization of the complex structure was repeated to avoid cases where the CNT surface was not fully covered by the whole alkane chain and the calculated complex formation energy would be significantly lowered (sometimes by over 20–30%).

It was shown that the relation between the length of the CNT and the alkane chain was not important. The alkane could be much longer than the CNT and could tightly coil around the CNT several times or adhere to the CNT surface along the CNT axis, creating a kind of clip as shown below.

3. Results and discussion

Computations were performed for six sets of open-end SWCNTs varying in their diameters, that is 0.4, 0.7, 0.9, 1.1, 1.3, and 1.7 nm. Each set contained three SWCNTs

isomeric models, namely armchair (A), zigzag (Z), and chiral (C) nanotubes. Their structure and atomic composition is presented in the first column of Table 1.

Table 1. Energies of the complex formation of *n*-alkanes with the isomeric open end, single wall carbon nanotubes calculated with HyperChem 7.0 and Gaussian 03[1]

Nanotube			Alkane				
			C_8	C_{16}	C_{40}	C_{80}	C_{96}
0.4	A	3,3 330C + 12H	7083.77 −42.22, −5.28	7040.85 −41.47, −2.59	7141.62 −56.33, −1.41	7248.09 −44.68,−0.56	7223.93, −43.19,−0.45
	Z	5,0 276C + 12H	4578.74, 14.08, 1.76	4561.96 32.02, 2.00	4557.94 64.02, 1.60	4534.41, 121.42, 1.51	4546.86 133.30, 1.39
	C	4,2 227C + 13H	4499.49, 17.09, 2.14	4498.32 26.73, 1.67	4499.13 62.79, 1.57	4446.67 118.22, 1.48	4461.53 148.04, 1.54
0.7	A	5,5 330C + 20H	3501.07, 13.48, 1.68	3499.25 25.43, 1.59	3485.57 68.46, 1.71	3471.69 136.07, 1.70	3456.85 164.73, 1.72
	Z	9,0, 432C + 18H	4406.58, 16.00, 2.00	4399.75, 30.03, 1.88	4396.49 65.46, 1.64	4392.46 132.43, 1.66	4383.12 159.86,1.67
	C	8,2 396C + 20H	3945.92 14.91, 1.86	3943.48 25.44, 1.59	3923.83 72.87, 1.82	3461.38 133.09, 1.66	3852.54 173.15, 1.80
0.9	A	7,7 476C + 28H	3655.74 19.57, 2.44	3659.42 29.74, 1.86	3632.16 81.22, 2.03	3608.14 157.00, 1.96	3604.01 172.36, 1.80
	Z	12,0 576C + 24H	4449.45 14.60, 1.83	4440.37 29.97, 1.87	4412.08 82.32, 2.06	4400.44 151.53, 1.89	4395.64 175.46, 1.83
	C	8,5 436C + 26H	3512.55, 16.23, 2.03	3506.95 32.47, 2.03	3496.09 75.89, 1.90	3461.37, 146.42, 1.83	3430.57 171.29, 1.74
1.1	A	8,8 480C + 32H	3325.35, 19.22, 2.40	3325.81, 30.61, 1.91	3296.31 82.35, 2.06	3253.96, 160.29, 2.00	3222.40 187.45, 1.95
	Z	14,0 672C + 28H	4809.44, 17.78, 2.22	4803.82 34.45, 2.15	4771.09, 85.02, 2.13	4748.70, 163.47, 2.04	4615.65 190.54, 1.98
	C	12,3 610C + 30H	4216.38, 19.73, 2.47	4205.72 37.10, 2.32	4186.78 79.49, 1.99	4148.49, 152.24, 1.90	4158.92 186.84, 1.95
1.3	A	10,10 460C + 40H	2772.46, 19.51, 2.44	2770.66 33.29, 2.08	2770.52 76.59, 1.91	2710.80, 162.15, 2.03	2710.47 184.35, 1.92
	Z	16,0 448C + 32H	2843.44, 15.30, 1.91	2868.28 29.28, 1.83	2944.89 73.44, 1.84	3052.39, 156.39, 1.95	3126.49 95.12, 0.99
	C	15,2 468C + 34H	2959.15, 12.51, 1.56	2966.08 34.36, 2.15	3038.62, 79.20, 1.98	3161.39, 165.23, 2.07	3258.00 186.18, 1.94
1.7	A	13,13 910C + 52H	5243.77, 20.13, 2.52	5126.39 30.98, 1.94	5326.56, 89.34, 2.23	5306.44, 169.32, 2.11	5367.71 194.79, 2.03
	Z	22,0 1056C + 44H	5516.16, 17.97,2.25	5555.23 32.31, 2.02	5591.21, 88.50, 2.21	5748.43, 163.21, 2.04	5781.10 202.65, 2.11
	C	18,6 826C + 48H	4366.10, 19.11, 2.39	4390.06 34.03, 2.13	4450.39, 87.59, 2.19	4576.79, 159.21, 1.99	4663.41 188.49, 1.96

[1]In the "Nanotube" column of the table the nanotube diameter [nm], type of isomer (A – armchair, Z – zigzac, C – chiral), structure of nanotube (*m*,*n*), and number of the carbon and hydrogen atoms are given. In the "Alkane" columns, subsequent values report energy [kcal/mole] of the SWCNT complex with a given alkane, difference between energy of the complex and the sum of energies of the non-complexed partners, and the complex energy calculated for one alkane carbon atom, respectively.

Although these SWCNTs had almost the same diameters and similar lengths, they differed from one another in the number of carbon and edge hydrogen atoms. In order to evaluate the effect of the SWCNTs length, computations were additionally performed for selected longer nanotubes. Subsequently, computations were performed for complexes of those SWCNTs with a series of *n*-alkanes of 8 (octane), 16 (hexadecane), 40, 80, and 96 carbon atoms in their chains. In every further column the first value is the energy of the complex, the second value is the complexation energy, presented as the difference of the energy of the complex from which the sum of energy of individual SWCNTs and the particular hydrocarbon was subtracted. The third value is the energy of the complex calculated per one hydrocarbon carbon atom. All energies are expressed in kcal/mole.

Simulations showed that octane and hexadecane positioned themselves on the SWCNT surface in a manner influenced by the pattern of the carbon atoms in the SWCNTs, that is in a manner dependent on the isomerism of the nanotubes (Fig. 1).
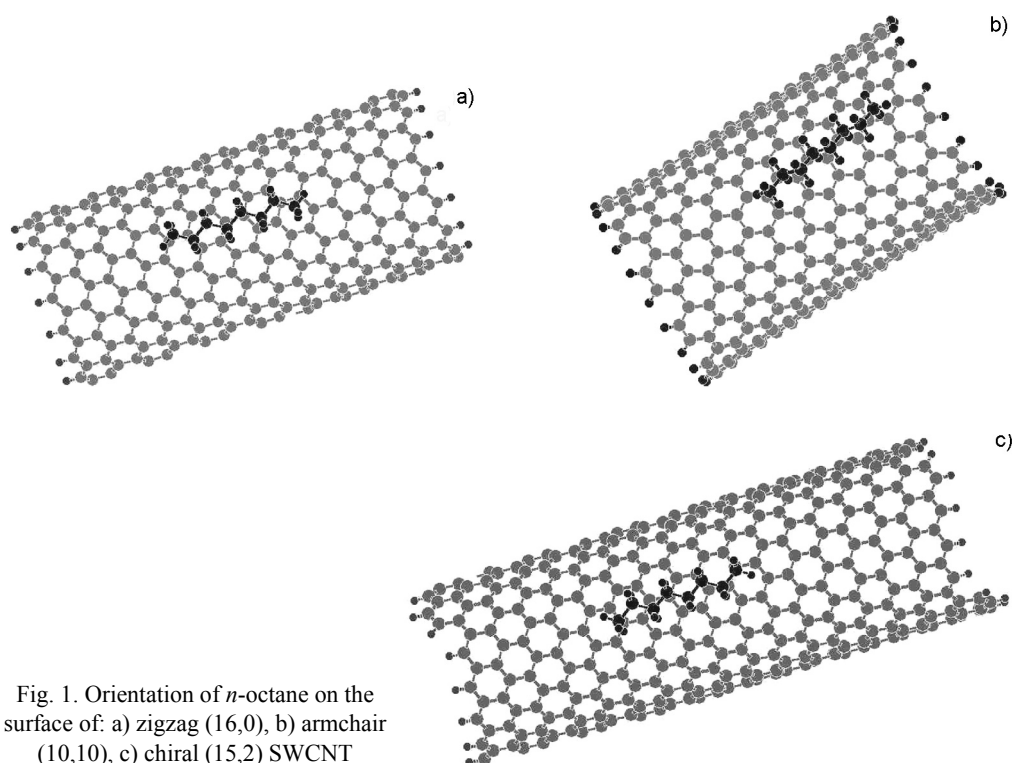

Fig. 1. Orientation of *n*-octane on the surface of: a) zigzag (16,0), b) armchair (10,10), c) chiral (15,2) SWCNT

In similar simulations for longer-chain hydrocarbons one could observe that in the case of 0.4 nm diameter SWCNTs, the hydrocarbon chains did not coil around the nanotubes but, instead, formed a kind of a clip shape along the long axis of the nanotubes (Fig. 2).
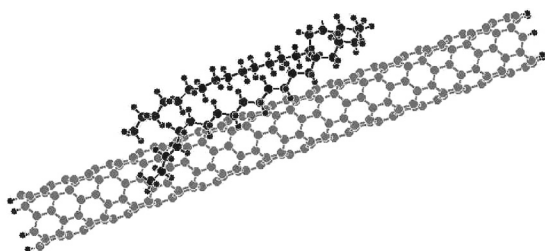
Fig. 2. Orientation of a C_{40}
hydrocarbon molecule along the 0.4 nm zigzag
(5,0) SWCNT

Table 1 shows that the complex energy for one of the narrowest SWCNT (3,3) was almost twice as large as that for the other narrowest SWCNTs: (5,0) and (4,2). Also, the energy benefit due to complexation was negative. This means the structure of the narrowest SWCNT (3,3) was very unstable and the formation of its complex with alkane was impossible. Our conclusion about the high instability of the narrowest CNT was in good agreement with results published previously [19, 20].

The sp^3 hybridization of the carbon atoms in the chain, and the resulting bond angles did not provide a diameter of the turn within the hydrocarbon coils offering the energy of the complex lower than that when the hydrocarbon chain formed a clip-shape on the SWCNTs' surface. As found by computations for the SWCNTs –hydrocarbon complexes, the atoms of the SWCNT surface and the atoms of the hydrocarbon chain were normally situated at the distance of about 0.3 nm from one another. Because of the C–C bond distances and C–C–C bond angles in the hydrocarbon chain, the distance between the alkane helical turn and the SWCNT surface exceeded 0.3 nm when the diameter of the SWCNT was 0.4 nm. Under such circumstances the "clip-like" arrangement of the hydrocarbon chain on the SWCNT surface was energy -beneficial. As the diameter of the nanotubes expanded, e.g. the curvature of the CNT structure decreased, the long-chain hydrocarbons preferably coiled around them (Fig. 3).
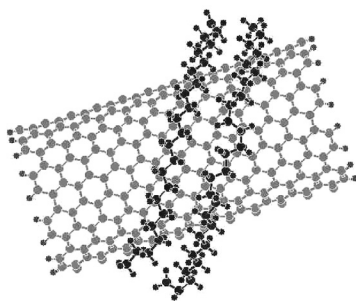
Fig. 3. Coiling of the C_{40} hydrocarbon around
1.3 nm (10,10) armchair SWCNT

The number of carbon atoms in one full turn of the hydrocarbon chain coiling around the SWCNT increased with the diameter of the SWCNTs, and amounted to 35, 40, 46, 52, and 64 carbon atoms for 0.7, 0.9, 1.1, 1.3 and 1.7 nm diameter SWCNTs, respectively.

Examination of Table 1 reveals that the energy of the complexes and the energy benefit due to complexation was usually independent of the SWCNTs diameter and

the hydrocarbon chain length. This pointed to the intervention of the effect of individual fitting of hydrocarbons to a given isomeric SWCNT. The comparison of the complexation energy calculated per one carbon atom in the nanotubes (Table 1) suggests that in some cases, complexation of long-chain normal hydrocarbons to SWCNTs could provide a separation of those nanotubes according to their diameter.

Computations for longer SWCNTs pointed to a negligible effect of the SWCNTs length on the complex energy. Thus, the complexation of SWCNTs with normal hydrocarbons as a means of separating them according to isomer type appeared fairly unlikely. The differences in the complexation energy, in particular for SWCNTs complexes of a given diameter, only randomly exceeded 10 kcal/mole, and they were within the portion of energy available from the thermal motions of hydrocarbons.

4. Summary and conclusions

Simulation of an optimized (even up to 10000 atoms) complex structure with CNT and hydrocarbons can be successfully performed by combining two programs: HyperChem and Gaussian. Using the HyperChem (Molecular Dynamics) program we can create an optimized complex structure starting from free CNT molecules and hydrocarbons. Then, by applying the Gaussian 03 program we can enhance the precision of the complex optimization. Independently on the standard convergence criteria set up in the HyperChem and Gaussian programs, additionally three criteria should be fulfilled to cover completely the CNT surface by the alkane chain: *i)* the long hydrocarbon chain should tightly adhere to the CNT surface regardless of the way the hydrocarbon adsorbs on the CNT surface (coil and/or clip shape), *ii)* after optimization no part of the hydrocarbon chain can protrude from the CNT structure (as well as along the CNT axis and also perpendicular or at an angle to the CNT surface), *iii)* the hydrocarbon chain cannot be self-crossed in the optimized complex structure.

The complexation of SWCNTs with normal hydrocarbons can be useful as a means of separating SWCNTs according to their diameter but is unlikely to work as way to separate them according to their isomeric type.

References

[1] BANERJEE S., HEMRAJ-BENNY T., WONG S.S., J. Nanosci. Nanotechnol., 5 (2005), 841.
[2] MAO Z., SINNOTT S.B., J. Phys. Chem., 194 (2000), 4618.
[3] TALAPATRA S., ZAMBANO A.Z., WEBER S.E., MIGONE A.D., Phys. Rev. Lett., 85 (2000), 138.

[4] MURIS M., DUFAU N., BIENFAIT M., DUPONT-PAVLOVSKY N., GRILLET Y., PALMARI J., Langmuir, 16 (2000), 7019.

[5] BIENFAIT M., ASMUSSEN B., JOHNSON M., ZEPPENFELD P., Surf. Sci., 460 (2000), 243.

[6] VALENTINI L., ARMENTANO I., LOZZI L., SANTUCCI S., KENNY J.M., Mater. Sci. Eng., C 24 (2004), 527.

[7] MAO Z., SINNOTT S.B., J. Phys. Chem. B, 105 (2001), 6916.

[8] JIANG J., SANDLER S.I., SCHENK M., SMIT B., Phys Rev., 72 (2005), 045447.

[9] JIANG J., SANDLER S.I., SMIT B., Nano Lett., 4 (2004), 241.

[10] JIANG J., SANDLER S.I., J. Chem. Phys., 124 (2006), 024717.

[11] BHIDE S.Y., YASHONATH S., J. Am. Chem. Soc., 125 (2003), 7425.

[12] JIANG J., SANDLER S.T., Fluid Phase Equil., 228 (2005), 189.

[13] BITTNER E.W., SMITH M.R., BOCKRATH B.C., Carbon, 40 (2003), 1231.

[14] AGNIKOTRI S., ROOD M.J., ROSTAN-ABADI M., Carbon, 43 (2005), 2379.

[15] SUPPLE S., QUIRKE N., J. Chem. Phys., 121 (2005), 8571.

[16] LI Q.L., YUAN D.X., LIN Q.M., J. Chromatogr. A, 1026 (2004), 283.

[17] HILDING J., GRULKE E.A., SINNOTT S.B., QIAN D., ANDREWS R.R., JOGTOYEN M., Langmuir, 17 (2001), 7540.

[18] KOSTOV M.K., CHENG H., COOPER A.C., PEZ G.P., Phys. Rev. Lett., 89 (2002), 146105.

[19] TANG Z.K., ZHANG L., WANG N., ZHANG X.X., WEN G.H., LI G.D., WANG J.N., CHAN C.T., SHENG P., Science, 292 (2001), 2462.

[20] SUN H.D., TANG Z.K., CHEN J., LI G., Appl. Phys. A, 69 (1999), 381.

Finite element method modelling of the properties of a Cu–SiC composite under cyclic loading conditions

M. A. Miśkiewicz[*], H. Matysiak, K. J. Kurzydłowski

Warsaw University of Technology, Materials Science and Engineering Faculty,
ul. Wołoska 141, 02-507 Warsaw

The paper reports on finite element method (FEM) analysis of Cu–SiC composites behaviour under cyclic loading conditions. In order to emphasise the influence of materials description on following results, there were two hardening rules used to describe the plastic behaviour of the matrix: (a) simple isotropic and (b) combined isotropic-kinematic. Reinforcing ceramics was assumed to be perfectly elastic. The analysis was carried out for Cu–SiC fibre–reinforced lamina composite. The fibre volume fracture was assumed to be 20%. The modelling was based on representative volume element (RVE) geometry. Additionally, the effect of thermal residual stresses was taken into account and its influence upon the Cu–SiC composite mechanical behaviour was clarified.

Key words: *finite element method; Cu–SiC composite; plastic behaviour; RVE geometry*

1. Introduction

Metal matrix composites (MMCs) are high-performance materials which are used for various applications demanding high strength but low weight. This feature of MMC is widely employed in automotive and aircraft industry [1]. In recent years, there has been a significant interest in copper metal matrix composites (CuMMCs) due to their high thermal conductivity and anticipated higher operating temperature which could be higher than in the case of high strength copper alloys (CuCrZr). Due to a good creep resistance and high strength at elevated temperatures, the most promising composites are fibrous CuMMC [2, 3]. This type of composites could replace CuCrZr alloys which cannot operate at temperatures exceeding 350 °C [4–6]. CuMMCs may be applied in particular elements of supersonic speed vehicles, like rockets and aircrafts, where they can be used as the attack edges of wings and the facing material in combustion chambers. It is also important that copper has a high resistance to hydro-

---

[*]Corresponding author, e-mail: mmiskiewicz@inmat.pw.edu.pl

gen embrittlement as hydrogen is likely to be the predominant fuel. Materials with high thermal conductivity are indispensable in order to reduce the temperature gradient in the high heat flux areas of engines. CuMMCs are also candidate materials for the next generation thermonuclear reactors [7, 8]. Recently CuSiC MMCs have been considered as heat sink materials for fusion energy applications. The most promising reinforcement material for a Cu matrix is silicon carbide fibre SCS-6 type produced by Speciality Materials (Fig. 1). It can be used to produce lamina or laminate composites of various fibre volume fractions and gives an opportunity to manufacture gradient materials, which is particularly important for the joining technology.

Fig. 1. SEM image of SCS-6 fibre

Due to the variation of temperature and external load applied to MMCs components, MMCs are usually subject to cyclic loading, which could lead to a quick component failure, especially if plastic flow occurs. In the case of CuMMC, plastic deformation of the Cu matrix can take place easily and more frequently than in other metal matrices. One can expect easy failure by means of low cyclic fatigue and debonding at the interface, leading to a deterioration of composite properties.

Internal stresses and residual deformation can be induced in MMC by the differences in the thermal expansion coefficients (CTE), usually small for ceramic fibres and much higher for metals matrices. Also, temperature fluctuation during the service of CuMMCs may lead to accumulation of plastic deformation that could be: (a) regressive (shakedown), (b) constant (plastic shakedown) or (c) progressive (ratcheting), depending on the load amplitude level, the microstructure and the properties of the components. Generally, MMCs are produced using high temperature techniques which create residual stresses in the composite during the cooling process. The magnitude and distribution of these stresses depend on the micro-geometry, properties of the components, and the manufacturing conditions [9].

Currently, step-by-step simulations based on well developed non-linear finite element method (FEM) solutions are efficient and sufficiently accurate to predict the properties of composites, including the residual stresses and loading history. These methods can also be used to simulate the lifetime of a composite under cyclic loading.

In this study, a unit cell approach was employed to predict the mechanical behaviour of CuMMC under various conditions of thermo-mechanical loadings. Simplified isotropic hardening and more advanced combined hardening plasticity models were used for the simulation of the stress-strain response of the Cu matrix. SiC fibres were considered to be perfectly adherent to the Cu matrix and no debonding effects at the interface were taken in to account.

1.1. Plastic deformation rules

The main concept of plastic deformation and hardening rules is based on the yield surface which is embedded in the stress domain. The shape of this surface depends on the behaviour of material. The plasticity surface is always convex. This is sufficient to determine the material's "reaction" during an arbitrary loading and unloading path. For most metals it has a cylindrical shape, axially symmetrical around a stress tensor direction describing pure hydrostatic stress state:

$$\sigma_H = \frac{\sigma_{ii}}{3}, \quad i = 1, 2. 3 \quad \text{for a principal stress} \tag{1}$$

When the stress tensor reaches the surface and when the product of the strain increment and stress increment is higher than/or equal zero, a plastic flow is possible. Plastic deformation is controlled by the stress and yield surface in accordance with an associated plastic flow rule described below:

$$\partial \varepsilon_{pl} = \frac{\partial F\left(\sigma_{ij}\right)}{\partial \sigma_{ij}} \tag{2}$$

where $F(\sigma_{ij})$ is the plastic potential associated with plastic surface [10];

$$F\left(\sigma_{ij}\right) = \sqrt{3}\, \frac{1}{2}\sqrt{S_{ij}S_{ij}} \tag{3}$$

where S_{ij} is the deviatoric stress tensor.

In the case of plastic deformation, the yield surface may change its shape, size, or both. A change of the yield surface size is connected to isotropic hardening and change of location of the centre (known as kinematic hardening). The transformation of the yield surface is related to material hardening or softening.

1.2. Isotropic hardening

The basic rule describing the behaviour in the plastic domain is the isotropic hardening. Isotropic hardening describes a uniform expansion of the yield surface (in the

deviatoric plane). It implies that the position of the centre of the yielding surface remains in the same position during plastic flow [11]. This property leads to the increase of yield stress irrespective of the loading direction. For isotropic hardening it is not important under what conditions (stress tensor structure) the yielding surface was reached (Fig. 2).
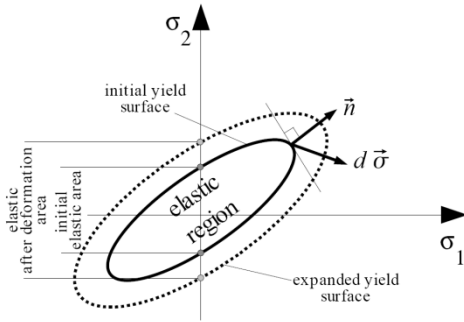
Fig. 2. Schematic evolution of isotropic
hardening model

Many materials exhibit such a type of plastic behaviour. Purely isotropic hardening provides elastic shakedown in the first cycles and is generally used for modelling under unidirectional monotonic loading. In many cases, kinematic hardening is neglected. For shakedown – ratcheting analysis, the kinematic rule plays a more significant role where the prediction of behaviour under cyclic loading is required [12]:

$$F(\sigma, H) = 0 \tag{4}$$

$$H = h(\sigma_0) \tag{5}$$

$$\sigma_0 = \sigma_{S0} + Q_\infty (1 - e^{-b\varepsilon_{pl}}) \tag{6}$$

Equation (6) describes the development of yield surface as a non-linear function of plastic deformation where ε_{pl} is the equivalent plastic strain. Q_∞ indicates the maximum change in the size of yield surface and is the rate at which the yield surface develops as ε_{pl} increases.

1.3. Kinematic hardening

Kinematic hardening takes place when the back stress tensor α translates the yield surface centre to a new position (Fig. 3). This rule was developed to model the Buschinger effect [13], where the yield stress is higher when the material is loaded in one direction and gets smaller for flowed reverse loading case. The back stress tensor depends on the plastic strain rate. This dependence between α and $d\varepsilon/dt$ could be simply linear or non-linear.
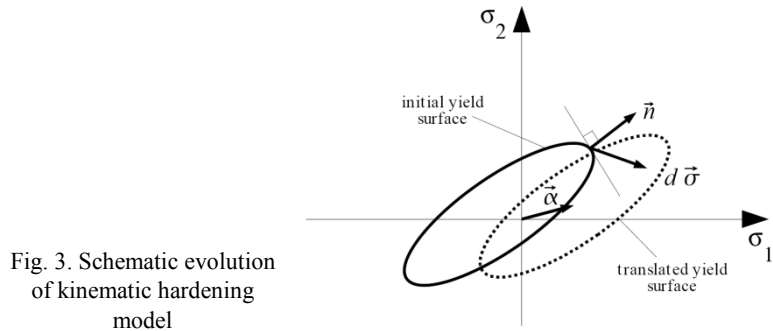
Fig. 3. Schematic evolution
of kinematic hardening
model

1.4. Combined model

The combined model is based on isotropic and kinematic systems interacting with one another which causes that the expansion and translation of the yield surface simultaneously take place. In this case, it is hard to distinguish which one dominates. The balance between them is set by the parameters of governing equations. The parameters can be determined only when the effects of both models can be separated. For example, it is possible, taking into account the unidirectional cyclic test, when the stress-strain loop is saturated and only kinematic hardening is active since the elastic domain has reached its maximum value Q_∞ [14].
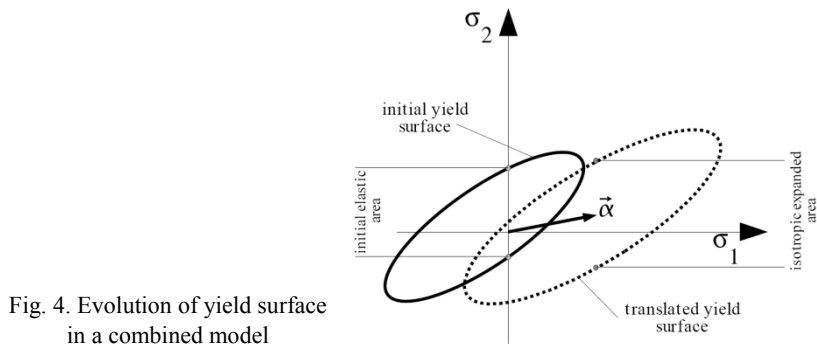
Fig. 4. Evolution of yield surface
in a combined model

2. Results

2.1. Unit cell model (UCM)

A composite structure is frequently periodic, which simplifies micro-modelling. For the entire volume of a composite, assuming a UCM, it is possible to define a rep-

resentative volume element (RVE) as the subject of simulation. The unit cell model is commonly used in the FEM to calculate the macroscopic properties of a material [15].

The UCM provides information on the micro-mechanical as well as the macroscopic properties of composites. For structural analysis, the UCM could deliver data for further homogenization. This approach is very effective and allows one to reduce the calculation time but in many cases requires developing new constitutive models.

2.2. Composite

The investigated material was a copper matrix composite containing embedded SCS-6 SiC fibres (Fig. 1). The fibre volume fraction was 20%. It was assumed that the fibres were well bonded and no interface cracking was taken into account. Because of the high strength of the SiC fibres, (Fig. 5, [16]) they were considered to be perfectly elastic. The Cu matrix exhibited the elastic-plastic behaviour (Fig. 6). Two constitutive models have been taken into account to describe the properties of copper: a) purely isotropic non-linear, b) combined non-linear isotropic-kinematic hardening, based on the Armstrong and Frederick rule, under the Lemaitre and Chaboche framework [17]. The parameters for the models were calibrated, based on experimental results obtained from cyclic tests.

The strain-controlled experiments were carried out using axial tension-compression unit made by Instron. The specimen deformations were measured by an extensometer. The stabilization of the stress-strain loop was considered to appear after 50 cycles, above this number there were no considerable changes of its shape.

The UCM contained SiC fibres 144 μm in diameter surrounded by the Cu matrix. Periodic boundary conditions were employed to simulate an ideal bulk composite without any influence of free surfaces (Fig. 7).

By introducing 3D geometry, it was possible to fully cover the longitudinal, as well as the transverse, response of the composite. The finite element (FE) model was assembled with C3D8R 3D solid elements of reduced integration. The overall dimensions of the model were 143×143 μm^2 in the transverse plane and the thickness of 10 μm.

Several numerical analyses were carried out using the commercial code ABAQUS. Calculations were performed for uniaxial straining and the macro stress−strain curves were modelled.

The residual stresses were introduced by simulating the fabrication processes. The composite was "numerically" annealed at 1000 °C and then cooled to room temperature. The material properties were calibrated from cyclic test experimental data. Calculations for the stress free state of the composite (without residual stresses) were carried out for comparison.

Monotonic stress-strain behaviour of the matrix material, for the isotropic model and the combined one, are presented in Fig. 9. It is shown that both strain–stress curves are initially the same.
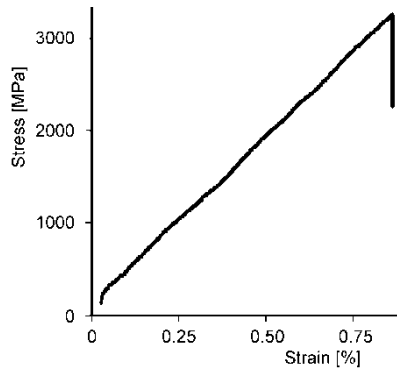
Fig. 5. Typical stress-strain
diagram for SiC fibres
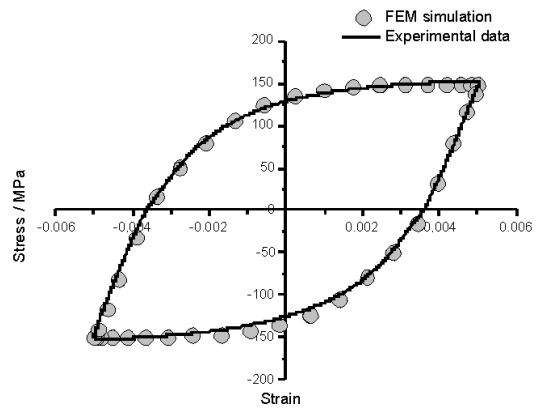
Fig. 6. Cu stress–strain curve for a saturated cycle
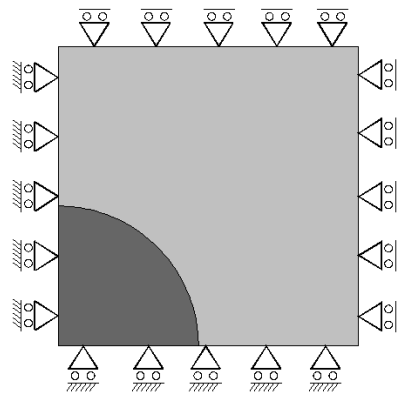
Fig. 7. Composite UCM constrains
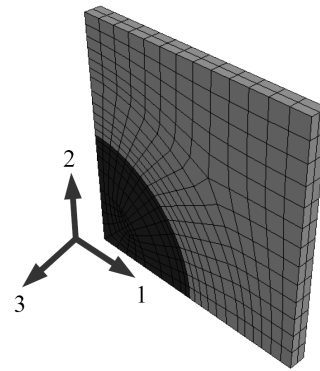
Fig. 8. Unit cell model of lamina (20% volume fraction
of SiC fibres) submitted for calculations

Fig. 9. Composite heating-cooling
step conditions
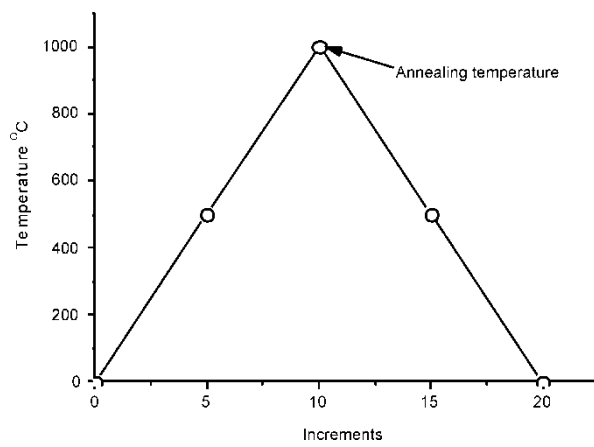
In the case of annealed copper, the experimental results as well as literature data [18, 19] show a strong Bauschinger effect which is more critical if reversible loading occurs in the issue, e.g., heating–cooling. During numerical analysis, the macroscopic strain-stress response of composite was obtained. The values were calculated as follows:

Macroscopic stress is defined as an integral

$$\Sigma_{ij} = \frac{\int\limits_{V} \sigma_{ij} dV}{V} \tag{7}$$

For discrete FE volume it becomes

$$\Sigma_{ij} = \frac{\sum\limits_{1}^{n} \sigma_{ij} V_n}{V} \tag{8}$$

where n is the number of finite elements and V_n is the volume of the n-th element.
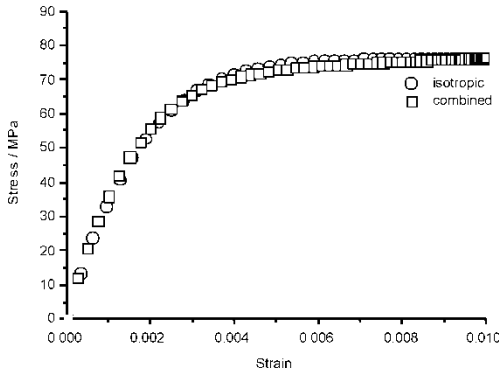
Fig. 10. Stress–strain response of pure copper (matrix material) calculated for various constitutive models (combined non-linear isotropic-kinematic hardening and non-linear isotropic hardening)

The strains are calculated in an analogous way:

$$E_{ij} = \frac{\sum\limits_{1}^{n} \varepsilon_{ij} V_n}{V} \tag{9}$$

3. Discussion

The materials used for plasma reactor applications, especially the heat sink components, are supposed to serve under cyclic loading conditions [8]. Such conditions may cause damage to the structure, especially when the difference in CTE of the com-

ponents is high and one of the components exhibits tendency for plastic deformation. However, it could be accommodated by shakedown, while progressive hardening of components causes the return of the structure to elastic regime. The aim of this work is to demonstrate that for prediction of the shakedown effect and stress limits for composite materials, realistic models are needed instead of the pure isotropic hardening model, commonly used in engineering practice. However, the simulation shows that the residual stresses in Cu–SiC do not affect strongly the composite response under monotonic loading for both material models (Figs. 11–13).
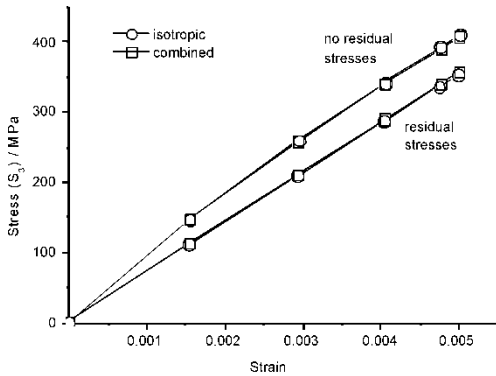
Fig. 11. Calculated macroscopic stress–global strain curves for composite axial loading case parallel to direction of fibres (with and without residual stresses)
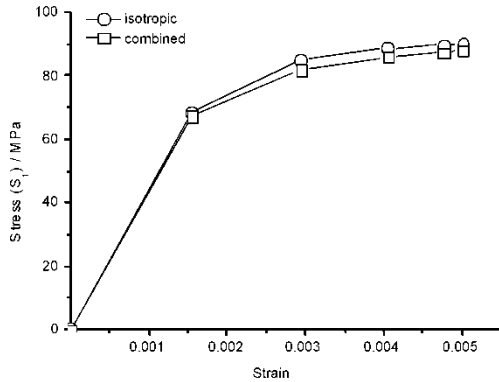
Fig. 12. Composite stress–strain curves for transverse loading case (perpendicular to direction of fibres) without residual stresses
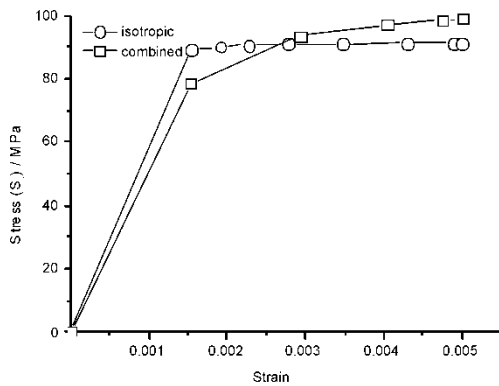
Fig. 13. Composite stress–strain curves for transverse loading case (perpendicular to fibres direction) with residual stresses

In this paper, some insight into the cyclic properties has been obtained. Calculations have been performed for strain- and stress-controlled modes. The cyclic simulations have been carried out for both presented constitutive models up to 10 cycles. The coefficient of amplitude asymmetry R was set to -1, which indicates a fully reversed loading case.

For stress-controlled, as well as for the strain-controlled mode, differences appeared after the first cycles between the two considered constitutive models of plastic-

ity. For Cu–SiC composite, the applied isotropic hardening model predicts elastic shakedown in the first few cycles while for the combined model only plastic shakedown is obtained (Figs. 14, 15). This is mostly due to a strong Bauschinger effect of Cu. Thus, it could be concluded that applying the isotropic hardening model one can overestimate the accommodation of plastic deformation (shakedown). However, for the combined model, due to the low initial yield stress σ_0, it is difficult to determine a safe load condition in stress space, which could bring composite back to the elastic domain. In fact, plastic energy dissipated in each cycle for the applied stress exceeded yield stress. The amount of plastic energy dissipated in each cycle could be used as a parameter to determine the load limits for the composite, assuming that a limited plastic deformation is allowed.
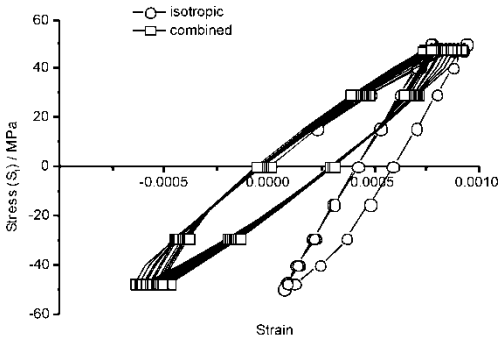
Fig. 14. Calculated global composite stress–strain curves for transverse cyclic loading case, stress controlled without residual stresses
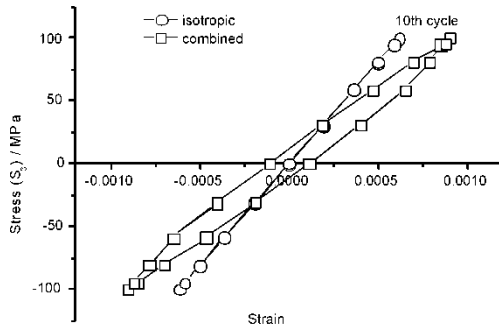
Fig. 15. Calculated global composite stress–strain curves for fibre direction cyclic loading case, stress controlled, without residual stresses
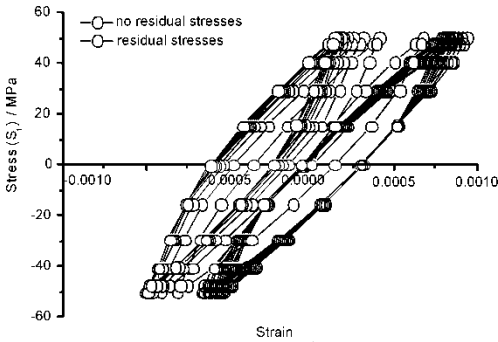
Fig. 16. Calculated global composite stress–strain curves for transverse direction cycling with and without residual stresses

4. Conclusions

The combined Armstrong–Frederick–Chaboche model has shown to be in good agreement with the experimental cyclic stress-strain curves. Micromechanical model-

ling of Cu–SiC composite, based on cyclic plasticity, is more relevant to predict load limits of composites under thermal and mechanical cyclic conditions, which is not covered by the non-linear isotropic model.

Residual stresses inducted during simulation of the manufacturing process do not influence further the cyclic behaviour of Cu–SiC composite and do not affect plastic energy dissipation. This is mostly due to low plastic yield of the annealed Cu.

References

[1] ISMAR H., SCHRÖTER F., Comp. Struct., 79 (2001), 1713.

[2] CHAWLA K.K., *Fibrous Materials*, Cambridge University Press, Cambridge, 1998.

[3] YOU J-H., BOLT H., J. Nucl. Mater., 305 (2002), 14.

[4] TAVASSOLI A.A., J. Nucl. Mater., 258–263 (1998), 85.

[5] FABRITSIEV S.A., ZINKLE S.J., SINGH B.N., J. Nucl. Mater., 233–237 (1996),127.

[6] BUTTERWORTH G.J., FORTY C.B.A., J. Nucl. Mater., 189 (1992), 237.

[7] EHRLICH K., GASPAROTTO M., GIANCARLI L., LE MAROIS G., MALANG S., VAN DER SCHAAF B., European Material Assessment Meeting, Karlsruhe, 5–8 June 2001.

[8] BOLT H., BARABASH V., FEDERICI G., LINKE J., LOARTE A., ROTH J., SATO K., J. Nucl. Mater., 307–311 (2002), 43.

[9] CIUPIŃSKI Ł., KRZESIŃSKI G., KURZYDŁOWSKI K.J., *FEM modeling of residual thermal stresses in CMM composites and their influence on macroscopic properties in a tensile test*, Third International Conference on Thermal Stresses, J.J. Skrzypek, R.B. Hetnarski (Eds.), Cracow 1999, pp. 553–557.

[10] SZCZEPAŃSKI W., *Mechanics of Plastic Flow*, PWN, Warszawa, 1978 (in Polish).

[11] HILL R., *The Mathematical Theory of Plasticity*, Oxford Univ. Press, Oxford, 1950.

[12] ABDEL-KARIM M., Int. J. Press. Vess. Piping, 82 (2005), 427.

[13] STOUFFER D.C., DAME L.T., *Inelastic Deformation of Metals*, Wiley, New York, 1996.

[14] Abaqus User Manual v. 6.6-1.

[15] BONORA N., RUGGIERO A., Comp. Sci. Techn., 66 (2006), 314.

[16] POPESCU C., *Processing and Characterisation of SiC–Fibre Reinforced Cu–Matrix Composites*, PhD Thesis, TU München, 2004.

[17] LEMAITRE J., CHABOCHE J.-L., *Mechanics of Solid Materials*, Cambridge Univ. Press, Cambridge, 1990.

[18] PENDERSEN O.B., BROWN L.M., STOBBS W.M., Acta Metall., 29 (1981) 1843.

[19] KHAN A.S., JACKSON K.M., Int. J. Plast., 15 (1999), 1265.

Fabrication and dielectric properties of Si_3N_4–MgO–Al_2O_3 by spark plasma sintering technique

J. Li[1,2], F. Chen[1], Q. Shen[1], H. Jiang[1], L. Zhang[1*]

[1]State Key Lab of Advanced Technology for Materials Synthesis and Processing,
Wuhan University of Technology, Wuhan 430070, P. R. China

[2]School of Chemical Engineering, Shandong University of Technology, Zibo 255049, P. R. China

In the present study, α-Si_3N_4 was prepared using MgO and Al_2O_3 as the sintering additives and spark plasma sintering (SPS) technique. The SPS sintering behaviour and mechanism have been discussed. The relationship between the content of sintering additives, sintering temperature, and relative densities of the samples have been analyzed. The phase composition was determined by XRD, the microstructures of the fracture surfaces were observed by SEM and the dielectric properties have been tested. The results suggest that when the sintering temperature is 1300–1500 ºC, the content of sintering additives – 6–10%, the relative density of the sintered samples is 64–96%. When the sintering temperature reaches 1400 ºC, the content of sintering additives 10%, the samples could be fully dense sintered (the relative density up to 95%) The sintering mechanism is liquid phase sintering. The electric permittivity of the sintered samples is 5–8 being in a close relationship with the relative density. The dielectric loss, influenced by the liquid phase, is less than 1×10^{-2}.

Key words: spark plasma sintering; α-Si_3N_4; sintering additive; microstructure; dielectric properties

1. Introduction

Silicon nitride (Si_3N_4) based ceramics have been studied intensively for more than 40 years and used in numerous applications as structural and functional ceramic materials due to its superior properties, such as high-temperature strength, good oxidation resistance, and low thermal expansion coefficient [1–3]. The Si_3N_4 ceramics has the best mechanical and thermo-structural properties for high temperature applications [4]. Previous studies focused mainly on achieving perfect mechanical and thermal properties of silicon nitride [5], and were aimed at obtaining high density products but a few have been reported on dielectric properties.

---

*Corresponding author, e-mail: chenfei81@sohu.com

Silicon nitride is strong covalently bonded and has two forms: α and β phase [6]. The unit cell of the α-Si_3N_4 structure is twice as long as that of the β-Si_3N_4. The stacking sequence of α-Si_3N_4 is ABCDABCD…, and β-Si_3N_4 is ABAB... It has been reported that β-Si_3N_4 has a higher electric permittivity than α-Si_3N_4 [7]. Thus studying dielectric properties of the material is of importance in view of fabrication of α-Si_3N_4 ceramics.

Spark plasma sintering (SPS) is a recently developed sintering method [8] being similar to conventional hot pressing in configuration. The precursor powders are loaded in a die and a uniaxial pressure is applied during the sintering. However, instead of using an external heating source, densification is enhanced with the use of a pulsed direct current passing through the electrically conducting die and the sample. High rates and possibly low temperatures of sintering are characteristic of this method. It has been reported that Si_3N_4 ceramics can be sintered for 15 min of heating and holding, but α to β transformation is not completed within such a short time [9]. It is assumed that the initial temperature of the α to β transformation is about 1400 ºC and the completion temperature is about 1800 ºC. The SPS technique thus provides us with unique possibilities to manipulate the sintering kinetics. The inherent advantages of the SPS technique are the reasons why it has been chosen for this study.

In the present study, we are motivated to prepare α-Si_3N_4 ceramics of various densities doped with mixed additions based on MgO and Al_2O_3 by the SPS technique, and to study correlations between the microstructure and relative densities. In addition, one of the important tasks of this paper is to explore the sintering behaviour and LPS mechanism. The goal of this study is to obtain a correlation as clear as possible between the microstructure and the dielectric properties.

2. Experimental procedure

Materials. Raw materials used in the study were as follows: α-Si_3N_4 rich powder, light magnesia (MgO) powder and aluminum phosphate ($AlPO_4$) powder. In Table 1, the main compositions of α-Si_3N_4 are given. Their grain size is about 1–2 μm. The grain size of commercial MgO was about 0.2 μm, and its purity was up to 99.9%. For Al_2O_3, the grain size was about 0.5 μm and purity was up to 99.9%.

Table 1. Phase and elemental composition of Si_3N_4 raw material, wt. %

Material	α-Phase	β-Phase	Si free	N	O	C	Fe
Si_3N_4	> 93	< 5	< 0.3	> 37.0	< 1.5	< 0.1	< 0.3

Preparation of materials. According to Table 2, the powder precursors in various ratios were mixed uniformly in a three-dimensional mixing for 5~7 h. The mixture was loaded in a graphite die with the inner diameter of 32 mm, pre-pressed and sin-

tered using an SPS system (model-1050, Sumitomo Coal Mining Co. Ltd., Tokyo). Figures 1, 2 show the schematic diagram of the SPS process.

Table 2. The contents [wt. %] of raw powders and theoretical densities of the samples

No.	Contents [wt. %]			Theoretical density [g/cm^3]
	Si$_3$N$_4$	MgO	Al$_2$O$_3$	
S1	94	4	2	3.283
S2	92	4	4	3.295
S3	90	4	6	3.307
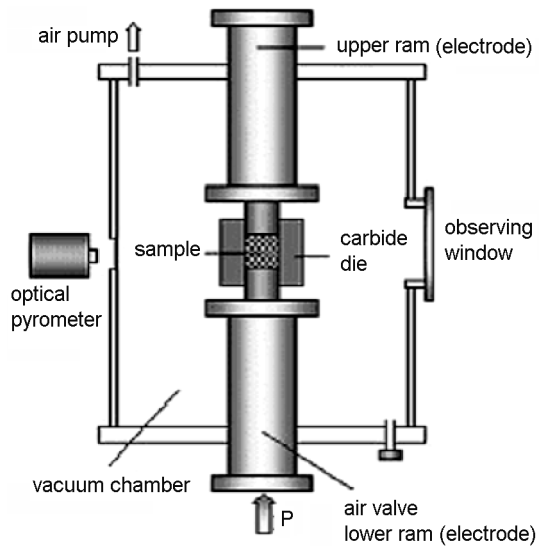
Fig. 1. Schematic drawing of the SPS system
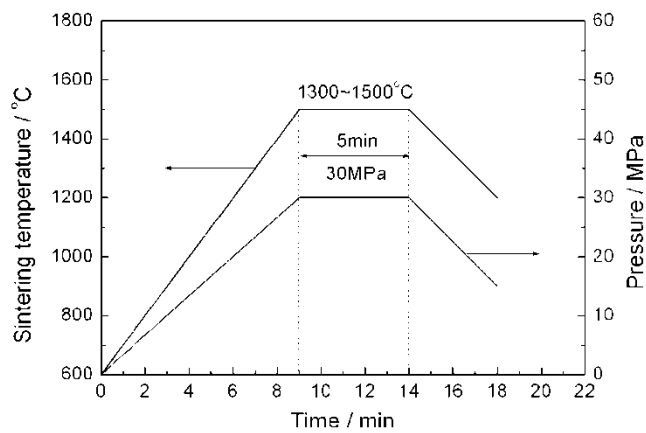
Fig. 2. The schematic diagram of the SPS process

The sintering temperature (1300–1500 ºC) of each sample was measured using an optical pyrometer focused on the surface of the graphite die. The average heating rate of about 100 ºC/min was maintained up to the sintering temperature and then the temperature was held constant for 5 min. A uniaxial pressure of nitrogen of 30 MPa was applied during the sintering cycle. Then the samples were cooled naturally under nitrogen atmosphere.

Sample characterization. After sintering, the bulk density of the sintered products was determined by the Archimedes immersion method using distilled water. Theoretical densities were calculated in terms of the rule of mechanical mixture. Phase compositions were analyzed by X-ray diffraction (XRD) using a Rigaku-D/Max-ⅢA diffractometer. Cu radiation was used operating at 35 kV and 30 mA. The microstructure of the fractured surfaces was observed by a scanning electron microscope (JSM-5610LV). The dielectric properties of the specimen were measured by the capacitive measuring mode while the test frequency was 1 MHz.

3. Results and discussion

3.1. Sintering behaviour

For the sake of constraining the conversion of α-Si_3N_4 to β-Si_3N_4, the powder mixtures were sintered at 1300–1500 ºC. The temperature was measured by an infrared pyrometer at the outer surface of the graphite die. It is believed that the discrepancy (underestimate) of about 150–200 ºC exists between the temperature at the surface and that at the interior under such circumstances [10]. So, α-Si_3N_4 can be sintered even at 1500 ºC by the SPS.
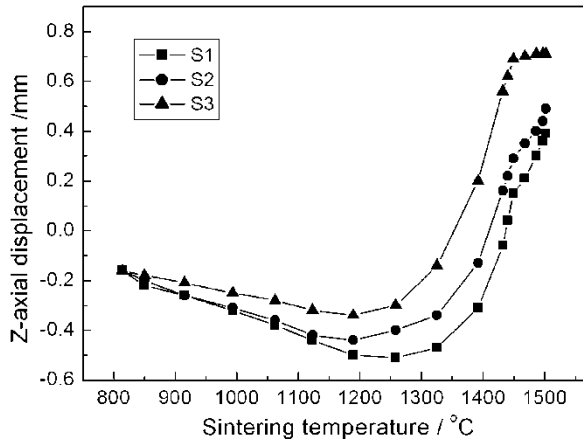
Fig. 3. The temperature dependence of Z-axial displacement (sintering at 1500 ºC)
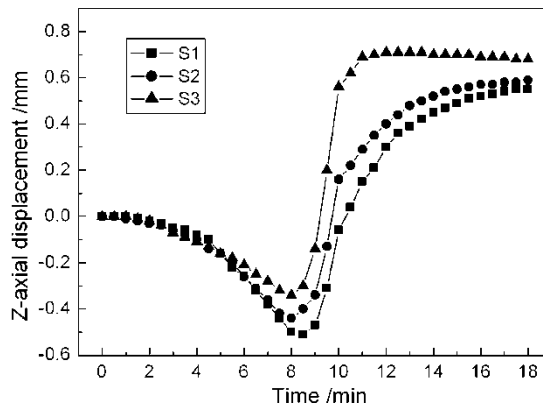
Fig. 4. The time dependence of *Z*-axial displacement (sintering at 1500 ºC)

The consolidation behaviour is best represented by the shrinkage concurrently measured during sintering. An example of such a dependence on the amount of additive in the powder mixtures is shown in Figs. 3 and Fig. 4, representing the temperature dependence and the time dependence of Z-axial displacement measured directly
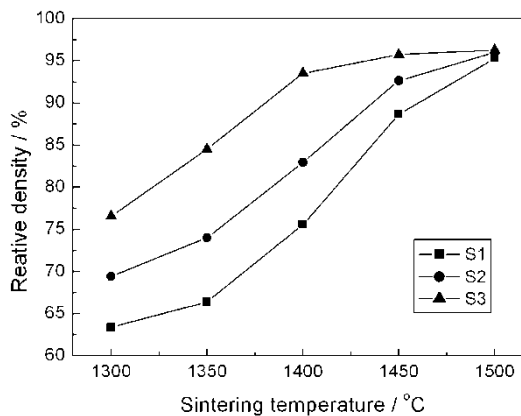
Fig. 5. The effect of sintering temperature and content of sintering additives
on the relative densities of the sintered samples

from the SPS system. In all these cases, the sintering temperature was 1500 ºC. The additive reduces the thermal expansion during sintering and the more of the additive is added, the more obvious this phenomenon is. Furthermore, the starting sintering temperature is lower (1200 ºC) upon addition of MgO and Al$_2$O$_3$ (Fig. 3). With a high additive level (e.g., S3, 10 wt. %), the densification is completed in a very short time, at 11 min according to Fig. 4, and at a relatively low temperature (1400 ºC), which is a behaviour typical of liquid-phase sintering. On the other hand, with a low additive level (e.g., S1, 6 wt. %), liquid phase sintering alone is not enough to bring the mate-

rial to high density at low temperature due to the lack of a continuous liquid phase. In such a case, the shrinkage does not stop during the sintering process and the consolidation of this material is not finished even at 1500 ºC.

The relative densities of S1–S3 samples at various sintering temperatures and the content of sintering additives are shown in Fig. 5. The relative densities show sharp variation against the sintering temperature from 1300 ºC to 1500 ºC. Relative density from 64% to 96% was obtained when the content of the sintering additive was from 6% to 10% and the sintering temperature varied from 1300 ºC to 1500 ºC. We can conclude that when the content of Al_2O_3 or the sintering temperature reached certain values, the material could be compactly sintered and the relative density changed a little. In this way, the density can be controlled by using different content of sintering additives and sintering temperature.

3.2. Microstructure

Fig. 6 shows the SEM observation of fractured surface of the sintered samples. It can be seen that the volume of pores decreased remarkably from S1 to S3 when the sintering temperature was 1400 ºC. These results are in agreement with those shown in Fig. 5. It is worthy to note that almost no β-Si_3N_4 was observed and the grain size was about 1μm, which indicates there was no obvious grain growth in the SPS process.
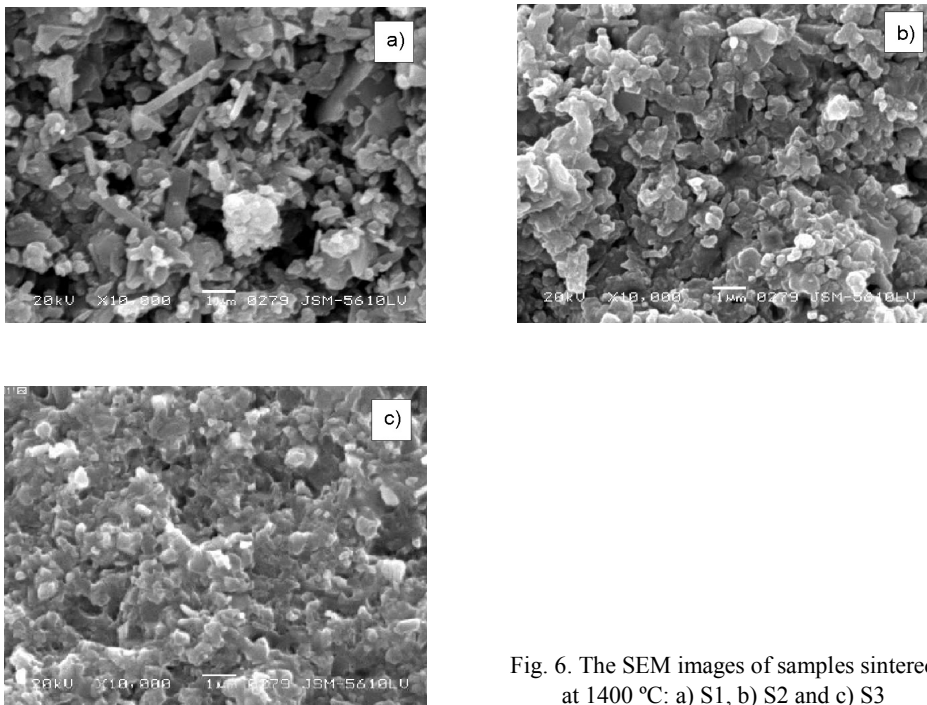
Fig. 6. The SEM images of samples sintered at 1400 ºC: a) S1, b) S2 and c) S3

Previous analyses prove that this sintering phenomenon is supposed to be due to liquid phase sintering [11], which is induced by the reaction among the components of the mixture. During the sintering process, the liquid phase attempts to occupy the lowest free energy position. Thereby, it flows to the smaller capillaries, which have the highest energy per unit volume. When there is not enough liquid to fill all the pores, the liquid tends to pull the particles together to minimize the free energy. So the increase in densification is attributed to the capillary forces exerted by the liquid phase on the solid particles. This effect results in the rearrangement stage and rapid initial densification.
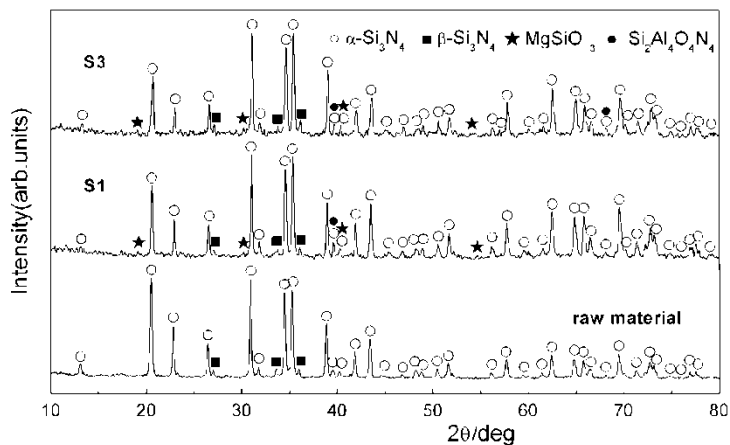
Fig. 7. The X-Ray diffraction patterns of sintered S1, S2
and Si_3N_4 samples of raw material at 1500 ºC

The identified phases for all compositions of samples S4 sintered from 1300 ºC to 1500 ºC are presented in Fig. 7, which are α-Si_3N_4, β-Si_3N_4, $MgSiO_3$ and $Si_2Al_4O_4N_4$ (β-sailon). The XRD indicates that the major phase is α-Si_3N_4, and that the sintered samples basically preserve the characters of the starting powders.

The product of the identified $MgSiO_3$ and $Si_2Al_4O_4N_4$ illustrates the sintering mechanism that the liquid phase promotes the mixture powders adherence [12, 13], which to some extent confirm certain mechanical properties of the sintered samples.

3.3. Dielectric properties

Electric permittivities of sintered samples are closely dependent on their relative densities as shown in Fig. 8. The value of ε is between 4.5 and 8.5. Since pores contain trapped gases of low conductivities, samples with low relative densities show low electric permittivities, as is clearly seen in Fig. 8. It is known that ε of α-Si_3N_4 is about 5.6 and of β-Si_3N_4 is about 7.9. Low sintering temperature helps to constrain the conversion of α-Si_3N_4 into β-Si_3N_4; the lower temperature can also reduce the production

of the liquid phase. These factors made the obtained samples maintain the properties of the initial powder. When the relative density is the same, ε increases by increasing the content of sintering additives, from 6 wt. % to 10 wt. %. This could be attributed to the amount of liquid phase which has a larger ε and tanδ. On the other hand, as can be seen in Fig. 9, the dielectric loss is less than 1×10^{-2} and it increases with increasing relative density when the content of sintering aids is low, i.e. 6 wt. %. However, when the content of sintering aids is high, i.e. 10 wt. %, because of the more generated polar liquid which is filled in the trapped gas, it first decreases and then increases by increasing the relative densities. This is how the liquid phase affects tanδ.
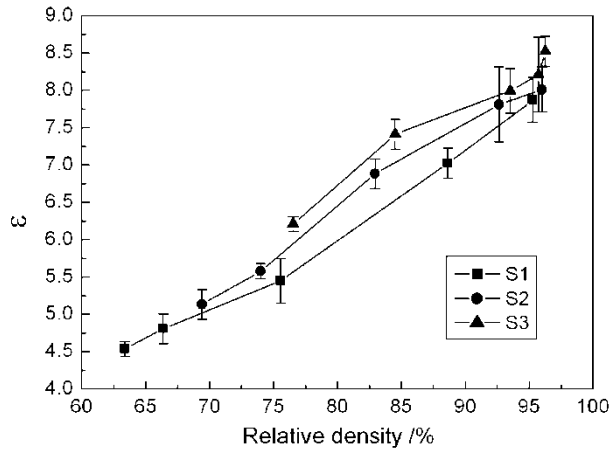
Fig. 8. Electric permittivities of the sintered samples vs. relative densities
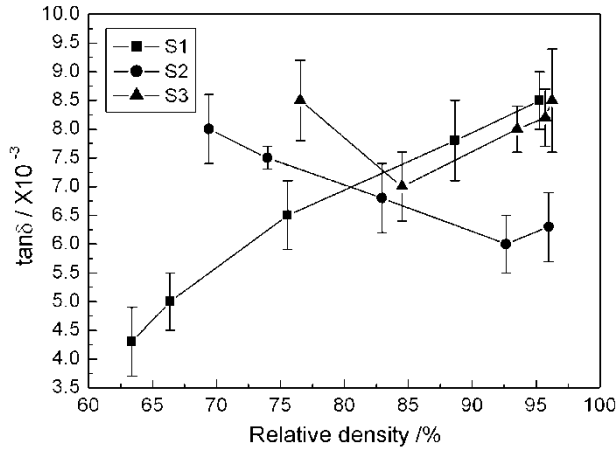
Fig. 9. Dielectric losses of the sintered samples vs. relative densities

4. Conclusions

- Relative density alters from 64% to 96% when the content of the sintering additives changes from 6% to 10% and the sintering temperature from 1300 ºC to 1500 ºC, which enables us to prepare α-Si$_3$N$_4$ matrix ceramics for various applications by adjusting the density of the samples. Nearly no grain growth and β-Si$_3$N$_4$ are observed by SEM.

- The main sintering mechanism of α-Si$_3$N$_4$ matrix ceramics by adding MgO and Al$_2$O$_3$ could be attributed to liquid phase sintering.

- Electric permittivity of a sintered sample lies in the range of 4.5–8.5 and has a close correlation with the relative density. Dielectric loss is less than 1×10^{-2} and is influenced by the liquid phase.

References

[1] POPER P., RUDDLESDEN S.N., Trans. Br. Ceram. Soc., 60 (1961), 603.
[2] ZIEGLER G., HEINRICH J.,, WÖTTING G., J. Mater. Sci., 22 (1987), 3041.
[3] GUGE E., WOETTING G., Ind. Cer., 19 (1999), 196.
[4] SIMPSON F.H., VERZEMNIEKS J., [In:] Proc. 16th Symp. Electromagnetic Windows, Georgia Institute of Technology, Atlanta, GA, 1982, p. 81.
[5] RILEY F L., J. Am. Ceram. Soc., 83 (2000), 245.
[6] WANG C.M., PAN X.Q., RUHEL M., RÜHLE F., RILEY L., MITOMO M., J. Mater. Sci., 31 (1996), 5281.
[7] CHEN C.L., CHEN F., SHEN Q., ZHANG L.M., YAN F.Q., J. Wuhan. Univ. Technol., 21 (2006), 98.
[8] TOKITA M., J. Soc. Powder. Tech. 30 (1993), 790.
[9] NISHIMURA T., MITOMO H.,, KAWAHARA M., J. Mater. Sci. Lett., 14 (1995), 1046.
[10] WAN J., DUAN R.G., MUKHERJEE A.K., Scripta. Mater., 53 (2005), 663.
[11] KINGERY W.D., J. Appl. Phys., 30 (1959), 301.
[12] FALK L.K.L., J. Mater. Sci., 39 (2004), 6655.
[13] KEPPELER M., REICHERT H.G., BROADLEY J.M., THURN G., WIEDMANN I., ALDINGER F., J. Europ. Ceram. Soc., 18 (1998), 521.

Determination of the thickness and optical constants of transparent indium-doped ZnO thin films by the envelope method

S. ILICAN[*], M. CAGLAR, Y. CAGLAR

Anadolu University, Science Faculty, Department of Physics, 26470 Eskisehir, Turkey

Transparent indium-doped ZnO thin films were deposited by the spray pyrolysis method onto glass substrates. The content of indium in the starting solution was 0.5 at. %. The crystallographic structure of the film was studied by X-ray diffraction (XRD). XRD measurement shows that the film is crystallized in the wurtzite phase and presents a preferential orientation along the *c*-axis. The texture coefficient (*TC*), grain size value and lattice constants have been calculated. The absorption coefficient and the thickness of the films were calculated from interference of transmittance spectra. Optical constants such as the refractive index *n* and extinction coefficient *k* have been determined from transmittance spectrum in the ultraviolet–visible–near infrared (UV–VIS–NIR) regions using the envelope method. The thickness of the films strongly influences the optical constants.

Key words: *ZnO; spray pyrolysis; envelope method*

1. Introduction

Recently, transparent conducting oxides (TCOs) have been widely studied. Among TCOs, zinc oxide (ZnO) is one of the most promising materials for the fabrication of the next generation of optoelectronic devices in the UV region and optical or display devices. ZnO is a wide-bandgap $A^{II}B^{VI}$ semiconductor with the bandgaps of about 3.3 eV. As a matter of fact, simultaneous occurrence of both high optical transmittance in the visible range, and low resistivity make ZnO an important material in the manufacture of heat mirrors used in gas stoves, conducting coatings in aircrafts glass avoiding surface icing, and as thin film electrodes in amorphous silicon solar cells. ZnO is a member of the hexagonal wurtzite class; it is a semiconducting, piezoelectric and optical waveguide material and has a variety of potential applications such as gas sensors [1], surface acoustic devices [2], transparent electrodes [3] and solar

_____

[*] Corresponding author, e-mail: silican@anadolu.edu.tr

cells [4, 5]. Some of these applications are based on the simultaneous occurrence of low resistivity and high transmittance in the visible spectrum, when ZnO is manufactured in the form of thin solid films.

For many of these applications, it is very important to control the ZnO physical properties by doping. Usually, n-type doping is obtained by Al, Ga or In. On the other hand, p-type doping is not easily obtained. Various deposition techniques have been widely used to produce semiconductor thin films. However, seeking the most reliable and economic deposition technique is the main goal. The most intensively studied techniques include: RF magnetron sputtering [6], metal organic chemical vapour deposition [7], sol-gel method [8] and spray pyrolysis [9, 10]. They have been studied intensively in the last three decades due to their simplicity and economy. The chemical bath deposition, chemical spray pyrolysis and sol-gel techniques are well known methods of preparation of thin films. The spray pyrolysis is an excellent method for the deposition of thin films of metallic oxides, as is the case for the ZnO material. In this deposition technique, a starting solution, containing Zn and dopant precursors, is sprayed by means of a nozzle, assisted by a carrier gas, over a hot substrate. When the fine droplets arrive at the substrate, the solid compounds react to become a new chemical compound.

The widely used envelope method has been developed for transmittance measurements to evaluate the refractive index, extinction coefficient, and absorption coefficient. Optical characterization of thin films gives information about other physical properties, e.g. band gap energy and band structure, optically active defects etc., and therefore may be of permanent interest for several different applications. Considerable differences between optical constants of bulk material and thin films or those of films prepared under varying growth characteristics are often reported. Therefore determination of optical constants for each individual film by a non-destructive method is highly recommended.

Generally, the optical band gap (E_g) and absorption coefficient α could be evaluated from transmittance or absorbance spectra. Swanepoel [11] has improved this method to determine more accurately the thickness (t), absorption coefficient (α), etc. There are several reports on this method [12–14]. In another conventional method, the reflectance (R) and transmittance (T) spectra are used to determine α. Since α is related to the extinction coefficient k, which is defined as the imaginary part of the complex refractive index, where n is the real part of refractive index, an accurate determination of n and k is possible. But this often becomes difficult due to the presence of multiple solutions. It is necessary to have a rough idea about the thickness t and refractive index n to start with, and by a judicious adjustment of the magnitude of thickness it is possible to secure a continuous solution of n and k throughout the whole spectral range.

There are a few papers on the determination of optical constants of the ZnO thin films by using the well-known envelope method [14–18], but there is no report on the indium-doped ZnO thin film. Therefore, in this paper, the optical constants of the in-

dium-doped ZnO thin films which have different thicknesses have been studied for the first time.

2. Experimental details

In-doped ZnO thin films of various thicknesses were deposited onto microscope glass (Objekttrager, 1×1 cm^2) substrates using the spray pyrolysis method at 350 ^{o}C. The experimental set-up was described elsewhere [19]. An aqueous solution of 0.1 M Zn(CH$_3$CO$_2$)$_2$ was used as a precursor, prepared from a mixture of methanol and water to a volume ratio of 3:1. The resulting solution was doped with indium by adding indium chloride (InCl$_3$) with an In/Zn ratio equal to 0.5 at. % in the starting solution. The mixture was continuously agitated until total dissolution. A small amount of acetic acid was added to obtain total dissociation of the zinc acetate. Nitrogen was used as the carrier gas, at the pressure of 0.2 bar. The ultrasonic nozzle was 28 cm distant from the substrate during deposition, the solution flow rate was held constant at 4 ml·min^{-1}. The substrate temperature was measured using an iron-constantan thermocouple.

The structural properties were studied by X-ray diffraction measurements (Rigaku Rint 2200 Series X-Ray automatic diffractometer with CuK$_\alpha$ radiation (λ =1.54059 Å)). The average dimensions of crystallites were determined by the Scherrer method from the broadening of the diffraction peaks taking into account the instrumental broadening.

The optical measurements of the In-doped ZnO thin films were carried out at room temperature using Shimadzu UV-VIS-NIR 3150 spectrophotometer in the wavelength range from 190 to 3200 nm. Swanepoel's envelope method was employed to evaluate the optical constants such as the refractive index n, extinction coefficient k, and absorption coefficient α from the transmittance spectra [11]. The thickness of the In-doped ZnO thin film was determined from the interference fringes of transmission data recorded over the visible range.

3. Results and discussion

3.1. Structural properties of the In-doped ZnO thin film

XRD spectrum of the In-doped ZnO thin film (t = 337 nm) is shown in Fig. 1. The peaks of the XRD pattern correspond to those of the theoretical ZnO patterns from the JCPDS data file [20], with a hexagonal wurtzite structure of the bulk and lattice constants: a = 3.24982 Å, c = 5.20661 Å. The analytical method [21] was used to calculate the lattice constants (a = 5.21580 Å, c = 3.26064 Å) for the film. The full width at half maximum (FWHM) of the (002) peak is 0.284°. Another major orientation present is (101), while other orientations like (102) and (100), are also seen with com-

paratively lower intensities. Therefore, the crystallites are highly oriented with their *c*-axes perpendicular to the plane of the substrate. *2θ* and *d* values are given in Table 1.
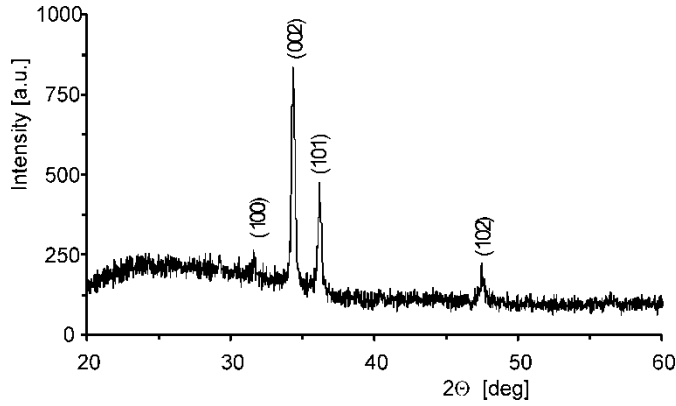
Fig. 1. XRD spectrum of the In-doped ZnO thin film

Table 1. The X-ray diffraction data results of the In-doped ZnO thin film

(*hkl*)	2θ [deg]	*d* [Å]	I/I_0	*TC* [%]
(100)	31.660	2.8238	11.5	6.58
(002)	34.360	2.6079	100.0	57.21
(101)	36.200	2.4794	48.3	27.63
(102)	47.443	1.9148	15.0	8.58

The grain size of the film from the XRD data was calculated using the Debye –Scherrer formula [21]:

$$D = \frac{0.9\lambda}{\beta \cos\theta} \tag{1}$$

where *D* is the grain size of the crystallite, λ (1.54059 Å) is the wavelength of the X-rays used, β is the broadening of diffraction line measured at the half of its maximum intensity in radians and θ is the angle of diffraction. The value found for the grain size is 31 nm.

The texture coefficient (*TC*) represents the texture of a particular plane, whose deviation from unity implies the preferred growth. Quantitative information concerning the preferential crystallite orientation was obtained from another texture coefficient *TC*(*hkl*) defined as [22]:

$$TC(hkl) = \frac{\dfrac{I(hkl)}{I_0(hkl)}}{\displaystyle\sum_n \dfrac{I(hkl)}{I_0(hkl)}} \times 100\% \tag{2}$$

where $I(hkl)$ is the measured relative intensity of a plane (hkl) and $I_0(hkl)$ is the standard intensity of the plane (hkl) taken from the JCPDS data. The value $TC(hkl) = 1$ represents films with randomly oriented crystallites, while higher values indicate the abundance of grains oriented in a given (hkl) direction. The variation of TC for the peaks of the wurzite lattice is presented in Table 1. It can be seen that the highest TC was in the (002) plane for In-doped ZnO thin film.

3.2. Determination of thicknesses of the In-doped ZnO thin films

An excellent surface quality and homogeneity of the film were confirmed from the appearance of interference fringes in the transmission spectra [23, 24] occurring when the film surface is reflecting without much scattering/absorption in the bulk of the film [24]. The optical constants were evaluated using the "envelope method" originally developed by Manifacier et al. [25]. Generally, outside the region of fundamental absorption ($hv > E_g$) or of the free-carrier absorption (for higher wavelengths), the dispersion of n and k is not very large [25]. If we assume that the film is weakly absorbing and the substrate is completely transparent, then using this method the refractive index (n), and extinction coefficient (k) of the film on a transparent substrate can be evaluated from the transmission spectra.
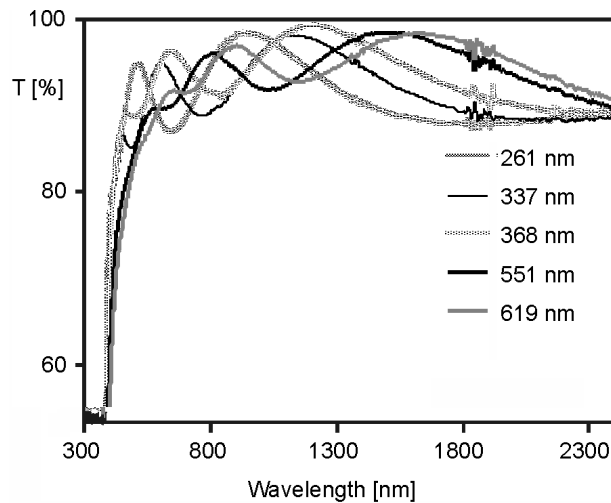
Fig. 2. Transmittance spectra of the In-doped ZnO thin films

Figure 2 shows transmittance curves for In-doped ZnO thin films at various thicknesses. These films exhibited good transparency (between 91% and 93%) in the visible and infrared region.

The refraction indices n at various wavelengths were calculated using the envelope curve for T_{max} (T_M) and T_{min} (T_m) in the transmission spectra [11]. The expression for the refractive index is given by

$$n = \left[N + \left(N^2 - n_s^2 \right)^{1/2} \right]^{1/2} \tag{3}$$

where

$$N = 2n_s \frac{T_M - T_m}{T_M T_m} + \frac{n_s^2 + 1}{2} \tag{4}$$

and n_s is the refractive index of the substrate ($n_s = 1.52$ for glass).

The extinction coefficient k can be calculated from the following formula [25]:

$$k = \frac{\alpha \lambda}{4\pi d} \tag{5}$$

$$\alpha = -\frac{1}{t} \ln \frac{(n-1)(n-n_s)\left(\dfrac{T_{max}}{T_{min}} + 1\right)^{0.5}}{(n+1)(n+n_s)\left(\dfrac{T_{max}}{T_{min}} - 1\right)^{0.5}} \tag{6}$$

where α is the absorption coefficient. λ_1 and λ_2 are the wavelengths at the two adjacent maxima or minima. The optical constants such as refractive index n and extinction coefficient k were determined from the transmittance spectrum by the envelope method as explained in the previous section. The variations of the refractive index n and extinction coefficient k with the wavelengths in the range 450–1800 nm are shown in Figs. 3a, b.

The thickness of the film was calculated using the equation

$$t = \frac{\lambda_1 \lambda_2}{2\left(\lambda_1 n_2 - \lambda_2 n_1\right)} \tag{7}$$

where n_1 and n_2 are the refractive indices corresponding to the wavelengths λ_1 and λ_2, respectively [11]. The thicknesses of the films are given in Table 2.
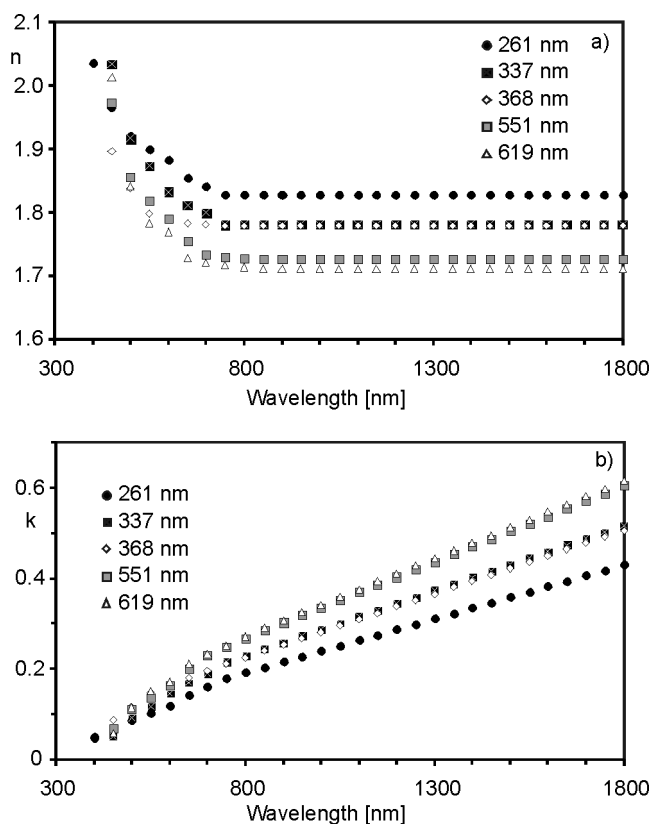
Fig. 3. Plots of refractive index (a) and extinction coefficient (b)
of the In-doped ZnO thin films as a function of wavelength

Table 2. The values of the band edge sharpness B_s
and optical band gap E_g of the In-doped ZnO thin films

Thickness [nm]	B_s [m^{-2}·eV^{-1}]	E_g (eV)
261	$(4.57\pm0.04)\times10^{13}$	3.29 ± 0.01
337	$(6.18\pm0.04)\times10^{13}$	3.30 ± 0.01
368	$(4.78\pm0.04)\times10^{13}$	3.30 ± 0.01
551	$(7.29\pm0.04)\times10^{13}$	3.30 ± 0.01
619	$(6.84\pm0.04)\times10^{13}$	3.30 ± 0.01

3.3. The band gap energy of the In-doped ZnO thin films

The absorption coefficient α of the In-doped ZnO thin films was determined from absorbance measurements. Since the envelope method is not valid in the strong ab-

sorption region, the calculation of the absorption coefficient of the film in this region was performed using the following expression:

$$\alpha(\upsilon) = 2.303 \frac{A}{t} \qquad (8)$$

where A is the optical absorbance. The optical absorption edge was analyzed by the following equation [26],

$$\alpha h\upsilon = B(h\upsilon - E_g)^{0.5} \qquad (9)$$

where B is a constant.
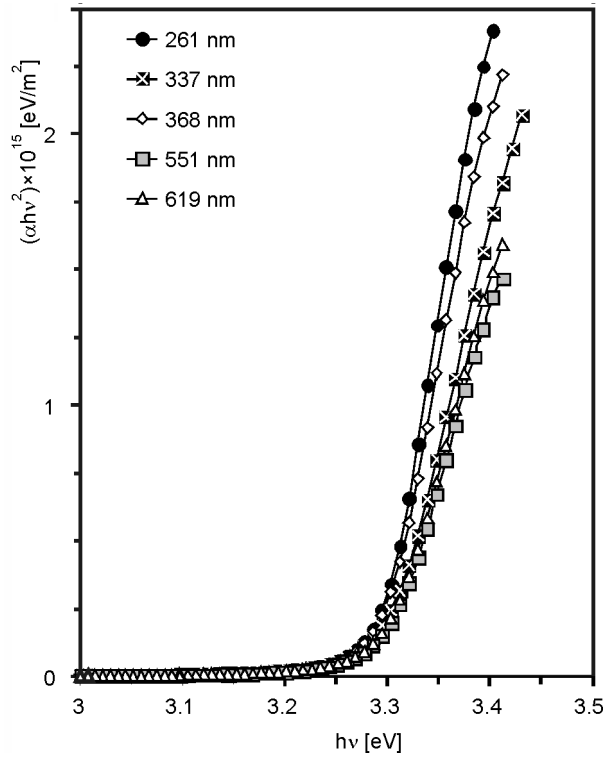
Fig. 4. Variation of $(\alpha h\upsilon)^2$ vs. $h\upsilon$ of the In-doped ZnO thin films

Figure 4 shows the plot of $(\alpha h\upsilon)^2$ vs. $h\upsilon$ for In-doped ZnO thin films. It has been observed that the plot of $(\alpha h\upsilon)^2$ vs. $h\upsilon$ is linear over a wide range of photon energies indicating a direct type of transitions. The intercepts (extrapolations) of these plots (straight lines) on the energy axis reflect the energy band gaps. The band edge sharpness value (B_s) was derived from the slope of the plot of $(\alpha h\upsilon)^2$ vs. $h\upsilon$ in the range of band-to-band absorption. The band edge sharpness B_s and optical band gap E_g

are given in Table 2. According to Table 2, a small difference occurred in the optical band gap.

4. Conclusions

In-doped ZnO thin films were deposited onto glass substrates by the spray pyrolysis method at 350 $^\circ$C substrate temperature. The crystal structure and orientation of the In-doped ZnO thin film ($t = 337$ nm) were investigated by the XRD pattern. The X-ray diffraction pattern of this film revealed its hexagonal wurtzite structure. The films exhibited high transparency ($\geq$ 91%) in the visible and infrared region. Optical constants such as the refractive index n and extinction coefficient k were determined from the transmittance spectra in the UV–VIS–NIR regions using the envelope method. The thicknesses of the films t were calculated from interference of the transmittance spectra. Also, E_g energy band gap values were calculated. The band gap of the films did not depend significantly on the film thickness. There was only a small change of the optical properties resulting from varying the film thickness.

References

[1] SUCHEA M., CHRISTOULAKIS S., MOSCHOVIS K., KATSARAKIS N., KIRIAKIDIS G., Thin Solid Films, 515 (2006), 551.

[2] WATER W., CHU S.-Y., JUANG Y.-D., WU S.-J., Mater. Lett., 57 (2002), 998.

[3] MICHELOTTI F., BELARDINI A., ROUSSEAU A., RATSIMIHETY A., SCHOER G., MUELLER J., J. Non-Cryst. Solids, 352 (2006), 2339.

[4] HUPKES J., RECH B., KLUTH O., REPMANN T., ZWAYGARDT B., MULLER J., DRESE R., WUTTIG M., Sol. Energ. Mat. Sol. Cells, 90 (2006), 3054.

[5] JEONG W.J., KIM S.K., PARK G.C., Thin Solid Films, 506-507 (2006), 180.

[6] XINGWEN Z., YONGQIANG L., YE L., YINGWEI L., YIBEN X., Vacuum, 81 (2006), 502.

[7] YE J.D., GU S.L., ZHU S.M., LIU S.M., ZHENG Y.D., ZHANG R., SHI Y., YU H.Q., YE Y.D., J. Cryst. Growth, 283 (2005), 279.

[8] GHOSH R., PAUL G.K., BASAK D., Mater. Res. Bull., 40 (2005), 1905.

[9] AYOUCHI R., LEINEN D., MARTIN F., GABAS M., DALCHIELE E., RAMOS-BARRADO J. R., Thin Solid Films, 426 (2003) 68.

[10] MARTINS R., IGREJA R., FERREIRA I., MARQUES A., PIMENTEL A., GONÇALVES A., FORTUNATO E., Mat. Sci. Eng. B, 118 (2005), 135.

[11] SWANEPOEL R., J. Phys. E: Sci. Instrum., 16 (1983), 1214.

[12] HOU Y.-Q., ZHUANG D.-M., ZHANG G., ZHAO M., WU M.-S., Appl. Surf. Sci., 218 (2003), 97.

[13] METIN H., ESEN R., J. Cryst. Growth, 258 (2003) 141.

[14] CAGLAR M., CAGLAR Y., ILICAN S., J. Optoelectron. Adv. Mater., 8 (2006), 1410.

[15] SENADIM E., KAVAK H., ESEN R., J. Phys. Condens. Mat., 18 (2006), 6391.

[16] GUMUS C., OZKENDIR O.M., KAVAK H., UFUKTEPE Y., J. Optoelectron. Adv. Mater., 8 (2006), 299.

[17] MULLEROVA J., MUDRON J., Acta Phys. Slovaca, 50 (2000), 477.

[18] SENADIM E., EKER S., KAVAK H., ESEN R., Solid State Commun., 139 (2006), 479.

[19] CAGLAR Y., ILICAN S., CAGLAR M., YAKUPHANOGLU F., Spectrochim. Acta A, 67 (2007), 1113.

[20] Joint Committee on Powder Diffraction Standards, Powder Diffraction File, card no: 36-1451.

[21] CULLITY B.D., STOCK S.R., *Elements of X-Ray Diffraction*, 3nd Ed., Prentice Hall, New York, 2001.
[22] BARRET C.S., MASSALSKI T.B., *Structure of Metals*, Pergamon Press, Oxford, 1980.
[23] BHIRA L., ESSAIDI H., BELGACEM S., COUTURIER G., SALARDENNE J., BARREAUX N., BERNEDE J.C., phys. status solidi (a), 181 (2000), 427.
[24] GEORGE J., JOSEPH K.S., PRADEEP B., PALSON T.I., phys. status solidi (a), 106 (1988), 123.
[25] MANIFACIER J.C., GASIOT J., FILLARD J.P., J. Phys. E, 9 (1976), 1002.
[26] MOTT N.F., GURNEY R.W., *Electronic Processes in Ionic Crystals*, Oxford Univ. Press, London, 1940.

Self-spreading high-temperature synthesis of TiB$_2$ powder

B. Shahbahrami[1*], R. Sarraf Maamoori[2], N. Ehsani[1]

[1]Faculty of Materials Science and Engineering, Malek-e-Ashtar University, P.O. Box 15875, Tehran, I.R. Iran

[2]Faculty of Engineering, Tarbiat Modares University, P.O. Box 14115-111, Tehran, I.R. Iran

TiB$_2$/Al$_2$O$_3$ powder composite was synthesized via simultaneous aluminum reduction of TiO$_2$ and B$_2$O$_3$ according to self-spreading high temperature (SHS) reaction in an oxidizing atmosphere. Using controlled atmosphere and high temperature is not necessary in this method. Based on the Taguchi experimental technique, various experiments were carried out and some characteristic parameters were determined. Due to the formation of intermolecular phases between Al$_2$O$_3$ and CaO which are soluble in HCl, CaO powder was added to the starting materials to make pure TiB$_2$. The most appropriate powder was obtained from the materials of stoichiometric composition, purified with an optimum amount of HCl. Characteristics of the produced samples were studied with X-ray diffraction, atomic absorption spectroscopy and particle size analysis.

Key words: *titanium diboride; SHS; aluminothermic reaction; Taguchi experimental design*

1. Introduction

TiB$_2$ with a high melting point and high hardness [1, 2], relatively low density [3], good electrical and thermal conductivity [4], and chemical resistance [5, 6] is a suitable candidate for applications such as refractory materials, nozzles, light armours, coatings, etc. [7–11]. In this work, the method of self-spreading high temperature synthesis (SHS), which is simple, low-cost, and needs no expensive facilities, was used. It also enables one to produce TiB$_2$ powder at low temperatures and in very short time [10, 12]. In the SHS method, the material is produced by thermal energy generated during the chemical reaction between precursor materials. The process begins with external heating, and then sufficient heat is generated by the chemical reaction between raw materials [13]. The powder produced has a very fine particle size, high surface area, and high reactivity. The powder can be sintered at 1300–1500 °C, while

_____

* Corresponding author, e-mail: behmut@yahoo.com

the powders produced by other techniques sinter at 1800–2200 °C [10, 12]. In this method, besides TiB_2, Al_2O_3 powder is also obtained as a product. Since Al_2O_3 is a material with a high melting point and high chemical resistance, its separation by chemical methods is difficult [14]. The addition of CaO to the precursor materials leads to the formation of an intermolecular phase ($CaO–Al_2O_3–B_2O_3$) which is soluble in HCl [14, 15]. The reaction between TiO_2, B_2O_3, and Al powders is as follows:

$$3TiO_2 + 3B_2O_3 + 10Al \rightarrow 3\ TiB_2 + 5Al_2O_3 \tag{1}$$
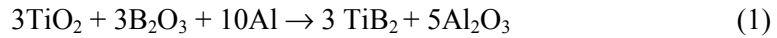
The effects of various parameters such as time, temperature, particle size of Al, B_2O_3, and TiO_2 powders, and the amount of Al and B_2O_3 powders on the produced TiB_2 were studied in this work.

2. Experimental procedures

The characteristics of the materials used are shown in Table 1. In this experiment, raw materials were mixed by a vibrator (200, Octagon). Then the batches (15 g) of mixed powders were heated in an electric furnace at various temperatures and times. The final products were milled using a planetary mill (6 Pulverisette, Fritsch), to make fine powders.

Table 1. The materials used

Raw material	Particle size [μm]	Purity [%]
Fine Al powder (F)	F < 44	99
Coarse Al powder (C)	63< C <149	99
Fine TiO_2 powder (F)	F < 44	99.9
Coarse TiO_2 powder (C)	63< C <149	99.9
Fine B_2O_3 powder (F)	F < 44	99.9
Coarse B_2O_3 powder (C)	63< C <149	99.9
Coarse CaO powder (C)	63< C <149	99.9

Using the Taguchi method, four levels and four parameters were selected (Table 2). In fact, before arranging the final process, eight experimental trials have been carried out and the effects of TiO_2, B_2O_3, and Al particle sizes were studied. The final experiments were arranged basing on the calculated coefficient k and the particle size groups were selected;

$$k = \frac{I_{100TiB_2}}{\sum I_{100}} \times 100\%$$

where I_{100TiB_2} is the intensity of the peak due to TiB_2, and I_{100} is a sum of peak intensities due to all phases existing in the sample.

In accordance with previous papers, four parameters (time, temperature, and the amounts of Al and B$_2$O$_3$ powders) were selected [16]. Therefore, with 5 factors and 4 variable levels, 16 experiments were preformed according to the Taguchi experimental design (Table 3). The best processing conditions have been identified from the experimental results (*k*). This experiment was repeated with CaO powder addition to the precursor powders (TiO$_2$, B$_2$O$_3$ and Al). The effect of CaO amount on the process was studied with the addition of various amounts of CaO powder (stoichiometric amount, 20 wt. % and 30 wt. % more than stoichiometric amount).

2. Variable levels and parameters

Parameter	Level			
	1	2	3	4
a) Particle size[1)]	F. F.F	F.F.C.	F.C.C	C.C.F
Temperature [ºC]	950	1050	1250	1350
Time [h]	0.5	1	1.5	2
b) Al powder content[2)]	1	1.1	1.2	1.3
b) B$_2$O$_3$ powder content	1	1.1	1.2	1.3

[1)] – the letters represent particle size of TiO$_2$, B$_2$O$_3$ and Al powders, respectively, from left to right.
[2)] – Al and B$_2$O$_3$ powder contents are given based on the stoichiometric amounts (Eq. (1)).

Table 3. Experimental design

No.	Particle size	Temperature [ºC]	Time [h]	Al powder content (stoichiometric ratio)	B$_2$O$_3$ powder content (stoichiometric ratio)	K[(1)]
n_1	F.F.F	950	0.5	1	1	12.67
n_2	F.F.F	1050	1	1.1	1.1	23.78
n_3	F.F.F	1250	1.5	1.2	1.2	46.94
n_4	F.F.F	1350	2	1.3	1.3	2.99
n_5	F.F.C	950	1	1.2	1.3	22.05
n_6	F.F.C	1050	0.5	1.3	1.2	26.28
n_7	F.F.C	1250	2	1	1.1	7.69
n_8	F.F.C	1350	1.5	1.1	1	12.45
n_9	F.C.C	950	1.5	1.3	1.1	0
n_{10}	F.C.C	1050	2	1.2	1	2.15
n_{11}	F.C.C	1250	0.5	1.1	1.3	7.71
n_{12}	F.C.C	1350	1	1	1.2	0
n_{13}	C.C.F	950	2	1.1	1.2	18.22
n_{14}	C.C.F	1050	1.5	1	1.3	8.48
n_{15}	C.C.F	1250	1	1.3	1	37.67
n_{16}	C.C.F	1350	0.5	1.2	1.1	43.62

[(1)]K is the average of repeated experiments

The reaction between stoichiometric amounts of precursor materials was as follows [14, 15]:

$$TiO_2 + 2B_2O_3 + 2Al + 2CaO \rightarrow TiB_2 + 2CaO \cdot Al_2O_3 \cdot B_2O_3 + O_2 \qquad (2)$$

The best sample (which had the highest amount of TiB_2) was treated with HCl to wash the impurities. Three different concentrations of HCl (pH equal to 1, 2 and 3) were used and each sample was passed through paper. After washing it a few times with deionized water, it was dried for 2 h. The phases formed in the samples were determined by the XRD (PW 1830, Philips). The particle size of the specimens was measured using a laser particle size analyzer (A22, Fritsch). The chemical composition was characterized by the atomic absorption spectroscopy (Pye Unicam SP9, Philips).

3. Results and discussion

Table 4 shows the effect percentage of variable parameters on the amount of the TiB_2 phase formed (K). These data were calculated using the Taguchi method. As is shown in the table, the coefficient of variation (CV) is relatively high. The most probable reason for this is the heat generated in the SHS reaction. Therefore, the measurement of temperature may not be accurate.

Table 4. The effect of parameters on the K index

Parameter		$K_{ave.}$	Variance (S^2)	Standard deviation (S)	Coefficient of variation (CV) [%]	Effect percentage on K
Temperature	Level 1	13.23	39.72	6.30	48	9.97
	Level 2	15.17	58.83	7.67	51	
	Level 3	25	177.21	13.31	53	
	Level 4	14.76	170.66	13.06	88	
Time	Level 1	22.57	110.8	10.53	47	15.14
	Level 2	20.87	103.95	10.20	49	
	Level 3	16.97	182.67	13.52	80	
	Level 4	7.76	23.38	4.84	62	
Al amount	Level 1	7.20	11.95	3.46	48	27.05
	Level 2	15.50	20.85	4.57	29	
	Level 3	28.70	186.35	13.65	48	
	Level 4	16.70	142.62	11.94	71	
B_2O_3 amount	Level 1	16.20	97.84	9.89	61	9.54
	Level 2	18.80	159.67	12.64	67	
	Level 3	22.90	162.24	12.74	56	
	Level 4	10.30	28.79	5.37	52	
Particle size	Level 1	21.59	153.28	12.38	57	38.30
	Level 2	17.17	31.28	5.59	33	
	Level 3	2.46	5.68	2.38	97	
	Level 4	27	115.74	10.76	40	

Figure 1 shows the effect of temperature on the formation of the TiB_2 phase (K_{ave} – average dependent variable). In this system, the boron oxide melts at 450 °C [11] and evaporates above 450 °C. Therefore, due to the B_2O_3 evaporation from the system at temperatures higher than 450 °C, its amount decreases upon increasing temperature [10, 16]. TiO_2 is solid in the reaction conditions. However, Al powder melts at 660 °C and reduces B_2O_3 and TiO_2. Then, boron (B) reacts with titanium (Ti) through the liquid–solid mechanism. At temperatures higher than 1000 °C, the gas-solid mechanism is predominant, and as a result the rate of the reaction increases [11, 16, 17].
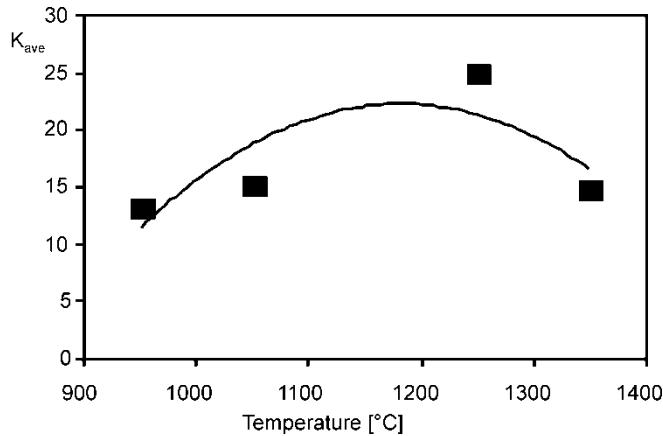
Fig. 1. Effect of temperature on TiB_2 phase formation
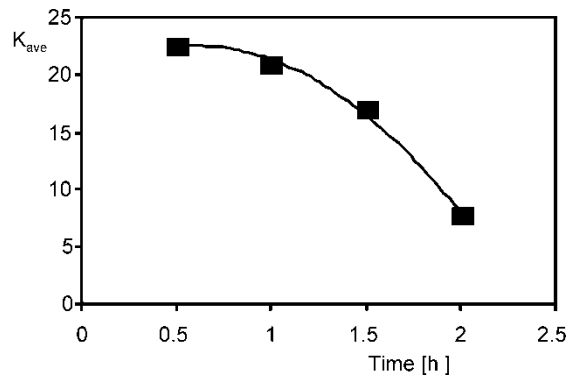
Fig. 2. Effect of time on TiB_2 phase formation

When the temperature increases, more B_2O_3 evaporates from the system. Therefore, sufficient amount of boron is not available to react with the entire titanium, thus the amount of TiB_2 decreases. It can be concluded that above 1170 °C, temperature has a negative effect on TiB_2 formation. As can be seen in Table 4, compared to the other variables, the effect of temperature is not remarkable because the rate of B_2O_3

evaporation rises with the increase of temperature. Furthermore, in the SHS or thermitic reactions, when temperature enhances to a specific level, they proceed independently. Therefore, heating is only needed for the initiation of the reaction [18].

The effect of time on the TiB_2 formation is shown in Figure 2. This figure shows that the amount of TiB_2 formed decreases with time. With time, more B_2O_3 evaporates from the system. Thermitic or SHS reactions are very fast, being accomplished in a very short time. In these reactions, temperature increases rapidly. Even under such conditions, the reaction needs some time to be completed [16, 19]. Therefore, 30 min was the minimum time applied.
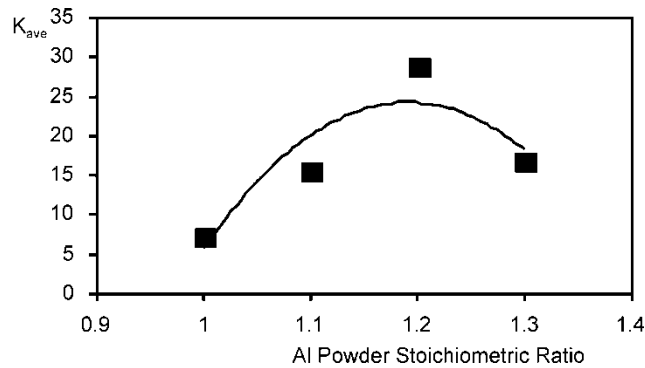
Fig. 3. Effect of Al powder content on TiB_2 phase formation

The effect of the amount of Al powder on the TiB_2 formation is presented in Fig. 3. By increasing the amount of Al powder (above the stoichiometric amount), the formation of TiB_2 also accelerated. This is due to the reduction mechanism of boron oxide and titanium oxide by the Al powder. In this mechanism, when the amount of Al powder increases, more B_2O_3 and TiO_2 were reduced by the Al powder. In addition, increasing the Al powder amount can hinder the escape of B_2O_3 [10, 16]. However, if the amount of Al powder increases by more than a certain value, it can cause an inverse effect on the amount of TiB_2 produced. In such a case, impurities such as Al, Al_2O_3, and compositions of Al and B are developed in the system. Compared to other parameters, the effect of this parameter on the TiB_2 formation (27.05%) was the most efficient. The optimum level of aluminum is 1.19.

Figure 4 shows the effect of B_2O_3 amount on the TiB_2 formation. The vapour pressure of boron oxide is high, thus high temperature leads to a rapid evaporation of B_2O_3. As a result, the level of boron oxide (B_2O_3) in the starting composition should be larger than its stoichiometric level [10, 16, 20–22]. Insufficient amount of boron oxide leads to the formation of an inadequate amount of TiB_2. In this case, the unreacted TiO_2 and Al are present in the final product. The amount of TiB_2 formed was raised by increasing the quantity of B_2O_3 up to an optimum level. Above this level, the additional Al reacted with B. Therefore, a sufficient amount of B was not available in the system to react with Ti. As a result, the impurities such as TiO_2 and various com-

positions of Al and Ti formed and the amount of TiB$_2$ decreased. So, the best level of B$_2$O$_3$ ratio was 1.12.
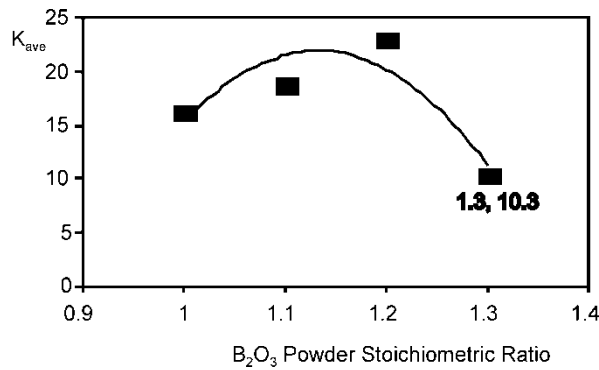
Fig. 4. Effect of B$_2$O$_3$ powder amount on TiB$_2$ formation

The effect of particle size on the yield of TiB$_2$ powder is illustrated in Fig. 5. As can be seen in this figure, group 4 of the starting materials gave the best result. It was found that decreasing the Al powder particle size increases the amount of TiB$_2$ produced. Therefore, batches containing powders with particle size characteristic of C.C.F. (coarse B$_2$O$_3$ and TiO$_2$ powders with fine Al powder) had the highest production yield.
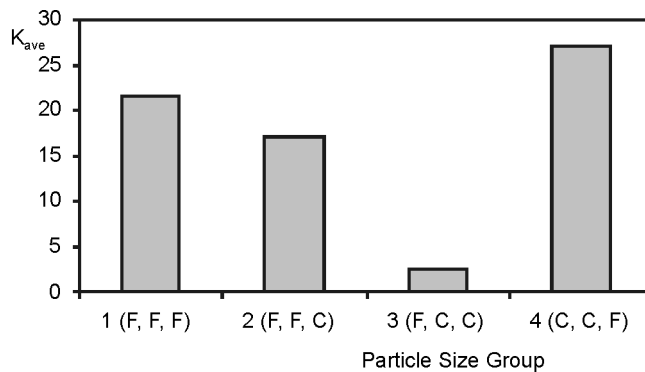
Fig. 5. Effect of particle size on TiB$_2$ formation

The effect of the CaO additive (according to the stoichiometric ratio, 20 wt. % and 30 wt. % over the stoichiometric ratio) on the XRD patterns of the final product is shown in Fig. 6. The patterns show that TiB$_2$, Al$_2$O$_3$, and CaAlB$_3$O$_7$ phases are present in each of them. It seems that the amount of amorphous phases increased with increasing amount of CaO powder. Therefore, due to the addition of CaO powder, the possibility of phase crystallization decreased. Furthermore, the SHS method is very fast, thus there is not enough time for crystallization in this technique [15].
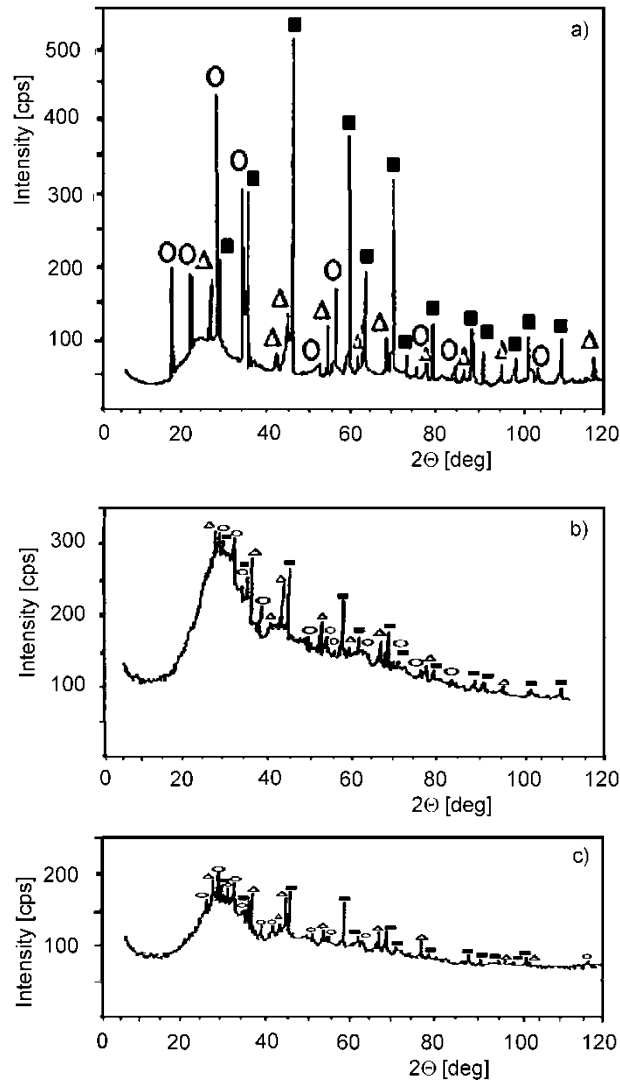
Fig. 6. XRD patterns of synthesized samples using CaO powder in: a) stoichiometric ratio,
b) 20 wt. % above the stoichiometric ratio, and c) 30 wt. % above the stoichiometric ratio;
○ – CaAlB₃O₇, △ – Al₂O₃, ■ – TiB₂

The k index of the specimens was 53 wt. %, 50 wt. %, and 45 wt. % for the synthesized powder using CaO powder in the stoichiometric ratio, and 20 wt. % and 30 wt. %, respectively.
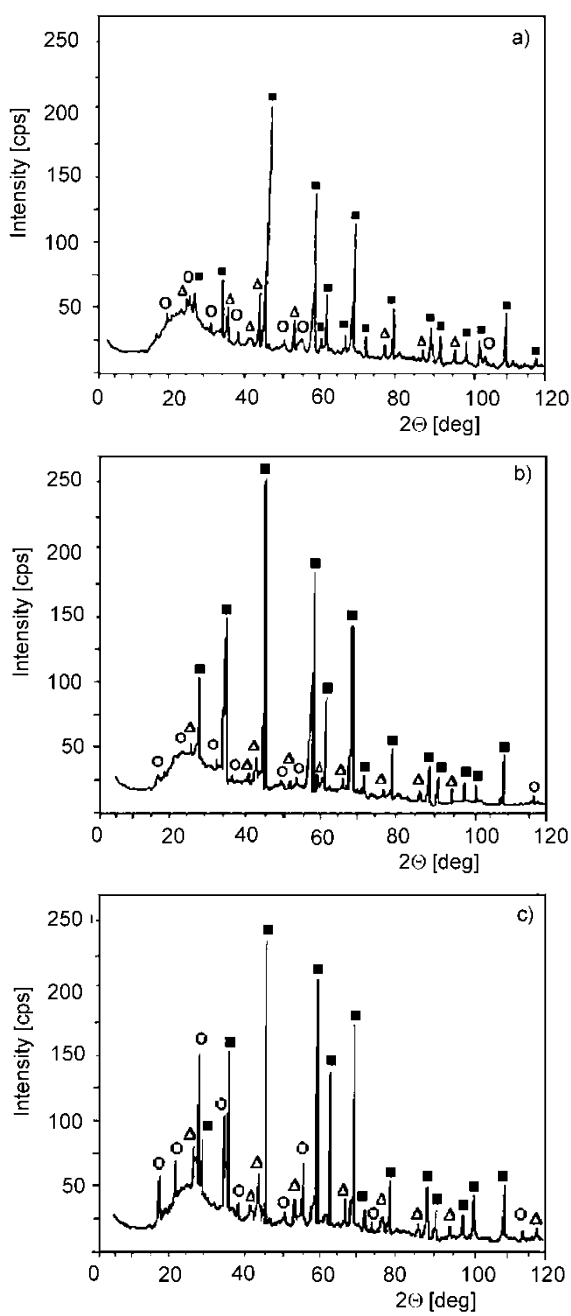
Figure 7. XRD pattern of purified sample (powder):
a) pH = 1, b) pH = 2, c) pH = 4; o – CaAlB$_3$O$_7$, Δ – Al$_2$O$_3$, ■ – TiB$_2$

Then, the samples obtained from stoichiometric amounts of precursor materials were treated with HCl. XRD patterns of purified specimens at various pH are presented in Fig. 7. The patterns show that after purification three phases (TiB_2, Al_2O_3 and $CaAlB_3O_7$) still exist in the specimens. It can be concluded that a perfect purification is not possible by this method. However, the intensity of $CaAlB_3O_7$ peaks decrease in the purified samples. Simultaneously, the intensities of TiB_2 peaks increase in the treated specimens. This was also confirmed by atomic absorption spectroscopy (AAS). Table 5 shows the atomic absorption spectroscopy results for the purified and unpurified powders. It can be seen that Ti content increases with purification and its maximum level was measured in the purified samples at pH = 2. It also shows that Ca and Al contents decrease with purification and their minimum level was obtained in the purified samples at pH = 2.

Table 5. AAS of the purified and unpurified powders

| Sample	Ti [wt. %]	B [wt. %]	Al [wt. %]	Ca [wt. %]
Unpurified	34	25	16	14
Purified (pH = 1)	52	25	19	2
Purified (pH = 2)	60	28	10	0.65
Purified (pH = 4)	41	27	17	11

The measured K indices of the treated and untreated specimens are presented in Table 6. The table shows that the K index and TiB_2 wt. % increase with treatment. The highest K index (TiB_2) was obtained for the purified sample at pH = 2. On the other hand, the amount of the $CaAlB_3O_7$ phase decreases with purification and reaches its minimum level when purified at pH = 2. It is evident that at a low concentration of HCl (pH = 4), the lowest amount of $CaAlB_3O_7$ impurity was eliminated. However, at a high concentration of HCl (pH = 1), in addition to the elimination of $CaAlB_3O_7$, a considerable amount of TiB_2 was also washed away with HCl. Therefore, due to the decreasing $CaAlB_3O_7$ and TiB_2 content, the content of Al_2O_3 increases. It can be concluded that because of a high chemical resistance of Al_2O_3 against acids and alkalis, it cannot be washed out in HCl [23, 24]. The best result was obtained with a moderate concentration of HCl (pH = 2). Under such conditions, without the elimination of TiB_2, a significant amount of $CaAlB_3O_7$ was removed.

Table 6. The K index and amounts of the phases

| Sample	K	TiB_2 [wt. %]	Al_2O_3 [wt. %]	$CaAlB_3O_7$ [wt. %]
Unpurified	53	58	7	35
Purified (pH = 1)	80	75.5	18	5
Purified (pH = 2)	91	87	10	2
Purified (pH = 4)	63	60	10	27
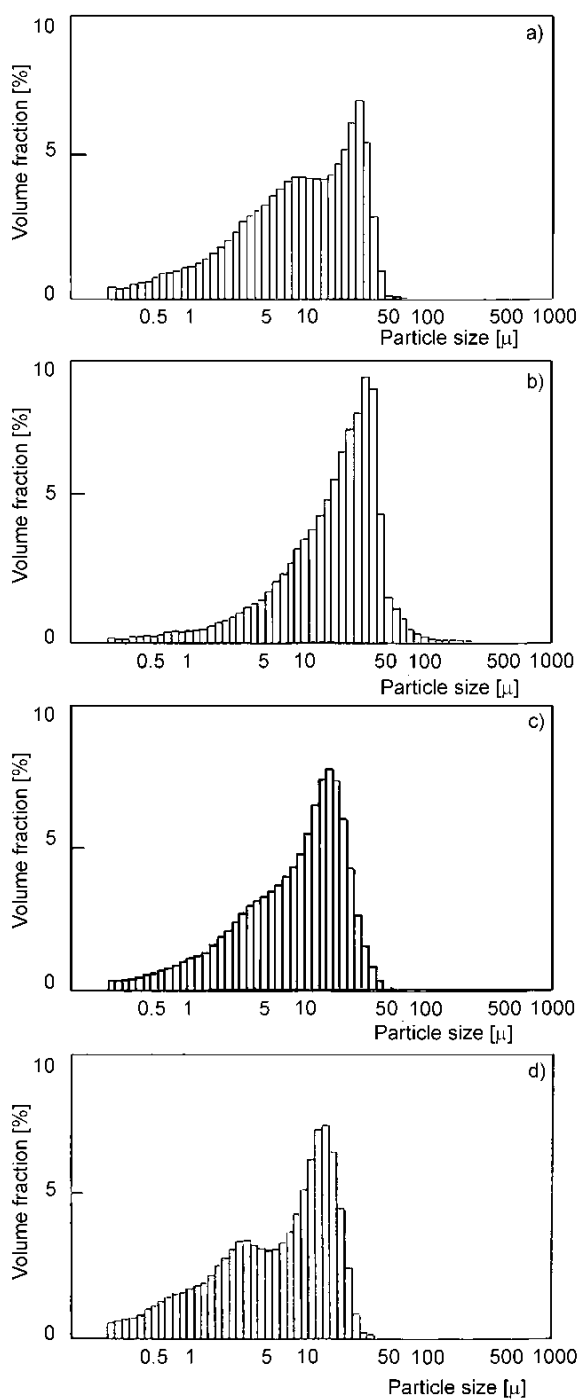
Fig. 8. Particle size distribution of: a) purified sample at pH = 4,
b) purified sample at pH = 2, c) purified sample at pH = 1, d) unpurified sample

Figure 8 shows the particle size distribution of the purified and unpurified samples. In these figures, the vertical axis indicates volume fractions percent of particle sizes, the sum of which is 100 percent. A comparison between the figures demonstrates that the unpurified samples (with $d_{50} < 7.41 \mu$m) have the finest particle size. The purified sample at pH = 2 (with $d_{50} < 21.76$ μm) has the most coarse particle size. A comparison between these data and Table 6 reveals that the purification increases the particle size. Therefore, it can be assumed that the impurities are smaller than TiB_2 particles.

4. Conclusions

The optimum temperature for TiB_2 powder formation was 1170 ºC. Compared to other methods, this is a low temperature. Beyond 30 min, the amount of TiB_2 formed decreases upon increasing time. Increasing the B_2O_3 and Al amounts above their stoichiometric values had a significant effect on TiB_2 powder formation. Particle size of the precursor powder had a pronounced effect on TiB_2 powder formation. Fine Al powder plus coarse B_2O_3 and TiO_2 powders led to the highest amount of products. Addition of CaO powder led to the reduction of Al_2O_3 and formation of $CaAlB_3O_7$, which is soluble in HCl. It decreased phase crystallization and caused amorphous powder formation. The optimum amount of CaO additive was equal to its stoichiometric level. The most suitable purification conditions were those with pH = 2, although a perfect elimination of impurities is not possible. A more efficient purification led to the production of a coarser powder.

References

[1] KANG E.S., JANG C.W., J. Am. Ceram. Soc., 72 (1989), 1868.
[2] RICCERI R., MATTEAZZI R., Mater. Sci. Eng. A, 379 (2004), 341.
[3] SHI L., GU Y., CHEN L., YANG Z., MA J., QIAN Y., Inorg. Chem. Commun., 7 (2004), 192.
[4] SCHNEIDER J., *Engineering Materials Handbook*, ASM International, 1991.
[5] WEIMER A.W., *Carbide, Nitride and Boride Materials Synthesis and Processing*, Chapman & Hall, London, 1997.
[6] MANDORF V., HARTWIG J., SELDIN E.J., *High Temperature Deformation of Titanium Diboride*, [in:] G.M. Ault (Ed.), *High Temperature Materials*, Vol. 2, Wiley-Interscience, New York, 1963, p. 455.
[7] BAIK S., BECHER P.F., J. Am. Ceram. Soc., 70 (1987), 527.
[8] CAPUTO A.J., LACKEY W.J., J. Electrochem. Soc., 132 (1985), 2274.
[9] BAUMGARTNER H.R., STEIGER R.A., J. Am. Ceram. Soc., 67 (1984), 207.
[10] LOGAN K.V., U.S. Patent 5 160 716, 1992.
[11] CHEN L., GU Y., QIAN Y., SHI L., YANG Z., MA J., Mater. Res. Bull., 39 (2004), 609.
[12] LOGAN K.V., U.S. Patent 4 888 166, 1989.
[13] MOSSINO P., DEORSOLA F.A., VALLAURI D., AMATO I., Ceram. Int., 30 (2004), 2229.
[14] ANDRIEUX J.L., PEFFEN R., U.S. Patent 3 016 288, 1962.
[15] YI ET AL., U.S. Patent, 6 645 424, 2003.
[16] LOGAN K.V., WALTON J.D., Ceram. Eng. Sci. Proc., 5 (1984), 712.

[17] WALTON J.D., POULOS N.E., J. Am. Ceram. Soc., 42 (1959), 40.

[18] MERIC C., ENGEZ T., Welding J., Jan. (1999), 33.

[19] GEIGER M.J., POIRIER D., Welding J., 61 (1999), 260.

[20] WALKER J.K., Adv. Ceram. Mater., 3 (1988), 601.

[21] WEIMER A.W., MOORE W.G., ROACH R.P., HITT J.E., DIXIT R.S., J. Am. Ceram. Soc., 75 (1992), 2509.

[22] TIMMS P.L., U. S. Patent 3 351 429, 1967.

[23] LEE W.E., *Ceramic Microstructure*, Chapman & Hall, New York, 1994.

[24] GITZEN W., *Alumina as a Ceramic Material*, The American Ceramic Society, Columbus, OH, 1970.

Processing, stabilization and applications of metallic foams. Art of science

V. C. Srivastava[*], K. L. Sahoo

Metal Extraction and Forming Division, National Metallurgical Laboratory, Jamshedpur-831007, India

Metallic foams have been of considerable interest both from the industrial applicability and scientific viewpoint. In the last three decades, since the inception of the metal foam, several processes have been developed to introduce large size pores, almost uniformly distributed, in the metallic materials. These processes include liquid metal route, powdered metal technique and some other methodologies in which pores are incorporated by direct sintering of foamed elements. Metallic foams have seen tremendous innovations for the last few years and efforts are being made to achieve foams with a low cost and with reliable properties. The stability of cell structure during the foaming process has also been a concern for researchers. Therefore, methods have been explored to increase the stability by introduction of ceramic particles in the material to be foamed, addition of alloying elements, secondary processing of precursor materials, and by optimizing the process parameters. To this end, experiments have also been made in microgravity conditions to study the mechanism of foam formation which can give a better understanding for controlling the processing conditions. Despite the current development, there are several limitations for a wide applicability of metallic foams in various industrial sectors, such as high cost of production, variability in measured properties, and unavailability of reliable testing methods. Taking these facts into consideration, the present paper is aimed at reviewing various foam processing techniques, the measures required to be taken for making stable foams and the industrial applications of the metallic foams in the current state of development.

1. Introduction

The stringent requirements of the market and the economics associated with light materials have driven our efforts to develop metallic foams with porosity ranging between 40 and 98 vol. %. In last three decades, several processing techniques have been developed to manufacture metallic foams [1–12]. The basic objective behind this developmental process is the unique combination of physical and mechanical properties expected from metallic foams such as high stiffness, low specific weight, high gas permeability, low thermal conductivity, unusual acoustic properties, high impact ab-

_____

[*]Corresponding author, e-mail: vcsrivas@nmlindia.org

sorption capacity, and good electrical insulating properties. The potential applications of metal foams have been envisaged in the area of automotive industries, light weight construction materials, silencers, flame arrester, heaters and heat exchangers, catalysts, electrochemical applications, military armour vehicles and aircraft industries [1, 12–15].

In general, a foamed material is understood to have a large volume fraction of gas pores uniformly dispersed in a liquid. A single gas inclusion is separated by liquid film making a cell. This morphology, however, can be preserved during solidification of liquid leading to solid foam. When we talk about metal foam, it is understood to have uniformly distributed gas pores with volume fraction in the range 40–98%. This kind of morphology is also known as cellular solid structure. There are three variants of cellular solids: open cell, closed cell structures [1], and a combination of the two [8]. Recently, a novel structure has been developed, which is known as lotus-type growth [4, 16]. The open cell structures incorporate interconnected pores, whereas close cell pores are surrounded by a metallic wall. The lotus-type morphology consists of long cylindrical pores aligned in one direction. These foam structures are shown in Fig. 1. However, in the subsequent sections we will be dealing mainly with closed cell and open cell structures.
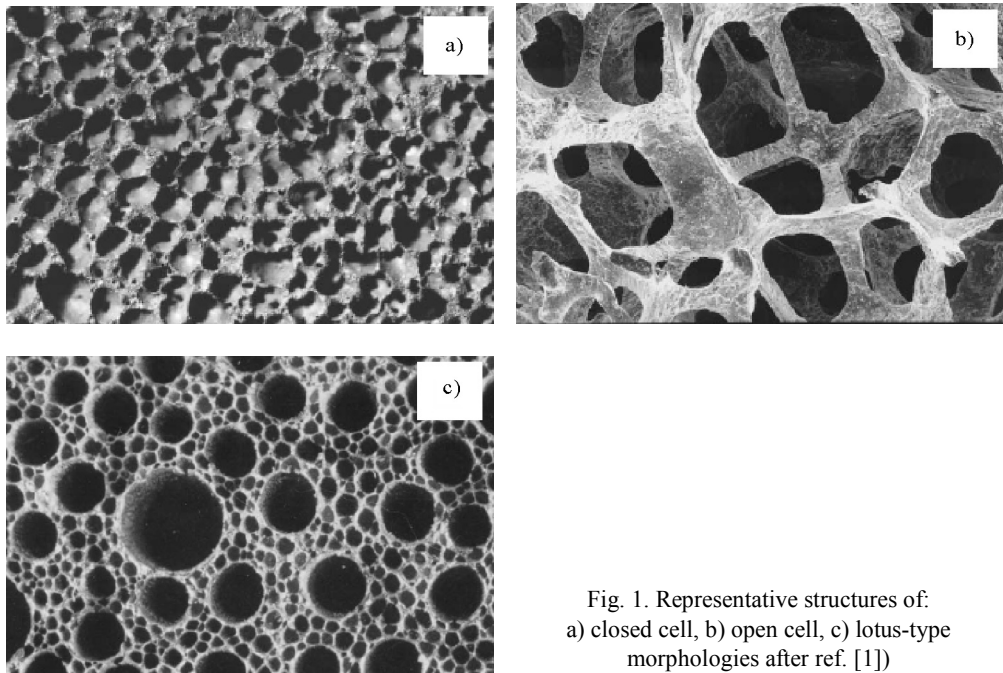
Fig. 1. Representative structures of:
a) closed cell, b) open cell, c) lotus-type
morphologies after ref. [1])

Depending on the requirements, several metals and alloy foams have been developed in the recent years, e.g. Al, Al–Si, Al–Mg [1], Cu [4, 6, 11, 16], Pb [17], Fe, steels [18–21], Ni$_3$Al [22], Zn [23], Mg and Ti [24], Al–Cu, MMCs etc. [1]. Out of these foams, tremendous development has taken place in the field of Al foams with

some industrial applications. However, a number of research groups throughout the world have been involved in the optimization of processing routes and, thereby, reduction in the cost of production of metal foams [25]. In general, two processes have been invariably used for metal foaming: (1) the liquid metal route where foaming is accomplished by direct foaming of melt with gas or some foaming agent [1, 26–29] and (2) the powder metallurgy route where foaming is affected by foaming a sintered compact [1]. Other routes include sintering of hollow spheres [30] and pressing the material around a filler followed by sintering with subsequent filler dissolution or decomposition [9–11, 31, 32]. Recently, experiments have been carried out in microgravity conditions to see its effect on the stability of foams and obtaining highly porous structures [33–36].

In view of the above facts, the aim of this paper is to review the recent developments in metallic foams. We will discuss various production techniques along with their advantages and limitations, the effect of processing parameters on the stability and/or morphology of foam structures, industrial viability of these techniques, and the potential of metallic foams as a prime structural material in the next generation.

2. Processing routes for metallic foams

There are many ways by which cellular metallic materials can be produced. As aqueous or polymeric liquid foaming is well established, we will consider only the processing of metallic materials. A processing map for the same is shown in Fig. 2.
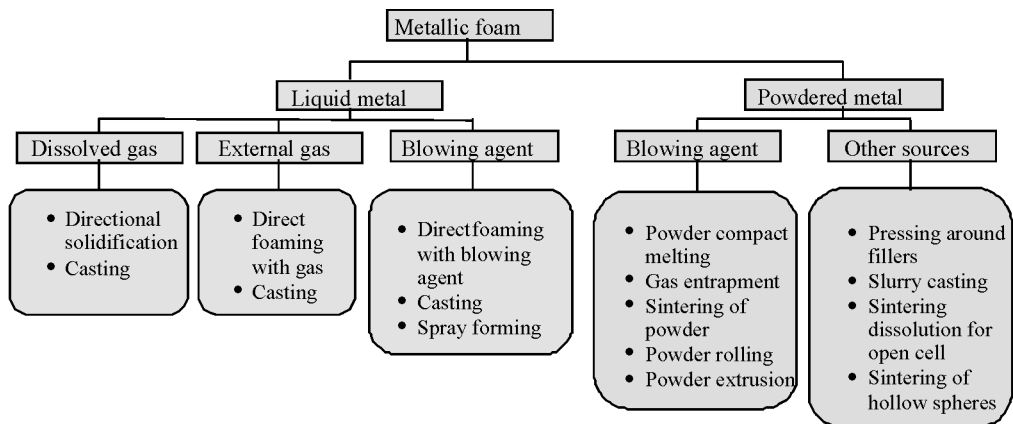

Fig. 2. The processing tree for metallic foams

This indicates the possibility to produce metallic foams in two materials states: liquid metal and powdered metal. As we know that the basic aim of foam processing is to incorporate large and uniformly distributed gas pores in the metallic materials, we

have summarized it as the gas source used in the two states of matter mentioned above. The external gas source means the melt has to be foamed with the help of gases such as air, nitrogen or argon. Dissolved gases lead to foaming because they precipitate from the melt during solidification and if they are not allowed to escape, they will give rise to a foamed structure. The gas source from a blowing agent implies decomposition of a chemical giving rise to a gaseous product. The gas generated from this source is entrapped in liquid or semi-solid material culminating into metallic foam. In the following sections, we will review various processes where different gas sources or other materials are utilized to produce cellular materials.

2.1. Liquid state processing

The liquid state foaming involves three different gas sources: external gas source, gases generated by some foaming agent and dissolved gases. The external gas source to make aluminium foam was first patented by Alcan International and utilized by Hydro Aluminium (Norway) and Cymat Aluminium (Canada) for commercial production [37]. This technique has also been used for the production of foams from metal matrix composites.

External gas source. This process consists in the blowing of liquid metal by gases and to ascertain uniform distribution of large gas pores in the liquid metal. This is accomplished by creating very fine gas bubbles in the melt via especially designed rotating impellers as shown in Fig. 3. However, the stability of the foamed structure is
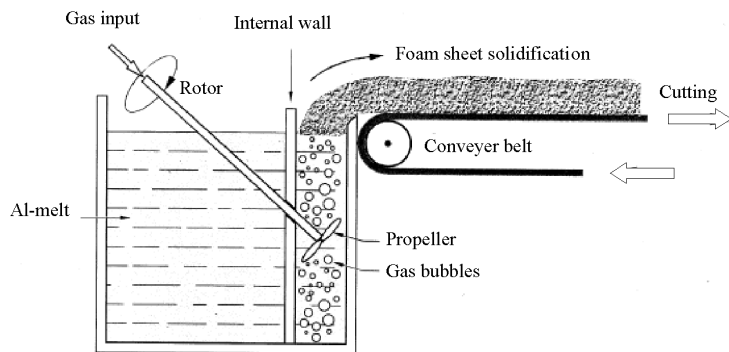
Fig. 3. A scheme showing direct foaming of liquid melt by gas injection [38]

an important factor. The movement of gas bubbles in the liquid becomes relatively easy when the liquid melt viscosity is very low, and the bubbles segregate and coalesce together giving rise to large pores. Keeping this in view, melt viscosity is enhanced by incorporating some second phase ceramic particles, e.g. SiC, Al_2O_3 or MgO [1, 39–41]. As the incorporation of ceramic particles in the liquid metal depends on

several factors, the first step in this kind of processing is to make metal matrix composite followed by gas injection. The stabilization of the foamed structure obtained via this route is derived from the presence of particles in the cell wall. Due to a high contact angles of most of the ceramic particles with Al melt, there are chances of particle strip off from the cell boundaries leaving the wall weak. Therefore, the imperative should be to select particles having good wetting with the liquid metal so that particles are not stripped off the cell wall. A very low contact angle also does not ensure the stabilization effect [1]. The volume fraction of the particles may range from 10% to 20% with a mean particle size of 5–10 μm. However, the size and fraction of particles for a good foaming have been empirically established as shown in Fig. 4 [39, 42].
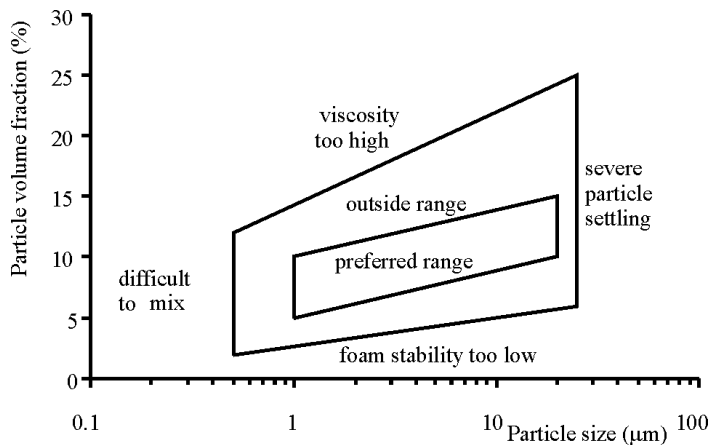
Fig. 4. Empirical guide for the selection of particle size
and its content for foaming MMC melts (after ref. [42])

Particles smaller than 1 μm are difficult to mix, and on the other hand particles bigger than 20 μm lead to severe particle settling. A low volume fraction does not stabilize the foam, whereas a high fraction of particles culminates into high viscosity leading to a difficulty in gas injection. This technique has been extensively used for foaming Al and its alloys, and porosities in the range of 80–95% with 3–25 mm cell size have been achieved. The process is very effective in producing large size foams continuously; however, the presence of ceramic particles leads to difficulties in machining due to high hardness and brittle behaviour of foams. To avoid these disadvantages, it was suggested that foaming should be carried out in a melt, without second phase particles, very close to its liquidus temperature with an arrangement to continuously cool the liquid metal during bubbling. This helps in keeping the viscosity of the melt at low level.

Blowing agent as gas source, direct foaming. As an alternative to the direct foaming of melt by an external gas source, a blowing agent can be added to a viscous melt, which decomposes on heating and releases gas leading to the foaming process. This

technique is being commercially exploited by Shinko Wire (Japan). Also in this processing route, the enhancement of melt viscosity is a prime requirement which can be accomplished by the incorporation of calcium, ceramic reinforcements, aluminium dross, metallic viscosity-enhancing additives and manganese dioxide, etc. [1, 39, 43]. A scheme of the process is shown in Fig. 5.
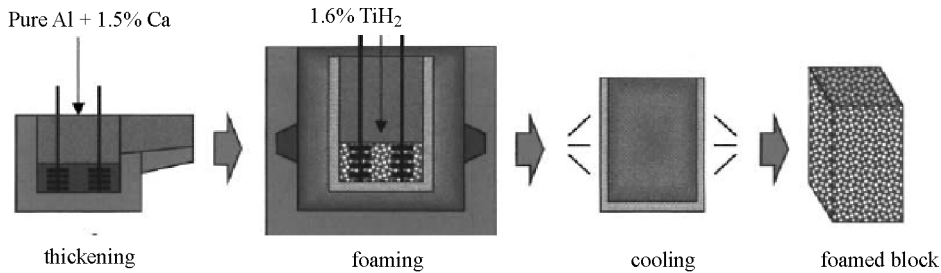
Fig. 5. Processing steps involved in liquid melt foaming with addition of a blowing agent [26]

For example, the addition of Ca to Al melt forms oxides and intermetallics (CaO, $CaAl_2O_4$ and Al_4Ca) which increase the viscosity by thickening the melt. To achieve high viscosity of the melt (($6-7)\times10^{-3}$ Pa·s), a continuous stirring for up to 8–12 min is required for calcium content of 1.8 wt. % [44]. The process is carried out by melting Al in a crucible followed by addition of about 1.5–3.0 wt. % Ca. Subsequently, the melt is stirred and a blowing agent (namely, 1.6 wt. % TiH_2 for Al) is added. The blowing agent releases hydrogen gas under the influence of hot viscous liquid, leading to gradual foaming of the melt. A careful control of the process parameters such as uniformity of temperature of the melt, viscosity and distribution of TiH_2 particles give rise to a homogeneous foam structure. The foaming is generally carried out at 680–720 ºC. Instead of TiH_2, ZrH_2 (0.5–0.6 wt. %) can also be used for the production of Al foam with a preferable temperature between 670 ºC and 700 ºC. Typical densities of such Al foams have been determined to be around 0.18–0.24 g·cm^{-3}. In some cases, it becomes difficult to mix the blowing agent in the liquid metal as it decomposes very fast at the liquidus temperature. To avoid such situations, a low melting point precursor e.g., Al–Si, Al–Cu or Al–Mg, with eutectic composition is prepared with dispersion of the blowing agent without decomposition, and subsequently added to the high temperature melting liquid in the second stage. In the second foaming step, therefore, it becomes easy to control the foam structure. Ferrous alloys have also been attempted by this route using tungsten powder as foam stabilizer; the blowing agent may be $MgCO_3$ or $SrCO_3$ [19, 20] which decompose around 1300 ºC giving out CO_2.

Blowing agent as gas source, spray forming. Spray forming is a technique utilized for the production of alloys and composites with fine and equiaxed grain, low oxide content, and low porosity compared to cast alloys. The technique consists of two distinct but integral processes of melt atomization into micron-sized droplets and their subsequent deposition onto a substrate. Metal matrix composites are produced by this

technique by injecting carbides or oxides in the spray of droplets. This way, the reinforcement is incorporated in the growing pre-form. In a similar manner, Kelly et al. [2] and Banhart et al.[45] have introduced blowing agents instead of ceramic particulate. Decomposition of blowing agent during deposition led to large amount of gases in the growing pre-form. They used $BaCO_3$ powder for foaming the $CuSn_6$ alloy and SiO_2 for carbon steel [45], respectively. The porosity of around 60% could be attained. However, the pore structure was highly inhomogeneous due to the fact that the deposition layer is always in turbulence condition and growing cells are destroyed, thus impairing the cell wall stabilization process. However, this technique is effective, as low temperature processing in this route leads to increased viscosity at the deposition layer.

Dissolved gas sources. In general, gases are dissolved in liquid metal depending upon the temperature and externally applied pressure. For example, hydrogen is dissolved in Al, Fe and Cu, nitrogen in Fe, whereas oxygen in Ag and Cu. Such metals with absorbed gases in liquid state eventually undergo a eutectic reaction to a two-phase system (gas + liquid) as the temperature is lowered. A co-ordinated effort to entrap the gas during solidification leads to a porous structure [4, 6, 46–48]. It is generally carried out by directionally solidifying the gas-saturated liquid with a controlled cooling, proper external pressure (usually of the order of gas partial pressure at a particular temperature) and solidification velocity [49, 50]. The process parameters have to be chosen such that the gas bubbles do not float to the surface of the melt but remain near the solidification zone and get entrapped in the solid. Ikeda et al. [21] have studied the lotus-type porous stainless steel by the continuous zone melting technique. They have shown that the porosity increases with increasing partial pressure of hydrogen and the pore diameter decreases with solidification front velocity. In this process, generally, large elongated pores are formed, which are oriented in the solidification direction. However, they appear spherical in a cross-section. A typical structure is shown in Fig. 1. Hyun et al. [16] have extensively worked with this technique and have shown that an increase in the solidification velocity from 0.697 $mm \cdot s^{-1}$ to 1.185 $mm \cdot s^{-1}$ leads to a decrease in pore diameter (from 100 μm to 50 μm), as well as porosity (29–26%) and an increase in pore number density (25–110) in the lotus-type porous copper. They have also shown that the tensile strength in the direction parallel to pore orientation is 120 MPa, compared to 80 MPa in the perpendicular direction [4]. The process is capable of producing porosities in the range of 5–75%. However, the pore size distribution is generally non-uniform due to concurrent growth of larger and smaller size pores and their coalescence. Based on this process, steels [21], cobalt, chromium, magnesium, copper [4, 6, 49, 50], Ni_3Al [51] and aluminium [46] have been studied.

In addition to the above methods of foaming from liquid metal, foams can also be produced by casting liquid metal in the interstitial space around spherical and randomly stacked space holding materials [1, 5]. The space holding materials can be inorganic [1, 3] or organic granules [52] or hollow spheres. The final product may contain the space holding material depending upon the requirement. However, to remove

the space holder by dissolution, burning or leaching, the content of the space holding fillers should be so high that they are interconnected. Materials containing the space holding fillers are known as "syntactic foams". This technique has been used for making foams of Al, Mg, Zn, Pb, and Sn etc. The main advantages of this process is the precise control over the size of the pore, which is close to the size of the space holders used, and capability to produce the predefined geometry of the component.

Aligned pore structures (similar to dissolved gas foaming) have also been made using directional solidification of monotectic or hypermonotectic alloys. It is well known that this type of alloys is made fibrous by direction solidification [53, 54]. However, if the second phase were removed by using some method, an aligned pore structure would form. This process gives rise to very uniform and evenly distributed cylindrical pores because of the second immiscible liquid phase. Monotectic systems such as Al–Bi, Al–In and Cu–Pb are ductile and thus can be shaped by plastic deformation. The process involves fabrication of aligned fibrous structure followed by removal of fibrous minor phases. Yasuda et al. [7] have used electrochemical etching to remove In from hypermonotectic Al–In alloy system. An aligned cell structure having the diameter in the range of 10–20 μm can be obtained. A typical morphological feature of this kind of foam is shown in Fig. 6.
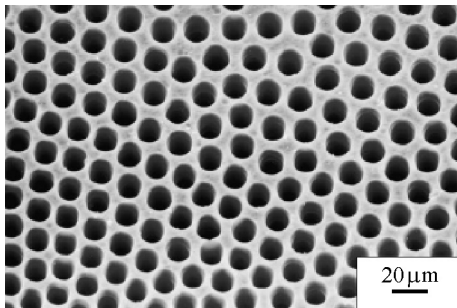
Fig. 6. A uniform distribution of aligned pores (cross-section) obtained from electrochemical etching of directionally solidified monotectic Al–In system [7]

2.2. Powdered metal processing

In the preceding sections, we have discussed the foaming of metallic materials in liquid state. However, solid powdered metal can also be used to make cellular metallic structures. The formation of metallic foam from powdered metal has been extensively studied [1, 14, 17, 32, 55]. Powdered metal can be foamed either by using a blowing agent as gas source or by other techniques where chemical reactions or solid parts are used to create pores during the process. In this section, we will describe these processes in view of the mechanisms of pore formation.

Blowing agent as gas source. Powder compact melting. The powder compact melting process comprises several steps, such as blending of metal or alloy powder with the foaming agent, compaction of powder blend, deformation or working and foaming. Compaction of powders can be accomplished in several ways, such as cold

compaction followed by sintering, hot pressing, powder rolling and powder extrusion. The fundamental aim of all such processes up to the foaming step is to form a very dense foamable precursor with uniform distribution of the embedded blowing agent and without any notable residual open porosity. The foamable precursor is subsequently heated to just below the melting point of the matrix material to affect the foaming process [55]. A schematic of the process is shown in Fig. 7.
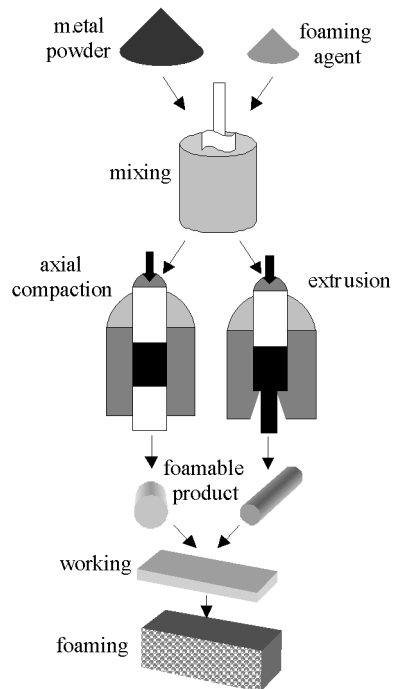
Fig. 7. Processing steps involved in powdered metal foaming with a blowing agent (after ref. [56])

As the temperature is increased, the blowing agent decomposes releasing gas, which in turn leads to expansion of very soft matrix metal. The selection of foaming agent depends upon the sintering and melting temperature of the matrix material. For example, TiH_2 and ZrH_2 are used to foam Al and Zn, respectively [55], $MgCO_3$ and $SrCO_3$ [19] can be used for foaming steels, $BaCO_3$ for copper [2], and $PbCO_3 \cdot Pb(OH)_2$ and MgH_2 for Pb [17]. The decomposition rate, heating rate, and the stability of cell wall structure determine the final density of the foam produced. To delay the decomposition of the foaming agent, it undergoes some heat treatment so that decomposition and melting take place simultaneously. In this way, a uniform foam structure can be developed [57–59]. It has been observed by us that the heating rate of the sample during foaming plays an important role in determining the size and distribution of pores. A relatively high heating rate leads to a smaller pore size with increased pore number density, whereas a slow heating results in larger pore size and the final foam density is higher. This work has been carried out on Al–6.5Si (wt. %) alloy with TiH_2 as the

foaming agent. The present authors have also tried out the same composition by the powder rolling technique. The foam structures obtained from these experiments are shown in Fig. 8.
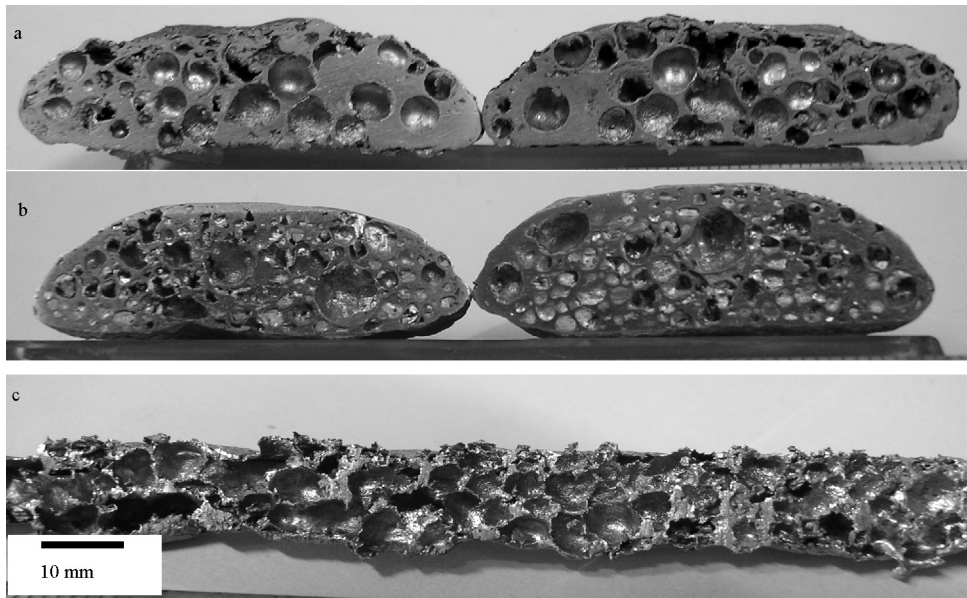
Fig. 8. Aluminium foams by PM route: a) slow heating rate, b) high heating rate
and c) by powder rolling technique at high heating rate

Here, it would be worthwhile to mention that the process has been developed where a purposefully incorporated inert gas source is used for the foam genesis instead of a blowing agent [60, 61]. In this process, the material to be foamed is canned and degassed, followed by refilling with an inert gas at a high pressure and sealing. To get a uniform distribution of the entrapped compressed gas in the powder compact, the sealed system is isostatically hot-pressed. Secondary processing of such compacts involves annealing the compact at around $0.6T_m$. The softening of the metal and a simultaneous increasing of pressure of the entrapped gases leads to creeping of the material. As a result, a porous body with 20–40% porosity and 10–100 μm cell size is obtained [60]. The second step of annealing treatment is a long process where foaming is accomplished slowly and, therefore, it takes around 6–24 h for a complete foam formation. Theoretical considerations show that this process cannot give more than 50% porosity [1].

Other foaming routes. As an alternative to the powder compact melting process, mere sintering of metal powders may also be used to produce fine pore structure up to 20–50% porosity. A large variety of materials have been used for this process including titanium, superalloys, bronze and steels. The porosity obtained from this technique

consists basically in the interstitial pores present in a powder compact prior to sintering. However, a material that is easily oxidized or produces a reaction product at the surface is not suitable for this process, as the oxide layer inhibits the sintering process. The strength of the foamed component produced via this route is generally very low.

A few processes have been developed where foams are produced by sintering of hollow spheres. There are several reported techniques [30, 62] that can be used to produce hollow spheres. The sintering of hollow spheres can produce both open and closed cell foams. Open structures are obtained by just sintering the hollow spheres, whereas closed cell structures can be generated by filling the interstices between the spheres with a metal powder followed by sintering. This kind of foam is known as syntactic foam. The density of as low as 0.9 g·cm^{-3} has been obtained for Ti–6Al–4V foam produced by this route. The advantage of this process is that the pore size distribution is not random but depends upon the size and distribution of the spheres used, and in this way the properties of the foams become more predictable compared to those having random pore size distribution. In principle, any materials available in powder metallurgy can be used in this route to make foamed parts.

Similar to the above process, IFAM (Bremen, Germany) has recently developed APM (Advanced Pore Morphology) process [63] where spherical foam elements, in the size range of 9–10 mm, have been produced (Fig. 9). The aim of the development was to separate the two steps of foaming and of shaping components. The process involves making a small volume foamable precursor (similar to powdered metal processing) and foaming it in a continuous manner on a conveyor belt furnace. The stack of spherical foamed elements is further sintered to get a component shape. In this way, two types of pore morphology are generated: inner closed porosity of foam elements and the open pores of bulk APM elements. Therefore, it is obvious that this process takes care of hollow sphere sintering as well as foaming by powdered compact melting. The process gives added advantage of open porosity thus decreasing the relative density of aluminium foam to 0.36 g·cm^{-3} compared to other processes. The advantage lies in the fact that the production process has two main steps that are fully independent of each other. They can be carried out at different times, in different locations, and by different companies. The main advantages of APM foam production lies in the fact that all sub-steps in the production of foam elements and components thereof can be fully automated even with the commercially available equipment. If we assume foam element delivery by a commercial supplier, the end-user is not necessarily required to gain any metal foaming know-how or buy cost-intensive high-temperature furnaces.

As we have already discussed the closed cell foam production by the hollow sphere sintering process, if the hollow spheres are replaced by granules of inorganic salts, polymeric materials or metal which can be taken out by various processes such as dissolution, burning or evaporation after sintering, we get an open foam structure. With this technique, Zhao and Sun [9] made aluminium foam using NaCl as the space holding material. The size of the NaCl powder was selected according to the pore size required. Al powder less than 450 µm and NaCl particles around 300–1000 µm were

mixed together, compacted and then sintered. The aluminium weight fraction varied between 0.2 and 0.75. Sintering temperature was chosen to be 680 ºC, which is far below the melting point of NaCl (801 ºC) [9]. The sintered samples were kept in warm running water for 45 min to get a porous structure with a relative density of 0.2 and 0.7 for aluminium weight fraction of 0.2 and 0.75, respectively. With the same technique, Zhao et al. [11] tried out the lost carbonate sintering process, where open cell copper was foamed with K_2CO_3 with the melting point of 891 ºC and decomposition temperature of 950 ºC. In this study, both the dissolution and decomposition routes were explored depending upon the production time and shrinkage concerns. The porosity of around 85% could be achieved in this study.
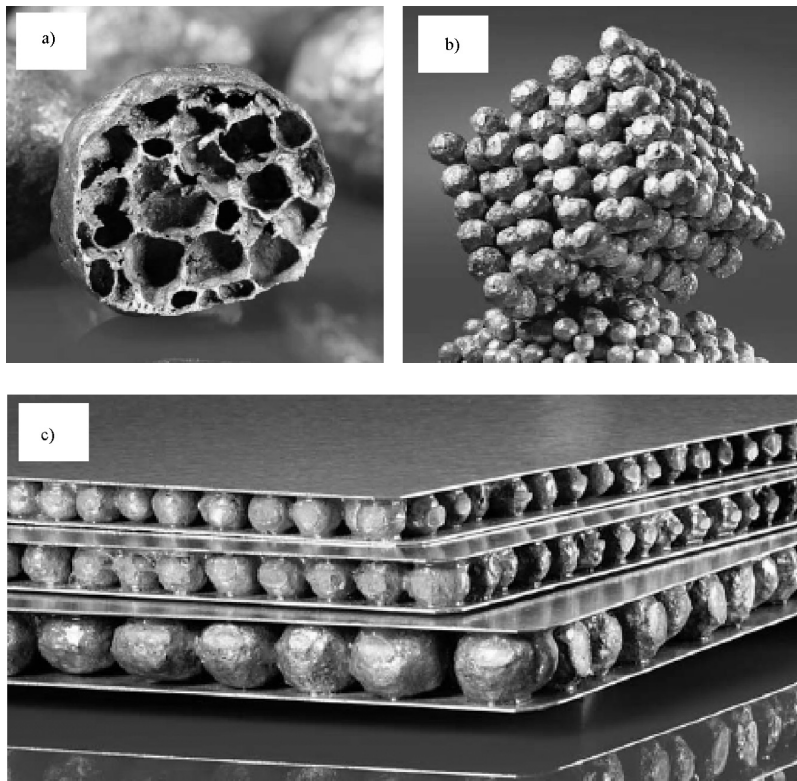
Fig. 9. Illustration of the IFAM (Bremen, Germany) produced: a) foamed spherical elements, b) pure foam parts, c) sandwich structure with a cellular core structure [63] (courtesy: IFAM, Bremen, Germany)

Metallic foams can also be produced by foaming metal powder slurries with an addition of chemicals, which led to the formation of gases as reaction product of the additives. A mixture of metal powder and chemicals are poured into a mould to form viscous slurry and kept there at an elevated temperature. The gases produced by the reaction lead to foaming. A controlled composition of reactants gives rise to stable porous slurry that is dried and sintered subsequently. Aluminium foams have been

produced by this route using orthophosphoric acid and hydrochloric acid as additives [64]. Bleck has recently developed steel foam using laminate silicate as dispersant for stabilising the slurry and alcohol solution containing orthophosphoric acid as additives [65]. This process has been named as SlipReactionFoamSintering or SRSS (SchlickerReaktionsSchaumSinter). This process has been utilised for iron and steel powders, 316 Stainless Steel, Hastealloy B and Inconel 625 [65].

3. Stabilisation of foam structure

In the previous sections, we have dwelt mainly on different processing routes for metallic foam. We have shown that the complete foaming process is concerned with foam inception or genesis where the blowing agent decomposes (1), its evolution and growth of spherical pores (2), further foaming that leads to thinning of cell wall and thus to change of pore shape from spherical to polygonal (3), and pore coalescence due to surface tension and gravitational pull (4). This means the eventful life of foams comprises birth, life and death. Our aim is to avoid the death or collapse of foam during the processing. The main convict for the death of foam is the instability of cell walls under the pressure differences or gravity. As we can see from the third and fourth steps, the death or collapse of foam occurs at the peak of third and start of the fourth step [35]. This part of the foaming process has constituted a tremendous challenge for the researchers. The stability of foam can be understood as the formation of a uniform distribution of large size pores, which in turn can be defined as foamability also. If we consider the physics of foaming, the growth of pores or cells lead to the thinning of cell walls and their consequent rupture. This is generally attributed to the drainage of liquid through the cell walls under gravity and also due to surface tension that leads to a positive pressure at the cell wall compared to the triple junctions (Fig. 10a). The pressure at triple junctions of cell walls is lower than that in the cell wall and the liquid on the cell wall tends to flow towards triple points during the foaming process. With the growth of cell size, gravity also comes into effect, and cell walls act as tunnels for the drainage of liquid. This leads to the final breaking of cell wall resulting in coarsening of pores. The drainage phenomenon has been of real scientific importance to understand the physics of the foaming process and efforts have also been made to model aqueous foams [66]. Therefore, it is obvious from the above that strengthening the cell walls can inhibit this phenomenon. This can be accomplished in several ways, e.g., by enhancing the viscosity of melt, using different alloying elements in the melt or employing ex- or in-situ particles that stabilize the wall [27, 40, 41, 67–70]. The breaking of cell walls becomes pronounced, due to pressure differences, when pores with a wide range of size are formed. Cell wall rupture also takes place due to changing rheological characteristics, and deformation and flow of foams. The effect of ceramic particles on the stability of foams has already been discussed in the previous sections. A detailed description is given by Babcsan et al. [41] and Deqing and Ziyuan [40], where they have discussed various aspects of particle rein-

forcement, such as particle materials, particle size and volume fraction, on foamability of Al alloys by the liquid metallurgy route. Similarly, Koerner et al. [68] discussed the aluminium foam stabilization by the presence of an oxide network. They have also suggested that the effect of the second phase on the stability of foam is due to its wetting characteristics with aluminium liquid. A good wetting (for example, Al/Al_2O_3 contact angle 63° at 1100 ºC) leads to a decrease in the pressure in particle-free regions of the cell wall which in turn reduces the tendency of liquid drainage and thus cell wall thinning. The ceramic particles are segregated at the cell boundaries, and as the cell grows particles are pushed away. Finally the particles mainly decorate the cell walls leading to its strengthening (Fig. 10b).
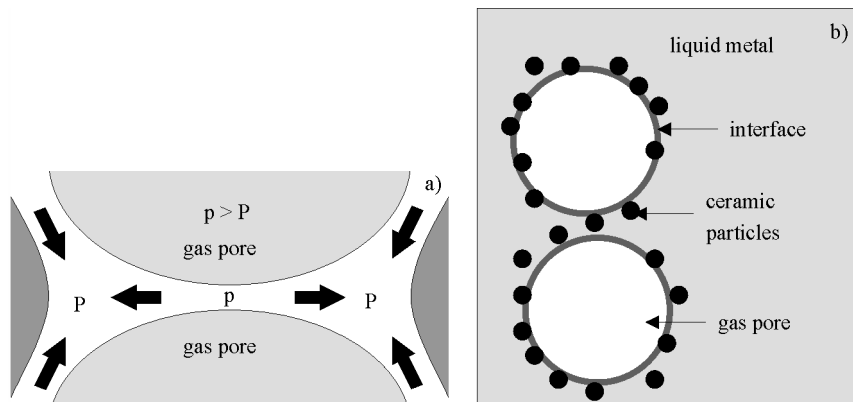
Fig. 10. Cell wall structure and related phenomena during foaming process (a) (after ref. [35]); the effect of ceramic particles for stabilization during the foaming process (b) (after ref. [36])

Sometimes, a pre-treatment of the blowing agent also gives better foaming action [57–59]. A prolonged heating of TiH_2 at different temperatures leads to the formation of an oxide layer on the surface delaying the reaching of decomposition temperature during foaming. Matijasevic and Banhart [58] reported that the delay can be up to 45 s, final expansion of the foam is increased from 4.5 to 5.5 times and a more uniform foam is formed with smoother cell walls and increased roundness of pores. Kennedy and Lopez [71] and Zeppelin et al. [55] have studied the decomposition behaviour of as received and oxidized TiH_2 powder and desorption behaviour of hydrides such as MgH_2, TiH_2 and ZrH_2 and their effect on foaming process.

The drainage phenomenon can also be subdued by foaming in a low gravity environment [33–36]. Foaming in low gravity delays the collapse of cells as the mass of the foam above the cell becomes negligible. The coalescence phenomena become more pronounced particularly when the size of the foaming material is large. Therefore, experiments have been carried out in microgravity conditions where a notable foam expansion is observed also for the material known to be unstable in the presence of gravity but coalescence creates very coarse bubbles. From the different structures of the solidified samples, it was concluded that the presence of oxide particles in the melt

hindered cell wall drainage by increasing the viscosity of the melt, and also suppressed the coalescence of the pores. Recently, Babcsan et al. [72] have demonstrated the feasibility of in-situ studies of liquid metal foaming. Otherwise, it would have been difficult to carry out liquid foaming in low gravity parabolic flights or drop towers. The Indian space research program has also highlighted the microgravity experiments and efforts are being made to study such systems in parabolic flight under microgravity conditions.
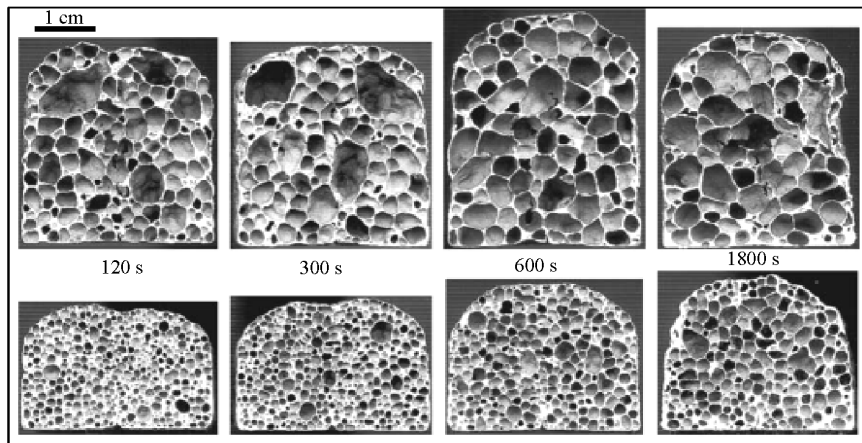

Fig. 11. Foam stability: Cell structure after heating to 665 ^{0}C and increasing the dwelling time at this temperature before solidification (upper row: 1000 mbar argon; lower row: 2800 mbar argon; precursor material: commercial AlSi10Mg0.5, extruded) [68]

In addition to the above foam stabilization techniques, the heating rate during foaming and compaction conditions also influence the final foam characteristics as discussed in detail by Duarte and Banhart [70]. According to them, hot compaction temperature for aluminium with TiH_2 as foaming agent should vary between 400–450 ºC. A higher temperature leads to loss of hydrogen due to early decomposition of the foaming agent, whereas lower temperature of compaction results in improper sintering leaving interconnected pores, and, consequently, in the escape of hydrogen prior to foaming. A high heating rate gives better foaming compared to slow heating. This is attributed to the sufficient time available for the foaming agent to decompose and escape at slow heating rate, and oxidation of a thick oxide layer on the surface as well as inside the precursor material, which inhibits the foaming process by mechanically hindering foam expansion. Koerner et al. [68] experimented with varying ambient argon pressure on aluminium foaming for different time periods. It has been concluded from their study that foaming for 600 s at 665 ºC and at ambient pressure of 1000 mbar does not lead to any drainage. When kept for 1800 s, gas loss was seen only from the top surface of the foam and material redistribution processes induced by the energetically unfavorable cell structures do not take place. A similar experiment at 2800 mbar led to an increase in foam density and decrease in cell size. The observed stability of foams seemed to be independent of the cell size (Fig. 11).

It has also been suggested by Frei et al. [73] that a prior deformation of precursor materials is beneficial to achieve high porosity levels with more uniform cell structures, and also an accelerated foaming. They observed that the as-cast precursor contained unreacted TiH_2 particles within the cell walls, which is not common in deformed precursors. The better stability of the foam has been attributed to the redistribution of the blowing agent within the precursor and deformation-induced damage of the oxide layer on the hydride particles. And also, the pore-free precursor after deformation leads to more dispersed nucleation of pores and prevents their early coarsening.

4. Industrial applications and future prospects

The projections of the future fuel crisis, the requirements of achieving high fuel efficiency along with higher passenger safety in the automobile industry, and the needs of creating light weight construction materials have attracted tremendous consideration for ultralight weight metallic foams. The implementation of metallic foams
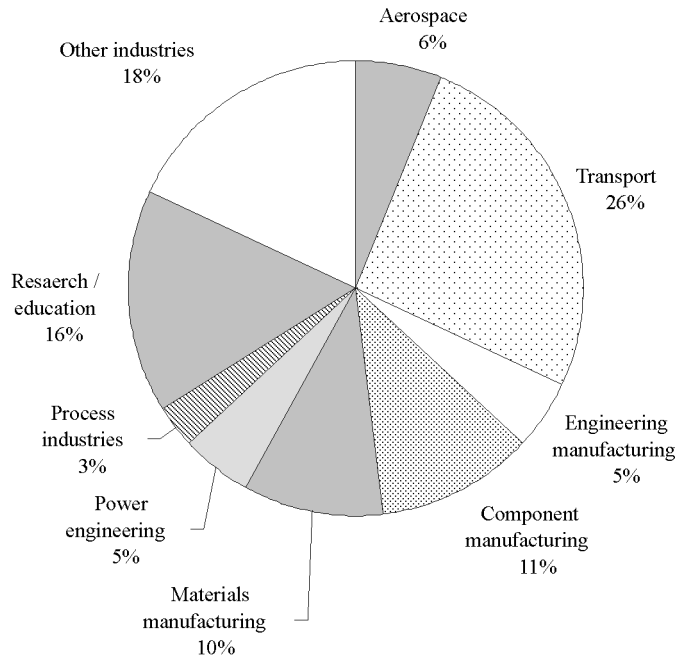
Fig. 12. Break-up of projected industrial sector requirements for metallic foam applications

in these industrial sectors depends to a large extent upon their manufacturing cost, the environmental durability, and fire retardancy [74]. In general, metallic foams possess a range of thermomechanical properties that suggest their application in areas demanding impact/blast amelioration, heat dissipation, acoustic isolation and heat exchange [60, 75]. The projected applications of metallic foams have already been recognised

and a detailed description of the requirements of various industrial sectors can be seen elsewhere [1, 12–15, 76]. Recently, National Physical Laboratory (UK) made a survey both in industries and in research institutions to have an idea of potential expectations from metallic foams. The survey indicated that the major applications of metallic foams, around 32%, in the near future would be directed towards automotive and aerospace industries (Fig. 12).

In addition to this, 26% of the demand would go to materials manufacturing, engineering manufacturing, and component manufacturing. As the transport industry will play a major part in the implementation of metallic foams, we have considered making an attempt to see where we need to use these foams in a car, for example. For this purpose, we should have an idea of the frequent accidental possibility in different parts of a car. We also know that foams in the transport industry are basically needed for weight saving, impact absorbing and thermal insulation. Figure 13 shows a sample car (designed by Karmann, Germany) with components made of Al foam. It is indicated in the figure that 67% of in-vehicle injury cost incurs when the collision takes place at the front end of the car and about 22% in-vehicle injury cost occur during collision from the side. This indicates that the front-end collision of a car is most detrimental during an accident and therefore the utilisation of foamed materials in these parts becomes necessary for passenger safety. As a result, the imperative should be to use metallic foams in the front end for crash safety and the rear end should be replaced with foam to reduce the weight. The difference between these two applications will be based on the quality of the foams to be used in these parts. Al foams have been sought to constitute the largest fraction of components in the automotive industry.
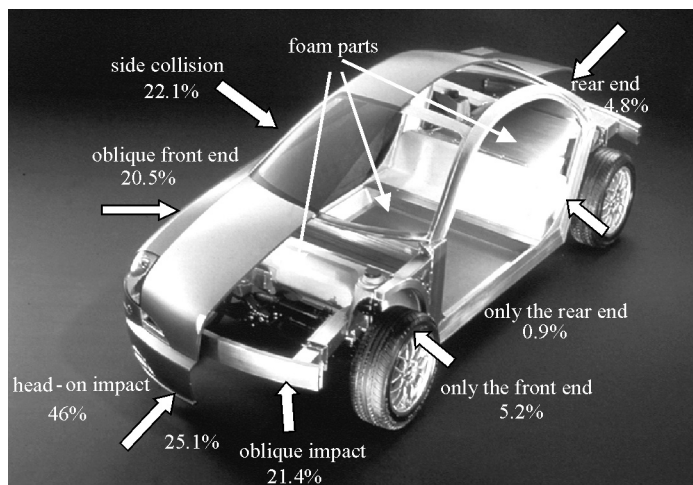

Fig. 13. Karmann car with parts made of aluminium foam (courtesy: IFAM, Bremen, Germany) along with the collision types and subsequent in-vehicle injury cost

The strength of Al foams and the weight saving resulting from their use are currently believed to be insufficient for critical areas of applications. Therefore, tremendous efforts have been recently directed towards steel foam development which, in principle, can have several potential advantages over aluminium foams, such as increased strength and specific stiffness, lower raw material cost, higher melting temperature, and compatibility with steel structures [19]. Initial developments in the processing of steel foams have already been done by conventional powder metallurgical routes, and also by space holding techniques. However, we have a long way to go to produce steel foams commercially, as the high operating temperature and the low viscosity of liquid steels are the major challenges to overcome. The authors of this paper are also actively engaged in the development of steel foams along with the process optimisation for Al foam production.

Similar to the development of steel foams, efforts have been made to develop bulk amorphous metal foams (AMFs). The amorphous foams are seen to have promising application prospects, such as sporting goods and cellular telephone housings due to their high strength, high eleastic strain, and high wear and corrosion resistance. The high corrosion resistance of AMFs compared to other metallic foams is advantageous in applications such as filters, electrodes, and catalyst supports [77–79]. As far as applicability in transport industry is concerned, AMFs may not prove to be a better option than metallic foam, despite its very high strength. Stronger foams may be able to mitigate heavy impacts but simultaneously transmit unacceptably large forces to delicate objects or human beings. Therefore, AMFs may be good for structural applications but not for the transport industry. The processibility and strength of metallic foams are determined by the processing temperature and strength of the parent material. For example, Al alloy-based foams can be easily fabricated by various processes but their mechanical properties are limited by the base alloys, while foams made of stronger crystalline alloys generally require higher-temperature and/or more difficult processing methods. Meanwhile, amorphous metal foams are easy to fabricate due to their low melting temperature and superplastic-like flow at higher temperatures [80]. Despite a low processing temperature, the application of such AMFs above the glass transition temperatures, where toughness is drastically reduced, is limited to 27–480 ºC for an extended period. However, the processing of bulk AMFs is still a challenge due to the compositional accuracy and cooling rate requirements. A slight deviation in composition, due to external additives for foaming, may lead to deviation from the deep eutectic composition resulting in stable crystalline phases. Even if the purity is overcome, the compatibility of external gas blowing phases or space holders and the processing equipment must be ensured to produce amorphous foams. The progress in the identification and understanding of new glass-forming systems with still higher robustness against contaminants and slow cooling, which is currently the subject of intensive research, should lead to an equivalent progress in AMFs [77].

Despite the current development and future possibilities in processing and application of metallic foams, there are several limitations that have to be considered and

addressed so as to open new avenues for the metallic foams. The primary hindrance for the wide applicability of metallic foams is the cost of production. The second concern is the variability in materials and the large scatter in measured properties [81]. And also, reliable test methods have to be invented to fully exploit the potential of these cellular materials. World-wide efforts are being made to model the mechanical behaviour of metallic foams, and researchers are, to some extent, successful in predicting the same. However, theoretical and numerical models related to the processing of metal foams, which could be useful in predicting the effect of process parameters, are not available. The developmental process could be made faster by drawing up process models, otherwise "trial and error" would be the only way. The lack of process models is due to the fact that the mechanism of the foaming process is still not fully understood.

5. Concluding remarks

Recent technological advances in the field of metallic foams have led to the development of a wide range of processing techniques for the open, as well as closed cell morphologies. The processing route has to be decided on the basis of the cost of production, materials properties, and the intended applications of the final product. However, as the cost of production of a good quality metallic foam is still high, continual innovations are underway so as to draw maximum benefit by opening new avenues for a wide range of industrial applications. Foams of novel, emerging materials, such as high temperature melting materials, superalloys, steels, bulk metallic glasses etc. are seeing tremendous application opportunities in the near future. However, the lack of full understanding of the mechanisms of foam formation and their theoretical/numerical models inhibits the developmental process to a large extent. A versatile predictive model for processing as well as property has become a necessity for a faster growth in this direction, as well as innovations in processing techniques.

References

[1] BANHART J., Prog. Mater. Sci., 46 (2001), 559.
[2] KELLY P., WONG C.R., MORAN A., Int. J. Powder Metall., 29 (1993), 161.
[3] BANHART J., Aluminium, 75 (1999), 1094.
[4] HYUN S.K., MURAKAMI K., NAKAJIMA H., Mater. Sci. Eng. A, 299 (2001), 241.
[5] RABIEI A., O'NEILL A.T., Mater. Sci. Eng. A, 404 (2005), 159.
[6] SIMONE A.E., GIBSON L.J., J. Mater. Sci., 32 (1997), 451.
[7] YASUDA H., OHNAKA I., FUJIMOTO S., SUGIYAMA A., HAYASHI Y., YAMAMOTO M., TSUCHIYAMA A., NAKANO T., UESUGI K., KISHIO K., Mat. Lett., 58 (2004), 911.
[8] STÖBENER K., BAUMEISTER J., RAUSCH G., BUSSE M., Metal Powder Rep., Jan. (2005), 12.
[9] ZHAO Y.Y., SUN D.X., Scripta Mater., 44 (2001), 105.
[10] CHOU K.S., SONG M.A., Scipta Mater., 46 (2002), 379.
[11] ZHAO Y.Y., FUNG T., ZHANG L.P., ZHANG F.L., Scipta Mater., 52 (2005), 295.

[12] Davis G.J., Zhen S., J. Mater. Sci., 18 (1983), 1899.
[13] Banhart J., Ind. Foundry Jo., 51 (2005), 36.
[14] Banhart J., MRS Bulletin, April (2003), 290.
[15] Banhart J., Weaire D., Phys. Today, July (2002), 37.
[16] Hyun S.K., Nakajima H., Mat. Lett., 57 (2003), 3149.
[17] Irretier A., Banhart J., Acta Mater., 53 (2005), 4903.
[18] Park C., Nutt S.R., Mater. Sci. Eng. A, 299 (2001), 68.
[19] Park C., Nutt S.R., Mater. Sci. Eng. A, 288 (2000), 111.
[20] Park C., Nutt S.R., Mater. Sci. Eng. A, 297 (2001), 62.
[21] Ikeda T., Aoki T., Nakajima H., Met. Mat. Trans., 36A (2005), 77.
[22] Hodge A.M., Dunand D.C., Intermetall., 9 (2001), 581.
[23] Banhart J., Bellmann D., Clemens H., Acta Mater., 49 (2001), 3409.
[24] Wen C.E., Mabuchi M., Yamada Y., Shimojima K., Chino Y., Asahina T., Scripta Mater., 45 (2001), 1147.
[25] Maine E., Ashby M.F., Adv. Eng. Mater., 2 (2000), 205.
[26] Miyoshi T., Itoh M., Akiyama S., Kitahara A., Proc. MRS Symp. D. S. Schwartz, D. S. Shih, A. G. Evans, H. N. G. Wadley (Eds.), 521 (1998), 133.
[27] Ip S.W., Wang Y., Toguri J.M., Can. Met. Quart., 38 (1999), 81.
[28] Deqing W., Ziyuan S., Mater. Sci. Eng. A, 361 (2003), 45.
[29] Llyod D.J., Mcleod A.D., Morris P.L., Jin I., Int. Patent (1991), WO 91/19823.
[30] Waag U., Schneider L., Loethmann P., Stephani G., Metal Powder Rep., 55 (2000), 29.
[31] Wada T., Inoue A., Mater. Trans., 44 (2003), 2228.
[32] Jiang B., Zhao N.Q., Shi C.S., Du X.W., Li J.J., Man H.C., Mater. Lett., 59 (2005), 3333.
[33] Weaire D., Adv. Eng. Mater., 4 (2002), 723.
[34] Banhart J., Baumgaertener F., Cox S.J., Kronberg B., Langevin D., Odenbach S., Weaire D., Wuebben T., Proc. 1st Int. Symp. Microgravity Research and Applications in Physical Sciences and Biotechnology, ESA Publications, ESTEC, Noordwijk, 2001, p. 589.
[35] Wuebben T., Odenbach S., Banhart J., Proc. Eurofoam 2000 P. Zitha, J. Banhart, G. Verbist, (Eds.), MIT-Verlag Bremen, 2000, pp. 98–103.
[36] Wuebben T., Stanzick H., Banhart J., Odenbach S., J. Phys.: Cond. Matter, 15 (2003), S427.
[37] Jin I., Kenny Sang L.D., Na H., US Patent 4,973,358.
[38] Asholt P., Proc. Int. Conf. Bremen, Germany, June 14–16, 1999, J. Banhart, M.F. Ashby, N. Fleck, (Eds.), MIT Press-Verlag, p. 133.
[39] Banhart J., JOM, 52 (2000), 22.
[40] Deqing W., Ziyuan S., Mater. Sci. Eng. A, 361 (2003), 45.
[41] Babcsan N., Leitmeier D., Degischer H.P., Mat.-Wiss. U. Werkstofftech, 34 (2003), 22.
[42] Prakash O., Embury J.D., Sang H., Sinclair C., Silvetti P., *The Minerals, Metals and Materials Society,* C.M. Ward-Close, F.H. Froes, D.J. Chellman, S.S. Cho (Eds.), 1997. p. 19.
[43] Simone A.E., Gibson L.J., Acta Mater., 46 (1998), 3109.
[44] Ma L., Song Z., Scripta Mater., 39 (1998), 1523.
[45] Banhart J., Knuewer M., Proc. PM 1998 World Congress, European Powder Metallurgy Association, 5 (1998), 265.
[46] Bonenberger R.J., Kee A.J., Everett R.K., Matic P., Proc. MRS Symp., D.S. Schwartz, D.S. Shih, A.G. Evans, H.N.G. Wadley (Eds.), 521 (1998), 303.
[47] Apprill G.M., Poirier D.R., Maguire M.C., Gutsch T.C., Proc. MRS Symp., D.S. Schwartz, D.S. Shih, A.G. Evans, H.N.G. Wadley, 521 (1998), 291.
[48] Tane M., Ichitsubo T., Nakajima H., Hyun S.K., Hirao M., Acta Mater., 52 (2004), 5195.
[49] Nakajima H., Hyun S.K., Ohashi K., Ota K., Murakami K., Colloids Surf., A179 (2001), 209.
[50] Yamamura S., Shiota Y., Murakami K., Nakajima H., Mater. Sci. Eng. A, 318 (2001), 137.
[51] Hyun S.K., Nakajima H., Mater. Sci. Tech., 74 (2004), 667.

[52] Ma L., Song Z., He D.P., Scripta Mater., 41 (1998), 785.

[53] Grugel R.N., Hellawell A., Metall. Trans. A, 12 (1981), 669.

[54] Dhindaw B.K., Stefanescu D.M., Singh A.K., Metall. Trans. A, 19 (1988), 2839.

[55] Zeppelin F., Hirscher M., Stanzick H., Banhart J., Composite Sci. Tech., 63 (2003), 2293.

[56] Banhart J., Baumeister J., J. Mater. Sci., 33 (1998), 1431.

[57] Matijasevic B., Fiechter S., Zizak I., Görke O., Wanderka N., Schubert-Bischoff P., Banhart J., Powder Metallurgy World Congress, H. Danninger, R. Ratzi (Eds.), European Powder Metallurgy Association, Vienna, 4 (2004), 149.

[58] Matijasevic B., Banhart J., Scripta Mater., 54 (2006), 503.

[59] Matijasevic B., Banhart J., Fiechter S., Görke O., Wanderka N., Acta Mater. 54 (2006), 1887.

[60] Kearns M.W., Blenkinshop P.A., Barber A.C., Int. J. Powder Metall., 24 (1998), 59.

[61] Murray N.G.D., Schuh C.A., Dunand D.C., Scripta Mater. 49 (2003), 879.

[62] Sypeck D.J., Parrisch P.A., Wadley H.N.G., Proc. MRS Symp. D.S. Schwartz, D.S. Shih, A.G. Evans, H.N.G. Wadley (Eds.), 521 (1998), 205.

[63] Stöbener K., Baumeister J., Rausch G., Metal Powder Rep., Jan. (2005), 12.

[64] Drolet J.P., Int. J. Powder Metall., 13 (1977), 223.

[65] Bleck W., Metal Powder Rep., March (2004), 18.

[66] Gergely V., Clyne T.W., Acta Mater., 52 (2004), 3047.

[67] Wasan D.T., Nikolov A.D., Lobo L.A., Koczo K., Edwards D.A., Progr. Surface Sci., 39 (1992), 119.

[68] Koerner C., Arnold M., Singer R.F., Mater. Sci. Eng. A, 396 (2005), 28.

[69] Esmaeelzadeh S., Simchi A., Lehmhus D., Mater. Sci. Eng. A, 424 (2006), 290.

[70] Duarte I., Banhart J., Acta Mater., 48 (2000), 2349.

[71] Kennedy A.R., Lopez V.H., Mater. Sci. Eng, A, 357 (2003), 258.

[72] Babcsan N., Garcia-Moreno F., Leitlmeier D., Banhart J., Mater. Sci. Forum, 508 (2006), 275.

[73] Frei J., Gergely V., Mortensen A., Clyne B., Adv. Eng. Mater., 4 (2002), 749.

[74] Beals J., Thompson M., J. Mater. Sci., 32 (1997), 3595.

[75] Lu T.J., Stone H.A., Ashby M.F., Acta Mater., 46 (1998), 3619.

[76] Banhart J., Proc. 9th Int. Conf. on Aluminium Alloys J.F. Nie, A.J. Morton, B.C. Muddle (Eds.), 2004, p. 764.

[77] Johnson W.L., Mater. Sci. Forum, 225 (1996), 35.

[78] Inoue A., Acta Mater., 48 (2000), 279.

[79] Brothers A.H., Dunand D.C., Scripta Mater., 54 (2006), 513.

[80] Wang W.H., Dong C., Shek C.H., Mater. Sci. Eng. R, 44 (2004), 45.

[81] Ramamurty U., Paul A., Acta Mater., 52 (2004), 869.

Sol-gel preparation and characterization
of perovskite gadolinium aluminates

S. Cizauskaite[1], V. Reichlova[2], G. Nenartaviciene[1],
A. Beganskiene[1], J. Pinkas[2], A. Kareiva[1*]

[1]Department of General and Inorganic Chemistry, Vilnius University,
Naugarduko 24, LT-03225 Vilnius, Lithuania

[2]Department of Inorganic Chemistry, Masaryk University Brno,
Kotlarska 2, CZ-61137 Brno, Czech Republic

The paper reports on the results concerning the sol-gel preparation of the nanocrystalline non-substituted and Sr-substituted gadolinium aluminate ($GdAlO_3$, GAP) ceramics at slightly varying conditions of synthesis. The metal ions, generated by dissolving starting materials of metals in the diluted acetic acid were complexed by 1,2-ethanediol to obtain precursors for the non-substituted and Sr-substituted GAP. In the sol-gel processing different starting gadolinium materials such as gadolinium nitrate or gadolinium oxide were employed. The influence of the temperature and the amount of substituent on the phase purity of GAP was also investigated. Phase transformations, composition and micro-structural features in the gels and polycrystalline samples were studied by thermal analysis, powder X-ray diffraction analysis, infrared spectroscopy and scanning electron microscopy.

Key words: *aluminate; perovskite; ceramics; aqueous sol-gel process*

1. Introduction

Ceramics based on the Ln_2O_3–Al_2O_3 system (Ln – lanthanide element) are promising materials for optical, electronic and structural applications [1–3]. Perovskite aluminates doped with a lanthanide element offer advantages of longer lifetimes and higher, polarized cross sections with respect to most other oxide matrices, and are useful as hosts for solid-state lasers, luminescence systems and window materials for a variety of lamps. For example, gadolinium aluminate is currently under development as candidate material for the neutron absorption and control rod applications. Related ceramic perovskite materials are currently being incorporated into automobile catalytic

_____

*Corresponding author, e-mail: aivaras.kareiva@chf.vu.lt

converters, are also promising substrates for the epitaxy of thin oxide films having potential use as buffer layers for the epitaxial growth of various perovskite-type films such as high temperature superconductors, ferroelectrics, piezoelectrics and colossal magnetoresistance oxides. Some perovskites also exhibit very large electric permittivities [4–9].

The unique properties of most of the mixed-cation oxide ceramics depend largely on the impurities or dopants. Such complex oxides with the perovskite structure also demonstrate an impressive range of electrical, optical and magnetic properties. These properties of perovskites can be tuned by substituting cations at both sites. For instance, recently a strong photoluminescence was obtained without luminance temperature-degradation in the mixed alkaline earth substituted lanthanide aluminates or lanthanide doped alkaline earth aluminates [10, 11, 12–15]. Strontium atoms can substitute into the perovskite $LnAlO_3$ structure possibly for the lanthanide cation [16].

In the context of doped materials, the incorporation of homogeneously distributed nanosized secondary phases in a host matrix, which can be realized by the molecular level fabrication of new materials, is of significant interest. Over the last few decades, the sol-gel techniques have been used to prepare a variety of mixed-metal oxides [17–21]. In this paper, we present results of a systematic study of aqueous sol-gel synthetic approach to pure $GdAlO_3$ and Sr-substituted gadolinium aluminates $Gd_{1-x}Sr_xAlO_{3-\delta}$. The results illustrate the influence of starting materials, annealing temperature and strontium concentration on the phase purity and crystallinity of the end products.

2. Experimental

2.1. Preparation of gels

Gadolinium aluminate and gadolinium–strontium aluminate ceramic samples were synthesized by the sol-gel method. The gels were prepared using stoichiometric amounts of analytical-grade $Gd(NO_3)_3 \cdot 6H_2O$ ($GdAlO_3$, sample I; $Gd_{0.9}Sr_{0.1}AlO_3$, sample II; $Gd_{0.75}Sr_{0.25}AlO_3$, sample III; $Gd_{0.5}Sr_{0.5}AlO_3$, sample IV; $Gd_{0.25}Sr_{0.75}AlO_3$, sample V) or Gd_2O_3 ($GdAlO_3$, sample VI; $Gd_{0.9}Sr_{0.1}AlO_3$, sample VII; $Gd_{0.75}Sr_{0.25}AlO_3$, sample VIII) as Gd^{3+} raw materials. Strontium acetate $Sr(CH_3COO)_2$ and aluminium nitrate $Al(NO_3)_3 \cdot 9H_2O$ have been used as Sr^{2+} and Al^{3+} sources, respectively. For the preparation of unsubstituted samples by the sol-gel process, gadolinium nitrate or gadolinium oxide were first dissolved in 50 cm^3 of 0.2 mol/dm^3 CH_3COOH at 65 ºC. To this solution, aluminium nitrate dissolved in 50 cm^3 of distilled water was added and the resulting mixture was stirred for 1 h at the same temperature. For the preparation of Sr-substituted samples an appropriate amount of strontium acetate dissolved in 50 cm^3 of 0.2 mol/dm^3 CH_3COOH at 65 ºC was added and the resulting mixtures were stirred for 1 h at the same temperature. Then 1,2-ethanediol (2 cm^3) as complexing agent was added to the reaction solutions. After concentrating the solutions by a slow evaporation at 65

ºC under stirring, the Gd–Al–O or Gd(Sr)–Al–O acetate–nitrate–glycolate sols turned into white transparent gels. The oven dried (100 ºC) gel powders were ground in an agate mortar and preheated for 3 h at 800 ºC in air. Since the gels are very combustible, a slow heating rate (~ 3–4 ºC·min^{-1}), especially between 100 ºC and 400 ºC was found to be essential. After an intermediate grinding in an agate mortar, the powders were additionally sintered in air for 10 h at 800 ºC (samples VII and VIII) and at 1000 ºC (the remaining samples).

2.2. Characterization techniques

Thermal decomposition processes of the precursor gels were studied in air atmosphere by thermogravimetric and differential thermal analyses (TGA and DTA, respectively) using a Setaram TG-DSC12 apparatus at a heating rate 10 ºC·min^{-1}. The infrared spectra in the range of 4000–400 cm^{-1} were recorded on an EQUINOX 55/S/NIR FTIR spectrometer. Samples were prepared as KBr pellets. Powder X-ray diffraction measurements were performed at room temperature on a Stoe-Cie Powder Diffraction System STADI P diffractometer operating with a CuK$_\alpha$ radiation. Scanning electron microscope (SEM) DSM 962 was used to study the surface morphology and microstructure of the ceramic samples.

3. Results and discussion

3.1. Thermal analysis of precursor gels

The main requirement for the sol-gel approach is to achieve a high level of precursor homogeneity to produce a homogeneous end product – ceramic oxide material. It is well known that thermal characterization of synthesized samples is important both for the control of the reaction process and for the properties of materials obtained. In this context, thermal analysis is a versatile aid to monitor preparative studies. The mechanism of the thermal decomposition in flowing air of Gd(Sr)–Al–O precursor gels was studied by TGA/DTA measurements. The TGA/DTA profiles for the precursor gel samples I, II and III are shown in Fig. 1.

All TGA curves show a three-step decomposition of the gel precursor to form the ceramic material. The initial weight loss below 175 °C observed in all TGA curves (~5–6%, Fig. 1) is due to the evaporation of water and solvent molecules as indicated by broad endothermic peaks on the DTA curves in this region. The temperature ranges of three main weight losses (175–400 °C, 400–805 °C and 805–1000 °C) are also very similar in the synthesized gel samples. The first two and most significant decomposition steps can be attributed to the pyrolysis and combustion of organic compounds and the degradation of intermediate species formed during the gelation process. This observation is corroborated by well-resolved exotherms in the DTA curves at approxi-

mately 400–500 °C. The final weight loss (~3–4%, Fig. 1) on the TGA curves of the gel samples was observed in the temperature range of 805–1000 ºC.
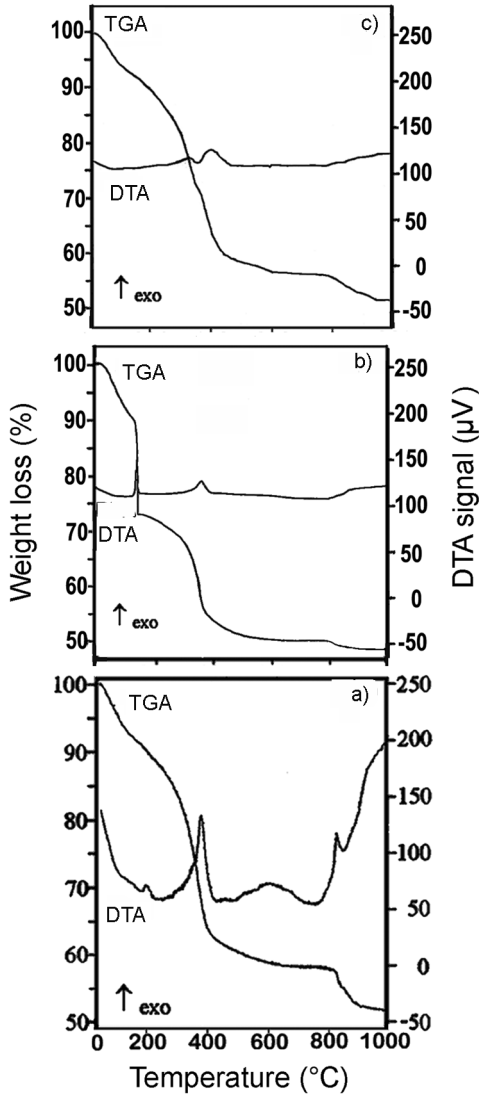
Fig. 1. TGA and DTA profiles of the Gd–Sr–Al–O precursor gels prepared using gadolinium nitrate in the sol-gel processing: a) 0% Sr, b) 10% Sr, c) 25% Sr. The heating rate was 5 ºC·min^{-1}

Furthemore, the thermal decomposition behaviour is associated with weak exothermic effects in the DTA curves. These peaks probably correspond to the decomposition and simultaneous solid-state reaction of the intermediate oxycarbonates $Gd_2O_2CO_3$ or $Al_2O_2CO_3$ to the mixed-metal oxides [3, 21, 26]. According to the thermal analysis data the crystallisation of $GdAlO_3$ ceramic oxides could vary from 800 to 1000 ºC. Therefore, the final annealing temperature of 800–1000 ºC for the preparation of GAP phase was selected.

3.2. Powder X-ray diffraction studies

The Gd(Sr)–Al–O precursor gel powders prepared using gadolinium nitrate in the sol-gel processing were calcined and sintered at 1000 ℃. The XRD patterns of the obtained GAP ceramics derived from the Gd(Sr)–Al–O precursor gels (samples I–V) are shown in Fig. 2.
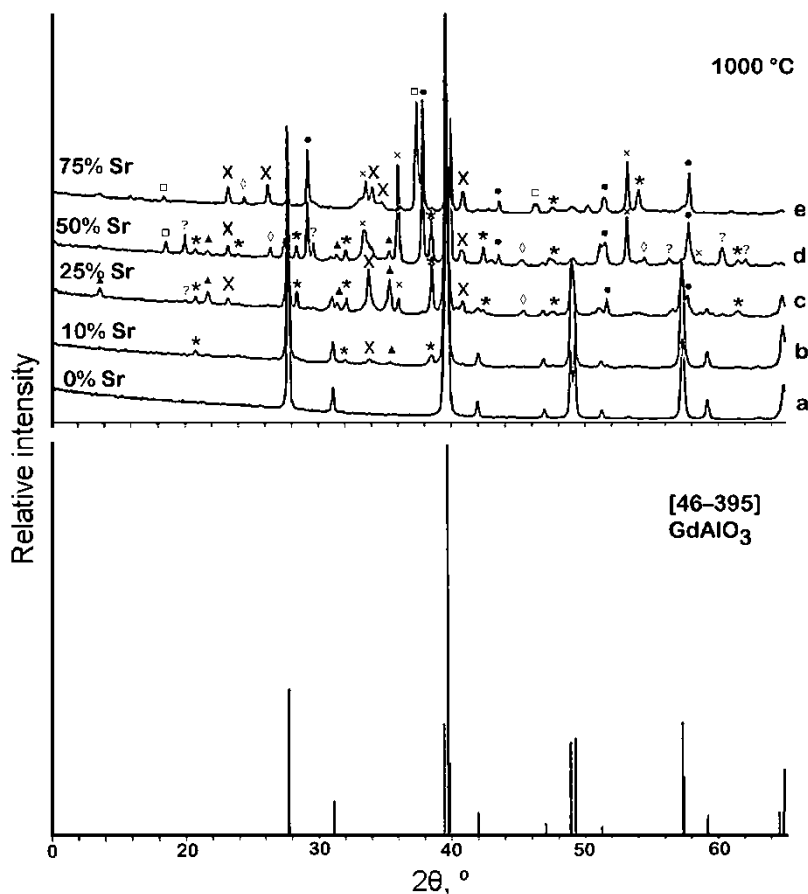
Fig. 2. X-ray diffraction patterns of: a) $GdAlO_3$, b) $Gd_{0.9}Sr_{0.1}AlO_3$, c) $Gd_{0.75}Sr_{0.25}AlO_3$, d) $Gd_{0.5}Sr_{0.5}AlO_3$, e) $Gd_{0.25}Sr_{0.75}AlO_3$ ceramics prepared using gadolinium nitrate in the sol-gel processing. Schematic presentation of the XRD pattern of $GdAlO_3$ from JCPDS is presented at the bottom. The impurity phases: $\times$ – $SrAl_4O_7$, ▲ – $Gd_4Al_2O_9$, ◊ – $Sr_4Al_2O_7$, X – $SrAl_2O_4$, * – $Gd_3Al_5O_{12}$, □ – $Sr_3Al_2O_6$, ● – $SrGdAlO_4$, ? – unidentified phases

According to the XRD analysis, fully crystallized single-phase oxide $GdAlO_3$ with well pronounced perovskite crystal structure has formed (Fig. 2a) (JCPDS file 46-395). The XRD pattern of the sample II (ceramic material with 10% of strontium) is presented in Fig. 2b. The XRD data confirm $Gd_{0.9}Sr_{0.1}AlO_{3-x}$ to be the main crystal-

line component. However the formation of certain amount of impurity phases was already detected. The diffraction lines at $2\theta \approx 22.8°$, $32.1°$ and $38.6°$ could be attributed to the $Gd_3Al_5O_{12}$ phase, at $2\theta \approx 33.8°$ to the $SrAl_2O_4$, and at $2\theta \approx 35.5°$ to the $SrGd_2O_4$. Figure 2c shows the X-ray diffraction pattern of the ceramic sample III with nominal composition of $Gd_{0.75}Sr_{0.25}AlO_{3-\delta}$. The diffraction lines assigned to the perovskite crystal structure at $2\theta \approx 27.5°$, $31.1°$, $39.2°$, $42.1°$, $46.9°$, $49.0°$, $51.3°$, $57.4°$ and $59.3°$ are well pronounced in the diffractogram. However, the intensities of diffraction lines corresponding to the impurity phases such as $Gd_4Al_2O_9$, $Gd_3Al_5O_{12}$ and $Sr_3Al_2O_6$ are much more intensive than those observed for the previous sample. On further increasing the Sr content, the formation of perovskite aluminate seems to be problematic. The impurity phases ($SrGdAlO_4$ and $SrAl_2O_4$) are already the dominating component formed during the synthesis of $Gd_{0.25}Sr_{0.75}AlO_{3-\delta}$ ceramics (Fig. 2e).
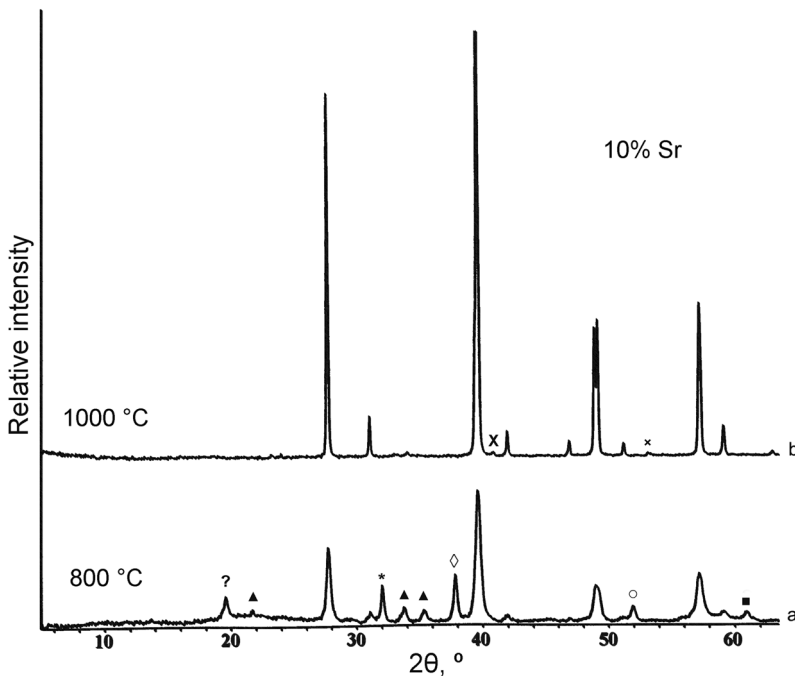
Fig. 3. X-ray diffraction patterns of $Gd_{0.9}Sr_{0.1}AlO_3$ ceramics prepared using gadolinium oxide in the sol-gel processing at various temperatures: a) 800 °C, and b) 1000 °C.
The impurity phases: $\times$ – $SrAl_4O_7$, $\blacktriangle$ – $Gd_4Al_2O_9$, $\Diamond$ – $Sr_4Al_2O_7$, X – $SrAl_2O_4$, * – $Gd_3Al_5O_{12}$,
$\circ$ – $SrGd_2O_4$, $\blacksquare$ – $GdAl_{11}O_{18}$, ? – unidentified phases

As was already mentioned, one of the goals of this study was to investigate the influence of nature of starting material used as gadolinium source on the sinterability and phase purity of the end ceramics. Again, according to the XRD analysis, the synthesized at 1000 °C non-substituted compound was a single-phase gadolinium aluminate ($GdAlO_3$). Next, the influence of sintering temperature on the quality of Sr-substituted

gadolinium aluminates was also estimated. The X-ray diffraction patterns of the $Gd_{0.9}Sr_{0.1}AlO_{3-x}$ (sample VII) ceramics prepared using gadolinium oxide in the sol-gel processing and annealed at various temperatures are shown in Fig. 3. Many different impurity phases in the X-ray diffraction pattern of the sample annealed at 800 ºC could be detected (Fig. 3a). Apparently, this temperature of synthesis is too low for the preparation of monophasic GAP. The diffraction lines assiged to the perovskite crystal structure at $2\theta \approx 27.5º$, 31.1º, 39.2º, 42.1º, 46.9º, 49.0º, 51.3º, 57.4º and 59.3º are well pronounced in the X-ray diffraction pattern of the sample annealed at higher temperature (1000 ºC, Fig. 3b).

The X–ray diffraction patterns of the $Gd_{0.75}Sr_{0.25}AlO_{3-x}$ (sample VIII) ceramics prepared using gadolinium oxide in the sol-gel processing at various temperatures are shown in Fig. 4.
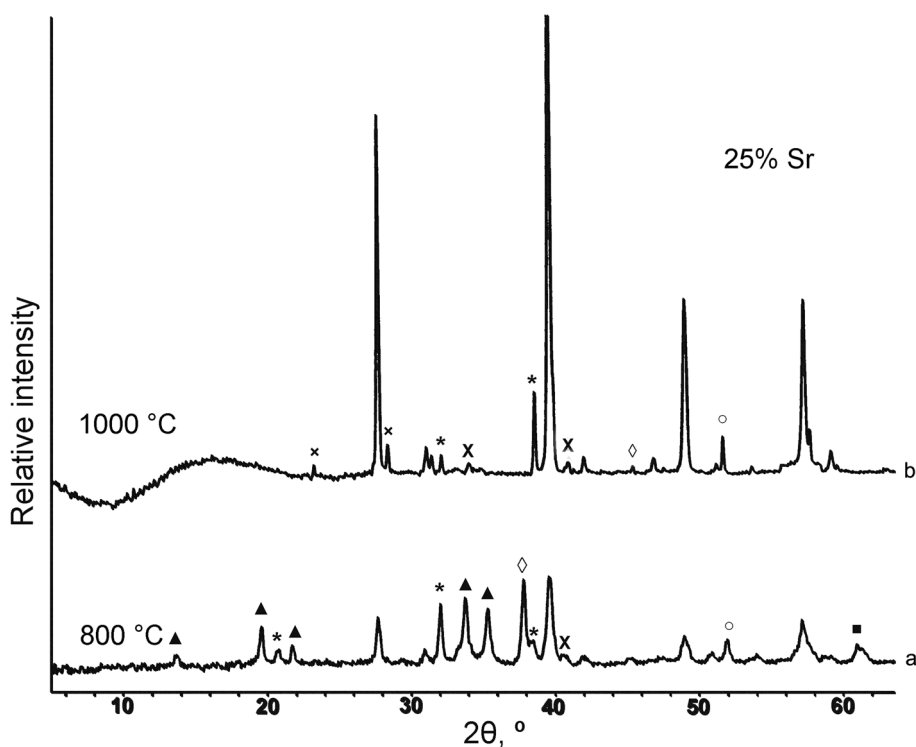

Fig. 4. X-ray diffraction patterns of $Gd_{0.75}Sr_{0.25}AlO_3$ ceramics prepared using gadolinium oxide in the sol-gel processing at various temperatures: a) 800 °C, and b) 1000 °C. The impurity phases: × – $SrAl_4O_7$, ▲ – $Gd_4Al_2O_9$, ◊ – $Sr_4Al_2O_7$, X – $SrAl_2O_4$, * – $Gd_3Al_5O_{12}$, ○ – $SrGd_2O_4$, ■ – $GdAl_{11}O_{18}$

The X-ray results confirm once again that the final annealing temperature should be higher than 800 ºC. Besides, the XRD powder pattern shows formation of broad peaks; their poor intensities suggest that a considerable amount of the material is either amorphous or nanocrystalline [22]. Moreover, with increasing the strontium concen-

tration the amount of impurity phases in the sample annealed at 1000 ºC (Fig. 4b) also increases. However, it is evident that upon using Gd_2O_3 as a starting material, the obtained GAP ceramics contain less amounts of impurities than those prepared using $Gd(NO_3)_3 \cdot 6H_2O$. We can thus conclude that for the preparation of GAP ceramics Gd_2O_3 instead of $Gd(NO_3)_3 \cdot 6H_2O$ should preferably be used as the starting material.

3.3. Infrared spectra

The results of the X-ray diffraction analysis are consistent with the crystallization process observed by the IR measurements. IR analysis of synthesized samples is important for the control of both the reaction process and of the properties of materials obtained. Figure 5 shows the IR spectra of Gd(Sr)–Al–O ceramics (samples VI–VIII) prepared by calcinations of gel precursors for 10 h at 1000 ºC.
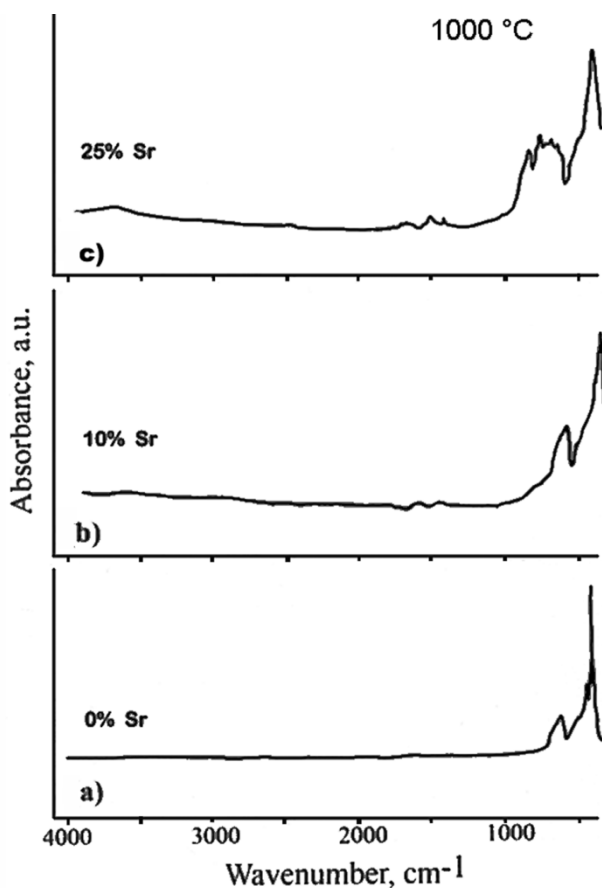
Fig. 5. Infrared spectra of: a) $GdAlO_3$, b) $Gd_{0.9}Sr_{0.1}AlO_3$, c) $Gd_{0.75}Sr_{0.25}AlO_3$
ceramics prepared at 1000 °C using gadolinium oxide in the sol-gel processing

The IR spectra of $GdAlO_3$ and $Gd_{0.9}Sr_{0.1}AlO_3$ (see Fig. 5a and b, respectively) display only two frequencies at 660 and 465 cm^{-1} which are typical of the M–O (possibly Al–O stretching frequencies) vibrations in the perovskite structure compounds [23, 24, 25]. The IR spectrum of Sr-substituted $Gd_{1-x}Sr_xAlO_{3-\delta}$ sample with 25% substitutional level of Sr, however, indicates the atomic-level reorganization. The strong bands of 660 and 465 cm^{-1} are replaced by several bands which may be assigned to stretching modes of different polyhedra in the multiphasic oxide materials. Thus, the results of IR analysis indicate as well that when Sr concentration $x \geq 0.25$, the formation of multiphase crystalline products occurs. Besides, the spectra of strontium substituted ceramic samples show the presence of new peaks in the region of 1660–1390 cm^{-1}. Moreover, their intensities increase with increasing amount of strontium in the samples. The origin of these peaks is not very clear. It is known that typical carbonate vibrations are correspond to ~1470–1390 cm^{-1} (triply degenerated stretching mode) and ~880–850 cm^{-1} (doubly degenerated stretching mode) [24]. Thus, these additional bands probably may be assigned to metal carbonates formed as intermediates during high-temperature treatments. It is well known that aluminium carbonate ($Al_2(CO_3)_3$) decomposes at relatively low temperatures (~500 ºC) [26]. Therefore, the carbonate peaks in the IR spectra of doped $Gd_{1-x}Sr_xAlO_3$ ceramic samples may correspond to strontium carbonate ($SrCO_3$) and/or gadolinium oxycarbonate ($Gd_2O_2CO_3$). Because the intensity of the 1460 cm^{-1} peak is relatively weak, it is likely that very little carbonate was formed. However, the IR spectrum of undoped $GdAlO_3$ sample calcined at 1000 °C does not feature any characteristic carbonate bands [22, 25].

3.4. SEM analysis

Figure 6 shows SEM micrographs (back scattered electron (BSE) images) of synthesized $GdAlO_3$ and $Gd_{0.75}Sr_{0.25}AlO_3$ powders using gadolinium oxide in the initial stage of preparation. As seen from Fig. 6 (left), the broad distribution of light or dark regions in the SEM micrograph of $GdAlO_3$ specimen is absent. There-
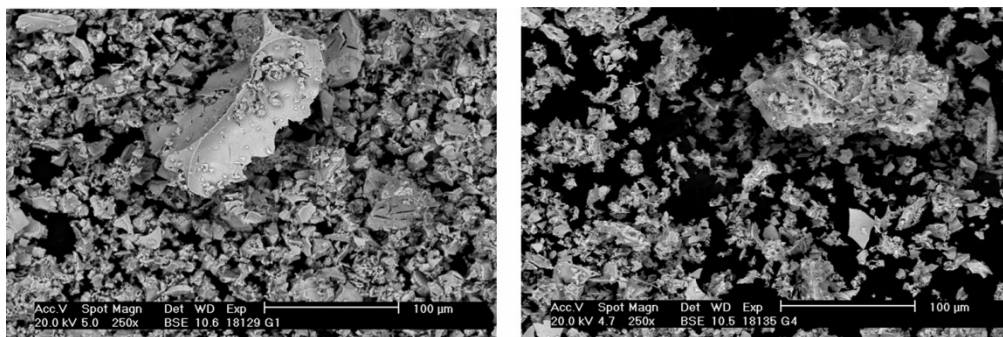

Fig. 6. Scanning electron micrographs in back scattering mode of $GdAlO_3$ (left) and $Gd_{0.75}Sr_{0.25}AlO_3$ (right) ceramics prepared using gadolinium oxide in the sol-gel processing. Magnification 250×

fore, the SEM image of the single-phase $GdAlO_3$ sample obtained using gadolinium oxide as starting material confirms that the most of the material is finely divided, i.e. the distribution of its chemical elements is highly uniform. Some individual particles seem to be plate-like crystals, most grains, however, are agglomerated having different shape and size ranging from ~5 µm to 30 µm. In the backscattered electron mode for the $Gd_{0.75}Sr_{0.25}AlO_3$ sample prepared using gadolinium oxide numerous light and dark regions are observed. Since the brightness of the specimen is highly inhomogeneous over the entire measuring area, the material is evidently composed of several phases.

4. Conclusions

Homogeneous gels in the Gd(Sr)–Al–O system were prepared by the complexation of metal ions with 1,2-ethanediol followed by a controlled hydrolysis and condensation in aqueous media. The obtained gels have been used for low-temperature synthesis of nano-scale gadolinium aluminate (GAP, $GdAlO_3$) and strontium substituted gadolinium aluminate ($Gd_{1-x}Sr_xAlO_{3-\delta}$) ceramics. The present study demonstrates the versatility of the solution method to yield a monophasic GAP sample at low sintering temperature (1000 ºC) when compared to the temperature required for the solid state synthesis (>1400–1600 °C). Furthermore, the Sr-substituted GAP ceramics (up to 25% of Sr) have also been successfully obtained by this method. In the view of the above results and the increasing importance of the nanomaterials, the nanocrystalline GAP and Sr-substituted GAP phases show a considerable application potential.

References

[1] Malinowski M., Piramidowicz R., Frukacz Z., Chadeyron G., Mahiou R., Joubert M.F., J. Opt. Mater., 12 (1999), 409.
[2] Atwood D.A., Yearwood B.C., J. Organomet. Chem., 600 (2000), 186.
[3] Chroma M., Pinkas J., Pakutinskiene I., Beganskiene A., Kareiva A., J. Ceramics Int., 31 (2005), 1123.
[4] Yada M., Ohya M., Machida M., Kijima T., J. Chem. Comm., 18 (1998), 1941.
[5] Nieminen M., Sajavaara T., Rauhala E., Putkonen M., Niinisto L., J. Mater. Chem., 11 (2001), 2340.
[6] Attfield J.P., Int. J. Inorg. Mater., 3 (2001), 1147.
[7] Tall P.D., Coupeau C., Rabier J., Scripta Mater., 49 (2003), 903.
[8] Zhydachevskii Y., Durygin A., Suchocki A., Matkovskii A., Sugak D., Loutts G.B., Nogikov M.A., J. Lumin., 109 (2004), 39.

[9] RETUERTO M., ALONSO J.A., MARTINEZ-LOPE M.J., MENENDEZ N., TORNERO J., GARCIA-HERNANDEZ M., J. Mater. Chem., 16 (2006), 865.

[10] ZVEREVA I., SMIRNOV Y., GUSAROV V., POPOVA V., CHOISNET J., J. Solid State Sci., 5 (2003), 343.

[11] LIU Y., XU C.N., J. Phys. Chem. B, 107 (2003), 3991.

[12] AITASALO T., HOLSA J., JUNGNER H., LASTUSAARI M., NIITYKOSKI J., J. Lumin., 94 (2001), 59.

[13] WANG D., YIN Q.R., LI Y.X., WANG M.Q., J. Lumin., 97 (2002), 1.

[14] SÀNCHEZ-BENÍTEZ J., DE ANDRÉS A., MARCHAL M., CORDONCILLO E., VALLET REGI M., ESCRIBANO P., J. Solid State Chem., 171 (2003), 273.

[15] AITASALO T., HOLSA J., LASTUSAARI M., LEGENDZIEWICZ J., NIITTYKOSKI J., J. Radiat. Eff. Def. Solids, 158 (2003), 89.

[16] BOSAK A.A., SAMOILENKOV S.V., GORBENKO O.YU., BOTEV A.N., KAUL A.R., Int. J. Inorg. Mater., 3 (2001), 1097.

[17] LIVAGE J., HENRY M., SANCHEZ C., J. Solid State Chem., 18 (1988), 259.

[18] BRINKER C.J., SCHERRER G.W., *Sol-Gel Science: The Physics and Chemistry of Sol-Gel Processing*, Academic Press, New York, 1990.

[19] SANCHEZ C., SOLER-ILLIA G.J.D.A.A., RIBOT F., GROSSO D., J. C. R. Chimie, 6 (2003), 1131.

[20] CUSHING B.L., KOLESNICHENKO V.L., O'CONNOR C.J., Chem. Rev., 104 (2004), 3893.

[21] LELECKAITE A., KAREIVA A., BETTENTRUP H., JÜSTEL T., MEYER H.-J., Z. Anorg. Allg. Chem., 631 (2005), 2987.

[22] LIU Y., ZHANG Z.F., KING B., HALLORAN J., LAINE R.M., J. Am. Ceram. Soc., 79 (1996), 385.

[23] SCHRADER B., *Infrared and Raman Spectroscopy. Methods and Applications*, VCH, Weinheim, 1995.

[24] NAKAMOTO K., *Infrared and Raman Spectra of Inorganic and Coordination Compounds*, Wiley, New York, 1986.

[25] VAQUEIRO P., LOPEZ-QUITELA M.A., J. Mater. Chem., 8 (1998), 161.

[26] LELECKAITE A., KAREIVA A., J. Opt. Mater., 26 (2004), 123.

Novel sol-gel derived films for luminescence-based oxygen and pH sensing

D. Wencel[*], C. Higgins, A. Klukowska, B. D. MacCraith, C. McDonagh

Optical Sensors Laboratory, National Centre for Sensor Research,
Dublin City University, Glasnevin, Dublin 9, Ireland

A range of both sol-gel and polymer derived sensor films have been developed for optical oxygen and pH sensing. Oxygen sensing is based on the luminescence quenching of the ruthenium complex [Ru(II)-tris(4,7-diphenyl-1,10-phenanthroline)]dichloride, ($[Ru(dpp)_3]^{2+}$), which is entrapped in the sol-gel matrix. The oxygen-dependent luminescence is detected using the principle of phase fluorometry, which facilitates indirect monitoring of the luminescence lifetime. The pH sensor uses excitation ratiometric detection of the fluorescence from the pH sensitive dye, 1-hydroxypyrene-3,6,8-trisulfonic acid, ion-paired with cetyl trimethyl ammonium bromide (HPTS_IP). The phase-based detection scheme, dual lifetime referencing (DLR), was also examined as an alternative sensing strategy. ORMOSIL oxygen sensor films were fabricated using a range of organosilicon precursors including methyltriethoxysilane (MTEOS), ethyltriethoxysilane (ETEOS), *n*-propyltriethoxysilane (PTEOS) and phenyltriethoxysilane (PhTEOS). In addition to optimising the sensor performance, issues such as the influence of humidity on oxygen sensing were addressed. By varying the processing parameters, the surface characteristics and microstructure were tailored to suit applications such as breath gas analysis and bioprocess monitoring. pH sensor films were prepared by hydrolyzing and co-condensing (3-aminopropyl) trimethoxysilane (APTMS) with an organosilicon monomer such as ETEOS or PTEOS or the polymer, ethyl cellulose (EC). Optimised pH sensors showed good reproducibility, reversibility and short response times. The dynamic range for these sensor films extends from pH 6.00 to 8.50 which is relevant for bioprocess monitoring applications. The spectral compatibility of the luminophores and the printability of the sol-gels present the possibility of simultaneous oxygen and pH sensing using low-cost LEDs as excitation sources along with common detection electronics.

Key words: *sol-gel; ORMOSIL; optical pH sensor; optical oxygen sensor; luminescence sensor*

1. Introduction

Luminescence-based chemical sensors have been extensively researched in recent years due to their importance in industrial, environmental, and biomedical applications [1]. These sensors combine the intrinsic sensitivity of the luminescence process with a wide availability of optoelectronic components, thereby enabling the design of a broad range of sensor configurations.

---

[*]Corresponding author, e-mail: Dorota.wencel2@mail.dcu.ie

Oxygen and pH are the two most important parameters in the area of continuous bioprocess monitoring [2]. Luminescence-based optical sensors for these analytes offer many advantages over conventional electrochemical sensors, as they do not suffer from electrical interference, are highly sensitive and easy to miniaturise [1]. The use of the sol-gel process when fabricating such sensors facilitates the tailoring of the structure, configuration and composition of the sensor films, thus providing a stable, transparent and permeable host matrix for the encapsulation of diverse reagents. This high degree of versatility makes sol-gel materials a more attractive alternative to organic polymers [3, 4]. In addition, the sol-gel process is compatible with a wide variety of thin film deposition techniques, for example dip-coating and spin-coating, as well as a range of printing techniques such as stamp, ink-jet and pin-printing [5–7]. Organically modified silicates (ORMOSILs) are a class of sol-gel materials that show great potential for the development of chemical sensors. In these materials, the functional group R is bound to silicon via a Si–C bond, ie., $R_{4-x}Si(OR')_x$, which is non-hydrolyzable. Through the correct choice of R, it is possible to impart specific properties such as polarity, flexibility, and porosity to the matrix [8-10].

In this paper, we report on a series of luminophore-doped ORMOSIL films, tailored for the optical detection of oxygen and pH. Oxygen sensor materials are doped with the oxygen-sensitive ruthenium complex tris(4,7-diphenyl-1,10-phenanthroline)ruthenium (II), ($[Ru(dpp)_3]^{2+}$). The pH sensor is based on a derivative of 1-hydroxypyrene-3,6,8-trisulfonic acid (HPTS), which is ion-paired with cetyl trimethyl ammonium bromide (HPTS_IP) and entrapped in a suitable matrix. Phase fluorometry and a referenced dual excitation scheme are used as detection methods for oxygen and pH sensing, respectively. These methods are insensitive to probe leaching, photobleaching, and instabilities in the light source or photodetector [11, 12].

2. Background

2.1. Oxygen sensing

The oxygen sensor described here exploits the well-known effect of oxygen quenching on the excited-state lifetime of the sol-gel-encapsulated, oxygen-sensitive luminophore $[Ru(dpp)_3]^{2+}$ [11, 13]. $[Ru(dpp)_3]^{2+}$ was selected as it has a high quantum yield, long luminescence lifetime (~5 µs) and can be excited using an inexpensive blue LED. The quenching process is described by the Stern–Volmer equation [11]:

$$\frac{I_0}{I} = \frac{\tau_0}{\tau} = 1 + K_{SV}[O_2] = 1 + k_q\tau_0[O_2] \tag{1}$$

where I and τ are the luminescence intensity and decay time of the luminophore, respectively, and the subscript 0 denotes the absence of oxygen; K_{SV} is the Stern–Volmer constant which represents sensor sensitivity; $[O_2]$ is the concentration of oxygen; and

k_q is the bimolecular quenching constant, which incorporates the oxygen diffusion coefficient for the matrix. For homogeneous environments, the dependence of I_0/I or τ_0/τ upon $[O_2]$ yields a linear plot with a slope equal to K_{SV} and an intercept of unity. In the case of luminophores entrapped in a solid matrix, these plots deviate from the Stern–Volmer equation and become non-linear [14–16]. This behaviour is associated with the distribution of the luminophore in the solid matrix, where the embedded luminescent species encounters different environmental influences. The host microheterogeneity causes luminophore populations in different sites to be quenched differently with a resultant downward curve in the Stern–Volmer plot.

2.2. pH sensing

HPTS is a widely known pH-sensitive dye, with pKa around 7.30 that has been extensively used for fluorescence-based pH and carbon dioxide detection [17–21]. The pH-dependent absorption and emission spectra of HPTS are shown in Fig. 1.
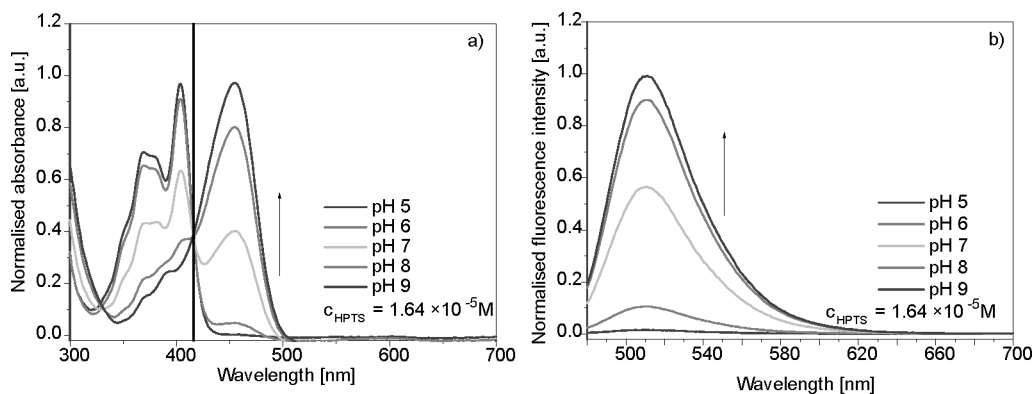

Fig. 1. Normalised absorption spectra (a) and fluorescence spectra ($\lambda_{exc} = 470$ nm) (b) of HPTS in 0.15 M phosphate buffers at various pH values
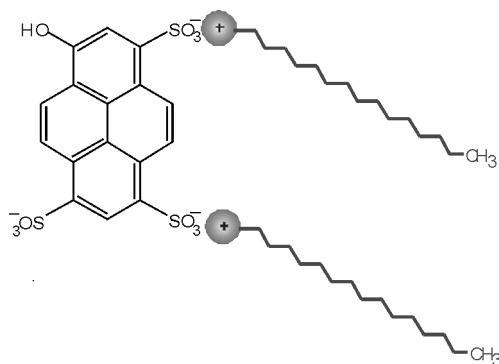

Fig. 2. Chemical structure of HPTS_IP

HPTS exhibits two absorption maxima, one at 404 nm corresponding to its acidic form, the other at 455 nm corresponding to its basic form. The emission spectra show one maximum at 510 nm. Therefore, HPTS can be used for single emission and dual excitation measurements. The excitation intensity ratio, R, defined as the emission intensity with 455 nm (blue) excitation divided by the emission intensity with 405 nm (UV) excitation ($I_{455\ nm}/I_{405\ nm}$), is related to pH [12].

In this report, we describe an optical pH sensor with a physically entrapped HPTS derivative, HPTS_IP (Fig. 2), in a variety of sol-gel and polymer matrices. HPTS_IP is more hydrophobic than HPTS and displays poor water solubility. By using such a dye, one can expect minimised leaching and improved sensor film stability. It exhibits the same pH-dependent absorption and emission maxima as the unmodified HPTS indicator.

3. Experimental

Chemical reagents. The following chemicals were purchased from Sigma Aldrich Chemicals (Ireland): tetraethoxysilane (TEOS), methyltriethoxysilane (MTEOS), ethyltriethoxysilane (ETEOS), *n*-propyltriethoxysilane (PTEOS), phenyltriethoxysilane (PhTEOS), ethyl cellulose (EC), absolute ethanol (EtOH), hydrochloric acid (HCl), HPTS, cetyl trimethyl ammonium bromide (CTAB), ruthenium (III) chloride (RuCl$_3$) and the (4,7-diphenyl-1,10-phenanthroline) ligand. (3-aminopropyl)trime-
thoxysilane (APTMS) and 1-methylimidazole (MI) was purchased from Fluka (Ireland). [Ru(dpp)$_3$]$^{2+}$was synthesised as described in the literature [22]. Glass slides were purchased from AGB Scientific Ltd.

Phosphate buffer solutions of defined pH were prepared from analytical grade potassium salts of hydrogen phosphate and dihydrogen phosphate (total concentration of phosphate 0.15 M) (Sigma Aldrich Chemicals, Ireland). Aqueous solutions were prepared from deionised (DI) water. All chemicals were used as received.

Sensor film fabrication. Oxygen sensor xerogels were prepared using the organosilicon precursors, MTEOS, ETEOS, PTEOS and PhTEOS. Sols were prepared by acid-catalyzed hydrolysis and condensation of these precursors. In a typical preparation, the precursor was combined with absolute ethanol (EtOH), followed by a dropwise addition of aqueous HCl at pH 1. The mixture was then stirred for 20 min. An ethanolic solution of [Ru(dpp)$_3$]$^{2+}$ was subsequently added to the sol to give a final dye concentration of 2.5 g/l with respect to the total volume of the solution. The final mixture was stirred under ambient conditions and aged for various times depending on the precursor used. The final molar ratio of silane:EtOH:water:HCl was 1:6.25:4:0.007.

In order to fabricate pH sensor films, an APTMS-derived sol was prepared by base catalysis using MI. All other aspects of APTMS sol preparation were as described above.

APTMS/ETEOS and APTMS/PTEOS composite sols were prepared by mixing the APTMS sol with the relevant precursor sol to form compositions that contained 0.1, 0.3, 0.5, 0.7 and 1 mol of APTMS. The HPTS_IP doped solutions were fabricated by mixing an ethanolic solution of the pH sensitive dye with the prepared sols to give a final silane/dye ratio of 10^{-3}. EC solutions were prepared by dissolving 5 g of the polymer in 100 ml of EtOH. The polymer-based solution was combined with the APTMS sol in a 50/50 molar ratio. Films derived from just EC were also prepared for the purpose of comparison.

All films were formed by dip-coating using a dip-speed of 3 mm·s^{-1} in a controlled environment using a computer-controlled dipping apparatus. The glass slides were treated with 30% HNO_3 for 24 h and then rinsed with copious amount of DI water and EtOH. After deposition, pH sensor films were cured at 140 ºC for 4 h. For the purpose of comparison, solutions of standard HPTS were also prepared and tested.

Instrumentation. The principles of phase fluorometry and the experimental system used to examine the performance of the oxygen sensors have been published previously [23, 24]. Briefly, the characterisation system consists of a blue LED (Nichia, NSPE590), which is modulated at the frequency of 20 kHz and provides excitation of the luminescent sensors. A silicon photodiode (Radionics 194-290) was used for the detection of the oxygen-sensitive luminescent signal. In order to examine their performance, oxygen sensor films were placed in a flow cell into which controlled mixtures of oxygen and nitrogen were flowed using mass flow controllers (Celerity, Ireland).

The pH fluorescence measurements were acquired using a FluoroMax-2 fluorometer (Jobin Yvon, USA). All spectra were recorded in a quartz cuvette fixed at 45º with respect to the incident beam. Films on the glass slides were immersed in phosphate buffer solutions adjusted to pH values ranging from 4.00 to 10.00. The fluorometer collected the emission intensity at 515 nm, employing excitation wavelengths of 405 nm and 455 nm. 2 nm passbands were used for both the excitation and emission monochromators. The pH values were verified with a commercial pH meter (Orion Benchtop 420 A+, USA.). All measurements were performed at room temperature.

Frequency domain dual lifetime referenced (DLR) measurements were performed using a dual phase lock-in amplifier (DSP 7225 Perkin Elmer Instruments, USA). This provided sinusoidal modulation of the LED and phase-shift detection of the photodiode output signal.Contact angle measurements were made using an FTA-200 contact angle analyzer (First Ten Angstroms, USA) by imaging a droplet of water that was dispensed onto the surface being characterised. The captured images were then analysed using dedicated software. The oxygen diffusion coefficient within the films was determined as a means to establish the origin of the observed oxygen sensitivity. This was achieved, as reported previously, by measuring the response time, t_{90}, for films of known thickness [25]. Diffusion coefficients were then recovered from the response time data via the Schappacher–Hartmann protocol [26]. Film thickness measurements were obtained using a white light interferometer (WYKO NT1100 Optical Profiling System, Veeco, USA).

4. Results and discussion

4.1. Oxygen sensor films with enhanced sensitivity

All oxygen sensor films exhibit excellent repeatability, reversibility, and fast response times (less than 1 s). An example of an ETEOS-derived oxygen sensor response is shown in Fig. 3.
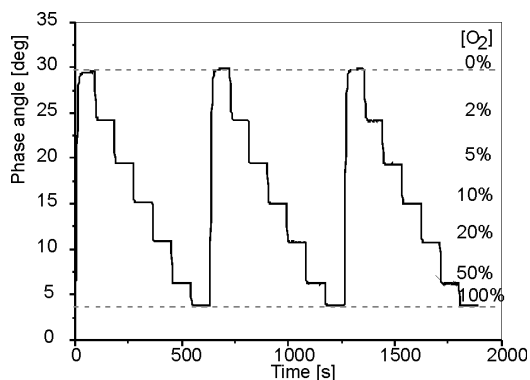
Fig. 3. Phase response for an ETEOS-derived film, doped with $[Ru(dpp)_3]^{2+}$

A linear Stern–Volmer plot indicates that the entrapped luminophore population reports from a homogeneous microenvironment. Strictly linear Stern–Volmer behaviour seems to be an exception as most solid oxygen sensors give non-linear curves, as discussed before. Various models have been developed and used to describe such responses [14–16]. In this study, the Stern–Volmer plots were analyzed using two models: the single-site Stern–Volmer model (Eq. (1)) and the two-site Demas model (Eq. (2)):

$$\frac{I_0}{I} = \frac{\tau_0}{\tau} = \left[\frac{f_1}{1 + K_{SV1}\ pO_2} + \frac{f_2}{1 + K_{SV2}\ pO_2} \right]^{-1} \tag{2}$$

where f_1 and f_2 denote fractional distribution of the total emission from the luminophore located at different sites, 1 and 2, respectively. K_{SV1} and K_{SV2} are the Stern–Volmer quenching constant for these sites.

The model is based on the assumption that the luminophore is distributed in the solid matrix at two different sites and that each fraction has a different quenching constant. Sensors were stored for 4 weeks in the dark prior to experiments, the results of which are shown in Fig. 4.

The fit to the Demas model was excellent for all films ($r^2 = 0.999$). Moreover, Stern–Volmer plots for ETEOS-, PTEOS- and PhTEOS-derived sensor platforms were also quite well described by Eq. (1) ($r^2_{ETEOS} = 0.985$, $r^2_{PTEOS} = 0.981$, $r^2_{PhTEOS} = 0.989$). This would allow a simple two-point calibration of these sensors if desired.
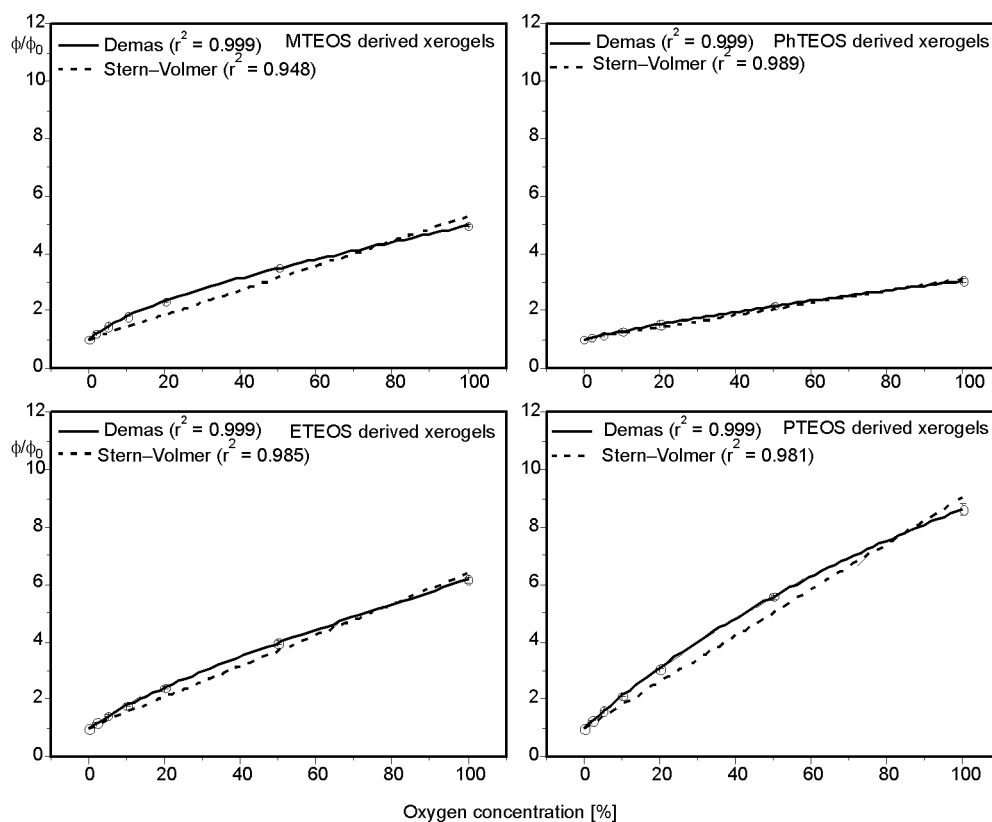
Fig. 4. Best fit to the Stern–Volmer and Demas models for various ORMOSIL oxygen sensor films

All sensors exhibit different sensitivities, as indicated by their respective K_{SV} values (Table 1). PTEOS-based films display the greatest sensitivity, with ETEOS, MTEOS, PhTEOS decreasing in oxygen sensitivity in that order. PhTEOS-derived films are the least sensitive due to the steric effect of the phenyl group. It has been demonstrated previously that films with increased hydrophobicity exhibit higher oxygen sensitivity, both in gas and dissolved phase [27]. Table 1 shows that there is a good correlation between K_{SV} and both the measured diffusion coefficients (*D*) and water contact angles (*CA*).

Table 1. Properties of ORMOSIL sensor films

Film	K_{SV} ($[O_2]^{-1}$)	*CA* [deg]	*D* [$cm^2 \cdot s^{-1}$]
PhTEOS	0.0212 ± 0.0007	93 ± 1	3.0×10^{-9}
MTEOS	0.0429 ± 0.0029	90 ± 1	9.9×10^{-7}
ETEOS	0.0540 ± 0.0020	97 ± 2	6.2×10^{-6}
PTEOS	0.0806 ± 0.0034	100 ± 1	6.7×10^{-6}

Clearly, the most hydrophobic films are PTEOS- and ETEOS-based xerogels with water contact angles of $100^o \pm 1^o$ and $97^o \pm 2^o$, respectively. High water contact angle measurements show that these coatings have a hydrophobic surface and are highly water-repellent. As such, these coatings are less prone to humidity interference than for example, MTEOS-based coatings. Figure 5 shows calibration curves for MTEOS- and ETEOS-derived oxygen sensor films recorded using dry and humidified gases. Figure 5b clearly demonstrates the humidity insensitivity of ETEOS-based oxygen sensors.

The parameters CA, D, and K_{SV} in Table 1 increase as the alkyl chain length increases. The sensitivity of PTEOS-derived films is twice that of MTEOS-based films. We can attribute the enhanced sensitivity to the increase of oxygen transport within the ETEOS- and PTEOS-derived oxygen films, as evidenced by the diffusion coefficients recorded for these films. The extension of this work will involve a study of the decay times of $[Ru(dpp)_3]^{2+}$ in these films. This, coupled with the diffusion coefficient data, will help to further elucidate the origins of film sensitivity, as K_{SV} depends not only on k_q but also on τ_0.
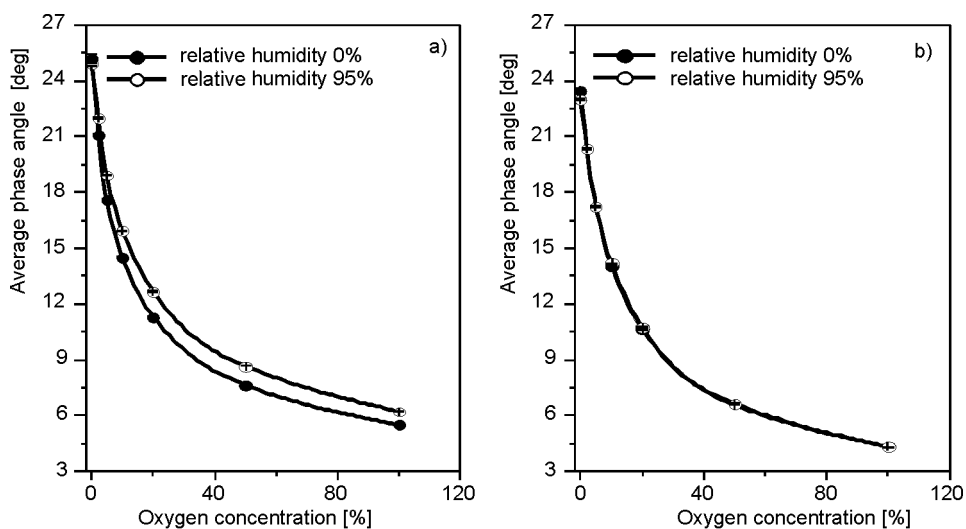

Fig. 5. Humidity interference for MTEOS- and ETEOS-derived films (error bars are within the symbols)

The ETEOS- and PTEOS-derived oxygen-sensitive films reported here are suitable for industrial and medical applications such as bioprocess management or breath monitoring, where the key sensor characteristics are: enhanced oxygen sensitivity and insensitivity to humidity.

4.2. Characterisation of the pH sensor

4.2.1. Dual excitation pH sensor

A range of sol-gel and polymer matrices were prepared in the course of this study. Both single (APTMS, ETEOS, PTEOS, EC) and binary systems (APTMS/ETEOS, APTMS/PTEOS and EC/APTMS) were prepared as described in section 3.3 and doped with HPTS_IP. Films were cured at 140 ºC. This high curing temperature was necessary, as pH sensor films for bioprocess monitoring should be autoclavable, usually at 121 ºC. Curing them at a temperature higher than that used during sterilisation minimises any structural changes of the sol-gel material. An important aspect of this work was to develop a sol-gel host matrix formulation that would give a satisfactory pH response after curing at 140 ºC.

Single and EC-based systems did not yield promising results. APTMS-, EC- and APTMS/EC-based films showed good sensitivity but poor adhesion and a high degree of leaching. In addition, the matrix became optically opaque after one pH cycle. ETEOS- and PTEOS-derived matrices display poor ion permeability as they are very hydrophobic, making them ill-suited to this application.

Binary systems represent a much better alternative, the most promising results being achieved by using a formulation comprising APTMS and PTEOS in a 50/50 molar ratio (formulation AP). Such sensors demonstrated good sensitivity and short response time after curing at 140 ºC. This is thought to be due to increased porosity and better accessibility of the dye in the material when compared to APTMS/ETEOS systems.

The excitation and emission spectra of the AP xerogel in a pH 7.00 buffer solution are shown in Fig. 6. The same spectra for HPTS in solution are also shown for comparison. As the dyes are closely related, the spectra are almost identical, the most notable difference being the fact that the excitation maxima of HPTS-IP, entrapped in the sol-gel film, are slightly red-shifted.
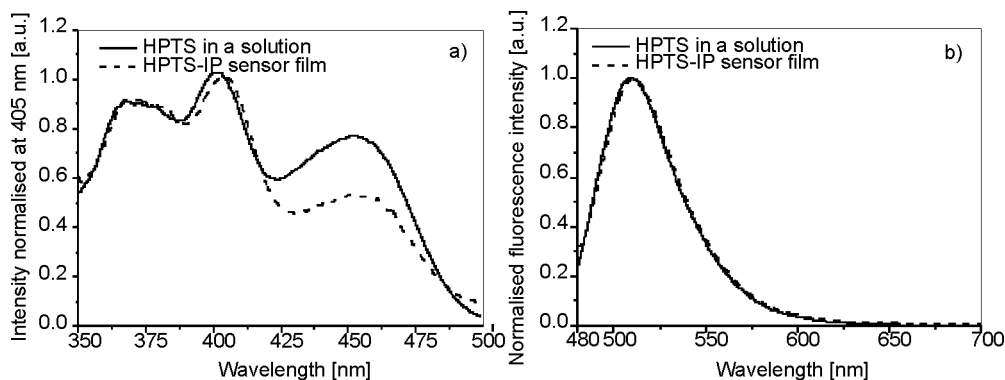
Fig. 6. Normalised excitation spectra (λ_{em} = 515 nm) (a) and emission spectra (λ_{exc} = 470 nm) (b) of 1.64×10^{-5} M HPTS solution and HPTS_IP based AP sensor xerogel in 0.15 M phosphate buffer at pH 7.00

The pH-dependent excitation spectra of the AP xerogel, normalised to intensity at 405 nm, are shown in Fig. 7. The calibration plot for this sensor film is shown in Fig. 8.
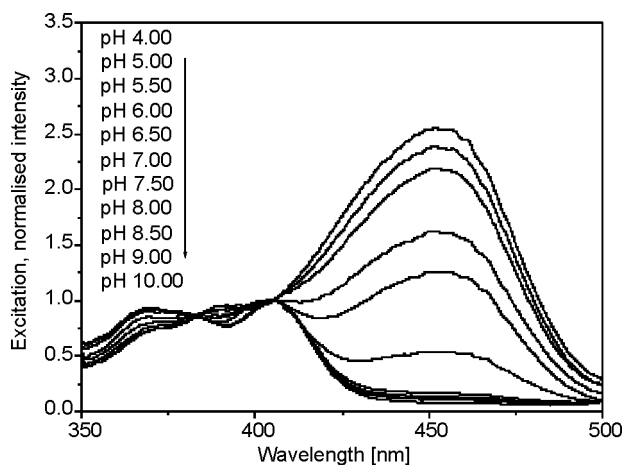
Fig. 7. Normalised excitation spectra (λ_{em} = 515 nm)
of the AP sensor film at various pHs
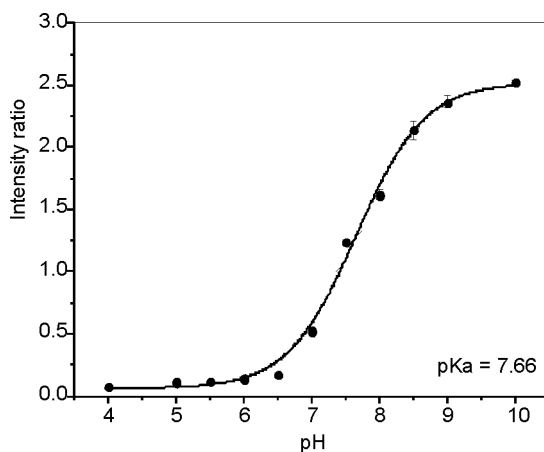
Fig. 8. Calibration plot of the AP sensor film;
intensity ratios at λ_{exc}= 455 nm /λ_{exc} = 405 nm

The calculated pK_a of the entrapped dye is 7.66, which is slightly higher than that for HPTS in solution (pK_a = 7.38). This indicates an apparent reduction in pH within the matrix. The sensor dynamic range extends from approximately pH 6.00 to 8.50 which is suitable for bioprocess monitoring applications [28, 29].

The sensor response is reversible and displays negligible drift, as shown in Fig. 9. The response time for a 90% change was approximately 2.5 min from pH 6.00 to 8.00

and about 3.3 min from pH 8.00 to 6.00. The response time could be further improved by fabricating thinner films (i.e., by using a slower dip-coating speed).
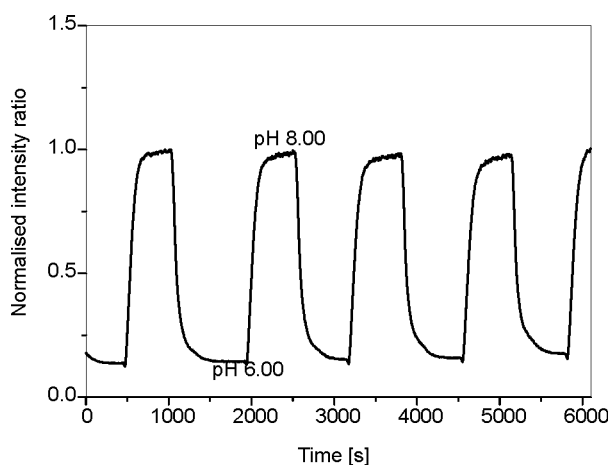
Fig. 9. Reversibility of the AP sensor film;
intensity ratios at $\lambda_{exc}= 455$ nm $/\lambda_{exc} = 405$ nm

For leaching studies, AP sensor films were soaked in pH 5.00 buffer solutions for a period of 2 weeks. With the exception of the first 24 h, during which 19% of the loosely incorporated dye leached out, no significant leaching was observed over the 2 week period, as verified using UV-Vis absorption studies. In contrast, single OR-MOSIL compositions showed much higher degrees of leaching within shorter periods of time. The improved stability may be attributed to the functional groups incorporated into the sol-gel film.

Future work will involve investigation of sensor sensitivity to ionic strength, temperature, and the ability of the sensor to withstand steam sterilization.

4.2.2. DLR optical pH sensor

The principle of DLR involves the use of two luminophores (an indicator and a reference) with different decay times and similar spectral properties, to obtain a referenced, phase-based measurement of an analyte. This is described in detail elsewhere [30, 31]. In this study, the short-lived pH sensitive fluorophore, HPTS-IP, was combined with the long-lived standard, $[Ru(dpp)_3]^2$ in a sol-gel matrix.

Figure 10 displays the pH-dependent phase shifts of TEOS-derived films cured at 70 ºC and 140 ºC for 24 h, which were fabricated as described for acid-catalysed sols. The dynamic range of the film cured at 140 ºC was about 1.5 times lower than of the film cured at 70 ºC. This is due to the fact that curing at higher temperatures produces a denser oxide network and the encapsulated pH dye is therefore less accessible to protons.
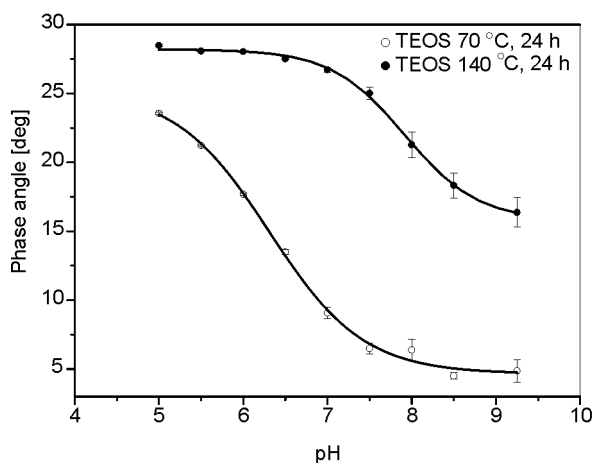
Fig. 10. Calibration plot of TEOS-based pH sensor films
measured using the DLR technique

The aim of this study was to investigate the compatibility of the pH sensor with both detection techniques: dual excitation and DLR. The DLR technique is advantageous over the dual excitation technique as it requires a single LED excitation source.

5. Conclusions

Phase fluorometric ORMOSIL oxygen sensor films, doped with $[Ru(dpp)_3]^{2+}$ exhibit enhanced oxygen sensitivity. The sensitivity was correlated with the alkyl chain length of the organosilicon precursor, with the highest sensitivity being achieved for PTEOS -derived sensor films. The variation in sensitivity arises from different values of k_q in each xerogel. In this way, one can tune the sensitivity of the sensor to suit the application.

pH sensor films were based on entrapped HPTS_IP in a sol-gel matrix. HPTS_IP has the same spectral characteristics as HPTS, allowing dual excitation detection and having sensitivity in the physiological pH range, which makes such a sensor a potential candidate for use in bioprocess management. The sensor films displayed a reversible response, short response times (2.5 min) and a dynamic range extending from pH 6.00 to 8.50. The use of a lipophilic dye, which minimized leaching from the host matrix, resulted in stable pH sensor films. This sensor is also compatible with the DLR sensing technique, its advantage being the ability to provide a referenced sensor output, using a single excitation source.

Optical sensing systems for oxygen and pH sensing have been presented, which have potential for multianalyte platform measurements using inexpensive, commercially available LEDs as excitation sources and a simple detection system. These sensors have potential applications in bioprocess monitoring. In addition, the developed oxygen sensor films are compatible with breath gas analysis for human health monitoring.

References

[1] WOLFBEIS O.S., *Fiber Optic Chemical Sensors and Biosensors*, Vol. 1, CRC, Boca Raton, 1991.
[2] KOSTOV Y., HARMS P., RANDERS-EICHHORN L., RAO G., Biotech. Bioeng., 72 (2001), 346.
[3] AVNIR D., Acc. Chem. Res., 28 (1995), 328.
[4] COLLINSON M.M., HOWELLS A .R., Anal. Chem., 72 (2000), 702A
[5] BRINKER J., SCHERER G.W., *Sol-Gel Science: The Physics and Chemistry of Sol-Gel Processing*, Academic Press, New York, 1990.
[6] CARTER C.J., ALVIS R.M., BROWN S.B., LANGRY K.C., WILSON T.S., MCBRIDE M.T., MYRICK M.L., COX W.R., GROVE M.E., COLSTON B.W., Bios. Bioelec., 21 (2006), 1359.
[7] CHO E.J., BRIGHT F.V., Anal. Chim. Acta, 470 (2002), 101.
[8] LEV O., TSIONSKY M., RABINOVICH L., GLEZER V., SAMPATH S., PANKRATOV I., GUN J., Anal. Chem., 67 (1995), 22A.
[9] COLLINSON M.M., Microchim. Acta, 129 (1998), 145.
[10] LAVIN P., MCDONAGH C.M., MACCRAITH B.D., J. Sol-Gel Tech., 13 (1998), 641.
[11] LAKOWICZ J.R., *Principles of Fluorescence Spectroscopy*, Kluwer Academic Plenum Publishers, New York, 1999.
[12] VALEUR B., *Molecular Fluorescence. Principles and Applications*, VCH Wiley, Weinheim, 2002.
[13] TRETTNAK W., *Optical sensors based on fluorescence quenching*, [in:] *Fluorescence Spectroscopy. New Methods and Applications*, O.S. Wolfbeis (Ed.), Springer Verlag, Berlin, 1992, p. 79.
[14] BACON J.R., DEMAS J.N., Anal. Chem., 59 (1987), 2780.
[15] CARRAWAY E.R., DEMAS J.N., DEGRAFF B.A., BACON J.R., Anal. Chem., 63 (1991), 337.
[16] XU W., MCDONOUGH R.C., LANGSDORF B., DEMAS J.N., DEGRAFF B.A., Anal. Chem., 66 (1994), 4133.
[17] WOLFBEIS O.S., FURLINGER E., KRONEIS H., MARSONER H., Fresenius Z. Anal. Chem., 314 (1983), 119.
[18] SCHULMAN S.G., CHEN S., BAI F., LEINER M.J.P., WEIS L., WOLFBEIS O.S., Anal. Chim. Acta, 304 (1995), 165.
[19] ZHANG S., TANAKA S., WICKRAMASINGHE Y.A.B.D., ROLFE P., Med. Biol. Eng. Comp., 33 (1995), 152.
[20] WOLFBEIS O.S., KOVACS B., GOSWAMI K., KLAINER S.M., Mikrochim. Acta 129 (1998), 181.
[21] MILLS A., CHANG Q., Analyst, 118 (1993), 839.
[22] WATTS R.J., CROSBY G.A., J. Am. Chem. Soc., 93 (1971), 3184.
[23] MCDONAGH C., KOLLE C., MCEVOY A.K., DOWLING D.L., CAFOLLA A.A., CULLENA S.J., MACCRAITH B.D., Sens. Act. B, 74 (2001), 124.
[24] WENCEL D., HIGGINS C., GUCKIAN A., MCDONAGH C., MACCRAITH B.D., Proc SPIE, 5826 (Dublin), (2005), 696.
[25] MCDONAGH C., BOWE P., MONGEY K., MACCRAITH B.D., J. Non-Cryst. Solids, 306 (2002), 138.
[26] SCHAPPACHER G., HARTMANN P., Anal. Chem., 75 (2003), 4319.
[27] MCDONAGH C., MACCRAITH B.D., MCEVOY A.K., Anal. Chem., 70 (1998), 45.
[28] KERMIS H.R., KOSTOV P., HARAS Y., RAO G., Biotechnol. Prog., 18 (2002), 1047.
[29] KERMIS H.R., KOSTOV Y., RAO G., Analyst, 128 (2003), 1181.
[30] VON BÜLTZINGSLÖWEN C., MCEVOY A.K., MCDONAGH C., MACCRAITH B.D., KLIMANT I., KRAUSE C., WOLFBEIS O.S., Analyst, 127 (2002), 1478.
[31] HUBER C., KLIMANT I., KRAUSE C., WOLFBEIS O.S., Anal. Chem., 73 (2001), 2097.

Determination of the lead titanate zirconate phase diagram by the measurements of the internal friction and Young's modulus

R. Zachariasz[*], A. Zarycka, J. Ilczuk

University of Silesia, Faculty of Computer Science and Materials Science,
Department of Materials Science, ul. Żeromskiego 3, 41-200 Sosnowiec, Poland

The paper presents investigations of the phase transitions for undoped PZT ceramics obtained by the conventional ceramic sintering from amorphous nanopowders prepared by the sol-gel method, with various compositions and Zr/Ti ratios. The phase transitions are also studied by electric conductivity (σ) measurements as a function of the temperature. The values of σ, till the point of phase transition (T_C), are low and are in the range of 10^{-7}–10^{-3} $\Omega^{-1} \cdot m^{-1}$. In the paraelectric phase (above T_C) the values of σ as a function of the Zr/Ti ratio are in the range of 5×10^{-3}–3×10^{-1} $\Omega^{-1} \cdot m^{-1}$. Phase transitions, identified by Young's modulus anomalies and internal friction peaks are in accordance with those found by electric conductivity studies and correspond to the transition point between cubic paraelectric phase and tetragonal or rhombohedral ferroelectric phase. The values of Young's modulus at room temperature are in the range of 80–140 GPa, and their rapid growth in the phase transition point is observed.

Key words: *sol-gel method; Young's modulus; internal friction; PZT phase diagram; electric conductivity*

1. Introduction

Lead titanate zirconate $Pb(Zr_xTi_{1-x})O_3$ (PZT) ceramics are among the most common piezoelectric materials in industry: they are used as transducers between electrical and mechanical energy, such as phonograph pickups, air transducers, underwater sound and ultrasonic generators, delay-line transducers, wave filters, piezoelectric micromotors, microrobots, actuators, etc. [1, 2]. All those applications need rather high piezoelectric constants and low dielectric and mechanical losses in the ceramics. The study of temperature dependences of internal friction Q^{-1}, and elastic moduli E of the materials can provide extensive information about the physics of the processes occurring within the materials, for example about the energy dissipation and phase

---

[*]Corresponding author, e-mail: rzachari@us.edu.pl

transitions. The investigations conducted for many years have shown that mechanical losses Q^{-1} and changes of Young's modulus E in the PZT are not only associated with domain walls motion but also with interaction of point defects with the domain walls [3–5]. The ratio Zr/Ti in $Pb(Zr_{1-x}Ti_x)O_3$, the method of the obtaining the materials, the sintering temperature and atmosphere are the controlling factors to obtain good PZT ceramics for the application. Therefore, variety of controlling factors and wide applications of the PZT materials are the base to continuous research of these materials.

This paper presents the investigations of the phase transitions in undoped PZT ceramics with various compositions, prepared by conventional ceramics sintering (CCS) with the following Zr/Ti ratio: $Pb(Zr_{0.75}Ti_{0.25})O_3$, $Pb(Zr_{0.65}Ti_{0.35})O_3$ (ferroelectric rhombohedral phase), $Pb(Zr_{0.48}Ti_{0.52})O_3$, $Pb(Zr_{0.47}Ti_{0.53})O_3$, $Pb(Zr_{0.46}Ti_{0.54})O_3$ (morphotropic area), $Pb(Zr_{0.35}Ti_{0.65})O_3$, $Pb(Zr_{0.25}Ti_{0.75})O_3$ (ferroelectric tetragonal phase). The preparation procedure, measurements of Young's modulus E, mechanical losses Q^{-1} and electric conductivity σ, till the point of phase transition (T_C) will be presented as well.

2. Experimental

The technological process of the production of PZT ceramics consists of two basic stages. In the first stage, amorphous nanopowders of solid solution $Pb(Zr_{1-x}Ti_x)O_3$ are prepared by the sol-gel method, whereas the second one consists in consolidation of nanopowders and preparation of fine-grained PZT ceramics by the conventional ceramic sintering (CCS). The preparation procedure of amorphous nanopowders is described in our previous publication [6]. The powder obtained after disintegrating the annealed pallets was mixed with liquid paraffin and it was finally used for preparation of the ceramic samples [3]. Ceramic bodies were produced by conventional ceramics sintering (CCS) [7]. After that, samples in rectangular bars ($80 \times 10 \times 1$ mm^3) were obtained. The average grain size for obtained samples was about 3.0 μm. The samples were annealed at $T = 1523$ K for $t = 4$ h and next were polished. Electrodes on their surface were deposited by the silver paste burning method.

The temperature dependences of the $Q^{-1}(T)$, $f_r(T)$ and $\sigma(T)$ were determined upon heating at the constant rate of 3 K·min^{-1}. The values of Young's modulus E were calculated from the measurements of resonance vibration frequency f_r of the sample, conducted simultaneously with the mechanical losses (internal friction Q^{-1}) measurements, using the dependence:

$$E = 94.68 \left(\frac{l_r}{h} \right)^3 \frac{m_d}{b} f_r^2 \tag{1}$$

where: l_r, h, b and m_d are: the length, thickness, width and mass of vibratile part of the sample, respectively.

3. Results and discussion

Figure 1 shows the variations of mechanical losses Q^{-1} and Young's modulus E as a function of the temperature for the PZT75/25 and PZT65/35 samples. Young's modulus shows three anomalies M_R, M_{RR} and M_F. The anomaly M_R corresponds to the peaks P_R on the mechanical losses (internal friction) curves, both for the ceramics with Zr/Ti 75/25 and 65/35. Based on investigations conducted so far, it is known that the P_R peak has a relaxation nature and it is connected with influence of the domain walls and point defects (oxygen vacancies) located in the ceramic structure [8, 9]. Minimum M_F on the $E(T)$ dependences correlates with P_F maximum on the $Q^{-1}(T)$ curves. In the case of the PZT 75/25 ceramics, the temperature of the M_F and P_F occurrence is T_F = 590 K, whereas for the composition PZT65/35 can be as high as T_F = 609 K. With reference to PZT phase diagram (Fig. 7) it appears that the T_F temperature determined for both chemical compositions is consistent with the temperature of the phase transition from ferroelectric rhomboedral phase to paraelectric regular phase [10–12]. Additionally, for the ceramics with the Zr/Ti = 75/25 composition, appearance of the M_{RR} minimum on the $E(T)$ dependence, correlating with P_{RR} maximum on the $Q^{-1}(T)$ curve was observed. Based on the analysis of the phase diagram it was shown that the M_{RR} minimum is connected with the phase transition from ferroelectric low temperature rhomboedral phase $F_{R(LT)}$ to ferroelectric high temperature rhomboedral $F_{R(HT)}$ phase.
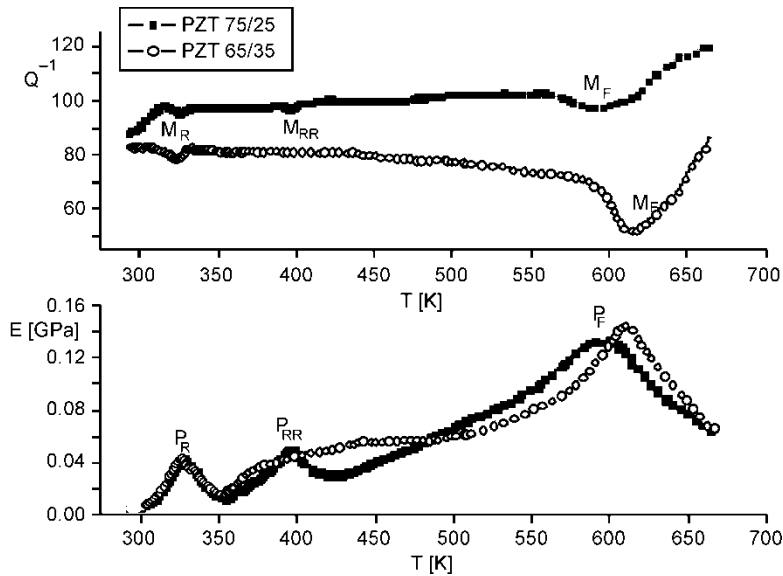
Fig. 1. Temperature dependences of the internal friction $Q^{-1}(T)$ and Young's modulus $E(T)$ obtained for PZT ceramic samples from ferroelectric rhombohedral phase

In order to confirm the determined values of the temperatures of phase transition T_F for the examined samples, temperature dependences of electric conductivity σ in

ferroelectric and paraelectric phases ($\ln\sigma = f(1/T)$) have been determined (Fig. 2). The changes of slope of rectilinear parts on the dependences were observed. This phenomena took place near the point of ferroelectric to paraelectric (T_F) phase transition, as well as for both phases for the investigated samples. For the PZT75/25 ceramics $T_F = 592$ K, whereas for samples PZT65/35 $T_F = 610$ K have been determined. It is evident that the values of temperatures determined correlate with the results obtained on the basis of the measurements of internal friction Q^{-1} and Young's modulus E.
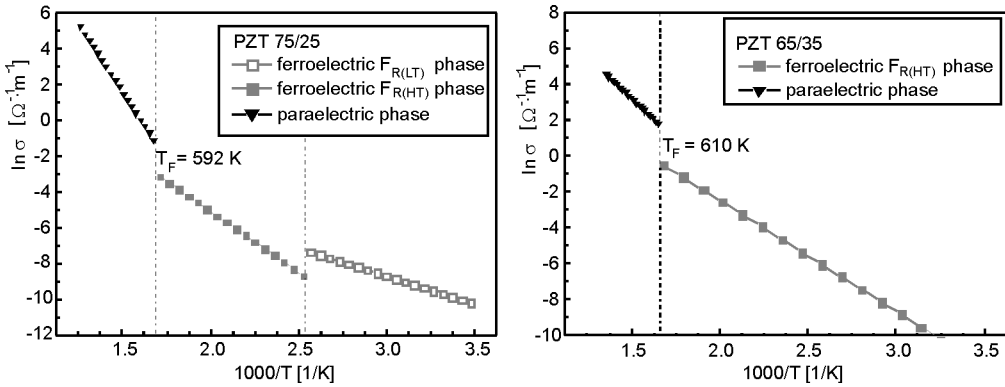
Fig. 2. Temperature dependences $\ln\sigma = f(1/T)$ obtained for the PZT ceramic samples from the ferroelectric rhombohedral phase
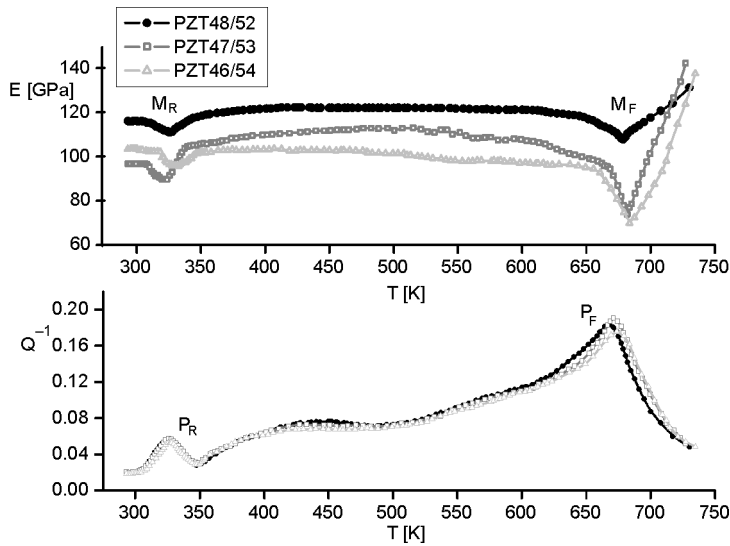

Fig. 3. Temperature dependences of the internal friction $Q^{-1}(T)$ and Young's modulus $E(T)$ obtained for the PZT ceramic samples from the morphotropic area

Then internal friction, Young's modulus and electric conductivity at various temperatures were measured for the ceramic samples from the morphotropic area (Fig. 7), i.e.: $Pb(Zr_{0.48}Ti_{0.52})O_3$, $Pb(Zr_{0.47}Ti_{0.53})O_3$, $Pb(Zr_{0.46}Ti_{0.54})O_3$. The analysis of the dependences obtained was made (Figs. 3, 4). The occurrence of the relaxation maximum P_R on the $Q^{-1}(T)$ dependences correlating with the M_R minimum on the $E(T)$ curves, was proved again. The temperatures of the phase transitions determined on the basis of the analysis of the $E(T)$ and $Q^{-1}(T)$ dependences were: for the PZT48/52 samples – T_F = 668 K, for the PZT47/53 ceramics – T_F = 671 K and for the PZT46/54 – T_F = 673 K. The values of these temperatures correspond to the temperatures determined from the analysis of $\ln\sigma = f(1/T)$ dependences (fig. 4) and they amount to: 668 K for Zr/Ti = 48/52, 670 K for Zr/Ti = 47/53 and 673 K for Zr/Ti = 46/54.
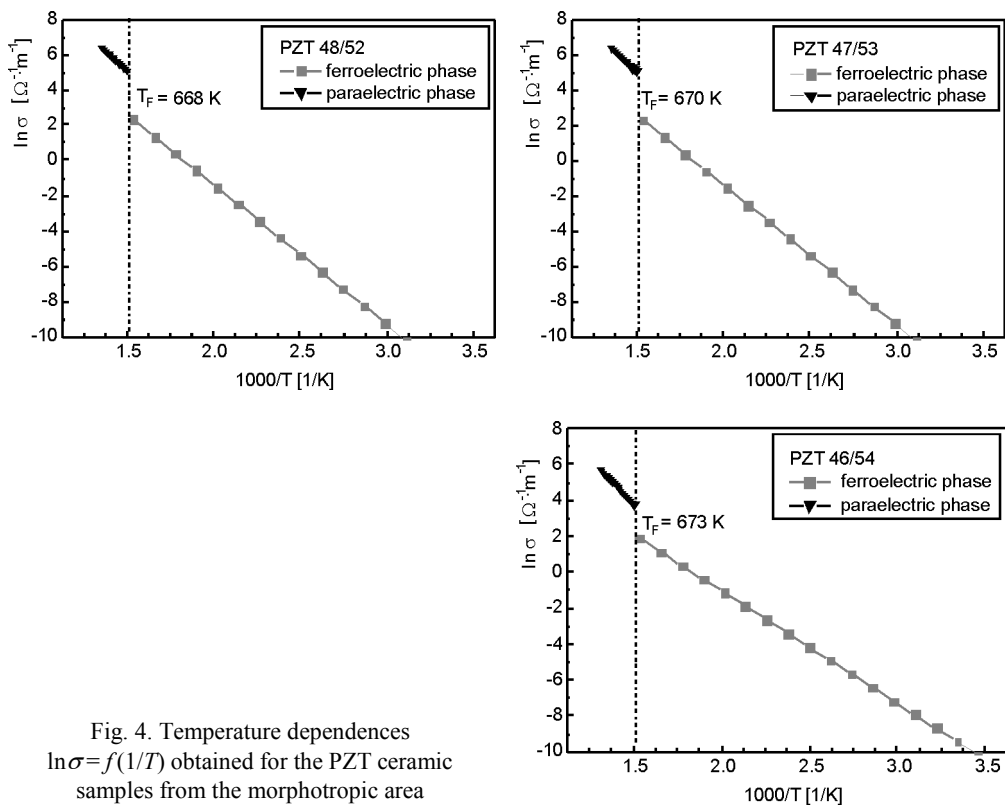
Fig. 4. Temperature dependences $\ln\sigma = f(1/T)$ obtained for the PZT ceramic samples from the morphotropic area

In the next stage of the investigations, the characteristics of the PZT35/65 and PZT25/75 ceramic samples with the ferroelectric tetragonal phase have been made. The temperature dependences $Q^{-1}(T)$ and $E(T)$ for the samples are presented in Fig. 5. As in the previous measurements, presence of two characteristic minima on the $E(T)$ curves was confirmed: M_R correlating with the P_R maximum, corresponds to relaxation phenomena, taking place in the structure of the ceramics examined and minimum M_F correlating with the P_F maximum, corresponds to the transition between ferroelec-

tric and paraelectric phases. The determined temperatures T_F for both compositions are shown in the PZT phase diagram (Fig. 7). Their values confirm the origin of the P_F maximum from phase transition (PZT35/65 – T_F = 681 K, PZT25/75 – T_F = 695 K). The $\ln\sigma = f(1/T)$ dependences (Fig. 6) and thence the temperatures T_F point out clearly to the phase transition (682 K for Zr/Ti = 35/65, 696 K for Zr/Ti = 25/75).
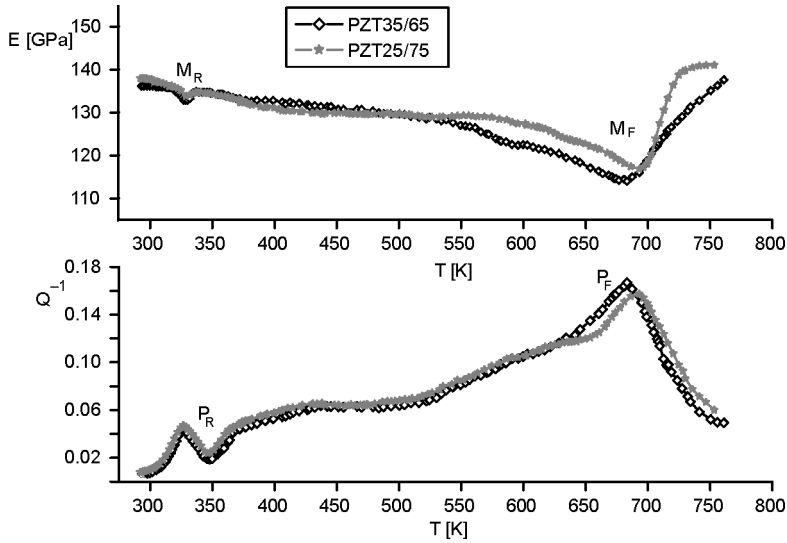

Fig. 5. Temperature dependences of the internal friction $Q^{-1}(T)$ and Young's modulus $E(T)$ obtained for the PZT ceramic samples from the ferroelectric tetragonal phase
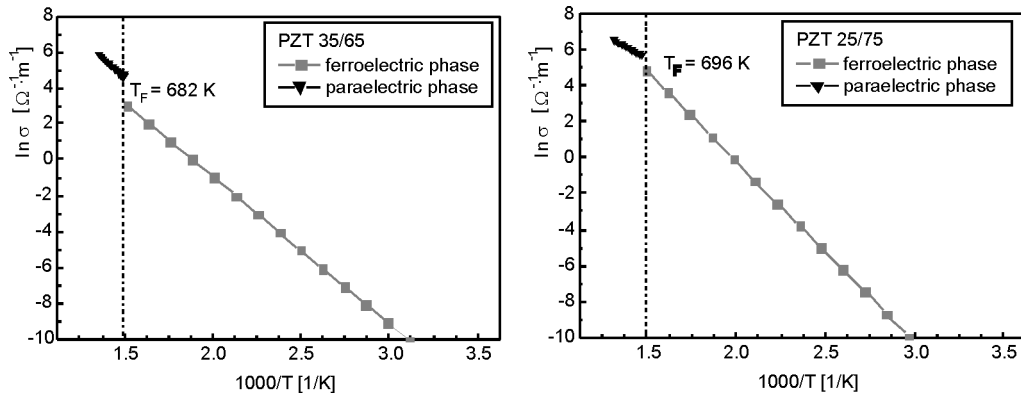
Fig. 6. Temperature dependences $\ln\sigma = f(1/T)$ obtained for the PZT ceramic samples from the ferroelectric tetragonal phase

Analysis of the temperature dependences of the Young's modulus $E(T)$ performed for all examined samples, confirm that the room-temperature values of the Young modulus increase with increasing $PbTiO_3$ concentration. This is caused mainly by the

growth of ferroelectric hardness and size of the grains along with the growth of the PbTiO$_3$ concentration.
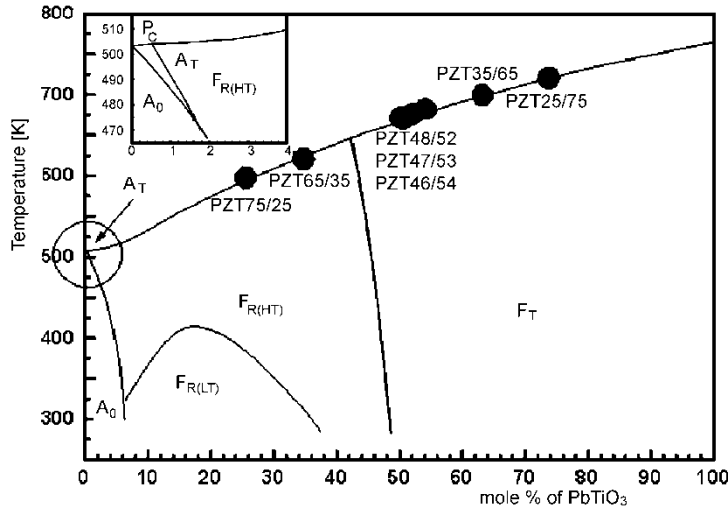
Fig. 7. PZT ceramics phase diagram: A$_0$ – antiferroelectric ortorhombic phase (*Pba*2), F$_{R(LT)}$ – ferroelectric rhomboedral phase (*R3c*), F$_{R(LT)}$ – ferroelectric rhomboedral phase (*R3m*), F$_T$ – ferroelectric tetragonal phase (*P4mm*), P$_C$ – paraelectric regular phase (*Pm3m*) [1]

It results in generating additional stresses on the boundaries of grains, their values being directly proportional to the *E* value (Eq. (2)). The determined values of Young's moduli at room temperature for various ratios of Zr/Ti are given in Table 1.

Table 1. The values of Young's modulus *E*
at room temperature for various Zr/Ti ratios

Zr/Ti ratio	E [GPa]
75/25	87
65/35	85
48/52	103
47/53	100
46/54	110
35/65	135
25/75	139

A decrease in the *E* values until they achieve a minimum at the phase transition and then, a rapid increase to infinity is a characteristic phenomenon observed on the *E*(*T*) curves (Figs. 1, 3, 5). At the point of transition, ferroelectric phase with tetragonal or rhomboedral structure undergoes a change to the paraelectric regular phase. This results in movement of deformity of lattice (*c*/*a* – 1) to zero, according to equation [13]:

$$3\delta = \left(\frac{c}{a} - 1\right)E \tag{2}$$

where: δ is a mechanical stress in the sample, c, a – the lattice constants, E – the value of Young's modulus.

4. Conclusions

A good compatibility was found between the results of the phase transition temperatures obtained from the measurement of internal friction, Young's modulus and electric conductivity on the PZT phase diagram, as shown in Fig. 7. The temperatures obtained of the ferroelectric ↔ paraelectric phase transition for the ceramic samples from the sol-gel powders are from 7 to 10 K higher than for the same chemical compositions obtained from oxides. The main cause of it is the size of grains in the structure of PZT materials. For the ceramics obtained from oxides the average size of grains amounts to about 10 μm, whereas for studied ceramics about 3.0 μm. In the case of larger grains, the structure is less stable, and a larger quantity of structural defects and strains appear. In such ceramic materials it is easier to cause changes of the structure by the action of external factors as for example temperature. The observed ferroelectric ↔ paraelectric phase transition is one of such changes.

The values of the electric conductivity up to the point of phase transition (T_C), are low being in the range of 10^{-7}–10^{-3} $\Omega^{-1}\cdot m^{-1}$. Such low values of σ show that dielectric losses are low, what is advantageous from the practical point of view. In the paraelectric phase (above T_C) the values of σ are in the range of 5×10^{-3}–3×10^{-1} $\Omega^{-1}\cdot m^{-1}$ being a function of the Zr/Ti ratio. This is connected with mobility of domain structure and their disappearance above T_C and with high values of dielectric loss in the vicinity of the phase transition.

The ceramics obtained from the sol-gel powders may work at a higher range of temperatures, which is very advantageous from the point of view of their practical use in converters. To sum up it should be emphasized that the measurement of Young's modulus provides a suitable method to determine the phase transitions in ceramics.

References

[1] Jaffe B., Cook W.R. Jr., Jaffe H., *Piezoelectric Ceramics*, Academic Press, London, 1971.
[2] Bourim E.M., Tanaka H., Gabbay M., Fantozzi G., Jpn. J. Appl. Phys., 39 (2000), 5542.
[3] Surowiak Z., Kuprianov M.F., Czekaj D., J. Eur. Ceram. Soc., 17 (2001), 1377.
[4] Wang C., Fang Q.F., Shi Y., Zhu Z.G., Mater. Res. Bull., 36 (2001), 2657.
[5] Soares M.R., Senos A.M.R., Mantas P.Q., J. Eur. Ceram. Soc., 20 (2000), 321.

[6] ZARYCKA A., ZACHARIASZ R., ILCZUK J., CHROBAK A., Mater. Sci.-Poland, 23 (2005), 159.

[7] ZARYCKA A., ZACHARIASZ R., BRUŚ B., ILCZUK J., Mol. Quant. Ac., 24 (2003), 255.

[8] ZACHARIASZ R., ILCZUK J., Mol. Quant. Ac., 23 (2002), 443.

[9] BRUŚ B., ZACHARIASZ R., ILCZUK J., Phys. Stat. Sol. (a), 201 (2004), 798.

[10] NOHEDA B., GONZALO J.A., CROSS L.E., GUO R., PARK S.E., COX D.E., Phys. Rev. B, 61 (2000), 8687.

[11] RAGINI R.R., MISHRA S.K., PANDEY D., J. Appl. Phys., 92 (2002), 3266.

[12] ZACHARIASZ R., BRUŚ B., BLUSZCZ J., ILCZUK J., Mol. Quant. Ac., 24 (2003), 249.

[13] BOURIM M., TANAKA H., CHEVALIER J., GABBAY M., FANTOZZI G., Proc. 6th Japan Int. SAMPE, 1 (1999), 187.

The sol-gel synthesis of
barium strontium titanate ceramics

B. WODECKA-DUŚ[1], A. LISIŃSKA-CZEKAJ[1*], T. ORKISZ[1],
M. ADAMCZYK[2], K. OSIŃSKA[1], L. KOZIELSKI[1], D. CZEKAJ[1]

[1]University of Silesia, Department of Materials Science, ul. Śnieżna 2, 41-200 Sosnowiec, Poland

[2]University of Silesia, Institute of Physics, ul. Uniwersytecka 4, 40-007 Katowice, Poland

The sol-gel derived powders of the chemical composition $(Ba_{0.6}Sr_{0.4})TiO_3$ (BST) were used in the preparation of ceramic samples. Barium acetate, strontium acetate and tetra-butyl titanate were used as starting materials. The free sintering method was used for the final densification of ceramics. The ceramic samples were characterized in terms of their crystalline structure (X-ray diffraction), microstructure (scanning electron microscopy), chemical composition (energy dispersive spectroscopy), and dielectric properties.

Key words: $(Ba_{0.6}Sr_{0.4})TiO_3$; perovskite; ferroelectric ceramics; sol-gel method; X-ray studies; electric permittivity

1. Introduction

Among various ferroelectrics, oxides crystallizing in the perovskite structure are of particular importance [1, 2]. The perovskite structure is a relatively simple crystal structure that has the ABO_3 stoichiometry. Typically, the A-site cation is large (e.g., rare earth cation), and is coordinated by 12 anions in the lattice. The B-site cation is typically smaller – frequently it is a transition metal, being six-coordinated, forming BO_6 octahedral. It is usually through distortions of such octahedral that deviations from perfect cubic symmetry occur.

Perovskites are known to exhibit a lot of useful properties [3]. Thanks to their high dielectric coefficients over a wide temperature and frequency range, they are used as dielectrics in integrated or surface mounted device capacitors. The remarkable piezoelectric effect is applied in a variety of electromechanical sensors, actuators and transducers [4]. Infrared sensors need a high pyroelectric coefficient which is available with

---

*Corresponding author, e-mail: czekaj@us.edu.pl

this class of materials [5]. Tunable thermistor properties in semiconducting ferroelectrics are used in positive temperature coefficient resistors (PTCR) [6]. Significant non-linearities in mechanical behaviour, field tunable permittivity and refractive indices, and electrostrictive effects open up a broad field of various further applications. In addition, there is a growing interest in ferroelectric materials for memory applications as ferroelectric dynamic random access memories (FEDRAMs), where the direction of spontaneous polarization is used to store information digitally or as replacement for SiO_2/Si_3N_4 dielectrics as the storage medium in conventional DRAMs [7, 8], etc.

ABO_3 oxides are very interesting because there are two cation sites which, upon substituting with lower valence cations, lead to a much wider range of possible oxygen ion conducting materials. A number of perovskite oxides are purely ionic conductors and, as such, have been used as solid electrolytes in devices such as solid oxide fuel cells (SOFCs). Of the perovskites investigated to date, lanthanum gallate ($LaGaO_3$)-based materials have been found to be suitable for ionic applications [9]. Apart from oxide ion conduction, there are also materials of the perovskite structure conducting protons, such as barium cerate ($BaCeO_3$), barium zirconate ($BaZrO_3$), and related [10, 11]. It is conceivable that a perovskite-based proton conducting SOFC could be an attractive competitor to the leading oxide ion conducting systems [12].

Barium strontium titanate $Ba_{1-x}Sr_xTiO_3$ (BST) which is known to adopt the ABO_3-type structure, is a continuous solid solution of $BaTiO_3$ (BTO) and $SrTiO_3$ (STO) over the whole concentration range. The properties of $Ba_{1-x}Sr_xTiO_3$ are known to depend dramatically on the composition x [13, 14]. Significant material modifications have to be introduced to transform pure components, such as BTO and STO, into formulae that have a suitable temperature coefficient of the electric permittivity. Partial substitution of either Ba ions or Ti ions in pure $BaTiO_3$ is often employed to modify the nature and temperature of the paraelectric-ferroelectric transition for a particular application. $SrTiO_3$ is usually added as a shifter in order to move the Curie point T_C to lower temperatures. It is well established that T_C of barium titanate decreases linearly with the amount of Sr^{2+} in place of Ba^{2+}. For bulk $Ba_{1-x}Sr_xTiO_3$ ceramics, the Curie point varies from 120 ºC to –240 ºC, whereas the relative electric permittivity (measured at room temperature and electric field of frequency $\nu = 1kHz$) decreases from ε' ~2000 to ε' ~300 for x from $x = 0.0$ to $x = 1.0$. As a result, the transition temperature, and hence the electrical and optical properties of $Ba_{1-x}Sr_xTiO_3$, can be tailored over a broad range to meet the requirements of various electronic applications. The nonlinearity of its dielectric properties with respect to applied DC voltage makes it attractive for tunable microwave devices such as filters, varactors, delay lines, and phase shifters. The tunable ferroelectric devices offer the advantage of broad tuning range compared to ferrites, reduced resistive losses compared to p-n junction varactor diodes, reciprocity, and fast switching times [15].

It is worth noting that BST bulk ceramics are mainly obtained by the conventional mixed oxide method (solid state reaction) [13, 14, 16], whereas the sol-gel method is rather rarely used for ceramics fabrication. Therefore, the goal of the present study

was to apply the sol-gel method for preparation of BST powders and utilize the sol-gel derived ceramic powders for sintering bulk ceramic materials with the Ba/Sr ratio of 60/40 (BST60/40). The obtained BST ceramics were characterized in terms of the crystalline structure, microstructure, chemical composition, and dielectric properties within the temperature region of the ferroelectric-paraelectric phase transition.

2. Experimental

Ceramic samples of the chemical composition $BaO_{0.6}Sr_{0.4}TiO_3$ were prepared by the free sintering method from the sol-gel derived powders. The sol-gel process used is shown schematically in Fig. 1.
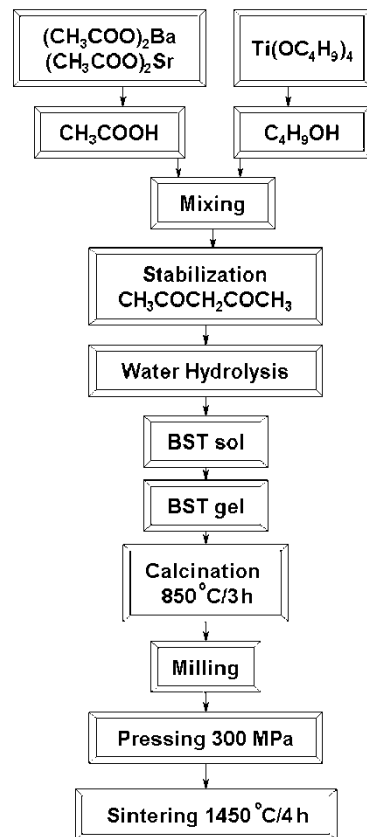
Fig. 1. Flow diagram of the synthesis
of BST60/40 powders by the sol-gel method

The starting materials were barium acetate ($Ba(CH_3COO)_2$, 99%), strontium acetate ($Sr(CH_3COO)_2$, 99%), and tetra-butyl titanate ($Ti(OC_4H_9)_4$, 97%). Glacial acetic acid (CH_3COOH, 99.9%) and butyl alcohol (C_4H_9OH, 99.9%) were used as solvents. The barium acetate and strontium acetate were dissolved in acetic acid and refluxed at 100 °C

for 0.5 h. Tetra-butyl titanate was mixed in butyl alcohol. After cooling down to room temperature, the Ba–Sr solution was mixed with Ti solution with a magnetic blender for 0.5 h. Small amounts of acetyloacetone ($CH_3COCH_2COCH_3$) were added as a stabilizer, followed by hydrolysis. The sol was relatively stable and gelated in a few days. Dry gel was calcinated at 850 °C for 3 h.

The dry gel was analyzed by the thermogravimetric analysis (TGA) and by differential thermal analysis (DTA). Simultaneous measurements were performed in air with a derivatograph of Q-1500D type (Paulik–Paulik–Erdey system). The BST powder was milled and die-pressed into 2 mm thick disks of the diameter of 10 mm under 300 MPa. The samples were sintered at 1350 ºC and at 1450 ºC for 4 h. The heating rate K for each firing was 3 ºC/min which has been reported to be slow enough to produce high density ceramics with small phase transition broadening [17].

The crystal structure was determined with an X-ray diffractometer (XRD, Philips PW 3710, $CoK_{\alpha 1\alpha 2}$ radiation). Microstructure was studied with a scanning electron microscope (SEM, Philips XL 30, ESEM/TMP, "Centaurus" BSE detector). The stoichiometry of BST ceramics was investigated using the chemical composition analysis system (EDS). All characterizations were carried out at room temperature.

For electrical measurements, the end surface electrodes were prepared using conducting silver paste. The dielectric properties were determined with the impedance analyzer HP41192A within the frequency range 100 Hz–1 MHz. Temperature dependence of the real (ε') and imaginary (ε'') part of electric permittivity was measured within the temperature range from –100 ºC to 100 ºC.

3. Results and discussion

The X-ray diffraction profiles of BST60/40 ceramic powders (Fig. 2) represent the influence of thermal treatment on 110 and 220 reflection of the perovskite cubic elementary cell. The peaks corresponding to BST60/40 gel after calcination at 850 ºC (Fig. 2a, d) are broad and the application of Pearson VII function for the profile fitting can lead to the deconvolution of components. On the other hand, fitting profiles of the peaks corresponding to the finally sintered ceramics (Fig. 2c, f) revealed that a good crystalline ceramic was already obtained (Fig. 3).

A careful examination of the XRD reflection intensities further indicates that no preferred orientation could be found for any sample. The lattice parameters for BST60/40 were calculated for cubic phase using the Rietveld refinement [18], embedded into the computer programme PowderCell 2.4 [19]. A model structure used for diffraction pattern fitting exhibited the space group $Pm3m$ (SG number: 221) (Fig. 3). Detailed information about the model structure used is given in Table 1, whereas the details of calculated X-ray spectrum are given in Table 2.

R-values of the Rietveld analysis obtained under the assumption of $Pm3m$ space group (setting 1) are as follows: $Rp = 13.72\%$, $Rwp = 19.44\%$, $Re = 3.67\%$. For fitting

the diffraction profile, the pseudoVoigt2 function was used and the following parameters were obtained: $u = 0.1755$, $v = 0.0022$, $w = 0.0213$. The calculated unit cell parameter a for the supposed cubic symmetry space group *Pm*3*m* was determined to be 3.962(3) Å.
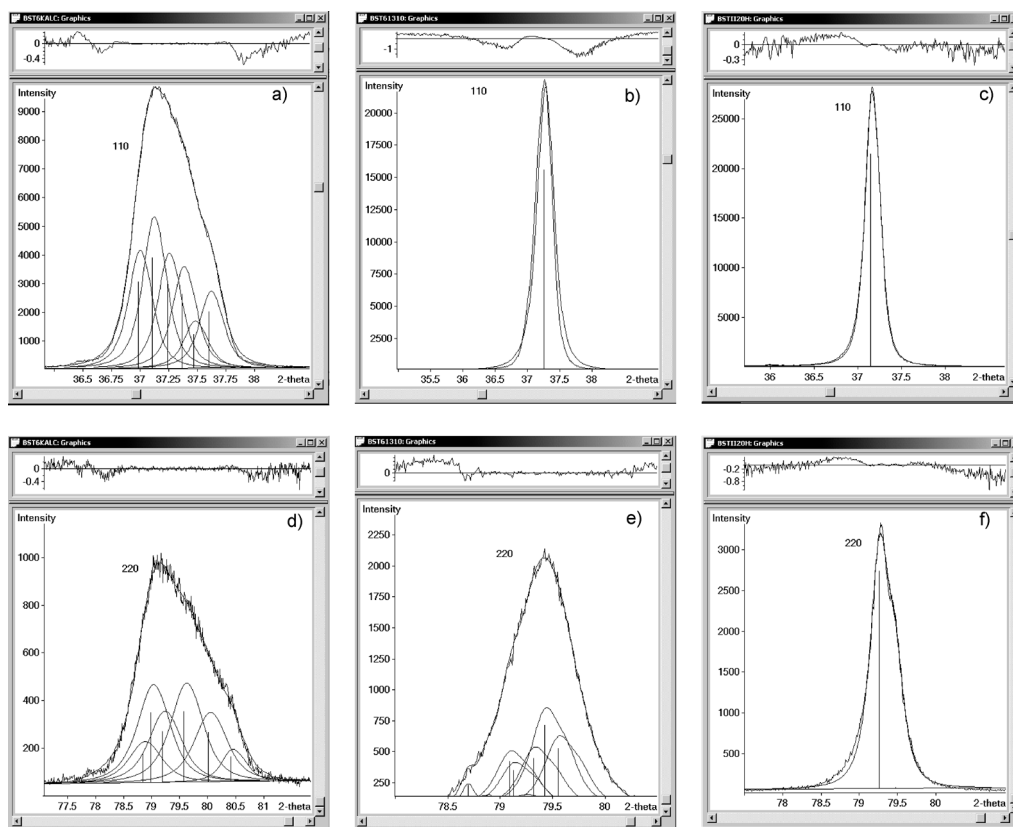
Fig. 2. Results of the profile fitting for diffraction lines 110 (a, b, c) and 220 (d, e, f) for BST gel after calcination (a, d), powdered BST ceramics after sintering at 1350 °C (b, e), and at 1450 °C (c, f)

Although numerical criteria of appropriateness of the fit (i.e. *R*-values) are very important, it is necessary to point out that they do not fully reflect the quality of fitting. Graphical criteria such as plots of the calculated and observed intensities, as well as a plot of the difference between the calculated and observed intensities are also necessary. From the trace on the bottom of Fig. 3, one can see that there are no gross errors of fitting coming from bad scaling parameters or incorrect crystalline structure used for simulation or incorrect unit cell parameters.
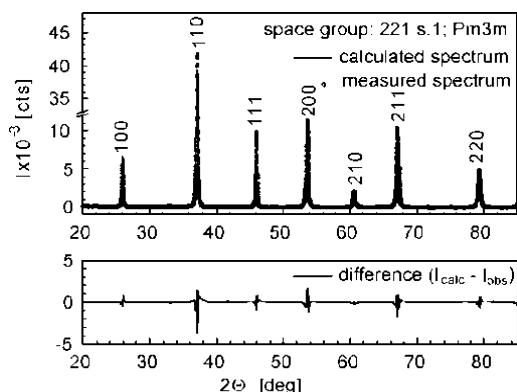
Fig. 3. Results of the X-ray pattern fitting for BST60/40 ceramics (circles – observed pattern, solid line – calculated pattern according to *Pm3m* space group) sintered at 1450 °C. The trace on the bottom is a plot of the difference between the calculated and observed intensities

Table.1. Parameters of the model structure used for the XRD pattern fitting (Fig. 4)[*]

Space group number	221	Atoms in a unit cell	4.9, 5 gen. positions
Space group	$P4/m\overline{3}2/m$	Volume of a cell	62.18Å^3
Cell choice	1	Relative mass of a unit cell	211.64
Lattice parameter s	3.962(3) Å, 3.962(3) Å, 3.962(3) Å	X-ray density	5.6519 g/cm^3
Angles	90.00º, 90.00º, 90.00º	Mass absorption coefficient	451.35 1/g·cm
Atoms in an asymmetric unit	3		

Atom	P. No.	Ion	Wyck.	x	y	z	SOF	B
Ba1	56	Ba^{2+}	1b	0.5000	0.5000	0.5000	0.6000	0.0000
Sr1	38	Sr^{2+}					0.4000	0.0000
Ti1	22	Ti^{4+}	1a	0.0000	0.0000	0.0000	1.0000	0.0000
O1	8	O^{2-}	3d	0.5000	0.0000	0.0000	0.9643	0.0000

[*]Abbreviations: P. No. – atomic number, Wyck. – Wyckoff position, SOF – site occupation factor, B – temperature factor, x, y, z – relative atomic coordinates.

Table 2. Details of the calculated X-ray spectrum (Fig. 3)

Source	X-ray Co Kα_{1+2} 1.789007 Å, 1.792892 Å ($\alpha_2/\alpha_1 = 0.497$)
2Θ	5.005º - 84.995º
Geometry	Bragg–Brentano, fixed slit, anomalous dispersion

hkl	2Θ [deg]	d_{hkl} [Å]	I [rel.]	$F(hkl)$	Mu	FWHM
100	26.094	3.96231	13.73	17.27	6	0.1768
110	37.237	2.80178	100.00	48.34	12	0.2049
111	46.035	2.28764	25.89	38.17	8	0.2322
200	53.681	1.98116	37.89	63.50	6	0.2595
210	60.636	1.77200	6.93	15.58	24	0.2874
211	67.143	1.61761	38.42	41.00	24	0.3163
220	79.364	1.40089	22.23	51.64	12	0.3794

Point analysis of the chemical composition in the microarea for BST60/40 ceramics was studied by EDS. Stoichiometric ratios of the main metallic components of BST60/40 ceramics recalculated to simple oxides are as follows (in mass %): BaO – 43.125%, SrO – 19.430%, TiO_2 – 37.445%. Results of the measurement, given in Fig. 4, have shown the following chemical composition: BaO – 43.98%, SrO – 18.92%, TiO_2 – 37.10%. Thus, the conservation of the chemical composition of the BST60/40 ceramics was proved and the accuracy higher than ±3% was found.
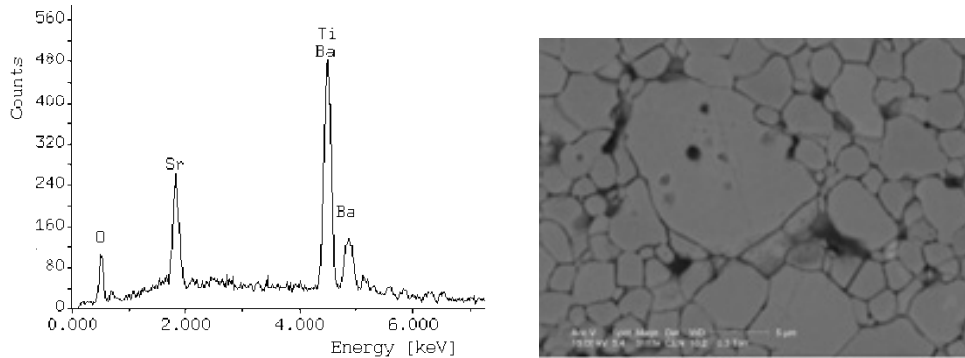
Fig. 4. Results of EDS analysis of BST60/40 ceramics (left)
and the SEM image of the surface taken at a magnification 3183× (right)

A typical SEM micrograph of as-sintered surface of BST60/40 ceramic sample sintered at 1350 ℃ is shown in Fig. 4. A noticeable difference in grain size was observed. The smallest grain size is of about 1 µ whereas the largest grain size is about 10 µm. It is worth noting that the low heating rate used in our experiment (3 ℃/min) for sintering was favourable to the grain growth.
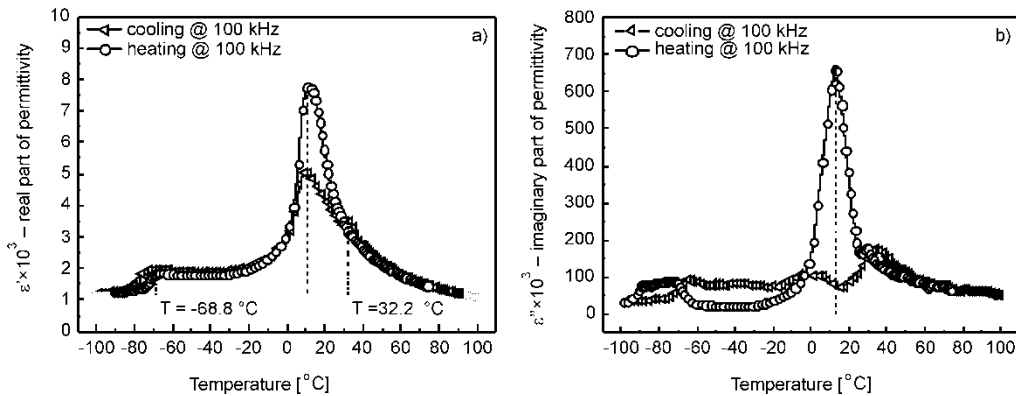
Fig. 5. Dependence of the real part ε' (*a*) and imaginary part ε''(*b*)
of the electric permittivity on temperature for BST60/40 ceramics sintered at 1450 ℃

Figure 5 shows the temperature dependences of electric permittivity (ε') and the coefficient of dielectric losses (ε'') for BST60/40 specimen sintered at 1450 °C for 4 h for both cooling and heating processes. One can see from Fig. 5a that the real part of electric permittivity ε' shows some peculiarities. It reaches its maximum at temperature $T_1(\varepsilon'_{max})$ = 10.2 °C while cooling, whereas temperature of maximum ε' during the heating cycle is shifted towards higher temperatures and amounts to $T_2(\varepsilon'_{max})$ = 11.8 °C. It is worth noting that temperature of ε'_{max} proves indirectly the molar ratio of Ba/Sr = 60/40 [13, 14].
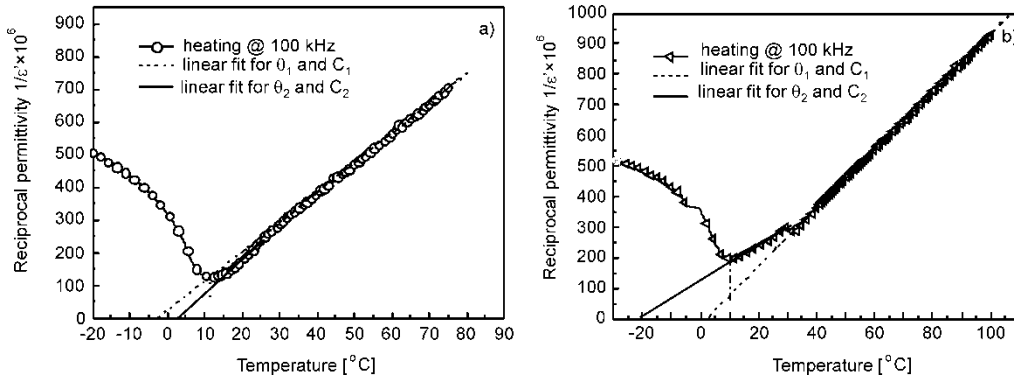
Fig. 6. Temperature dependence of the reciprocal permittivity $1/\varepsilon'$ at 100 kHz of BST60/40 ceramics for the heating (*a*) and cooling (*b*) cycles. The solid and dashed lines represent fittings to the Curie–Weiss law

Fitting the temperature dependence of electric permittivity ε' to the Curie–Weiss law made it possible to determine the Curie–Weiss temperature (θ) and the Curie–Weiss constant (*C*). It can be seen from Fig. 6 that for temperature $T > T(\varepsilon'_{max})$ two sets of parameters θ_1, C_1 and θ_2, C_2 were found for the heating (Fig. 6a) and cooling (Fig. 6b) cycles, respectively. The values of the parameters were as follows: $\theta_1 = -1.95$ °C, $C_1 = 1.09 \times 10^5$ K^{-1} and $\theta_2 = 3.45$ °C, $C_2 = 0.91 \times 10^5$ K^{-1} during the heating cycle, whereas for the cooling cycle: $\theta_1 = 1.40$ °C, $C_1 = 1.05 \times 10^5$ K^{-1} and $\theta_2 = -21.84$ °C, $C_2 = 1.74 \times 10^5$ K^{-1}.

3. Conclusions

The sol-gel method was successfully employed for the synthesis of BST60/40 ceramic powder from barium acetate, strontium acetate and tetra-butyl titanate. Free sintering was used for the final sintering of ceramic samples. It was found that good crystalline ceramic samples exhibiting the regular symmetry of *Pm3m* space group were obtained after sintering at 1450 °C for 4 hours. Analysis of the chemical composition of the final ceramics have proved the conservation of stoichiometry with an accuracy better than ±3%. Temperature dependence of electric permittivity (ε') was

studied in the temperature range of ferroelectric–paraelectric phase transition. It was found that the temperature of electric permittivity maximum value $T(\varepsilon'_{max})$ fits well the Ba/Sr ion ratio. The Curie-Weiss temperature θ as well as the Curie-Weiss constant C were determined for BST60/40 ceramics from the dielectric measurements.

Acknowledgement

References

[1] *Complex perovskite-type oxides*, K.H. Hellwege, A.M. Hellwege (Eds.), *Landoldt–Börnstein, Oxides*, Vol. 16a, Springer, 1981.
[2] *Complex perovskite-type oxides*, E. Nakamura, T.Mitsui (Eds.) *Landoldt–Börnstein: Oxides*, Vol. 28, Springer, 1990.
[3] XU Y., *Ferroelectric Materials and Their Applications*, North Holland, New York, 1991.
[4] JAFFE B., COOK W.R., JAFFE H., *Piezoelectric Ceramics*, Academic Press, London , 1971.
[5] LIU S., LIU M., ZENG Y., HUANG Y., Mater. Sci. Eng., B 20 (2002), 149.
[6] BOMLAI P., SIRIKULRAT N., TUNKASIRI T., Materials Letters, 59 (2005) 118.
[7] SCOTT J.F., *Ferroelectric Memories*, Springer, Berlin, 2000.
[8] WASER R., *Nanoelectronics and Information Technology*, VCH-Wiley, Weinheim, 2005.
[9] KHARTON V.V., MARQUES F.M.B., ATKINSON A., Sol. State Ionics, 174 (2004), 135
[10] NORBY T., Sol. State Ionics, 125 (1999), 1.
[11] HAILE S.M., Acta Mater., 51 (2003), 5981.
[12] SKINNER S.J., KILNER J.A. Mater. Today, 6, 3 (2003), 30.
[13] JEON J.-H., J. Eur. Ceram. Soc., 24 (2004), 1045.
[14] ZHOU L., VILARINHO P., BAPTISTA J.L., J. Eur. Ceram. Soc., 19 (1999), 2015.
[15] JOSHI P.C., M.W.COLE, Appl. Phys. Lett., 77, (2000), 289.
[16] ZHOU L., VILARINHO P., BAPTISTA J.L., J. Electroceram., 5 (2000), 191.
[17] HU T., JANTUNEN H., UUSIMAKI A., LEPPAVOURI S., Mat. Sci. Semicond. Proc., 5 (2003), 215.
[18] *The Rietveld Method*, R.A.Young (Ed.), Oxford University Press, 1995.
[19] NOLZE G., KRAUS W., Powder Diff., 13, (1998), 256.

Phenomena responsible for energy dissipation in fine-grained PZT-type ceramics

A. ZARYCKA[*], B. BRUŚ, J. RYMARCZYK, J. ILCZUK

University of Silesia, Faculty of Computer Science and Materials Science,
Department of Materials Science, ul. Żeromskiego 3, 41-200 Sosnowiec, Poland

Description of the mechanisms responsible for the dissipation of energy in materials is possible thanks to the internal friction (IF) method – a non-destructive method thought to be one of the most sensitive ones [1–3]. The method is based on measurements of mechanical losses at various temperatures or various frequencies. The study of the IF of ferroelectrics can provide extensive information about the physics of processes within these materials, and about their domain structures and their interactions with various structural defects. The aim of the present study was to describe the mechanisms responsible for energy dissipation in PZT ceramics obtained by the sol-gel method and sintered by conventional ceramics sintering (CCS). This work presents results of investigations of the influence of $PbTiO_3$ concentration in PZT ceramics on these processes.

Key words: *PZT; sol-gel method; internal friction*

1. Introduction

PZT ceramics, solid solutions of titanate and lead zirconates, have been widely investigated due to its electromechanical properties allowing them to be used in a lot of devices of a practical character such as electromechanical transducers, vibration pickups, filters, ultrasonic generators, resonators, transformers, stabilizers, modulators, parametric amplifiers, frequency multipliers, and ferroelectric memories [4–6].

Since it is necessary for the materials to have specific properties for given applications, it is essential to find out the correlation between the structure, chemical composition, and the ceramics properties. For this reason, non-destructive investigation methods have been developed for some years and the internal friction method belongs to this type. The method is very sensitive to changes in the structure of the materials under the influence of external factors such as e.g. temperature. Its use to examine

_____

[*]Corresponding author, e-mail: azarycka@us.edu.pl

phenomena responsible for energy dissipation enables us to get information about processes taking place in the material under the influence of temperature, including both relaxation processes (migration of defects, mutual interaction of the domain walls), and occurring phase changes [3, 7].

The objective of this work was to determine the phenomena responsible for energy dissipation in the fine-grained PZT- type ceramics.

2. Materials

Fine-grained PZT-type ceramic with the concentration of 25, 35, 52, 53, 54, 65, 75 mol % of $PbTiO_3$ was used for the tests. The synthesis of powders was carried out using the sol-gel method. Lead acetate, zirconium(IV) propoxide, and titanium(IV) propoxide were used as precursors. The synthesis leading to the formation of the complex of alcoholates lasted 2 hs. The reaction by-product (ester – propyl acetate) was removed in the distillation process. After cooling the solution to room temperature, acetylacetone was added to stabilize the complex of alcoholates. The hydrolysis process, resulting in a change of sol into gel, was initiated by adding H_2O. The gel obtained was calcinated at 573 K for 2h in order to remove organic residues. The powders made in this way were compressed and condensed by two methods: free sintering (1523 K/5 h) and uniaxial (1473 K/2 h). The specimens prepared by this method were ground and polished. Conductive electrodes were made with the silver paste by the burning method at the temperature of 1123 K for 15 min.

3. Results of measurements and their discussion

The dependence of the internal friction on the temperature obtained for the ceramics in question (PZT 25/75, PZT 35/65, PZT 46/54, PZT 47/53, PZT 48/52, PZT 65/35, PZT 75/25) during heating at the rate of 3 K/min and at the frequency of 850 Hz by a resonance mechanical spectrometer RAK-3 [1] are presented in Fig. 1. The presence of two peaks of the internal friction P_{R1} and PF was observed on all dependences. On the $Q^{-1}(T)$ plot, obtained for the PZT 75/25 ceramics, a third peak P_p, between the P_{R1} and P_F peaks, was also observed. The maximum of the P_F peak moved toward higher temperatures with an increase of $PbTiO_3$ concentration (Fig. 1, Table 1). In order to determine the mechanism responsible for the formation of this maximum, measurements of the internal friction dependence on temperature at different frequencies were conducted. On changing the measurement frequency, there occured a change in the temperature position of the maxima of IF peaks of relaxation character, originating from, e.g., mutual interaction of domain walls, and the interaction of defects and domain walls. However, in the case of peaks originating from phase changes, their temperature should be independent of the frequency [8–10]. Thus, the presence of the P_F peak at a stable temperature during the measurements

conducted at different frequencies (Fig. 2, Table 1) points to the origin of the P_F peak from the phase change.
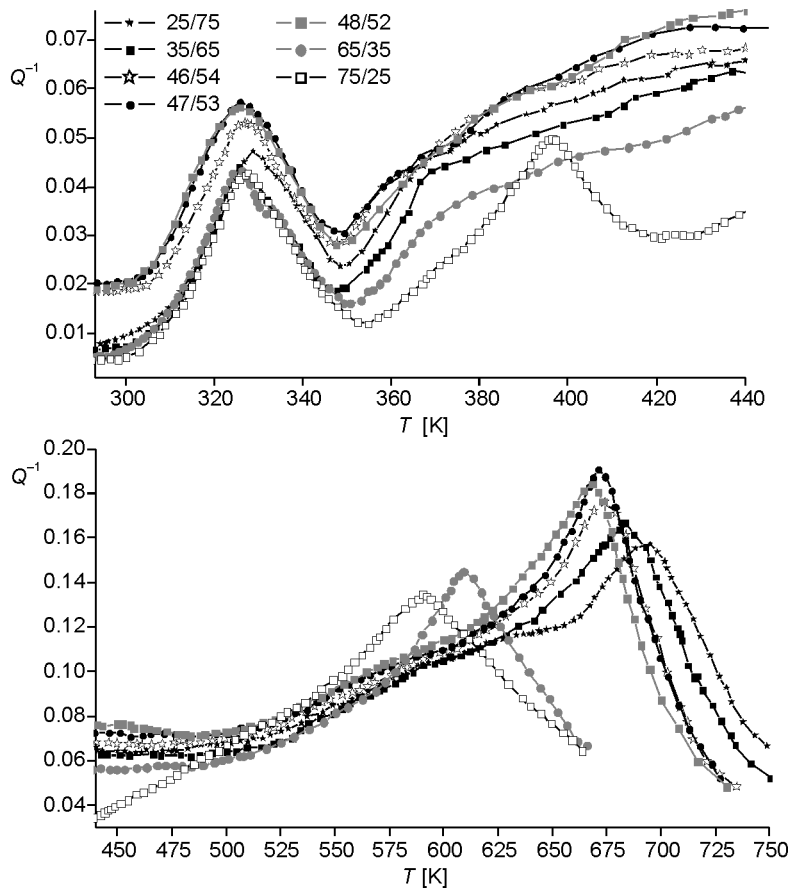
Fig. 1. Dependences of the internal friction on the temperature obtained
for the PZT ceramics during heating at the rate of 3 K/min at the frequency of 850 Hz

An increase in the Curie temperature with the increase in the lead titanate concentration in the solid solution is a generally known property of PZT ceramics. For this reason, the dependence of electric permittivity on temperature determined from the Curie temperature values (Table 1) confirm the origin of the P_F peak from a phase transition from the ferroelectric phase to the paraelectric one. The observed decrease in the *IF* value after the P_F maximum is connected with the disappearance of the domain structure as the result of the transition to the paraelectric state.

With an increase of $PbTiO_3$ concentration, the increase in the height of P_F was also observed until 53 mol %, and then a decrease in the peak height occurred. It is generally known that with a change of $PbTiO_3$ concentration in the PZT ceramics there is a change in the maximum permittivity value at the Curie temperature. For the non-

polarized PZT ceramics the highest values are observed for the compositions near the morphotrophic boundary and there is a decrease in its value as it moves away from the morphotropic boundary toward compositions with the rhombohedral and tetragonal structure [11]. Changes in the P_F peak height are similar to changes in the electrical permittivity values.
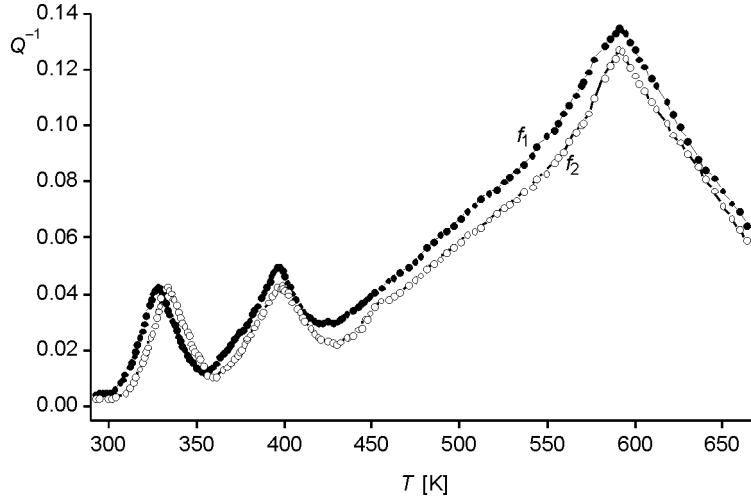
Fig. 2. Temperature dependences of the internal friction obtained
for PZT 75/25 at various measurements frequencies; $f_1 = 850$ Hz, $f_2 = 960$ Hz

Table 1. Temperatures of the P_F peak occurrence
and the Curie temperatures for the PZT ceramics ($f_1 < f_2$)

Type of specimen	T_F [K] at f_1 $\Delta T = \pm 1.5$ K	T_F [K] at f_2 $\Delta T = \pm 1.5$ K	T_c [K] $\Delta T = \pm 2.0$ K
PZT 25/75	695	695	694
PZT 35/65	681	681	678
PZT 46/54	673	674	671
PZT 47/53	671	671	668
PZT 48/52	668	667	665
PZT 65/35	609	609	607
PZT 75/25	590	590	589

The observed temperature changes of the P_{R1} peak position (Fig. 2) at the measurements $Q^{-1}f(T)$ for various frequencies (a movement toward higher temperatures) suggests that a relaxation process is responsible for its formation. In order to prove the above thesis, calculations of the activation energy H and the pre-exponential factor τ_0 were made based on the Arrhenius law [3]. The values of H and τ_0 (Table 2) confirm the origin of the P_{R1} peak from the relaxation process. The activation energy of about

1 eV is a typical value of interaction of point defects with domain walls [9, 12]. This phenomenon is also proved by the τ_0 value (Table 2). Oxygen vacancies are the prevailing defects in PZT ceramics, therefore the interaction of oxygen vacancies with domain walls is responsible for the P_{R1} peak formation. The τ_0 value obtained for PZT 65/35 is an exception. The value of the pre-exponential factor (2.94×10^{-17}) points out that a simple relaxation process described by a single relaxation time cannot be responsible for the P_{R1} peak formation for the PZT 65/35 ceramics.

Table 2. Values of the activation energy
and pre-exponential factor

Specimen	H [eV]	τ_0 [s]
PZT 25/75	1,04±0,02	$(3,17±0,04)\cdot10^{-15}$
PZT 35/65	1,02±0,02	$(2,46±0,04)\cdot10^{-15}$
PZT 46/54	1,10±0,02	$(1,54±0,04)\cdot10^{-15}$
PZT 47/53	0,97±0,02	$(1,07±0,04)\cdot10^{-15}$
PZT 48/52	0,98±0,02	$(1,02±0,04)\cdot10^{-15}$
PZT 65/35	1,00±0,02	$(2,94±0,04)\cdot10^{-17}$
PZT 75/25	1,05±0,02	$(2,01±0,04)\cdot10^{-15}$

No changes in the temperature position of the P_{R1} peak were observed for the examined ceramics with an increase in $PbTiO_3$ concentration (Fig. 1). Small fluctuations of the H activation energy values (Table 2) point to small differences in the concentration of defects in the examined ceramics, introduced during the technological process [13]. Thus the position and height of the peak originating from the interaction of point defects and domain walls do no depend on changes in $PbTiO_3$ concentration, but only on the concentration of defects in the examined ceramics. Regarding the P_{R1} peak in PZT 65/35 ceramics as as resulting from an overlapping of several processes, an attempt was made to find the mechanisms responsible for its formation. The analysis of the shape of the P_{R1} peak obtained for different measurement frequencies for PZT 65/35 ceramics shows that it can be deconvoluted into two peaks (Fig. 3): P'_{R1}, for which the temperature position undergoes a change with the change in the measurement frequency and the P_p peak for which the temperature position does not undergo a change with the change in the measurement frequency.

During the measurement of the internal friction in the temperature range of the P_{R1} peak at lower frequency, a movement of the P'_{R1} peak toward lower temperatures is observed which proves its relaxational character. The calculated values of the activation energy $H = 0.97$ eV and the pre-exponential factor $\tau_0 = 1.8 \times 10^{-15}$ s show that it comes from the interaction of the point defects with the domain walls. In the phase diagram (Fig. 4) for the solid solution of lead titanate and zicronate, a phase change from the rhombohedral phase II (R3c) to the rhombohedral phase I (R3m) can be observed in the range of $PbTiO_3$ concentrations from 4.2 mol % to about 38 mol %.

Thus, the stability of the temperature position of the P_p peak with the change in the measurement frequency shows that the phase composition of the ceramic material is responsible for its formation.
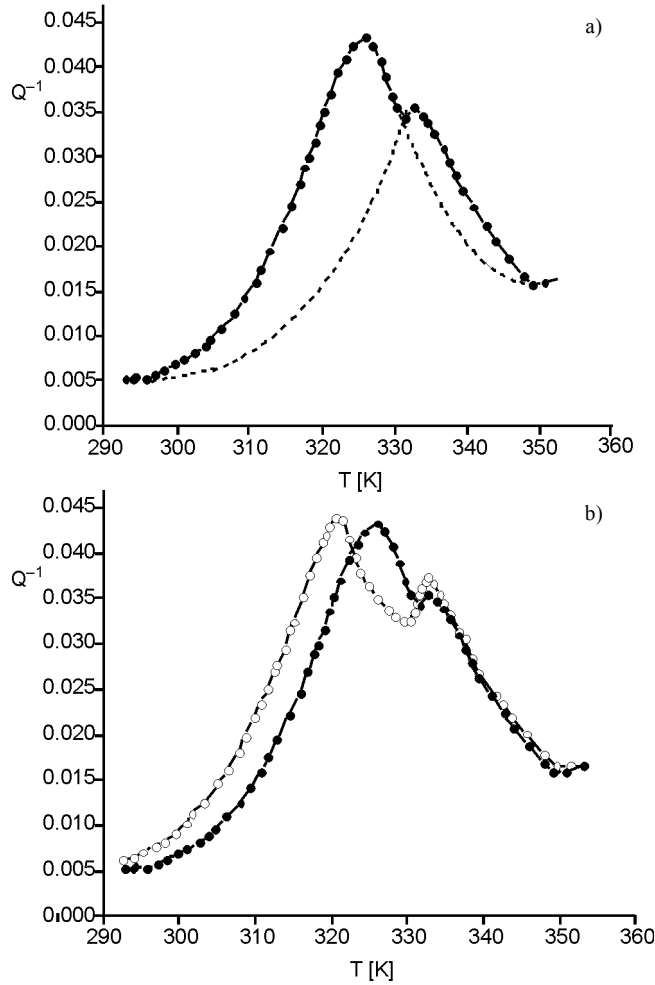
Fig. 3. Temperature dependences of the internal friction obtained in the temperature range of the P_{R1} occurrence: a) the division of the P_{R1} peak into components, b) for the frequency $f_1 = 960$ Hz, $f_2 = 850$ Hz

Changes in the height of P_F and P_p peaks also point to their dependence on the phase changes. According to the model developed by Delorme and Gobin, the dependence of $Q^{-1}(T)$ on the internal friction in the area of the phase change is described by the equation [14]:

$$Q^{-1} = \frac{KG}{\omega} \frac{\partial m}{\partial T} \frac{\partial T}{\partial t}$$

where: K is a material constant, G – modulus of rigidity, ω – angular frequency of the specimen vibrations ($\omega = 2\pi f$, f – frequency), $\frac{\partial m}{\partial T}$ – quantity of the material undergoing the change at the unit temperature change, $\frac{\partial T}{\partial t}$ – rate of temperature changes (heating or cooling). Therefore, the increase in the P_F and P_p peak heights with a decrease in the measurement frequency is fully confirmed by the Delmore–Gobin model.
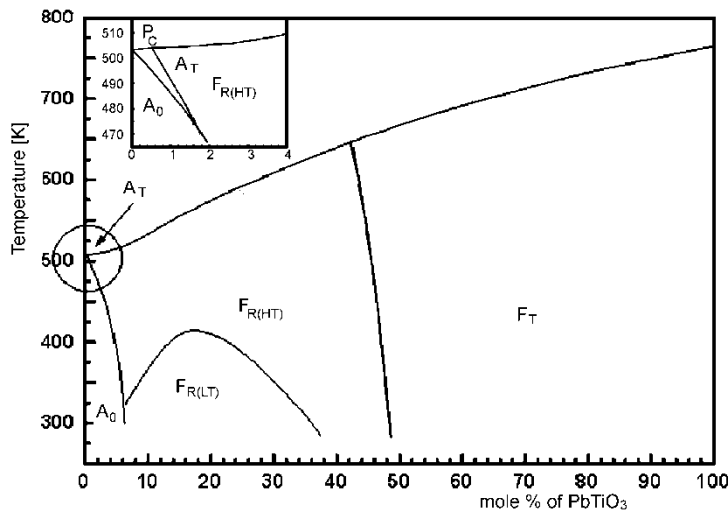
Fig. 4. Phase diagram PbTiO$_3$–PbZrO$_3$– PZT [15]

The PZT 75/25 ceramics group also includes PZT ceramics for which a change from the II rhombohedral phase to the I rhombohedral phase is observed. This change takes place at a temperature higher than a change into the PZT 65/35 composition (Fig. 4). Thus, the P_p maximum observed on the temperature dependences of the internal friction (Figs. 1, 2), moving toward neither higher nor lower temperatures with a change in the measurement frequency is related to the phase change.

4. Conclusions

Variations of internal friction as a function of temperature and excitation frequency can provide direct information on energy dissipation in the materials. In the fine-grained PZT type ceramics phase changes (from the ferroelectric to paraelelectric and from the II rhombohedral phase to the I rhombohedral phase) and the relaxation process, the inte-

raction of the point defects with the domain walls are responsible for the energy dissipation. An increase of the concentration of lead titanate causes a shift of the position of the peak connected with the ferroelectric-paraelectric phase toward higher temperatures (a Curie temperature change). A change in $PbTiO_3$ concentration does not have an influence on the height and the temperature position of the peak connected with the interaction of the oxygen vacancies with the domain walls. However, all wet, chemistry-based methods, for example the sol-gel method, have a very strong influence on the occurrence of particle agglomerates in the resulting PZT powder. In PZT powders with a high $PbTiO_3$ concentration, hard particle agglomerates will significantly reduce the stability of the powders and lead to the formation of microstructural defects in the sintered PZT ceramics, particularly during the free sintering (CCS) method.

References

[1] ZACHARIASZ R., ILCZUK J., CHROBAK A., Ceramics, 66 (2001), 710.

[2] ZARYCKA A., ZACHARIASZ R., BRUŚ B., ILCZUK J., Mol. Quant. Acoust., 24 (2003), 255.

[3] XU Y.H., *Ferroelectric Materials and Their Applications*, New York, North Holland, 1991, pp. 72–100.

[4] SUROWIAK Z., KUPRYANOV M.F., CZEKAJ D., J. Eur. Ceram. Soc., 21 (2001), 1377.

[5] YI C.H., CHIA C. W., CHENG C.L., CAO G.Z., SHEN I.Y., Sensors Act. A, 116 (2004), 369.

[6] YAN F., CHEN X., BAO P., WANG Y., LIU J., J. Appl. Phys., 87 (2000), 1453.

[7] ZACHARIASZ R., ILCZUK J., CHROBAK A., Ceramics, 66 (2001), 630.

[8] BOUZID A., GABBAY M., FANTOZZI G., Mater. Sci. Eng, A 370 (2004), 123.

[9] WANG C., FANG Q.F., SHI Y., ZHU Z.G., Mater. Res. Bull., 36 (2001), 2657.

[10] BRUŚ B., ZACHARIASZ R., ILCZUK J., Phys. Stat. Sol. A, 201 (2004), 789.

[11] KUPRIYANOV M.F., KONSTANTINOV G.M., PANICH A.E., *Segnetoelektritcheskiye morphotropnye* perekhody, Izd. Rostovskogo Uniwiersiteta, Rostov na Donu (1992).

[12] WANG Z.Y., CHEN T.G., Phys. Stat. Sol. A, 167 (1998), R3–R4.

[13] WANG C., FANG Q.F., ZHU Z.G., J. Phys. D: Appl. Phys., 35 (2002), 1545.

[14] DELORME J.F., GOBIN P.F., Metaux, Corr. Ind., 573 (1973), 185.

[15] CZEKAJ D., *Technology*, *Properties and Applications of PZT Thin Films*, University of Silesia, Katowice, 2002.

[16] ZARYCKA A., ZACHARIASZ R., ILCZUK J., CHROBAK A., Mater. Sci.-Poland, 23, (2005), 159.

[17] GUO L., LYASHCHENKO A., DONG X., Mater. Lett. 56 (2002), 849.

Photoconductivity in sol-gel TiO$_2$ thin films with and without ammonia treatment

A. VOMVAS[1*], K. POMONI[1], C. TRAPALIS[2], N. TODOROVA[2]

[1]University of Patras, Physics Department, 26500 Patras, Greece

[2] Institute of Materials Science, NCSR "Demokritos", 15310 Ag. Paraskevi, Greece

Thin TiO$_2$ sol-gel films, with and without ammonia treatment, were prepared using the dip-coating technique and then heat treated at 500 ºC. The time dependences of the photoconductivity at various light intensities were studied in vacuum and in air at 27 ºC. The transient photoconductivity is very sensitive to the environment and dramatically higher than the dark one for samples both in vacuum and in air. The results are discussed in terms of the competition of the photogeneration, recombination, thermal release, and the influence of NH$_3$ treatment.

Key words: *transient photoconductivity; nanocrystalline; TiO$_2$; ammonia treatment; sol-gel method*

1. Introduction

In nature, titanium dioxide occurs in three phases, such as brookite (orthorhombic), anatase (tetragonal) and rutile (tetragonal). It is amorphous for deposition temperature up to 300 ºC, whereas anatase and rutile are formed typically at ~350 ºC and 800 ºC, respectively. Anatase nanocrystalline TiO$_2$ thin films have attracted considerable attention because of low production cost, photostability, and their application in photocatalysis, electrochromics, gas sensing, and solar cells devices.

The use of TiO$_2$ films is restricted, in a way, because of their wide band gap (3.2 eV for the anatase phase) which does not permit the response to visible light. Doping with transition metals reduces this wide band gap, but the doped materials appear to have higher concentration of recombination centres and higher instability [1]. Recently there have been reports that the introduction of small amounts of N in the TiO$_2$ lattice increases its optical absorption in the visible light, though it is not clear yet if this is an effect due to the narrowing of the optical gap [2] or to N 2p states isolated above the valence band [3, 4].

---

*Corresponding author, e-mail: avomvas@physics.upatras.gr

In this work, we present results of measurements of transient photoconductivity, σ_p, for TiO_2 sol-gel thin films with and without ammonia treatment, heat treated at 500 ºC. We study the effect of light intensity, at 27 ºC, in vacuum and in air.

2. Experimental

TiO_2 thin films were prepared on carefully cleaned (in an ultrasonic water bath and then in absolute ethanol) quartz glass substrates by the dip-coating sol-gel technique. The starting solution was prepared by mixing tetrabutyl orthotitanate ($Ti(C_4H_9O)_4$ – TBOTi) (Aldrich) with ethyl alcohol (Panreac) in molar ratio 2:57, in a closed beaker. 10% (towards Ti) of polyethylene glycol-2000 was added to the mixture in order to obtain porous films without cracks [5]. The solution was stirred upon heating (at 70 ºC) for 15 min for PEG2000 dissolution. pH of the sol was adjusted to 1.5 with the addition of 2 ml of HNO_3. Distilled water (1.5 mol) was added and the solution was refluxed under dry atmosphere for 2 h at 60 ºC. For completion of the hydrolysis process, the solution was kept stirred at room temperature for 20 h.

The substrate was dipped in the solution and then pulled out with a constant speed of 3.33×10^{-3} m/s. The gel samples were treated at 450 ºC for 30 min in a Carbolite muffle furnace. The heating rate of 5 ºC/min was applied. The dipping and the heating procedures were repeated in order to obtain five-layer porous TiO_2 films.

After that the films were heat treated at 500 ºC for two hours, in either an O_2 atmosphere (sample A), or in an NH_3 atmosphere (sample B) and left to cool down slowly to 25 ºC. A Thermawatt tube furnace with controlled gas flow was used. The total thickness after the final heat treatment, measured with a profilometer, was 3.22 μm for sample A and 3.10 μm for sample B.

The structure of the films was studied by the X-ray diffraction method, using a Siemens D 500 diffractometer with CuK_α radiation from a secondary graphite monochromator. Photoconductivity was studied at various light intensities, as a function of time at 27 ºC. All measurements were carried out in vacuum (10^{-2} Pa) and in air. The pressure in "air" was 5.5×10^4 Pa. This pressure was chosen in order to enable measurements of the dark current and the photoconductivity with temperature (to be published). The measurements were carried out in a vacuum cryostat with coplanar electrodes separated by 0.8 mm. The temperature was controlled by an Oxford ITC4 controller and a constant bias of 5 V was applied to the sample. As a light source, a 100 W Xenon lamp was used with a full light intensity F_0 of 500 W/m^2 on the sample, which was switched on and off every 20 min. Neutral density filters were used to vary the intensity. The current was measured with a Keithley 617 electrometer and was recorded in a computer every 10 s. The samples were annealed before any measurements at 167 ºC for 90 min in order to eliminate the persisting effects of any previous light exposure.

3. Results and discussion

3.1. Structure

The identification of the phase of the films and the grain size was done with XRD. The measurements were carried out with the following combination of slits: $1.0^o/1.0^o$ as aperture diaphragms, 0.15^o as detector diaphragm and 0.15^o as diffracted beam monochromator diaphragm. The measured 2θ range was scanned in steps of 0.03^o in 10 s/step.
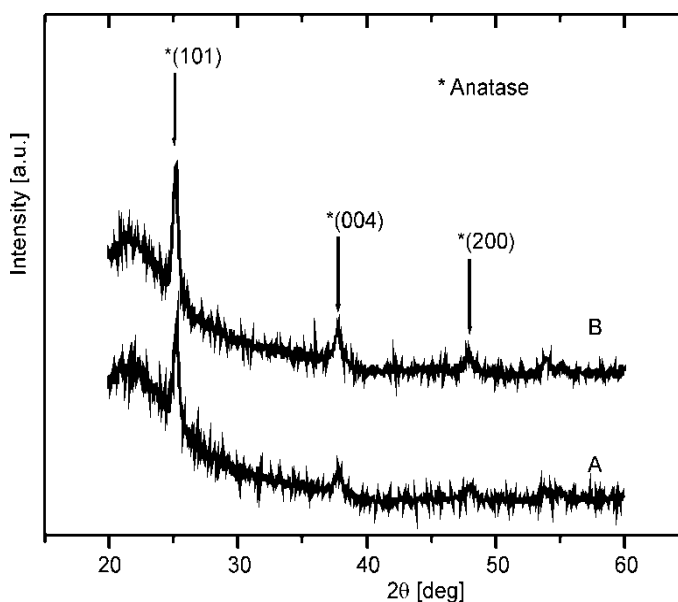
Fig. 1. XRD patterns of TiO$_2$ thin films treated in O$_2$ atmosphere
(curve A) and in NH$_3$ atmosphere (curve B) at 500 ºC

Figure 1 shows the XRD patterns for the undoped and N-doped samples. An intensive peak at $2\theta = 25.30^o$ in both patterns corresponds to the (101) reflection while the peaks at 38° and 48° correspond to (004) and (200) reflections, respectively. These peaks confirm the presence of the anatase phase in the films with no rutile phase detected. Sherrer's semi-empirical formula $d = K\lambda/\beta\cos\theta$ can be used for the evaluation of the average crystallite size. In the formula, λ is the wavelength of X-rays (0.154 nm), β is the full width at the half maximum (in radian), θ is the Bragg angle, and K varies with (*hkl*) and crystallite shape but is usually nearly equal to 1. From the stronger peak the mean crystallite size d was found to be 21.0 and 27.4 nm for samples A and B, respectively.

3.2. Photoconductivity

3.2.1. Photoconductivity in vacuum

Figures 2 and 3 show the dependences of photoconductivities of samples A and B on time in vacuum at 27 °C, at various light intensities. Because of the difference in scales, the plots at 10% F_0 are given as insets.
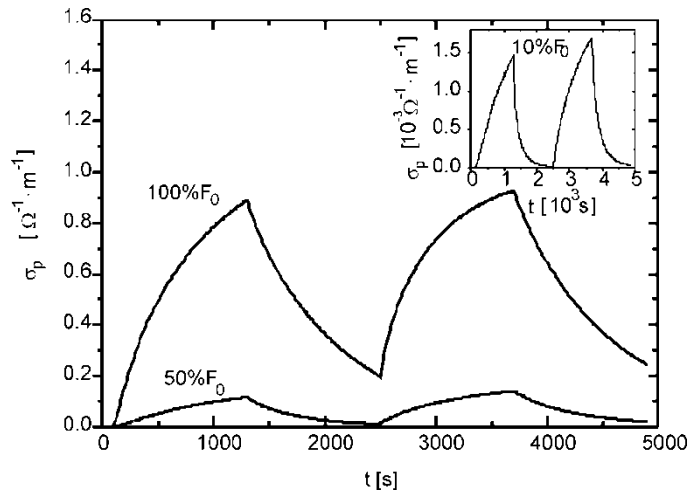
Fig. 2. The photoconductivity response of sample A in vacuum, at 27 °C, for various light intensities. The photoconductivity response, for 10% of the full light intensity ($F_0 = 500$ W/m^2), at 27 °C is given as an inset of the figure
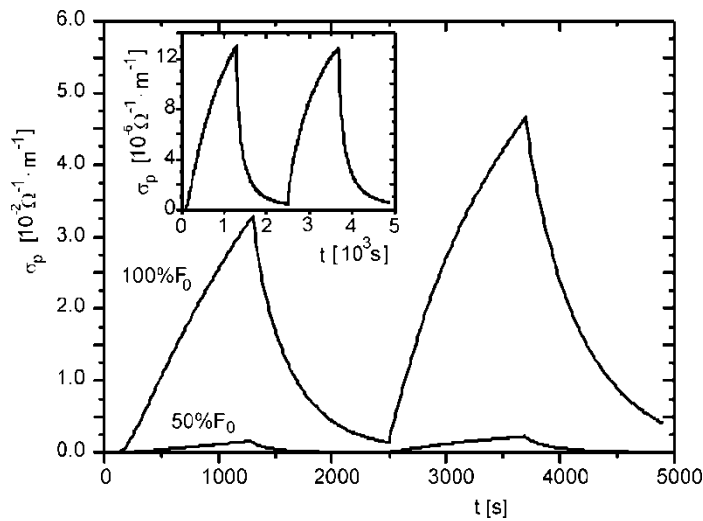
Fig. 3. The photoconductivity of sample B in vacuum, at 27 °C, illuminated at various light intensities as a function of time. The photoconductivity, for 10% of the full light intensity ($F_0 = 500$ W/m^2), at 27 °C is given as an inset of the figure

The photoconductivity of sample A (heat treated under O_2 atmosphere), after a quick rise, shows the usual sublinear behaviour [6, 7] resulting from the competition between photogeneration, recombination and thermal release. When the light is turned off, the decay becomes slower as time passes, due to the thermally excited electrons from the traps.

The photoconductivity σ_p after 20 min of illumination with 100% F_0 is 0.89 $\Omega^{-1} \cdot m^{-1}$ for sample A. This value is found to be nine orders of magnitude higher than its dark conductivity σ_d. This behaviour can be attributed to a high porosity and high density of trapping states in the energy gap of the sample. At the end of the second illumination, the σ_p maximum value shows an increase of about 4% compared to that at the end of the first illumination. Some traps, which remained still filled at the end of the decay period, allow the excitation of more photogenerated electrons to the conduction band, thus increasing σ_p [8]. The observed increase is not high, since the recombination rate at this level of illumination is significant. At 50% F_0, where the recombination rate is lower, the corresponding increase is higher (19%), as expected. At 10% F_0, the increase at the end of the second illumination is somehow lower (16%) than that at 50% F_0 because of the lower density of traps that still remained filled at the end of the decay time at this low level of intensity.

In the case of sample B, heat treated under NH_3 atmosphere (Fig. 3), σ_p shows a less pronounced sublinear behaviour, indicating that the thermal release rate dominates after the initial stage of illumination. σ_p at the end of the 20 min of illumination with F_0 was 3.3×10^{-2} $\Omega^{-1} \cdot m^{-1}$, which is more than eight orders of magnitude higher than its σ_d but smaller than the photoconductivity of sample A. This was caused by the ammonia treatment, which created additional oxygen vacancies which increased the dark conductivity, but acted as recombination centres [9] upon illumination and did not permit the further increase of σ_p.

The increase in the photoconductivity values at the end of the second illumination period was high enough (about 43%) for the 100% and the 50% F_0, compared to that of the first illumination. This is caused by the fact that the concentration of the trapping states that remained filled was high enough because of the modification that the ammonia treatment caused. As for the 10% F_0, σ_p at the end of the second illumination was found to have the same value as in the first illumination, because of the decrease of density of the filled traps at the end of the preceded decay time.

3.2.2. Photoconductivity in air

The photoconductivity responses of samples A and B, at 27 ºC, in air, at various light intensities, are shown in Figs. 4 and 5, respectively. Because of the difference in scales, the plots at 10% F_0 are given as insets.

At the beginning of illumination in air with F_0, σ_p of both samples increases rapidly reaching a maximum and then slowly decreases. This behaviour suggests that recombination is the predominant mechanism in air. The σ_p values are again much higher than the respective σ_d ones but lower than their photoconductivities in vacuum.

This different behaviour in vacuum and in air indicates that when the pressure increases the then created electron scavengers O_2^- result in the decrease of σ_p [10]. When the light is switched off, σ_p falls rapidly in both samples indicating again the significant role of recombination in air.
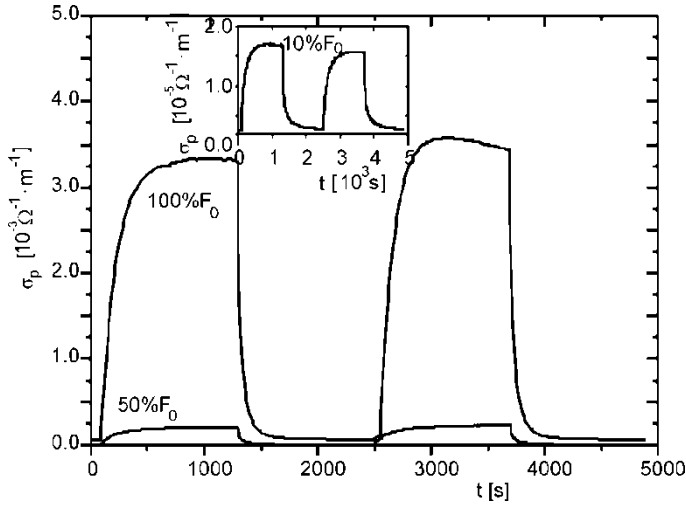

Fig. 4. The photoconductivity response of the sample A in air, at 27 ℃, for various light intensities. The photoconductivity response, for 10% of the full light intensity ($F_0 = 500$ W/m^2), at 27 ℃ is given as an inset of the figure
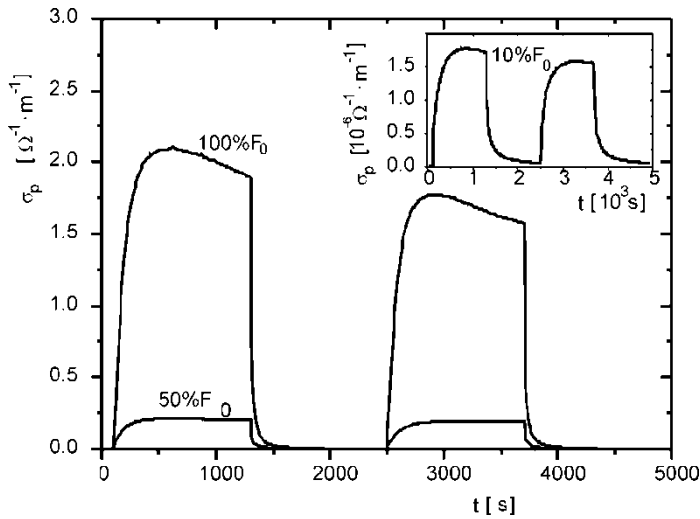

Fig. 5. The photoconductivity of sample B in air, at 27 ℃, illuminated at various light intensities as a function of time. The photoconductivity for 10% of the full light intensity ($F_0 = 500$ W/m^2), at 27 ℃ is given as an inset of the figure

In the case of sample A, at full light intensity F_0, photoconductivity reaches quickly high values (3.2×10^{-3} $\Omega^{-1} \cdot m^{-1}$ at the end of the first illumination). When the light is switched off, σ_p decays rapidly almost near to the initial dark value. During the second illumination, photoconductivity reaches quickly its maximum, then falls slowly and at the end of this illumination period its value is about 3% higher than that at the end of the first illumination. It seems that even in air some traps remain occupied at the end of the decay time and permit the photogenerated electrons to move quickly to the conduction band and increase the photoconductivity. The observed slow fall may be attributed to the recombination rate that is dominant from the very early stage of illumination.

As the light intensity decreases, the photoconductivity of sample A takes, as is expected, lower values. For 50% F_0, σ_p at the end of the second illumination period shows a higher increase (about 11%) compared to that of the first one, as a consequence of the lower recombination rate at this level of illumination, while for 10% F_0, a decrease in σ_p of almost 6.5% is observed. It seems that the thermal release rate becomes significant because of the low photogeneration rate during the second illumination period. This enhances the recombination rate and causes a decrease in photoconductivity.

When sample B is illuminated in air at various light intensities, the corresponding photoconductivity (Fig. 5) follows a similar behaviour to that of sample A but with σ_p values lower (1.9×10^{-4} $\Omega^{-1} \cdot m^{-1}$ at the end of the first illumination), as the modification caused by the NH$_3$ treatment, adds recombination centres in the gap of the TiO$_2$ semiconductor.

For all used light intensities, a decrease in photoconductivity values at the end of the second illumination is observed and can be attributed to a high recombination rate created by the ammonia treatment.

4. Conclusions

A study of the transient photoconductivity of thin TiO$_2$ sol-gel films, with and without ammonia treatment, in vacuum and in air, as a function of the illumination time and the light intensity, has been presented in this work.

The photoconductivity for full light intensity F_0 is much higher than the dark conductivity of both samples, in vacuum and in air.

In vacuum, the value of σ_p for samples A and B at the end of the second period of illumination was found to be higher than in the first one for almost all the used light intensities, as a result of the competition between recombination and the release of electrons from traps.

In air, at the end of the second illumination, the values of σ_p were found to be higher than in the first one for sample A for light intensities 100% and 50% F_0. On the

contrary, for sample B in air, σ_p was lower at the end of the second illumination period for all light intensities because of the NH_3 treatment.

References

[1] SAKATA Y., YAMAMOTO T., OKAZAKI T., IMAMURA H., TSUCHIYA S., Chem. Lett., 12 (1998), 1253.
[2] ASAHI R., MORIKAWA T., OHWAKI T., AOKI K., TAGA Y., Science, 293 (2001), 269.
[3] IRIE H., WATANABE W., HASHIMOTO K., J. Phys. Chem. B, 107 (2003), 5483.
[4] LINDGREN T., MWABORA J.M., AVENDANO E., JONSSON J., HOEL A., GRANQVIST C., LINDQUIST S., J. Phys. Chem. B, 107 (2003), 5709.
[5] GUO B., LIU Z., HONG L., JIANG H., LEE J., Thin Solid Films, 479 (2005), 310.
[6] SCHWARZBURG K., WILLING F., Appl. Phys. Lett., 58 (1991), 2520.
[7] POMONI K., VOMVAS A., TRAPALIS C., Thin Solid Films, 479 (2005), 160.
[8] EPPLER A.M., BALLARD I.M., NELSON J., Physica, E, 14 (2002), 197.
[9] LINDGREN T., LU J., HOEL A., GRANQVIST C., TORRES G., LINDQUIST S., Sol. Energy Mater. Sol. Cells, 84 (2004), 145.
[10] WEIDMANN J., DITTRICH T., KONSTANTINOVA E., LAUERMANN I., UHLENDORF I., KOCH F., Sol. Energy Mater. Sol. Cells, 56 (1999), 153.

Sol-gel derived antireflective coating with controlled thickness and reflective index

A. BEGANSKIENE[1*], S. SAKIRZANOVAS[1], I. KAZADOJEV[1],
A. MELNINKAITIS[2], V. SIRUTKAITIS[2], A. KAREIVA[1]

[1]Department of Chemistry, Vilnius University, Naugarduko 24, LT-03225 Vilnius, Lithuania

[2]Laser Research Center, Vilnius University, Sauletekio al. 10, LT-10222 Vilnius, Lithuania

Optical properties and structure of antireflective coatings (AR) deposited from hydrolysed TEOS sol have been characterized in detail. The influence of various parameters on the formation of colloidal silica antireflective coatings by the dip-coating technique has been investigated. For the characterization of colloidal silica films, the UV-visible spectroscopy, laser ellipsometry, and atomic force microscopy were used. Using optimal sol-gel processing conditions (dipping rate – 40 mm/min, coating time – 20 s, and temperature – 20 ºC), the colloidal silica coatings were obtained and characterized in comparison with non-coated glass substrate. The reflectance of AR coatings increased with increasing the temperature of sol-gel processing. The laser damage threshold of as deposited films was measured at 1064 nm (1H) and 335 nm (3H) wavelength using a Nd:YAG lasers. The laser damage threshold of AR coating exceeded 15.22 J/cm^2 at 1064 nm and 26.82 J/cm^2 at 355nm.

Key words: *antireflective coating; colloidal silica; sol-gel method; laser threshold*

1. Introduction

Light reflections from computer monitors, car dashboards, and TV screens impair the legibility of the displays by degrading the transmission of optical components. The decrease in transmission of a transparent optical medium is caused by an abrupt change in the refractive index at the interface between the medium and its environment. Antireflection (AR) coatings reduce the reflection considerably improving the quality of optical lens systems [1–5]. The refractive indices of glass and transparent plastic substrates are typically $n_s \approx 1.5$. The optimum refractive index for a single-layer broad-band antireflection coating is $n_f = (n_s)^{1/2} \approx 1.22$. The lowest refractive indices for the dielectrics are about 1.35 (CaF$_2$, MgF$_2$). The value of $n_f = 1.22$ is therefore

---

*Corresponding author, e-mail: aldona.beganskiene@chf.vu.lt

unreachable for conventional single layer AR coatings. Despite intensive research, the availability of broadband antireflection coatings is still limited by the lack of materials with low refractive indices.

Recently, Thomas [6–8] suggested using porous silica films for this purpose. When the pore size is much smaller than the visible wavelengths, the effective refractive index of the nanoporous medium is dependent on the film porosity. To reduce the refractive index to up to ~1.23 using the material with a refractive index of ~1.5, the porosity of ~60% has to be introduced. The coatings of layers of colloidal silica nanoparticles, which are packed in a manner that results in an overall porosity of ~50%, have the refractive index of about 1.22 [9–11]. Besides, such silica AR coatings are distinguished for a high threshold of the laser damage, which is very important for the optics used in high-peak-power laser systems.

The monodispersed silica colloidal suspension that was mostly synthesized with the modified Stoeber method [12–17] was used to prepare single-layer porous AR films. This was done by hydrolysis of tetraethylorthosilicate (TEOS) in ethanolic medium and in the presence of ammonia.

Wet chemistry has already been used for a long time for the preparation of oxide powders and the first synthesis of silica from silicon alkoxide was reported long time ago [18]. One of the main advantages of the sol-gel process is the easy deposition of thin films directly from the solution by techniques such as dip-coating, spin-coating, or spray technique [19]. The commercial production of sol-gel coatings onto flat glass was developed in the seventies; however, researchers still are very interested in this process. High quality coatings for various uses constitute one of the most important applications of the sol-gel process. This is because of the possibility of using liquid solutions to fabricate solid films with an extremely wide range of chemical compositions on a variety of substrates at relatively low temperatures.

The sol-gel derived thin films have many applications, especially in modifying the reflectivity of the substrates surface, altering its rigidity or modifying its surface chemistry. In general, many interdependent factors can play a part in the final physical properties of sol-gel derived coatings: sol-gel solution (starting chemicals, sequence of mixing, concentration and ratio of components, temperature, pH) (i); method of application (dip, spin, spray, laminar flow) (ii); substrate (glasses, plastics, metals, ceramics) and its surface conditions (iii); coating (porosity, residual OH, structure, roughness, thickness) (iv). Dip-coating is the most popular method in which the colloids are evaporation-induced and self-assembled on the substrate as it is slowly withdrawn from the colloidal suspension. The reproducible deposition by dip-coating enables systematic control over coating thickness and refractive index (coating porosity) for a given substrate.

In the present study, we demonstrate the preparation of AR coatings with tunable microstructure on lime glass substrates by dip-coating technique and show the dependence of variation of the AR behaviour on different deposition process parameters and particle volume fraction.

2. Experimental

The IR spectra of the materials were recorded in KBr powders using Perkin-Elmer Spectrum BX FT-IR spectrometer. Transmission electron microscopy was performed with the PEM-100 electron microscope. A copper grid with a holey carbon film was dipped in the sol, dried at room temperature and analyzed in TEM. Coating transmittance and reflectance of the normally incident light was measured using UV-vis spectrophotometers (Perkin-Elmer Spectrum Lambda 19 and LOMO) over the spectral range of 350–900 nm. For the glass substrates, variable angle spectroscopic ellipsometry (SOPRA) was used to characterize the film thickness and transmittance. The angle of incidence was fixed at 70° (from the normal), and the spectral range probed was 350–850 nm. The AFM analysis was used for the morphological characterization of the antireflective coatings. The particle size was determined from the micrographs obtained from TEM measurements. These results, summarized from over hundred particles, were used for the calculation of average particle size and standard deviations of each sample.

The laser damage tests were carried out by Nd:YAG lasers (the output laser pulse duration – 4.6 ns, frequency – 10 Hz) using a spot size of approximately 586 μm diameter. The laser damage threshold of the coatings, i.e. the lowest intensity to cause an irreversible change, was evaluated using a high power laser system. The energy H radiated on the sample was calculated by the following formula $H = Q_{max}/A_{eff}$, where Q_{max} is the output energy of Nd:YAG lasers and A_{eff} is the effective area of laser spot on the sample. The damage morphology of the AR coatings was obtained with Ergolux optic microscope.

The dip-coating method on both sides of the glass was employed to produce AR films. For the preparation of thin colloidal silica films, the KSV D™ dip-coating apparatus, KSV Instruments Ltd., was used. Various rates of dip-coating were applied (5, 10, 20, 40, 60, and 80 mm/min). The coating procedure was also performed at various temperatures (26, 30, and 34 ºC).

The sol-gel synthesis of colloidal SiO_2 nanoparticles was performed in non-aqueous system of TEOS. The precursor of SiO_2 colloidal sol was prepared by the base catalyzed hydrolysis of tetraethylorthosilicate (Fluka, 99%) [12]. The required amount of ammonium hydroxide (33%, Riedel-de Haen) was added to half of the required volume of anhydrous ethanol. The alkaline solution was added to the solution of TEOS in ethanol continuously stirred at room temperature (20±2 ºC). The solutions with final silica concentration of 2%, 3%, and 5% SiO_2 were prepared. The molar ratio of ammonium hydroxide to alkoxide was 0.2 mol, to water – 0.4 mol, to ethanol – from 25 to 39 mol. The obtained reaction mixture was stored for 14 days at room temperature to allow hydrolysis as much as possible. The final product consisted of colloidal suspension of SiO_2 nanoparticles in an anhydrous solvent.

3. Results and discussion

Several different silica sols were used to find the optimum deposition conditions on the microscope glass substrates for antireflective behaviour. The spherical silica particles formed via the base-catalyzed hydrolysis and condensation of tetraethylorthosilicate in an aqueous mixture containing ethanol and ammonia were found to be colloidally stable, having a narrow size distribution. The silica nanoparticles dip-coated onto the glass substrate were transparent, possibly due to a small particle size. The transmission spectra of silica coatings obtained on the glass substrate using various concentrations of SiO_2 and deposition rates were recorded. The variation of AR behaviour for different silica coatings on glass obtained from 2% and 3% SiO_2 sol solution are shown in Figs. 1 and 2, respectively. It is evident that in all cases the coatings visibly reduced the reflectance of the glass substrate. As seen, the transmission spectra showed a sinusoidal shape with a single maximum if the quarter-wave thickness occurred over the range of 400–850 nm. Such behaviour is typical of single layer coatings. However, non-optimal coatings exhibited minima over this "visible" wavelength range (Fig. 1) because they were either too thick or too thin compared to the desired quarter-wave thickness.
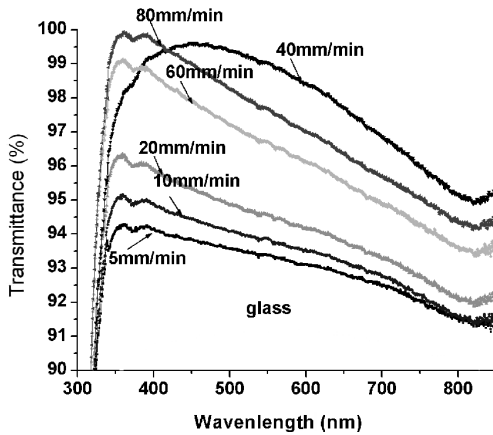

Fig. 1. Transmission spectra for silica coating on glass substrates obtained from 2% SiO_2 using various deposition rates
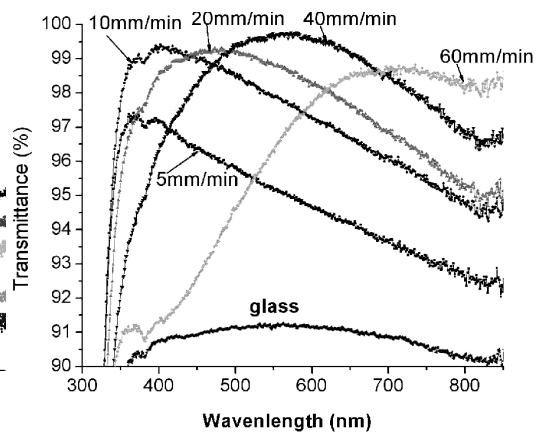
Fig. 2. Transmission spectra for silica coating on glass substrates obtained from 3% SiO_2 using various deposition rates

The determined maximum of transmission for a film coated on both sides and obtained from 2% SiO_2 sol on glass was about 94.5–99.7% (Fig. 1). The data collected for deposition rates of 5, 10, 20, 40, 60, and 80 mm/min showed a precise tuning of the spectral maxima. The optimal value of the deposition rate for these coatings was found to be about 40 mm/min. The relative difference in spectral behaviour for different rates was caused mostly by the variation of film thickness. The observed shift in

the transmission maxima correlates very well with the deposition rate, proving that the optical properties of the coatings can be controllably varied by the deposition process.

The maximum transmission for a both-sided coating obtained from 3% SiO_2 sol on glass was found to be about 97.5–99.7% (Fig. 2). As is seen, the intensity of transmission increases with increasing the immersing rate from 5 mm/min (97.5%) to 40 mm (99.7%). Besides, the transmission maximum is shifted from 380 nm to longer wavelength. Thus, the changes in the deposition rate resulted in the changes of the coloration of the reflected light from the coating, ranging from a blue tint to a yellowish tint as the deposition speed decreased.
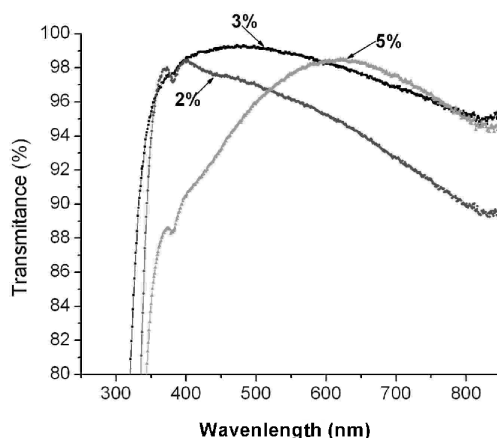
Fig. 3. Transmission spectra for silica coating on glass substrates obtained from 2%, 3%, and 5% SiO_2; the dipping rate – 40 mm/min

Three colloidal SiO_2 sols of different concentrations (2%, 3%, and 5% SiO_2) were selected to study the influence of particle size and concentration on the coating transmittance (Fig. 3). The coatings were obtained with the optimal dipping speed (40 mm/min) and temperature (20 ºC). The best AR behaviour was exhibited by the coatings obtained from 3% SiO_2 sol. The highest absolute transmittance (99.3%) was achieved at 480 nm. The coatings obtained from 2% and 5% SiO_2 showed the highest transmittance of 98.5% at 400 nm and 610 nm, respectively. The thickness of AR coating increases with increasing the silica concentration in the sol solution.

Temperature can influence the final physical properties of sol-gel derived coatings as well. The sol viscosity decreases with increasing the dipping temperature, while the velocity of solvent evaporation increases dramatically with temperature. The coating samples were prepared from 3% SiO_2 sol at 26, 30, and 34 ºC with the dipping rate of 40 mm/min. The reflectance spectra of silica coatings obtained at various temperatures are shown in Fig. 4. As is seen, the reflectance spectra for the samples obtained at different temperatures are qualitatively the same. However, for higher deposition temperatures the minimum value of reflectance is shifted to longer wavelengths. The coatings deposited at 26 ºC showed the best antireflective properties in the range of 375–400 nm, while the coatings deposited at 34 ºC turned out the most antireflective in the range of 400–450 nm. The highest reduction (0.31%) in the reflectance occurred at 26 ºC.
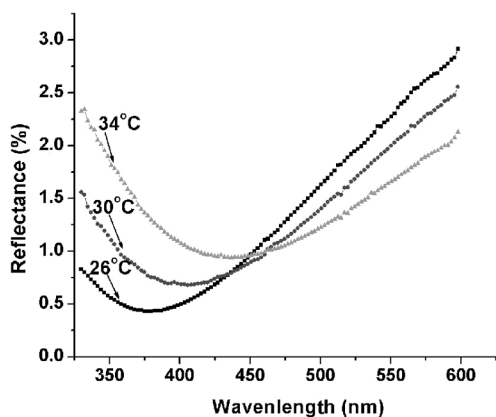
Fig. 4. Reflectance spectra for glass surface
coated with silica at various temperatures

The colloidal silica coatings were obtained at the optimum sol-gel processing conditions (dipping rate – 40 mm/min, coating time – 20 s, and temperature – 20 ºC) and characterized in comparison with non-coated glass substrate. Particle size was determined by the transmission electron microscopy. The results of the examination of particle size, thickness (d) and refractive index (n) of the investigated samples are summarized in Table 1.

Table 1. Colloidal particle size and AR coating data

Material	Particle size [nm]	Refractive index, n_c	Thickness d [nm]
Glass	–	1.465	–
SiO$_2$ (2%)	20–35	1.230	92
SiO$_2$ (3%)	30–45	1.234	108
SiO$_2$ (5%)	40–55	1.235	132

Atomic force microscope (AFM) was used for the characterization of the surface morphology of silica coatings. AFM images of silica coatings (just obtained and heated) are shown in Figs. 5a, b, respectively.
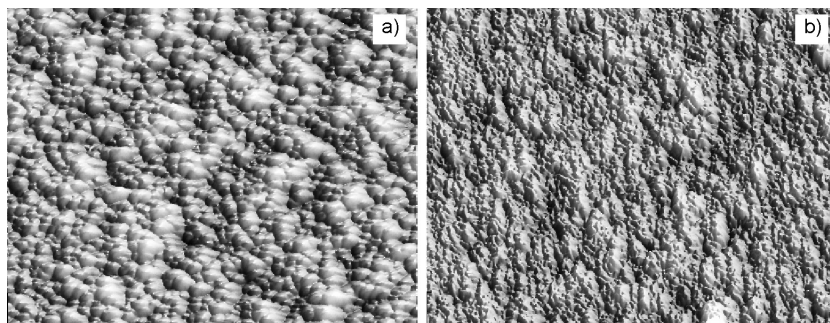

Fig. 5. AFM images of surface morphology of silica coatings:
a) non-heated; 1.96×1.96 μm^2, and b) heated for 2 h at 80 ºC; 1.96×1.96 μm^2

From the AFM image (Fig. 5a) we can conclude that the just obtained colloidal silica coating is composed of silica particles ca. 40 nm in diameter. However, the particles show a tendency to form agglomerates of ca. 100–200 nm in size. The following experimental results are obtained from the AFM measurements: A – maximum roughness height 31.26 nm; R_a – average roughness 3.8 nm; R_m – root-mean-square roughness 4.34 nm. The fracture surface of the AR coatings heated for 2 h at 80 ºC was also observed using AFM. The roughness and the globule dimension were smaller (A – 24.96 nm; R_a – 2.10 nm; R_m – 2.76 nm) compared with the non-heated sample. As can also be seen, the morphology of AR coating is sensitive to drying temperature. However, the transmittance maxima of the heated and non-heated coatings were almost identical.
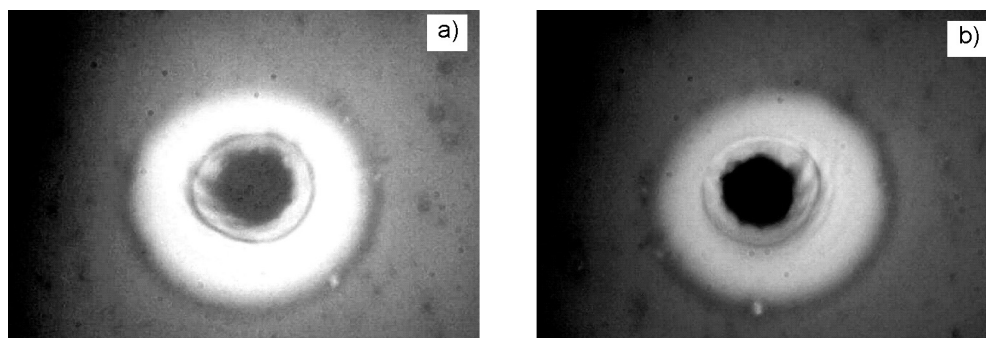

Fig. 6. The damage morphologies of silica coatings: a) non-treated side sample, and b) treated side sample

A very important property of silica antireflective films is a high laser damage threshold. While conventional multiple layer dielectric stacks are typically designed to withstand 4 to 6 J/cm² in pulses a few to ten nanoseconds wide, AR obtained via sol-gel method coatings can handle 40 J/cm² in this pulse regime at 1064 nm. The laser damage tests were carried out on Nd:YAG lasers at 1064 nm (1H) and 355 nm (3H) (single-shot 4.61-ns, pulse repetition rate 10Hz). The laser damage threshold of the AR coating exceeded 15.22 J/cm^2 at 1064 nm and 26.82 J/cm^2 at 355 nm. The damage morphology of the AR coatings was mapped with an optical microscope, and the onset damage morphology of treated and non-treated side of sample is shown in Fig. 6.

4. Conclusions

Optical properties and structure of antireflective coatings (AR) deposited from hy-drolysed TEOS sol were characterized in detail in this study. The formation of colloi-dal silica antireflective coatings with the dip-coating technique, by changing different preparation parameters has been investigated. Using optimal sol-gel processing condi-tions (dipping rate – 40 mm/min, coating time – 20 s, and temperature – 20 ºC), the colloidal silica coatings were obtained and characterized in comparison with the non-

coated glass substrate. It was determined that the reflectance of AR coating increases with increasing temperature of the formation process. The laser damage threshold of as deposited films was measured at 1064 nm (1H) and 335 nm (3H) wavelength using a Nd:YAG laser. The laser damage threshold of the AR coating exceeded 15.22 J/cm^2 at 1064 nm and 26.82 J/cm^2 at 355nm. In conclusion, the obtained antireflective coatings accept higher intensities than conventional dielectric AR coatings promoting more effective utilization of nonlinear optical media.

References

 [1] CHEN D., Sol. Energy Mat. Sol. Cell, 68 (2000), 313.
 [2] GOMBERT A., GLAUBITT W., ROSE K., DREIBHOLZ J., BLASI B., HEINZEL A., SPORN D., DOLL W., WITTWER V., Thin Solid Films, 351 (1999), 73.
 [3] NOSTELL P., ROOS A., KARLSON B., Thin Solid Films, 434 (1999), 170.
 [4] NOSTELL P., ROOS A., KARLSON B., Sol. Energy Mat. Sol. Cell, 54 (1998), 223.
 [5] HAMMARBERG E., ROOS A., Thin Solid Films, 442 (2003), 222.
 [6] THOMAS I., Appl. Opt., 31 (1992), 6145.
 [7] THOMAS I., Appl. Opt., 25 (1986), 1447.
 [8] THOMAS I., SPIE, 2114 (1993), 230.
 [9] DAS S., ROY S., PATRA A., BISWAS P.K., Mater. Lett., 57 (1999), 2320.
[10] XU Y., ZHANG B., FAN W.H., SUN H.Y., Thin Solid Films, 440 (2003), 180.
[11] OKUDERA H., HOZUMI A., Thin Solid Films, 434 (2003), 62.
[12] STOBER W., FINK A., BOHN E., J. Colloid. Inter. Sci., 26 (1968), 62.
[13] GREEN D.L., LIN J.S, LAM Y., HU M.Z., SCHAEFER D.W., HARRIS M.T., J. Colloid Inter. Sci., 266 (2003), 346.
[14] BOGUSH G.H., ZUKOVSKI C.F., J. Colloid. Inter. Sci., 142 (1991), 1.
[15] BOGUSH G.H., TRASY M.A., ZUKOWSKI C.F., J. Non-Cryst. Solids, 104 (1988), 95.
[16] COSTA C.A.R., LEITE C.A.P., GALEMBEC F., J. Phys. Chem. B., 107 (2003), 4747.
[17] GREEN D.L., JAYSUNDARA S., LAM Y., HARRIS M.T., J. Non-Cryst. Solids, 315 (2003), 166.
[18] HENCH L.L, WEST J.K., Chem. Rev. 90 (1990), 33.
[19] CATHRO K.J., CONSTABLE D., SOLAGA T., Sol Energy, 32 (1984), 573.

Preparation and structure of stable dispersions of uniform TiO$_2$ nanoparticles

O.B. PAVLOVA-VEREVKINA[1*], S.N. CHVALUN[1],
YU. A. SHEVCHUK[1], L.A. OZERINA[1], A.N. OZERIN [2]

[1]Karpov Institute of Physical Chemistry, Vorontsovo Pole 10, Moscow 105064, Russia

[2]Institute of Synthetic Polymeric Materials, Russian Academy of Sciences,
Profsoyuznaya 70, Moscow 117393, Russia

A set of narrow fractions of anatase TiO$_2$ nanocrystals was isolated by the stepped coagulation of polydisperse hydrosols using strong acids as coagulators. The sols and gels prepared from the fractions were studied by LAXS, SAXS, turbidimetry, dynamic light scattering, and other methods. The shape of uniform titania nanocrystals in the fractions was determined to be plate-like; thickness of the platelets was 2–3 nm and their lateral sizes differed considerably in the fractions. A rapid partial coagulation and slow sol separation processes were observed after the addition of HCl and KCl to the sols. The rapid coagulation threshold was shown to depend essentially on nanoparticles size; the rate of the slow process depended strongly on the electrolyte concentration. Some stable concentrated dispersions of nanometer periodicity were formed from the narrow titania fractions.

Key words: *titania; nanocrystals; hydrosol; fractionation; coagulation*

1. Introduction

Highly ordered titania nanostructures of nanometer periodicity are very promising materials [1, 2]. Their properties depend on the size and shape of nanocrystals, as well on the type of superlattice. These structures can be obtained from titania nanodisperse hydrosols. It is necessary to prepare sols of uniform (monodisperse) nanocrystals and then to conduct sol-gel-xerogel transformations under the control of structural changes.

The fractionation method has been developed, allowing one to isolate uniform titania nanocrystals from hydrosols [3, 4]. From the fractions, stable sols and gels of various dispersity can be prepared. This work concerns the preparation and study of these dispersions.

---

*Corresponding author, e-mail: bvpv@orc.ru

2. Experimental

Nanodisperse TiO_2 hydrosols stabilized by HCl and HNO_3 were used for fractionation. The initial sols were synthesized by hydrolysis of Ti alkoxides and chloride and contained mainly the anatase nanoparticles with brookite impurity [5]. The fractionation was effected by the stepped sol coagulation using the same acid that stabilized the initial sol [3, 4].

The hydrodynamic particle radius R_{HD} was measured by the dynamic light scattering (DLS) method [3]. The optical density D, turbidity spectra, and coagulation thresholds C_c of the sols were studied by UV-vis spectroscopy [4]. TiO_2 weight concentration in the sols was determined by the gravimetric analysis. TiO_2 volume concentration ϕ was calculated from TiO_2 weight concentration and the anatase density equal to 3.84 g/cm^3.

The X-Rays diffraction patterns of titania xerogels were recorded with a diffractometer DRON-3 [4]. Mean sizes of primary anatase crystals L_{hkl} along different directions were calculated by the Scherer formula

$$L_{hkl} = \frac{\lambda}{\Delta \cos \theta}$$

where θ is the diffraction angle, λ – the wavelength, $\Delta = (\Delta_1^2 - \Delta_2^2)^{1/2}$ – the true halfwidth of reflection, Δ_1 – measured halfwidth, Δ_2 – instrumental peak broadening determined from a standard sample.

The SAXS measurements of the sols were carried out using a KRM-1 diffractometer [4]. The scattering coordinate was measured in terms of the scattering vector modulus $s = 4\pi\sin\theta/\lambda$ in the range of s from 0.07 to 4.26 nm^{-1}. The preliminary treatment of the initial scattering curves (smoothing, normalization) was made with the SYRENA software [6].

3. Results and discussion

3.1. Properties of the TiO_2 hydrosols

Nanodisperse sols of anatase particles are stable in the acidic medium at $0.5 < pH < 2.5$ [5]. Positive charge and the surface hydrophilic layer stabilize the particles. These sols have an absorbance peak with a maximum at $\lambda \approx 214$ nm. In the visible range at $\lambda > 450$ nm and at $\phi = $ const, the sols reveal the Rayleigh scattering:

$$I \propto V \lambda^{-4}$$

where I is the intensity of the scattering light, V – the particle volume. The turbidimetry is thus an effective method for studying stabilization and destabilization of sols.

After sol synthesis, the anatase particles usually do not grow bigger but decrease and then stabilize [5]. Thus the aged sols can be divided into two groups – "equilibrium" and "nonequilibrium" sols. The former ones have stable particles which were shown to be the individual anatase nanocrystals. The particles in "nonequilibrium" sols are likely the aggregates of nanocrystals which slowly disintegrate. Some conditions accelerate their disintegration, in particular the acid concentration. It was found [5] that in the "equilibrium" sols synthesized and then aged at room temperature, R_{HD} is usually equal to 8–13 nm.

3.2. Fractionation of TiO$_2$ nanocrystals

For the purpose of fractionation, the "equilibrium" sols are used. Although they have relatively narrow particle size distribution, they are still polydisperse, and narrower fractions can be isolated. The method is based on the partial coagulation of the sols by electrolytes. To initiate the rapid partial coagulation, the electrolyte is introduced into the initial sol in a concentration exceeding the rapid coagulation threshold C_c. For fractionation, three conditions should be fulfilled. The first one is the existence of a strong dependence of the rapid coagulation threshold on particles size. That is, larger nanocrystals should coagulate at lower electrolyte concentrations. The second is the reversibility of the rapid coagulation. This means that if the electrolyte is removed from coagulates, they will be dissolved and transparent sols will be formed again. And the last condition is that the sols prepared from the fractions should be stable at long storage. These conditions are fulfilled if either HCl or HNO$_3$ is used as the coagulator.

By the stepped coagulation we succeeded to isolate five fractions of varying dispersity from the same sol. The initial sol was synthesized from Ti(OBu)$_4$ and stabilized by HNO$_3$. Table 1 shows HNO$_3$ concentrations at which the coagulation was conducted. From these fractions five sols were prepared stabilized by HNO$_3$ with pH 1.

Table 1. HNO$_3$ concentrations used for precipitation of the TiO$_2$ fractions,
R_{HD} and L_{hkl} values of the fractions

Fraction No.	[HNO$_3$] [mol/dm^3]	R_{HD} (± 1) [nm]	L_{101} (± 0.4) [nm]	L_{200} (± 0.4) [nm]
1	0.5–0.8	16	5.6	4.6
2	0.8–1.0	13	4.5	3.6
3	1.0–1.2	9	4.1	3.5
4	1.2–1.5	7	3.9	3.4
5	1.5–1.8	5	2.9	3.3

Figure 1 shows the mean particle radius R_{HD} for the initial sol and its fractions measured at various Ti concentrations. The figure clearly reveals the varying dispersity of the fractions. The sols obtained were found to be very stable: their turbidity did not change during 1.5 year of observation.
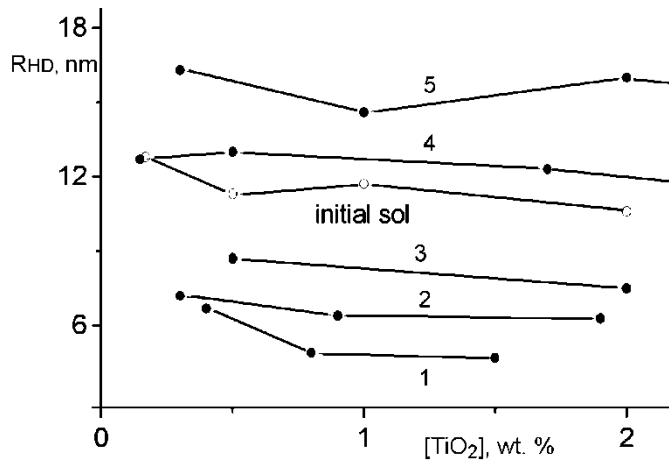
Fig. 1. Dependences of the mean hydrodynamic particle
radius on TiO$_2$ concentration for the initial sol and its fractions.
Numbering of fractions corresponds to that in Table 1

Figure 2 shows the diffraction patterns of the same fractions. All patterns are charac-
teristic of the nanocrystalline anatase. Curve 5 has the broadest peaks, thus fraction 5 is
composed of the smallest nanocrystals. Curve 1 represents the biggest ones.
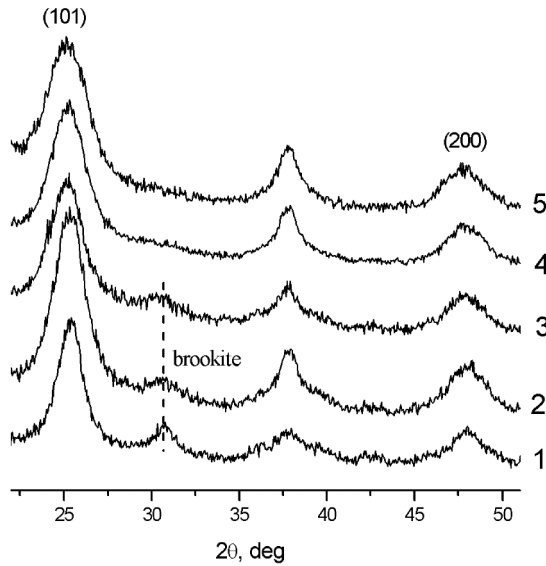

Fig. 2. Diffraction patterns of the TiO$_2$ fractions

The sizes L_{101} and L_{200} of anatase crystals as well as R_{HD} values in the fractions are
shown in Table 1. One can see that in the series of the five fractions, these sizes

change consecutively and larger nanocrystals coagulate at lower acid concentrations. Because the initial sol contained the brookite impurity, the brookite phase is also present in the isolated fractions. However, brookite is present only in three coarser fractions (1–3). Thus the fractionation method allows us also to purify anatase nanocrystals of brookite impurity or, on the contrary, to concentrate the brookite nanocrystals.

For many titania applications (in particular for the catalysis) it is necessary to remove water and acid from xerogels by thermal treatment. Figure 3 shows the diffraction patterns of the fractions after their annealing at 500 ºC for 2 h. It can be seen that after annealing, the anatase nanocrystals grew in all fractions and in the coarsest fraction 1 the large rutile crystals appeared. This experiment reveals that to obtain uniform anhydrous TiO₂ with high surface area one should use sols of pure anatase.
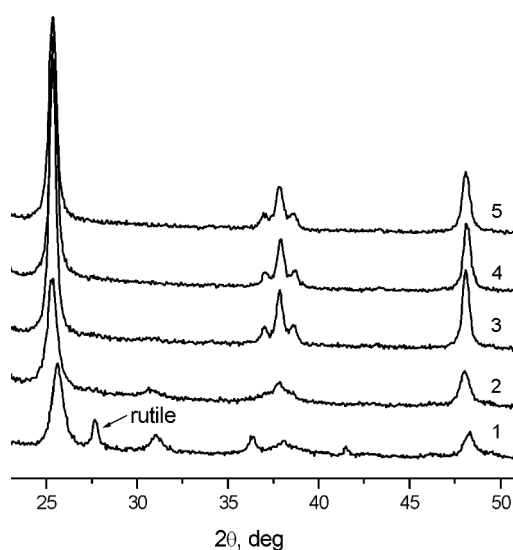

Fig. 3. Diffraction patterns of TiO₂ fractions after annealing at 500 ºC for 2 h

The fractions were also compared by SAXS. Figure 4 shows the scattering curves of the diluted sols prepared from fractions 1 and 5. Their analysis [4] allowed us to determine not only the particle gyration radius R_g but also the particle shape.

Table 2. R_g and characteristic sizes of TiO₂ platelets
for fractions 1 and 5 determined by SAXS

Parameter	Fraction 5	Fraction 1
R_g (±0.2), nm	7.6	10
Characteristic size, nm³	2×7×20	3×18×35

It was established that the anatase particles in these fractions are platelets. Their thickness was 2–3 nm and their lateral sizes differed considerably. The characteristic sizes of the platelets, as well as the R_g values, are given in Table 2.
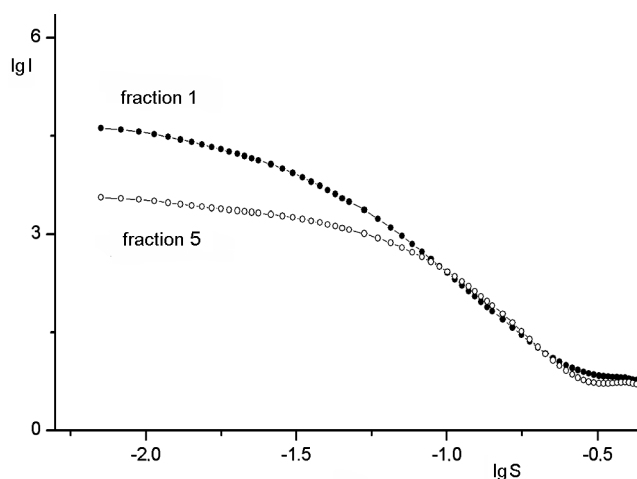
Fig. 4. SAXS curves of fractions 1 and 5

3.3. Destabilization of TiO$_2$ hydrosols by electrolytes

Since the fractionation method is based on the coagulation, the coagulation has been studied in more detail to improve the method. After introducing the electrolyte into the sol prepared from a fraction at least two different processes can occur – rapid partial coagulation and slow sol separation. The rapid coagulation occurs only above the threshold electrolyte concentration C_c, while the slow process takes place at both low and high electrolyte concentrations. The slow process appears at the beginning as monotonous growth of turbidity, and then the graduate sol separation appears. The rapid and the slow processes are studied separately.
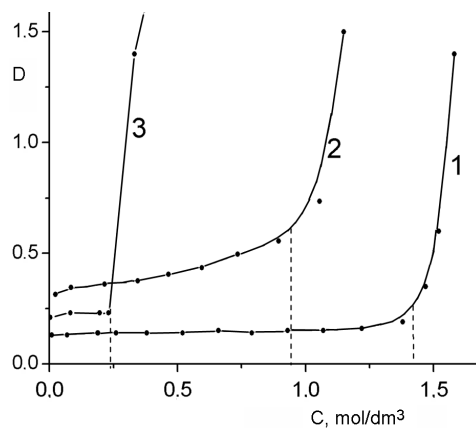

Fig. 5. Turbidity of the sols prepared from three fractions via HCl concentration.
R_{HD} of the initial sols are 5 (1), 8 (2) and 14 (3) nm.
The dashed lines represent rapid coagulation thresholds of the fractions

At first, the rapid coagulation was studied by turbidimetry. Figure 5 shows the rapid coagulation by HCl of three fractions with R_{HD} equal to 5, 8 and 14 nm. The turbidity was measured 2 min after adding acid additives to the initial sol. The inflection points on the turbidity dependences on HCl concentration are the rapid coagulation thresholds. It can be seen that C_c does depend strongly on the particle size. When KCl was used as the coagulator, the picture was rather similar, but C_c depended also on pH.

The complex of long-term experiments on the slow sol separation is in progress now. The nature and mechanism of this process is not clear yet. It may include the Ostwald ripening and slow coagulation. Its rate depends on electrolyte type and concentration, nanocrystals dispersity, medium pH. To understand the separation process, the impact of the factors mentioned and its reversibility should be studied. Figure 6 shows the first kinetic dependences obtained for a series of sols with KCl added.
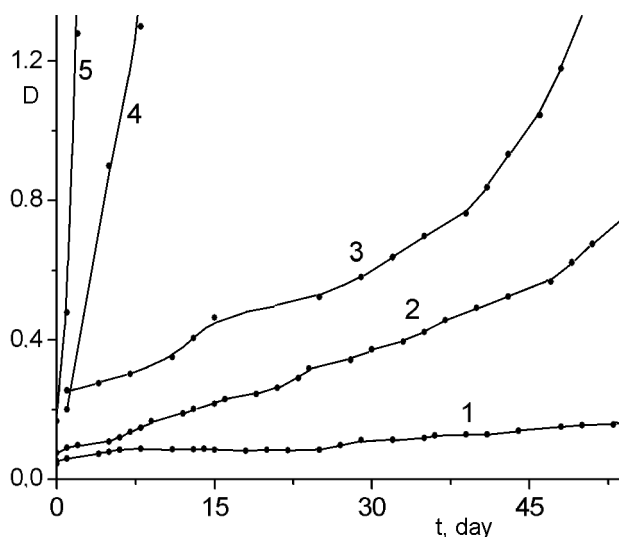

Fig. 6. Kinetics of the slow growth of turbidity of the sols
with KCl concentration 0.25 (1), 0.5 (2), 0.7 (3), 1.1 (4) and 1.4 (5) mol/dm^3

Different ammounts of KCl were introduced into the initial stable sol with an R_{HD} = 5 nm, pH 2.1, and low turbidity. KCl concentration in the sols varied from 0.25 to 1.4 mol/dm^3, which was below C_c of the given fraction (1.6 mol/dm^3 KCl). After introducing the salt, slow clouding of the sols instantly began. From Figure 6 one can see that for a moderate initial period, the turbidity grew monotonously, the process rate increasing strongly with salt concentration. Then the process accelerated and later the sols separated slowly into two layers. The dispersion pH did not change during the whole experiment.

Preliminary DLS and SAXS measurements show that during the slow separation process the mean particle radii increase. First investigations of the reversibility of the

process reveal that the process is partially reversible. One can hope that further investigations of the peculiarities of sol destabilization by electrolytes will allow us to isolate even narrower fractions of titania nanocrystals.

3.4. Preparation of concentrated dispersions of uniform nanocrystals

We have succeeded in obtaining some stable concentrated dispersions (sols and gels) of nanometer periodicity from narrow fractions of anatase nanocrystals. The concentrated sols appeared to be stable only at a very narrow interval of pH close to 1. To prepare them, the dilute sols prepared from fractions and stabilized by HCl were ultrafiltrated and then evaporated in air. A series of sols with titania concentration ϕ from 1 to 21 vol. % and pH 1 was prepared from the fraction with $R_g = 5.5$ nm. The initial sol was obtained by electrolysis of $TiCl_4$ [7]. Its fractionation was done with HCl. The sols prepared were studied by SAXS. Some of the scattering curves obtained are shown in Fig. 7. From curve 1 corresponding to the diluted (1 vol. %) sol, the shape of nanoparticles in the fraction was determined. The particles found to be also plate-like, but the characteristic sizes of the platelets were $3\times14\times18$ nm^3.
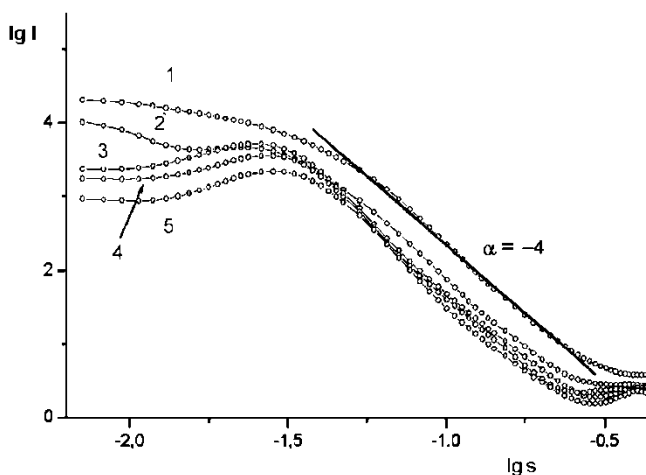
Fig. 7. SAXS curves of the sols with pH 1 and TiO_2 concentration
1(1), 12 (2), 15 (3), 18 (4) and 21 (5) vol. %

It can be seen from curves 2–5 in Fig. 7 that the scattering curves of the concentrated sols with $\phi = 12$–21 vol. % have a maximum whose position depends on ϕ. The estimated long period L is equal to 21–29 nm.

Figure 8 shows the dependence $L(\phi)$ in the logarithmic scale. The slope of the straight line was found to be equal to 0.43 ± 0.05. This value is essentially larger than the value 0.33 that is known to be characteristic of the isotropic liquids. Obviously, the plate-like shape of titania nanoparticles governs their slight orientation in plane.
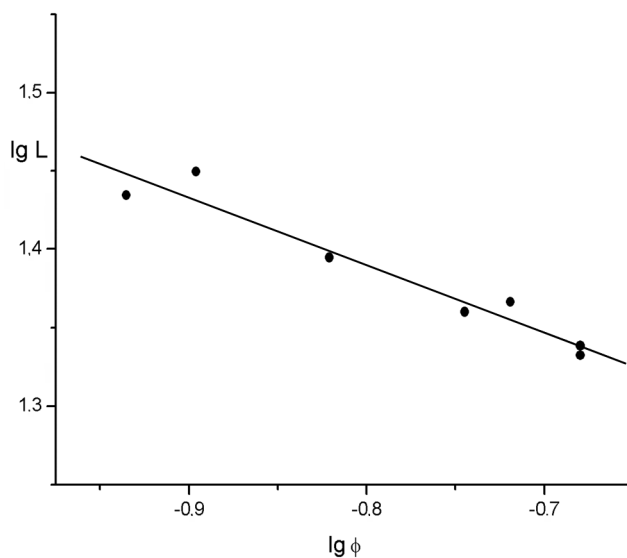
Fig. 8. Dependence of long period on volume concentration of the concentrated sols

Upon further concentrating the sol, at titania concentrations above 21–23 vol. %, the sols either gelate remaining uniform in volume or separate into two stable phases – dilute blue sol on top and viscous concentrated gel below. The consistence and structure of various titania gels were found to depend mostly on the content of acid in the dispersion medium.
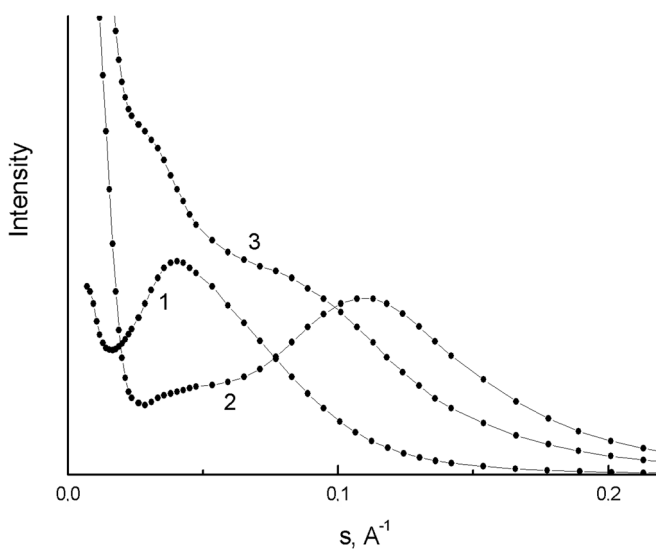
Fig. 9. SAXS curves of the gels with HCl concentration 0.2 (1), 0.6 (2) and 1.4 (3) mol/dm³

Figure 9 shows scattering curves of three gels prepared by different methods. The gels were relatively similar in titania concentrations (ϕ = 24–30 vol. %) and in dispersity (R_g = 5–6 nm) but differed in HCl concentration in the dispersion medium: 0.2, 0.6 and 1.4 mol/dm^3. The latter concentration exceeded the coagulation threshold for this fraction (C_c = 1.2 mol/dm^3 HCl). It can be seen that the three gels have qualitatively different structures characterized by nanometer periodicity. The long periods calculated from the maxima are in the interval 6–20 nm. Two of the curves have two maxima each. One could propose that the structure of some such ordered dispersions is close to liquid crystals. It should be emphasized that the ordered structures of nanometer periodicity were formed only from very narrow titania fractions but not from the initial polydisperse sols.

4. Conclusions

- A set of narrow fractions of anatase TiO$_2$ nanocrystals was isolated by the stepped coagulation of the polydisperse hydrosols using strong acids as the coagulator.
- After annealing, the fractions had different phase composition and dispersity.
- Stable hydrosols and ordered dispersions of nanometer periodicity were prepared from the fractions isolated.
- Electrolytes initiate rapid and slow separation of TiO$_2$ sols. The rapid coagulation threshold depends essentially on nanoparticles size; the rate of the slow process depends strongly on electrolyte concentration.
- Hydrosols of uniform TiO$_2$ nanoparticles can be precursors for preparation of novel highly ordered nanomaterials.

References

[1] Burnside S.D, Shklover V., Barbé C., Comte P., Ardense F., Brooks K., Grätzel M., Chem. Mater., 10 (1998), 2419.
[2] Chemseddine A., Moritz T., Eur. J. Inorg. Chem., (1999), 235.
[3] Pavlova-Verevkina O.B., Shevchuk Y.A., Nazarov V.V., Coll. J., 65 (2003), 474.
[4] Pavlova-Verevkina O.B., Chvalun S.N., Politova E.D., Nazarov V.V., Ozerina L.A., Ozerin A.N., J. Sol-Gel Sci. Techn., 35, (2005), 91.
[5] Pavlova-Verevkina O.B., Politova E.D., Nazarov V.V., Coll. J., 61, (1999), 359.
[6] Feigin L.A., Svergun D.I., *Structure Analysis by Small-Angle X-ray and Neutron Scattering,* Plenum Press, New York, 1987.
[7] Sharigin L.M., Malih T.G., Loguntzev E.N., Shtin A.N., Zh. Prikl. Chim., 6 (1980), 1277.

Organization of silica spherical particles into different shapes on silicon substrates

B. KORUSIEWICZ[1], K. MARUSZEWSKI[1,2*]

[1]Wrocław University of Technology, Institute of Materials Science and Applied Mechanics, ul. Smoluchowskiego 25, 50-370 Wrocław, Poland

[2]Electrotechnical Institute, ul. Skłodowskiej-Curie 55/61, 50-369 Wrocław, Poland

One of the classes of materials that can be obtained via the sol-gel method are uniform sub-micron silica spherical particles. When deposited on a substrate, they typically form random patterns. In this work, we introduce a method allowing one to influence the shape of the structures created on a substrate by the silica spheres. The silica spherical particles with diameter of about 500 nm where deposited on silicon substrates using a simple process of sedimentation. Various structures, like grooves and pits, were earlier prepared by wet etching on surfaces of these silicon substrates. The process led to arranging the silica spheres within the silicon structures, reproducing the shapes of the substrates. The preliminary results are documented by the images from a scanning electron microscope (SEM). Further research on improvement of the patterns forming is under way.

Key words: *silica spherical particles; the sol-gel method; patterning*

1. Introduction

One of the classes of materials that can be obtained via the sol-gel method are uniform sub-micron silica spherical particles [1]. The process of producing them is simple and cheap, and they can be easily modified or doped. Due to this fact, they have found a wide range of applications. For example, uniform sub-micron silica spherical particles can be used as drug carriers [2] or, by adding silver, they gain bacteriostatic properties and can be added to textiles [3]. One of the most interesting possible applications of such particles is creation of photonic crystals [4]. The function of photonic crystals is based on periodical change of the refractive index. A three-dimensional photonic crystal can be achieved by creating a "crystal" from regularly arranged, closely packed sub-micron spheres. This has been already demonstrated [5] but the

_____

[*]Corresponding author, e-mail: krzysztof.maruszewski@pwr.wroc.pl

methods used are sophisticated and expensive. We propose another, simple and cheap method of organizing silica spherical particles into different shapes by using silicon substrate with earlier prepared structures. The possibility of creating various shapes from sub-micron spherical particles could be very useful, not only for obtaining photonic crystals.

2. Experimental

The uniform sub-micron silica particles were synthesized following the modified Stöber method [6]. A mixture of ethanol (EtOH), aqueous ammonia solution (NH$_4$OH) and deionized water was mixed with tetraethoxysilane (TEOS). The solution was stirred in a plastic flask with a magnetic stirrer at room temperature for 1.5–2 h. Then the material was left to dry and after the evaporation of the solvent, white powder was obtained. This powder consisted of sub-micron silica spherical particles with diameter of about 500 nm. The morphology of the particles has been characterized with a transmission electron microscope (TEM).

Silicon substrates with earlier prepared various structures, like grooves and pits on their surfaces, were used. These structures were made using the standard procedure of anisotropic, wet silicon etching in KOH [7]. Before putting the silica particles on the silicon substrates, they were cleaned using the standard silicon wafer cleaning procedure. The substrates were first immersed in a hot mixture of NH$_4$OH, hydrogen peroxide (H$_2$O$_2$), and deionized (DI) water (the ratio of 1:1:5), in order to remove traces of organic residues. After that, they were rinsed with deionized water. Next, a thin layer of silicon dioxide (SiO$_2$) was removed by dipping in a hydrofluoric acid (HF) and DI water solution (1:50) followed by another rinsing with DI water. Then, the substrates were immersed in a mixture of hot hydrochloric acid (HCl$_{(aq.)}$), H$_2$O$_2$, and DI water (1:1:6). This mixture was used to remove ionic contaminants, especially metals. Finally, they were again rinsed with DI water and dried. The pictures of cleaned silicon substrates characterized with a scanning electron microscope (SEM) are shown in Fig. 1. SEM measurements of cleaned silicon substrates were performed on a scanning electron microscope Joel JSM 5800LV.

The silica spherical particles where deposited on silicon substrates using a simple process of sedimentation. They were dispersed in DI water with ultrasonic stirring and then directly applied onto the silicon substrates and left to sediment. Some of the samples were dipped in the colloid, so they were fully covered with the liquid and on some of them, a small amount of the colloid was gently dropped. The effects of this procedure were investigated using a scanning electron microscope (SEM). SEM measurements of silicon substrates with silica spheres were performed on a scanning electron microscope Hitachi S-570.
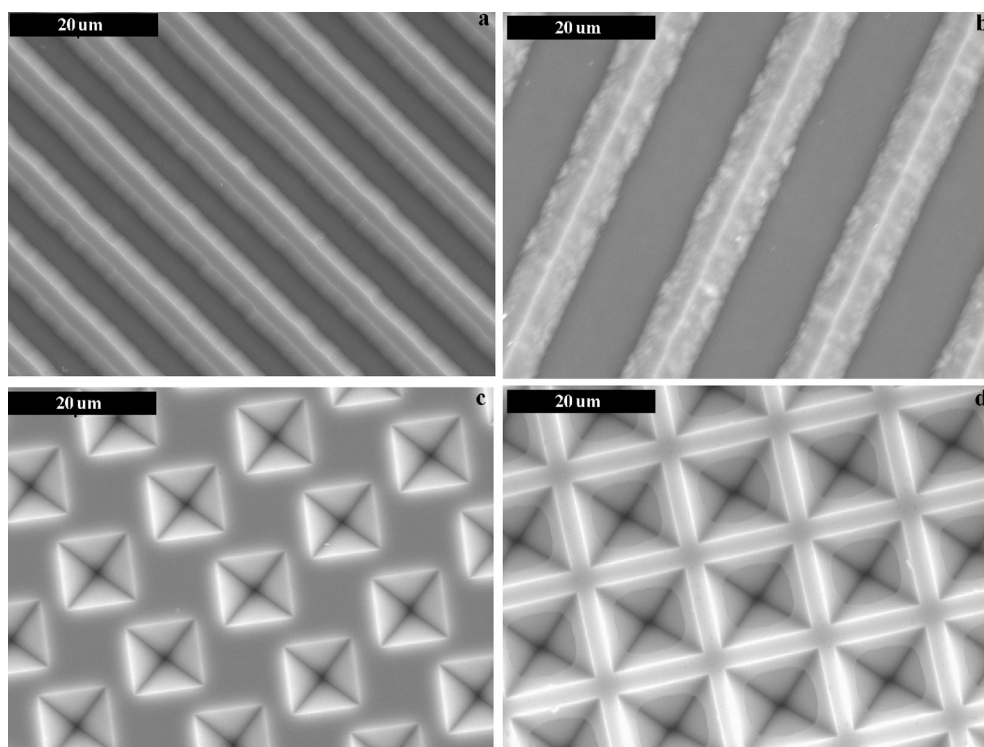
Fig. 1. SEM micrographs of the silicon substrates with etched structures: grooves (a, b) and pits (c, d)

3. Results and discussion

The effect of this approach was the forcing of the silica spheres to create definite patterns by arranging them in the silicon structures. It could be said that, instead of creating random patterns, they reproduced the shapes of the substrates. Figure 2 shows silica spheres within the silicon grooves. As it can be seen in Fig. 2a, all the particles are inside the structures – there are no spheres outside the grooves. Even at the ends of the grooves, the silica spheres perfectly fit within them (Fig. 2b) and there are only a few particles outside the grooves in some distance from their ends. The silica spheres on other silicon structures are shown in Fig. 3. Almost all particles are inside the pits, as in the previous case.

In the presented experiments, the amount of silica spheres on the substrates was relatively small. When the number of the particles is increasing, then, after filling up the pits or grooves, they start to fill out the space between the structures, as can be seen in Fig. 4. However, the order in their arrangement is still clearly visible. When the number of the particles is still increased they tend to create "continuous" layers on

the substrates (Fig. 5). However, even then, instead of creating random patterns, they "imaged" the distribution of the structures on the substrate surfaces.
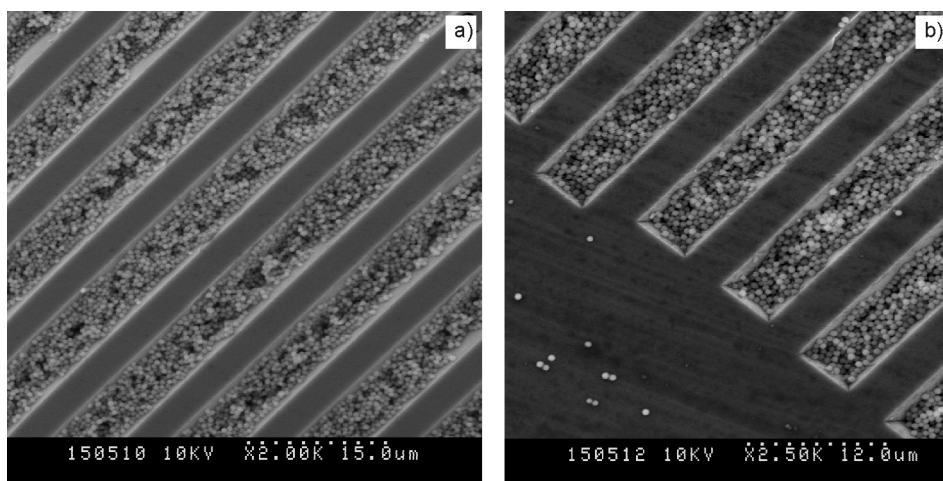
Fig. 2. SEM micrograph of the silica spherical particles within the silicon grooves;
b) – view at the end of the grooves
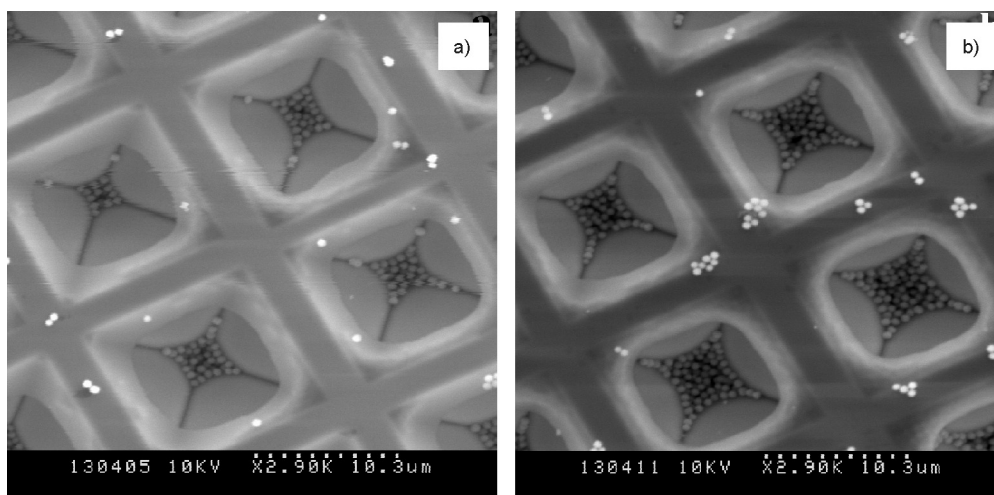
Fig. 3. SEM micrographs of the silica spherical particles
within the silicon pits (a, b – two different samples)

As has already been mentioned, the effect of the described process strongly depends on the amount of silica spherical particles deposited on the silica surface. This of course can be controlled by the concentration of the colloid put on the samples. Another parameter which can be controlled is the amount of the colloid, which indi-

rectly defines the time of the deposition – more of the colloid means longer time needed for evaporation of the liquid. However, because of the simplicity of the sedimentation process used, the possibility to control this process is very limited. The "continuous" layer of the silica particles was obtained by using relatively large amount of the colloid with a high concentration.
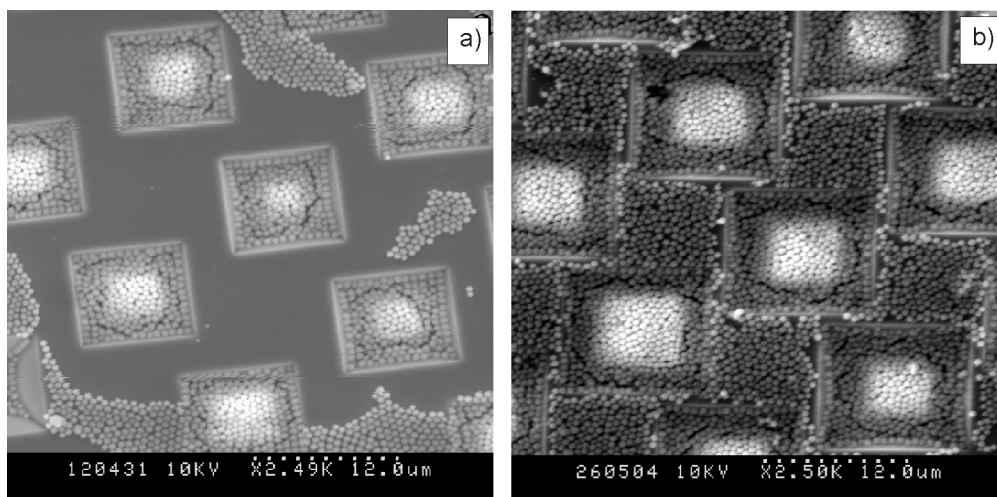

Fig. 4. SEM micrographs of the silica spherical particles within and outside of the silicon structures: a) smaller amount of the deposited particles, b) bigger amount of the deposited particles
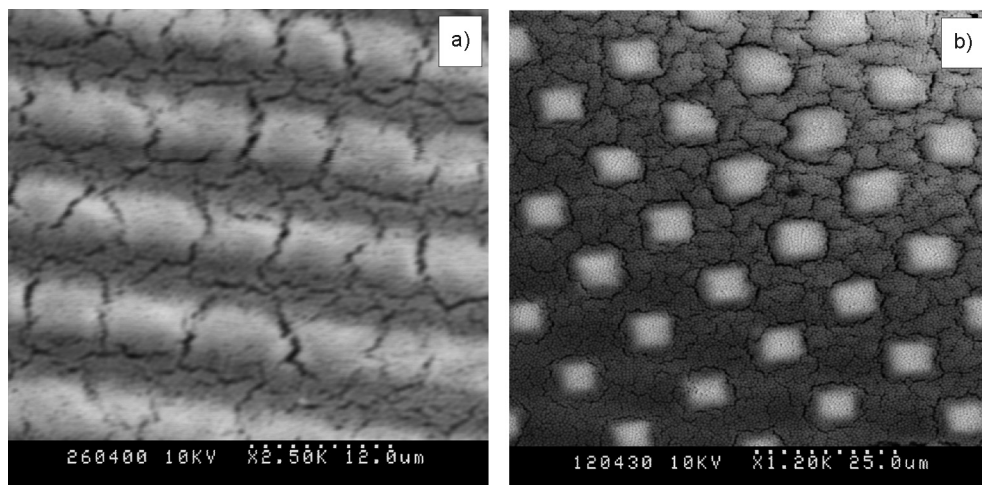
Fig. 5. SEM micrographs of the silica spherical particles creating a "continuous" layer on the silicon substrates with grooves (a) and pits (b)
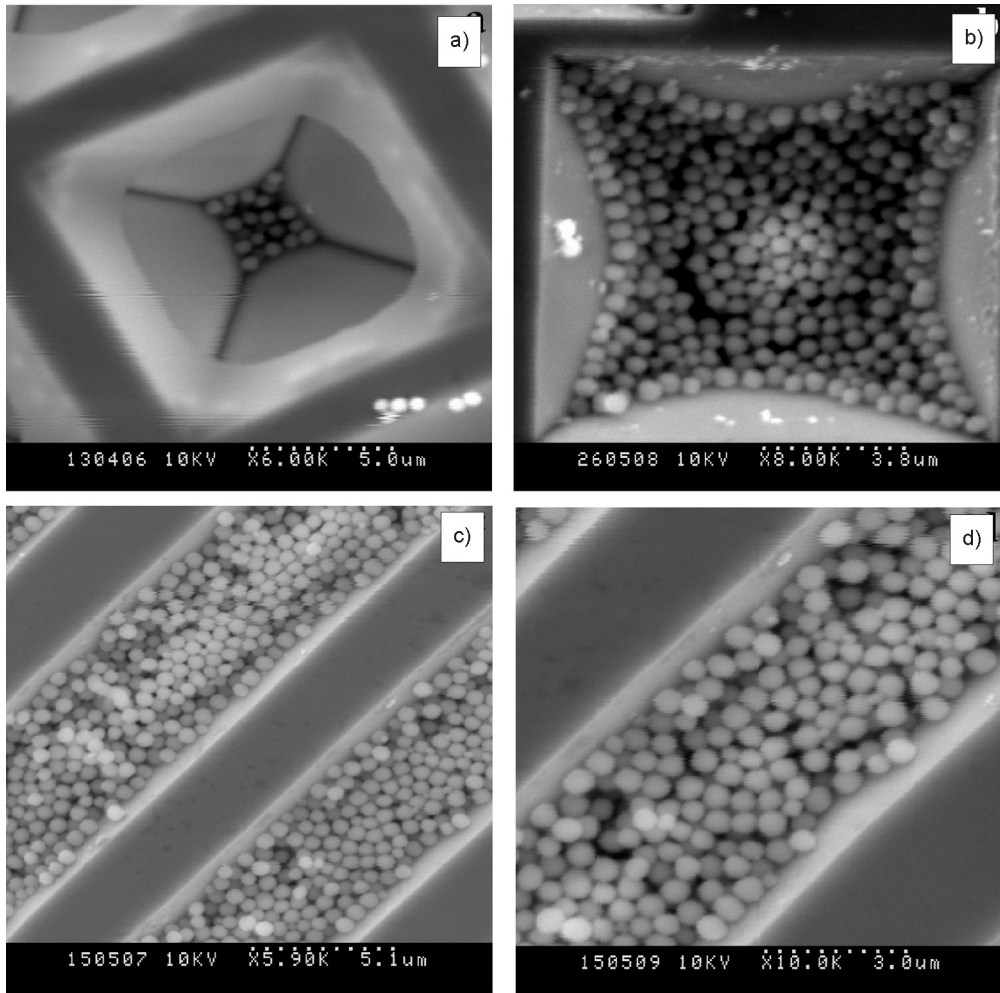
Fig. 6. SEM micrographs close-up of the silica spherical particles
within silicon structures: pits (a, b) and grooves (c, d)

Figure 6 presents the close-up of the silica spherical particles inside the silica pits (Fig. 6a, b) and grooves (Fig. 6c, d). As can be seen, the arrangement of the silica spheres within the single structure is no longer so ideal. The edges of the pits and grooves limit the place for the silica particles to settle, but within the structure the positions of the spheres are more or less random. This is so because the dimensions of the silicon structures are 5–10 μm so they are 10–20 times larger then the diameter of the silica spherical particles. The results could be improved by reducing the size of the structures. Another factor is that the silica particles have a tendency to attract each other and create larger structures. It is caused by the process of coagulation. This can

be either undesirable or desirable if the growing structures reproduced the given pattern.

It has to be mentioned that not for all the prepared samples, and in some cases not for the whole surface of the sample, we have achieved so encouraging effects. It is related to the method of deposition of silica spheres on the substrates by using the simple process of sedimentation. This could be improved by a more "active" way of deposition, for example by some mechanical shaking of the substrates or by using electrical field to organize the depositing particles.

4. Conclusions

We have presented a simple method of organization of silica sub-micron spherical particles into different shapes by using various silicon substrates with earlier prepared structures. The use of silicon substrates with structured surfaces and filling them with the silica spheres presents the possibility to arrange the spherical particles into various shapes. We can fill the structures with small amounts of spheres for precise arrangement or cover them with a "continuous" layer which images the distribution of the structures on the surface. The precision and resolution of the created patterns can be improved by reducing the size of the structures. The effectiveness of arranging the silica spheres can be also increased by more "active" methods of depositing them on the substrates. Further research on the improvement of pattern-forming by silica spherical particles, not only by using silicon substrates with structures, is under way.

References

[1] BRINKER C.J., SCHERER G.W., *Sol-Gel Science*, Academic Press, San Diego, 1990.
[2] LI ZH.-ZH., WEN L.-X., SHAO L., CHEN JI.-F., J. Contr. Rel., 98 (2004), 245.
[3] JASIORSKI M., BAKARDIJEVA S., DOROSZKIEWICZ W., BRZEZIŃSKI S., MALINOWSKA G., MARCINKOWSKA D., ORNAT M., STRĘK W., MARUSZEWSKI K., Mater. Sci.-Poland, 22 (2004), 137.
[4] JASIORSKI M., MARUSZEWSKI K., STRĘK W., Mater. Sci.-Poland, 20 (2002), 51.
[5] RECULUSA S., MASSÉ P., RAVAINE S., J. Coll. Int. Sci., 279 (2004), 471.
[6] STÖBER W., FINK A., BOHN E., J. Coll. Int. Sci., 26 (1968), 62.
[7] ZUBEL I., *Forming spatial structures in silicon by anisotropic etching for applications in microelectronics* (in Polish), Wrocław Technical University Press, Wrocław, 2004.

Enhanced corrosion resistance for silsesquioxane coatings by diglycidyl ether of biphenol A

P. Chen[1], L. Hu[2*], X. Zhang[2], D. Sun[2]

[1]Chemical Center, Harbin University of Commerce, Harbin 150076, China

[2]Department of Environment engineering and Department of Applied Chemistry,
Harbin Institute of Technology, Box 713, Harbin 150001, China

Based on silsesquioxanes (SSO), derived from hydrolytic condensation of (γ–glycidoxylpropyl)-trimethoxysilane (GPMS) and various amounts of tetraethoxysilane (TEOS), hybrid films (f-GST) were prepared using the sol-gel process. Because the epoxy-ring opening or the silica chains were not fully cross-linked, the f-GST was more susceptible to corrosion due to higher hydroxyl content and its hydro-philicity. Diglycidyl ether of biphenol A (DGEBA) was added into the reaction system to enhance the density of the film and to prevent epoxy ring opening during condensation. The film prepared with DGEBA, GPMS-SSO (GS) and 20 wt. % TEOS (f-GSTD) exhibited the best corrosion resistance compared with f-GST and bare aluminum alloy (AA). The f-GST and f-GSTD were studied as anticorrosion coatings on AA by electrochemical measurement. The results clearly demonstrate that samples with higher TEOS fractions have better anticorrosive performance and DGEBA obviously enhances the anti-corrosion effect of f-GST.

Key words: *silsesquioxane; sol-gel; coatings; anticorrosion; electrochemical measurement*

1. Introduction

Silsesquioxane (SSO) compounds play an important role in coating film applications. These attractive engineering materials provide new opportunities to incorporate and release corrosion inhibitors due to their properties [1, 2]. In the early 1950s, Brady's group [3] at Dow Corning produced SSO copolymers (phenylsilsesquioxane-alkylsilsesquioxane) which were of low molecular weight but with high hydroxyl functionality on superstructures for corrosion protection of naval aircraft coatings. Du et al. [1, 4, 5] examined epoxy-SSO hybrid coatings on aluminum alloy (AA) substrates for corrosion protection using wet adhesion testing and electrochemical analy-

---

ses. However, epoxy rings open in the hydrolytic condensation of GPMS, which may result in an incomplete crosslinked network and cracks in the film allowing water to be absorbed to the metal surface where corrosion occurs. Schmidt [6] found that controlled ring-opening reactions increased wettability, and diol crosslinking was found to improve corrosion resistance.

In the previous study, we reported the synthesis and characterization of SSO obtained from the hydrolytic condensations of (3-glycidoxypropyl)trimethoxysilane (GPMS-SSO, GS), with spectroscopic techniques (FTIR, NMR and UV-MALDITOF MS) [7, 8]. Properties (hardness, modulus, scratch, and abrasion) of the GS films (f-GSs) were measured with nanoindentation and nanoscratch techniques [9]. In this work, f-GSs are investigated as anticorrosion coatings on AA. Diglycidyl ether of biphenol A (DGEBA) and tetraethoxysilane (TEOS) are added to the reaction system to enhance the density of the f-GS and to prevent epoxy ring opening during condensation. The modified films act as corrosion inhibitors and enhance corrosion resistance.

2. Experimental

Reagents. Commercial (3-glycidoxypropyl)trimethoxysilane (GPMS, Sigma G 1535) was used in the examination of hydrolytic condensation reactions; diglycidyl ether of biphenol A (DGEBA) and tetraethoxysilane (TEOS) were employed as modifiers; formic acid (HCOOH, 98%), an analytical grade reagent, was used as a catalyst, ethanol (C_2H_5OH, 99.7 %) was used as a solvent, and ethylenediamine (EDA), an analytical grade reagent, was the hardener.

GPMS-TEOS SSO. The hydrolytic condensation of GPMS with different fractions of TEOS (0, 5, 10, 15, 20, 25 and 30 wt. %) was carried out in beakers placed in a water bath using HCOOH in the molar ratio HCOOH/Si = 3. The reaction was performed in three stages: plastic films were used to seal the beakers for 3 days (1); then several small needle-sized holes were made on the films before the reaction continued for another 3 days (2); and, finally, the film was removed and the reaction was continued for 4 days (3). The temperature at every stage was maintained at 35 ºC. The TEOS-modified SSO based on GPMS will be denoted as GST (GPMS–SSO–TEOS).

GPMS–TEOS-DGEBA SSO. To produce GPMS–TEOS-DGEBA SSO (GSTD), the same procedure as above was carried out with the fraction of TEOS 15 wt. %, and a the third stage DGEBA was added as a solvent (50% of the total number of epoxy groups were supplied by the solvent).

SSO films. The resulting SSO was diluted with ethanol (molar ratio Si/C_2H_5OH = 1/4) and then a theoretical amount of EDA (molar ratio Si/EDA = 4/1) was added. Dip-coating on the AA LY12 ($40 \times 10 \times 2$ mm^3) was performed three times at 6-hour intervals with a dipping speed of 300 mm/min. After dipping, the coated samples were

put into a heating oven at 80 ºC for 6 hours, followed by 4 hours at 120 ºC. Coatings based on GST will be denoted as f-GST; f-GST with a different TEOS content will be denoted as f-GST$_{i\%}$ (i = 0, 5, 15, 20, 25 and 30 wt. %); f-GSTD will be denoted as f-GST$_{10\%}$ containing 50 wt. % DGEBA modifier; and the AA coated with f-GST$_{i\%}$ will be denoted as AA–GST$_{i\%}$.

Electrochemical test. Electrochemical measurements were performed using an M 263A device (AMETEK) and a three-electrode cell equipped with a saturated calomel reference electrode (SCE), a platinum counter electrode, and a coated or non-coated AA panel as the working electrode with an exposed area of 1.0 cm^2. All measurements were conducted in an aqueous 3.5 wt. % NaCl working solution at room temperature. The electrodes were kept in the working solution for 30 min prior to measurements, with the electrical circuit opened. 352 SoftCorr III corrosion measurement software was used to analyze the potentiodynamic polarization curves. The potential scanning range was from –1 V to ca. 1.2 V with a scanning rate of 2 mV/s.

Salt spray test. Corrosion protection properties of the coated and non-coated AA substrates were evaluated by exposing the substrates to a salt spray atmosphere of 5 wt. % aqueous NaCl solution at 35 ºC. After removing from the salt fog chamber, all samples were rinsed with distilled water to remove any residues. Scanning electron microscopy (SEM) was performed on the bare and coated substrates to characterize the surface morphology before and after running the corrosion test.

3. Results and discussion

The anticorrosive performance of different sample coated films can be examined from the values of corrosion potential (E_{corr}) and corrosion current (I_{corr}). As listed in Table 1, the AA-GST shows a higher E_{corr} and lower I_{corr} than bare AA, but a lower E_{corr} and higher I_{corr} than the AA-GST$_{i\%}$ (i = 5, 10, 15, 20, 25 and 30 wt. %). Figure 1 shows typical polarization curves of bare AA, AA-GST$_{10\%}$ and AA-GSTD. The polarization curves among AA-GST, AA-GSTD, and AA are different:

• The open circuit potentials of the AA-GST$_{10\%}$ and AA-GSTD are significantly higher than those of the bare AA.

• The rather lower current density of 6.02×10^{-9} A/cm^2 results from the f-GSTD barrier that breaks down at a high electric potential and results in a failure of corrosion.

• The AA-GST$_{10\%}$ exhibits a different potentiodynamic polarization curve from AA-GSTD and AA and there is no obvious passivation region.

The I_{corr} values of three samples are in the order of AA-GSTD<AA-GST$_{10\%}$<AA, which implies that the AA-GSTD and AA-GST$_{10\%}$ coatings indeed provide a physical barrier for blocking the electrochemical corrosion process. Current density initially increases rapidly, indicating an active electrochemical reaction. Furthermore, a rapid increase in electric potential results in the current density. For f-GSTD, a combination

of DGEBA, GS and 20 wt. % TEOS content produces hybrid materials with the best corrosion resistance properties. It is not prone to cracking during the curing period due to the slower speed used to produce homogeneous and dense coatings. This novel enhanced anticorrosion f-GSTD effect (as compared to the effect of f-GST) might have arisen from dispersing SiO_2 dense particles and organic fractions in a GSTD matrix to block the diffusion pathway of oxygen and water (see Figure 2). The previous study has evidenced the barrier effect of the PMMA-clay nanocomposites on O_2 and H_2O molecules [10].

Table 1. Electrochemical parameters of bare AA
and AA coated with films of various compositions

| Sample	Feed composition [wt. %]			Electrochemical parameter	
	GPMS	TEOS	DGEBA	E_{corr} [mV]	I_{corr} [nA/cm^2]
AA	0	0	0	−1016.0	5755.00
AA-GS	100	0	0	−735.8	2089.00
AA-GST$_{5\%}$	95	5	0	−721.2	287.50
AA-GST$_{10\%}$	90	10	0	−713.4	173.50
AA-GST$_{15\%}$	85	15	0	−745.8	19.08
AA-GST$_{20\%}$	80	20	0	−725.0	12.42
AA-GST$_{25\%}$	75	25	0	−645.4	73.71
AA-GST$_{30\%}$	70	30	0	−696.7	55.14
AA-GSTD	40	10	50	−595.5	6.02
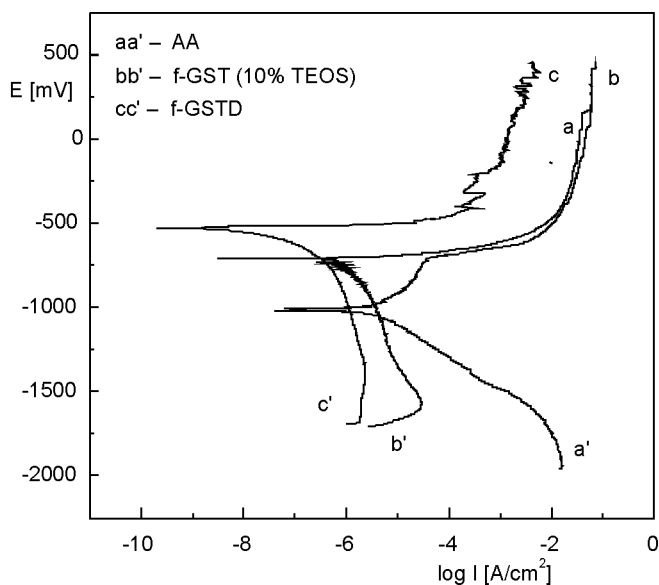
Fig. 1. Typical polarization curves of bare AA, AA-GST$_{10\%}$, and AA-GSTD.
The data were for a 3.5 wt. % NaCl aqueous solution
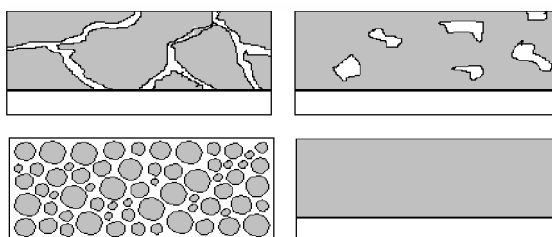
Fig. 2. Dispersion results of SiO$_2$ particles and organic fractions in a GTS
matrix block (down) and the diffusion pathway of oxygen and water (up)

The SSO films and processing conditions strongly influence the anticorrosion properties of coatings. A sol-gel network based on linear silica chains would undergo an extensive cross-linking by hardener EDA leading to the formation of a dense coating. f-GST derived from the hydrolysis-condensation of GPMS, TEOS and EDA curing, unlike the f-GSTD coatings, produces relatively brittle films prone to cracking and degrades corrosion resistance. Although all six SSO films (f-GST$_{5-30\%}$) show significantly improved anticorrosion properties of coatings, there are obvious differences among those coatings (Table 1). AA-GST$_{20\%}$ shows better corrosion current due to an adequate amount of TEOS to fabricate a denser structure, and AA-GSTD shows the best anticorrosion properties as to corrosion current and corrosion potential. Previous studies have shown that GPMS is susceptible to ring opening reactions that form diol, alkoxy alcohol, and polyether products during the hydrolytic condensation [11–14]. Additional reaction products of the diol groups are possible in the presence of excess of alcohol and metal alkoxide leading to etherification or esterification between the OH groups and epoxy groups of DGEBA with the production of –CH$_2$–CH(OH) –CH$_2$OR functionalities [15]. R may be –CH$_3$, –C$_2$H$_5$, –SiO$_{1.5}$ and Si–(O$_{0.5}$)$_2$R′ units [16]. Polyether formation is also possible in GS films [17]. This additional reaction can make the crosslinking network denser and inhibit corrosion.

In the GSTD sol process, DGEBA was added into the GPMS system to control the ring-opening reaction. Williams et al. [18] found that the high stability of the GPMS -SSO/DGEBA solution and the epoxy rings of both GPMS and DGEBA were intact during the synthesis, which stemmed from the very low concentration of SiOH groups.

Figures 3a–c show the camera images of three samples after electrochemical measurements in 3.5 wt. % NaCl solution. Compared with the image of AA-GSTD, significant corrosion was found in both AA and AA-GST$_{20\%}$ but no obvious corrosion phenomena were found in the f-GSTD. Figure 3d-f shows the SEM images of the three samples after 282 hrs of salt spray tests. Although significant corrosion is found in all three samples, the extent of corrosion is appreciably different. The corrosion pits in the bare AA are much larger than in the coated AA. The corrosion area of AA-GST$_{20\%}$ is larger than the corrosion area of AA-GSTD. Obvious cracking and delamination phenomena are observed in the AA-GST$_{20\%}$ surface but are absent in the AA-GSTD surface. Trends of salt spray corrosion are similar to electrochemical corrosion.
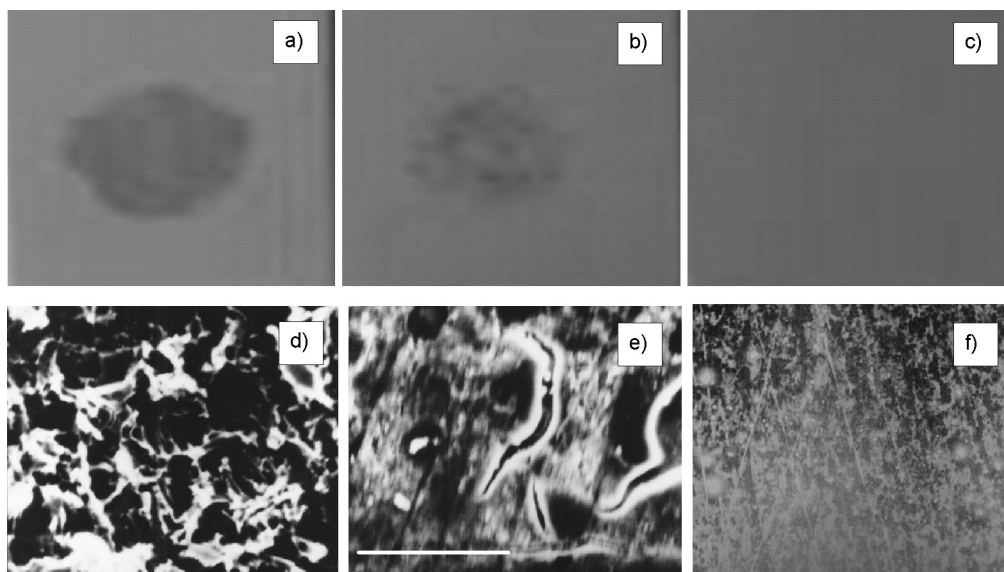
Fig. 3. Camera images (a–c) after electrochemical measurements in a 3.5 wt. % NaCl solution
and SEM images (d–f), 800×, 15 kV, 100 μm, after salt spray tests at 282 hour for three samples:
(a, d) AA, (b, e) AA-GST$_{20\%}$ and (c, f) AA-GSTD

4. Conclusions

Because the epoxy-ring opening or cross-linkng of silica chains was incomplete, the GPMS-POSS film was more susceptible to corrosion due to the higher hydroxyl content and its hydrophilicity. The f-GSTD prepared with DGEBA, GS and 20 wt. % TEOS exhibited the best corrosion resistance compared with the f-GST and bare AA. The results clearly demonstrate that the sample with higher TEOS fractions had better anticorrosive performance and DGEBA obviously enhances the anticorrosion effect of f-GST.

References

[1] Metroke T.L., Kachurina O., Knobbe E.T., Prog. Org. Coat., 44 (2002), 295.
[2] Lichtenhan J.D., *The Economics and Commercialization of Nanostructured^{TM} Hybrid Chemicals*, [in:] *Organic/Inorganic Hybrid Materials*, F.D. Blum, R.M. Laine (Eds.), Division of Polymer Chemistry, Inc. ACS, Hattiesburg MI, 2003, p. 17.
[3] Arkles B., MRS Bull., 26 (2001), 402.
[4] Du Y.J., Damron M., Tang G., Zheng H., Prog.Org. Coat., 41 (2001), 226.

[5] CHOU T.P., CHANDRASEKARAN C., LIMMMER S.J., SERAJI S., WU Y., FORBESS M.J., NGUYEN C., CAO G.Z., J. Non-Cryst. Solids, 290 (2001), 153.
[6] SCHMIDT H., J. Non-Cryst. Solids, 178 (1994), 302.
[7] HU L., SUN Y., ZHAO S., LIU Z., Polym. Prepr., 43 (2002), 1114.
[8] HU L., ZHANG X., YOU H., LIU Y., ZHANG H., SUN D., J. Mater. Sci., 39 (2004), 1331.
[9] HU L., ZHANG X., HUANG Y., Plast. Rub. Comp., 33 (2004), 457.
[10] YEH J., LIOU S., LIN C., YU C., CHANG Y., LEE K., Chem. Mater., 14 (2002), 154.
[11] LONG F.A., PRITCHARD J.G., J. Am. Chem. Soc., 8 (1956), 2663.
[12] BRØNSTED J.N., KILPATRICK M., J. Am. Chem. Soc., 51 (1929), 428.
[13] POCKER Y., RONALD B.P., FERRIN L., J. Am. Chem. Soc., 102 (1980), 7725.
[14] PARKER R.E., ISSACS N.S., Chem. Rev., 59 (1959), 737.
[15] SOLOMONS T.W.G., *Organic Chemistry*, Wiley, New York, 1992.
[16] HOEBBEL D., NACKEN M., SCHMIDT H., J. Sol-Gel Sci. Technol., 12 (1998), 169.
[17] PHILLIP G., SCHMIDT H., J. Non-Cryst. Solids, 31 (1986), 82.
[18] WILLLIAMS R.J.J., ERRA-BALSELLS R., ISHIKAWA Y., NONAMI H., MAURI A.N., RICCARDI C.C., Chem. Phys., 202 (2001), 2425.

Identification problem of interface boundary conditions for diffusive transport between water and silica hydrogel

M. KACZMAREK[*], K. KAZIMIERSKA-DROBNY

Kazimierz Wielki University, ul. Chodkiewicza 30, 64-085 Bydgoszcz, Poland

Diffusion is the process of transport due to gradient of concentration and random molecular motion. In low permeability materials like clay or gels, diffusion is the most important transport mechanism [1, 2] and therefore identification of an appropriate model and parameters describing the process of diffusion is essential to design e.g. waste containment facilities, controlled drug release or to model contaminants migration in ground water through very low permeability soils. This paper discusses the form of boundary conditions between water and hydrogel appropriate for the diffusion process. The analytical solutions of equilibrium models describing the diffusive transport of solute from porous material to water assuming arbitrary initial concentrations and Dirichlet or mixed boundary conditions are considered. The estimation of the diffusion coefficient, retardation factor, partition or mass transfer coefficients of silica hydrogel were carried out with the Levenberg-Marquardt optimization method, implemented in the Matlab numerical computing environment

Key words: *diffusion; interface boundary condition; estimation*

1. Introduction

The identification of a model of diffusive transport in porous materials is usually focused on the selection of a type of sorption and boundary conditions [1, 3]. The evaluation of parameters depends on the adopted model, particularly the number of parameters and the easiness (or difficulty) of their identification depends on the properties and complexity of the model. This paper deals with the single reservoir method assuming a linear model of diffusive transport and equilibrium model of sorption. In order to formulate the general model of such transport from the viewpoint of initial and boundary conditions, arbitrary uniform in space, initial concentrations in the tested material and reservoir and different conditions at the interface between the res-

---

[*]Corresponding autor, e-mail: mkk@rose.man.poznan.pl

ervoir liquid and the sample are considered. The interfacial conditions are modelled 1) by continuity or jump of concentration represented by the interfacial distribution coefficient or 2) by the flux of mass proportional to the concentration difference through a thin interfacial layer.

The purpose of this paper is to identify the form of boundary condition at the interface between water and hydrogel for diffusive transport. Analytical solutions of equilibrium models of diffusive transport of solute from porous material to water are used, assuming arbitrary initial concentrations and Dirichlet or mixed type of boundary conditions. The solutions and experimental data for silica hydrogel allowed for the estimation of model parameters carried out with the Lavenberg-Marquardt optimization method, implemented in the Matlab numeric computing environment.

2. Experimental

Samples of silica hydrogel were prepared by mixing pure water-glass with hydrochloric acid and distilled water at room temperature. The mixture was poured to PMM cylinder and left for gelation. The measurements were done using the experimental setup shown in Fig. 1, which includes: the diffusion chamber (1), the conductometer (2) made by Elmetron, model CPC – 551, which measures continuously the conductivity and temperature of the reservoir liquid, the controlled adapter (3) which powers the stirrer located in reservoir, and the thermostat (4) which stabilizes temperature during the test.

Fig. 1. Experimental set-up

The concentration of sodium chloride (in g/dm^3) in the reservoir was determined taking into account its linear relationship with conductivity, while the scaling factor for concentrations above 100 mg/dm^3 was assumed to be 0.55 [4]. For each test fresh samples were prepared and reservoir conductivity was sampled every 3 minutes on the average for about 30 hours.

3. Mathematical model of diffusion in a single reservoir test

The mathematical model corresponding to the applied experimental test assumes that the cylindrical sample of gel is isolated at the bottom and remains in contact with a constant amount of liquid in the reservoir, where the concentration is homogeneous due to stirring, Fig. 2.
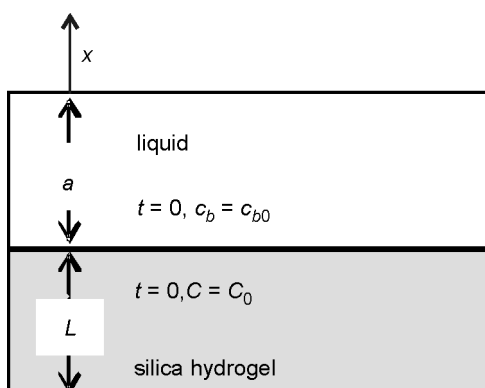

Fig. 2. The schematic diagram of the experiment with boundary conditions

The model of transport is a superposition of models of diffusive migration in gel and mass exchange between the gel and the reservoir liquid. The process of one-dimensional diffusion with equilibrium sorption in hydrogel can be represented by the second Fick's law

$$\frac{\partial}{\partial t}C - \frac{D}{R}\frac{\partial^2}{\partial x^2}C = 0 \tag{1}$$

where C denotes the mass concentration of salt in a gel referred to the elementary volume of the sample, t and x are time and spatial coordinates, D stands for the effective coefficient of diffusion, and R is the retardation factor. The effective diffusion coefficient is smaller than the diffusion coefficient in a free solution because of the tortuous pathways of molecules of solute within a porous medium. The relation of the diffusion coefficient in a free solution D_t to the effective diffusion coefficient D is represented by the tortuosity factor [5]

$$\tau = \frac{D_t}{D}$$

The equation of mass exchange between the sample and the reservoir is obtained from the condition that the change in mass of solute in reservoir liquid c_b must be balanced by the mass flux of the diffusing substance from or to the sample described by the first Fick law. The equation reads:

$$a\frac{dc_b}{dt} = -D\frac{\partial C}{\partial x}\bigg|_{x=L} \tag{2}$$

where a is the height of the liquid in reservoir.

Taking into account the possible different ways in which the interfacial transport between the liquid and the porous sample can occur, the boundary and initial conditions, corresponding to the considered single reservoir configuration were determined by the following set of equations:

$$x = L \quad \Rightarrow \quad c_b = \frac{1}{K'}C_s, \quad C_s = C(x = L, t) \tag{3}$$

or

$$x = L \quad \Rightarrow \quad -D\frac{\partial C}{\partial x} = h(C_s - nc_b) \tag{4}$$

and

$$x = 0 \quad \Rightarrow \quad \frac{\partial C}{\partial x} = 0 \tag{5}$$

$$t = 0 \quad \Rightarrow \quad C(x) = C_0 \tag{6}$$

$$t = 0 \quad \Rightarrow \quad c_b = c_{b0} \tag{7}$$

Equation (3) refers to the model assuming continuity or surge of concentration at the interface and which is further called DKR. The effective partition coefficient K' for continuous concentration is equal to porosity n, i.e. $K' = n$, while for surge of concentration $K' = K_n$, where parameter K denotes the interfacial partition factor. The possibility of occurrence of the latter case is assumed by reference to polymer materials [1, 2]. Equation (4) describes an alternative interfacial condition formulated for the flux of mass which is proportional to the difference between the actual concentration of solute at the boundary of porous material C_s and the concentration in the stirred liquid in the reservoir multiplied by porosity. The constant h is called the mass transfer coefficient in the boundary layer and the model is referred to as DhR. The boundary condition (5) is the consequence of the assumption that there is no mass transport at the bottom of the sample. The initial conditions (6) and (7) assume uniform, and in general non-zero, concentrations in pore fluid and the reservoir. Because of using the equilibrium model of sorption $C_0 = 1/RC_{tot}$, where C_{tot} comprises the mass of solute in pore liquid and mass adsorbed on the internal surface of the porous material.

The analytical solution of equations describing the evolution of solute in the reservoir liquid with boundary and initial conditions for the DKR model can be found through reformulation of the problem to the form of the Sturm–Liouville problem (see [6]) and can be written as the following

$$c_b(t) = \frac{C_0 + \alpha K' c_{b0}}{K'(1+\alpha)} + \sum_n \frac{2a(K' c_{b0} - C_0)}{K'(1 + \alpha + q_n^2 \alpha^2)} e^{-\gamma q_n^2 t} \tag{8}$$

where q_n is the root of the transcendental equation $\tan q_n = -\alpha q_n$, and $\alpha = a/K'RL$, $p_n = Dq_n^2/RL^2$, $\gamma = D/RL^2$. Since the porosity of the gel was not determined in the performed tests, instead of distribution coefficient K, the $K' = Kn$ parameter, called the effective coefficient of surface distribution, was introduced.

The analytical solution corresponding to the DhR model, i.e. the model with specified mass flux at the interface and both initial conditions being inhomogeneous, are obtained by the rearrangement of the considered problem and application of the solution given by Carslaw and Jaeger [7] (see discussion in [6]), and the evolution of concentration in the reservoir c_b is :

$$c_b(t) = \frac{1}{n}\left(\frac{n c_{b0} - C_0}{1+k} + 2k\overline{\lambda}^2 (n c_{b0} - C_0) \sum_{i=1}^{\infty} \frac{1}{P_i} e^{-\alpha_i^2 T t} + C_0 \right) \tag{9}$$

where:

$$\tan \alpha = \frac{\overline{\lambda}\alpha}{\alpha^2 - k\overline{\lambda}}$$

and

$$\overline{\lambda} = L\frac{hR}{D}, \quad k = \frac{LnR}{a}, \quad T = \frac{D}{RL^2}$$

$$P_i = \alpha_i^4 + (\overline{\lambda}^2 + \overline{\lambda} - 2k\overline{\lambda})\alpha_i^2 + k\overline{\lambda}^2(1+k)$$

4. Results and discussion

We present the discussion of some numerical results obtained from the above analytical solutions of equilibrium models being interesting from the viewpoint of the reservoir method of identification of transport parameters. The diffusive transport of solute from porous material to reservoir and the two types of the interfacial boundary conditions are considered. Figure 3 shows the results obtained from Eq. (8) and (9) representing the evolution of concentration in the reservoir liquid for the DKR model (a) and DhR model (b). The role of the parameters describing interfacial conditions: the effective partition factor K' and mass transfer coefficient h, was examined. The parameters assumed for simulation are following: the thickness of sample $L = 0.01$ m, the height of liquid in reservoir $a = 0.04$ m, the porosity $n = 0.8$, the effective diffusion coefficient $D = 1.5\times10^{-9}$ m^2/s, the retardation factor $R = 1$, the effective distribution coefficient K' takes the values 0.8, 1 and 1.5, the mass transfer coefficient in the

boundary layer takes the values 6×10^{-7}, 2×10^{-6}, 2×10^{-5} m/s, the initial concentration in the reservoir and the sample are $c_{b0} = 1$, and $C_0 = 2$ g/dm^3, respectively.
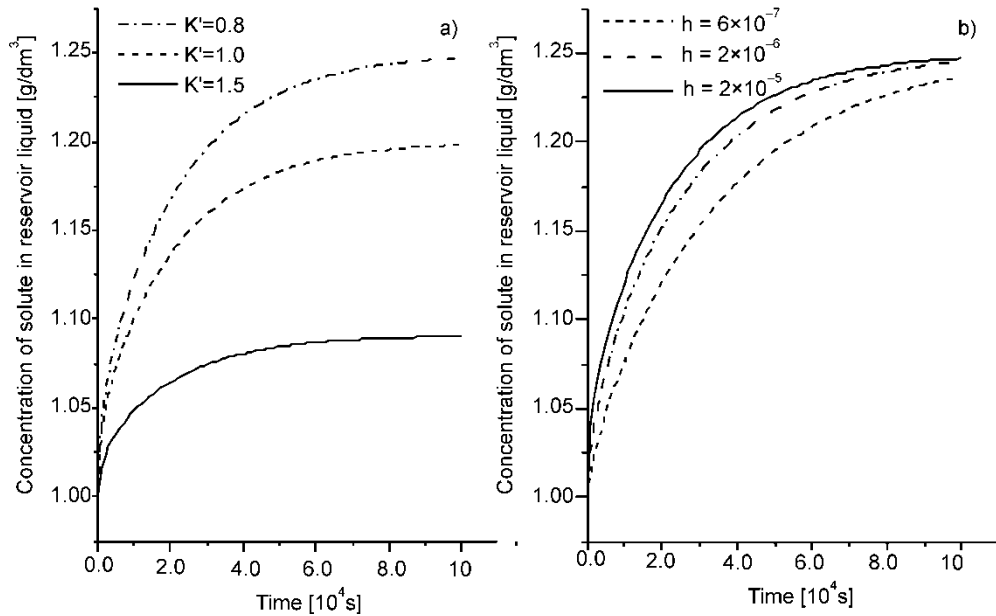

Fig. 3. The evolution of solute concentration in the reservoir liquid
from the DKR model (a) and the DhR model (b)

The value of the distribution coefficient influences significantly the intensity of the process of diffusion and the final concentration of solute in the reservoir. The value of h also influences the intensity of mass transfer to the reservoir but unlike in the DKR model, the final value of concentration tends to reach the same level. It is interesting to note that the value of h parameter equal to 2×10^{-6} m/s gives a very close prediction of the DhR model as it results from the DKR model with continuous concentration at the interface (where $K' = 0.8$). This means that for a given coefficient of diffusion, there is a boundary value of the mass transfer coefficient beyond which it ceases to control the mass exchange between the reservoir and the material.

The solution of the inverse problem, aimed at identifying of the interfacial boundary condition and estimation of the appropriate parameters of diffusive transport was performed within the Matlab environment. The least squares error function is defined and its minimum is identified to evaluate the set of parameters D, K', R or D, h, R. The minimization of the error function is performed using optimization toolbox of Matlab, particularly the function lsqnonlin, which uses the Levenberg–Marquardt method. The set of parameters characterizing the experimental configuration of the reservoir test is the following: $L = 10.5$ mm; $a = 43.8$ mm; $c_{b0} = 0$ and $C_0 = 22.4$ g/dm^3. The initial concentration of sodium chloride in silica hydrogel C_0 was determined from the

stoichiometry of chemical reaction between sodium silicate (water glass) and hydrochloric acid. The results of numerical optimization for the data obtained for two temperatures 23 and 26 °C are given in Table 1.

We notice that the effective coefficient of diffusion is identical for the two models and does not exceed the coefficient of molecular diffusion in pore fluid which, for temperature of 25 °C, amounts to 1.6×10^{-9} m^2/s [8]. The ratio of the two models, defined as tortuosity of the porous material, is equal to 1.02. The values of the effective coefficient of surface distribution K' and retardation factor R indicate that from the macroscopic viewpoint of the DKR model predicts a significant surge of concentration of sodium chloride at the interface between the reservoir liquid and the pore liquid in the gel and a negligible sorption of sodium chloride in silica hydrogel. The latter effect is in conformity with the prediction of the DhR model.

Table 1. The values of the estimated parameters

Temperature [°C]	Model DKR			Model DhR		
	$D \times 10^9$ [m^2/s]	K'	R	$D \times 10^9$ [m^2/s]	$h \times 10^{-5}$ [m/s]	R
23	1.57	1.88	1.08	1.57	1.04	1.72
26	1.57	1.84	1.00	1.57	1.05	1.56

For further evaluation of the role of the surge of concentration at the interface between the gel and the liquid within the DKR model, the range of values for K' parameter in the optimization procedure was restricted assuming that it must be equal or less than one (because of high porosity of the gel it means that K is approximately continuous). Running the optimization procedure again for both temperatures (Table 2), we obtain the same values of the effective diffusion coefficient as previously (Table 1), and essentially higher values of retardation factors.

Table 2. The values of estimated parameters of the DKR model
obtained from optimization for $K' \leq 1$

Temperature [°C]	Model DKR		
	$D \times 10^9$ [m^2/s]	K'	R
23	1.57	1.00	1.57
26	1.57	1.00	1.42

Figure 4 shows the comparison of the experimentally measured evolution of concentration for temperature 23 °C and theoretical curves corresponding to the DKR model with continuity ($K' = 1$) or surge ($K' = 1.88$) of concentration at the interface and the DhR model assuming parameters from Tables 1 and 2. It can be seen that there is almost perfect agreement between the experimental data and the theoretical curve for the DKR model with the surge of concentration at the interface hydrogel–water.

The two other models give a significant difference between the experimental results and the theoretical predictions.
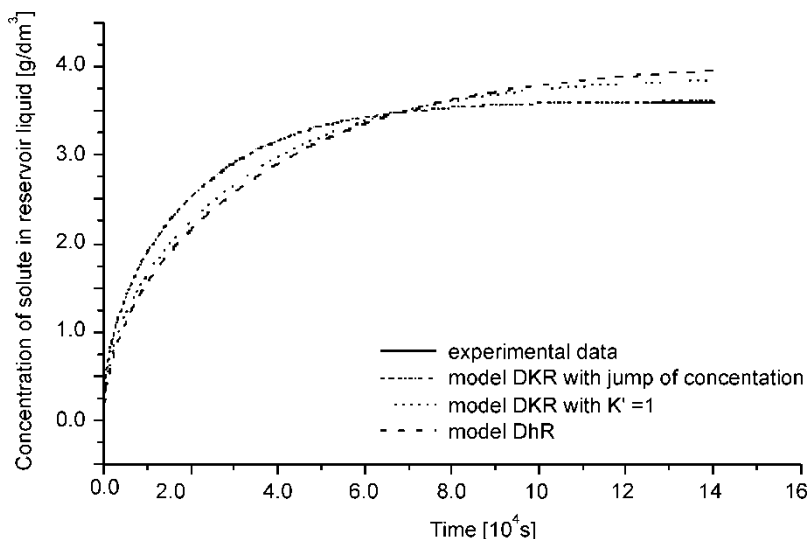

Fig. 4. The comparison of experimental and theoretical curves

5. Conclusions

The main purpose of this paper was to identify the proper form of boundary condition at the interface between water and silica hydrogel for diffusive transport. Analytical solutions of the transport of solute from the porous material to water with equilibrium model of sorption are used, assuming arbitrary homogeneous initial concentrations and boundary conditions represented by 1) the continuity or surge of concentration measured by interfacial distribution coefficient or 2) the flux of mass proportional to the concentration difference through a thin interfacial layer.

First, based on the considered models the role of the effective partition factor K' and mass transfer coefficient in the boundary layer h were studied. The solutions and the experimental data from the single reservoir test were used in estimation of effective diffusion coefficient, retardation factor and partition coefficient or mass transfer coefficient. The results have shown that the values of distribution coefficient and mass transfer coefficient influenced the intensity of the process of diffusion while the final concentration of solute depended only on the former parameter. The estimated values of effective diffusion coefficient were lower than the values of molecular diffusion in free liquid which means that tortuosity factor was greater than unity. From the comparison of the two models and the experimental data it is evident that the model assuming a surge of concentration at the interfacial layer represents a better model describing the diffusive mass transport between silica hydrogel and water.

References

[1] CRANK J., PARK G., *Diffusion in Polymers*, Academic Press, New York, 1968.

[2] VERGNAUD J. M., *Liquid transport process in polymeric materials*, Prentice Hall, 1991.

[3] FINSTERLE S., PERSOFF P., *Water Res. Research*, 33 (1997), 1803.

[4] DOJLIDO J., ZERBE J., *Instrumentalne metody badania wody i ścieków*, Arkady, Warszawa, 1997.

[5] GARROUCH A.A., LIAQAT A., FUAD Q., Ind. Eng. Chem. Res., 40 (2001), 4363.

[6] KACZMAREK M., KAZIMIERSKA-DROBNY K., J. Coll. Int. Sci., 311 (2007), 262.

[7] CARSLAW, H.S., JAEGER, J. C., *Conduction of Heat in Solids*, Oxford University Press, London, 1986.

[8] SHACKELFORD C.D., DANIEL D.E., J. Geotechn. Eng., 117 (1991), 467.

Application of an artificial neural network in the processing of output signals from a gas sensor with sol-gel-derived TiO$_2$ film

A. Łukowiak[1], K. Kozłowska[1*], K. Urbański[2],
A. Szczurek[3], K. Dudek[4], K. Maruszewski[1,5]

[1]Institute of Materials Science and Applied Mechanics, Wrocław University of Technology, ul. Smoluchowskiego 25, 50-370 Wrocław, Poland

[2]Faculty of Microsystem Electronics and Photonics, Wrocław University of Technology, ul. Janiszewskiego 11/17, 50-372 Wrocław, Poland

[3]Institute of Environmental Protection Engineering, Wrocław University of Technology, pl. Grunwaldzki 9, 50-370 Wrocław, Poland

[4]Institute of Machine Design and Operation, Wrocław University of Technology, ul. Łukasiewicza 7/9, 50-371 Wrocław, Poland

[5]Electrotechnical Institute, Skłodowskiej-Curie 55/61, 50-369 Wrocław, Poland

TiO$_2$ thin film obtained by the sol-gel technique was used as the active layer in an electric sensor to distinguish the vapours of four volatile organic compounds: hexane, hexanol, cyclohexane and benzene. The measurements were performed at various temperatures of the sensing layer. Some of the output signals obtained from the sensor were characterized by low reproducibility, even within the data series obtained for the same gas. With the current design of the gas sensor, it was sometimes impossible to obtain a reproducible and stable output signal. Therefore, a neural network was used to pre-process the data. A bipolar transfer function of neurons was used as it had the shortest learning time of the network and produced the most stable results. The best results were obtained for a 4-4-4 topology of the neural network, where the input data were the values of the current at 440 and 360 °C when the sensor was exposed to a flow of air with or without organic vapours, with a 4-neuron hidden layer, and BE, CH, HL, HX outputs, each one associated with specific substance (benzene, cyclohexane, hexanol and hexane). The neural network was configured as a classifier recognizing four specific gases.

Key words: *smart sensor; volatile organic compound; sol-gel; artificial neural network; signal conditioner*

_____

[*]Corresponding author, e-mail: katarzyna.kozlowska@pwr.wroc.pl

1. Introduction

Thin titania films obtained by the sol-gel technique can be used as the active layers in electric sensors for various kinds of gases (e.g., CO, O_2, NO_x or vapours of volatile organic compounds [1–3]). By changing the precursors and solvents, choosing the method of layer deposition or setting the annealing temperature, a material with a controlled crystal structure, particle size, and surface area can be obtained. Unfortunately, the method may lead to low reproducibility and instability of the prepared material. It has been observed that the output signal of the sensor can exhibit low reproducibility even within the data series obtained for the same gas. To overcome this problem, pattern recognition (PARC) techniques can be applied in order to improve the quality of input data by means of data processing. Artificial neural networks (ANNs) are a promising technique which can be applied in chemical sensors [4–6].

In this paper, both the software and hardware implementation of a multilayer perceptron (MLP) are presented. The artificial neural network, complete with control software, was embedded into an analog microcontroller (8051-compatible core with integrated precision analog-to-digital and digital-to-analog converters). Considering its future use as a portable device, the system was designed to be compact and fully autonomic.

2. Experimental

The sensing titania thin film was prepared by means of the sol-gel method. The sol was obtained from titanium *n*-butoxide (TNBT) mixed with butanol and acetylacetone in the molar ratio of 1:20:2.3. After one hour of mixing in an ultrasonic bath, a small amount of distilled water was also added to the solution. All the compounds were further mixed together for 30 minutes and later left for 24 hours at room temperature.

The film was deposited with the modified dip coating technique [7]. An alumina plate with interdigital gold electrodes on one side and a Pt heater on the other side were used as a substrate. The part of the substrate with the electrodes and heater were immersed in the solution. Next, the sol was slowly poured out through a hole at the bottom of the container. After 10 min required for drying, the deposition was repeated three times to obtain a thicker film. The titania film was annealed in air for one hour at 600ºC with a heating rate of 10ºC/min.

The measurement system used in this project consisted of the following components: a gas sensor, a measuring chamber, a pure air generator, a chamber for vapour generation, a voltage supply, a measuring device, a rotameter, and a pump (the details can be found in [8]). The sensor was tested through the same sequential exposures. The sensing plate was exposed in turns to pure dry air and to air mixed with vapours of organic compounds. The exposure time was set at three minutes. To prepare the gaseous mixture, the stream of pure air flowed over a flask with liquid organic com-

pound thermostated at 50 ºC. The sensor response could be measured at various temperatures (in the range 275–440 ºC), depending on the voltage applied to the heater. The voltage supply was also connected to the sensor electrodes and changes of current during the exposure to gases were considered the response of the sensor.

3. Results and discussion

A thin film of titania with no cracks nor scratches was deposited on the alumina substrate. Some details about the film properties have been described earlier [9]. A typical response of the sensing layer for benzene and hexanol is shown in Fig. 1. The largest changes of current were usually observed for hexanol, while lower ones for hexane and cyclohexane, and the lowest for benzene.
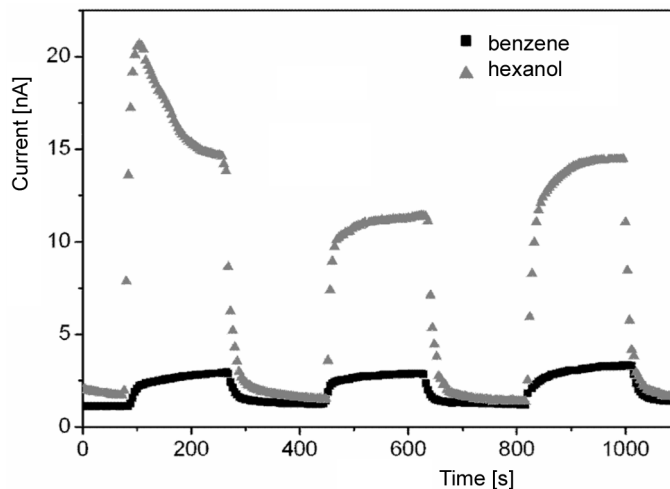

Fig. 1. The response of the sensor to the vapours of benzene and hexanol at 360 °C

Some of the output signals obtained from the sensor were characterized by low reproducibility even within the data series obtained for the same gas, as can be seen in Fig. 1 (the response to hexanol). The main reasons for this phenomenon could be: changes in the characteristics of the gas sensitive layer over time, changes of the sensor temperature during measurement, and variation of gas flow.

The sol-gel TiO_2 organic vapour sensor does not provide a direct output signal to distinguish between different gasses. It is also very hard to find an accurate mathematical model of the sensor [9]. In this work, after some investigations, an artificial neural network was chosen as the processing component for the sensor data.

There are two commonly used transfer functions of neurons: tanh() and sigmoid. Both are non-linear; tanh() is bipolar (–1…1 output range), while the sigmoid function is unipolar (0…1 output range). In our case, we observed that the bipolar transfer

function is the best choice since it ensures the shortest learning time of the network and the most stable results. The next step was to select the topology of the ANN. After screening (experimental data analysis), both dual- and triple-layer networks were selected for further experiments. Generally, the 1- or 2-neuron single hidden and 2-hidden-layer topology was not a good choice due to problems with local minima during learning. These networks were unstable and their learning time was relatively long.

Given the experimental data, the optimal network topology (with the shortest learning time and the lowest error) is 4-4-4 with min440, max440, min360 and max360 inputs, a 4-neuron hidden layer and BE, CH, HL, HX outputs (Table 1 and Fig. 2). The values for min440 and min360 represent the current at 440 or 360 °C when pure air is passed through the measuring cell and for max440 and max360 are the highest values of the current at 440 or 360 °C when the sensor is exposed to a flow of organic vapours. The outputs BE, CH, HL and HX are assigned to benzene, cyclohexane, hexanol, and hexane, respectively. During normal operation, only one output is activated, indicating a specific compound.
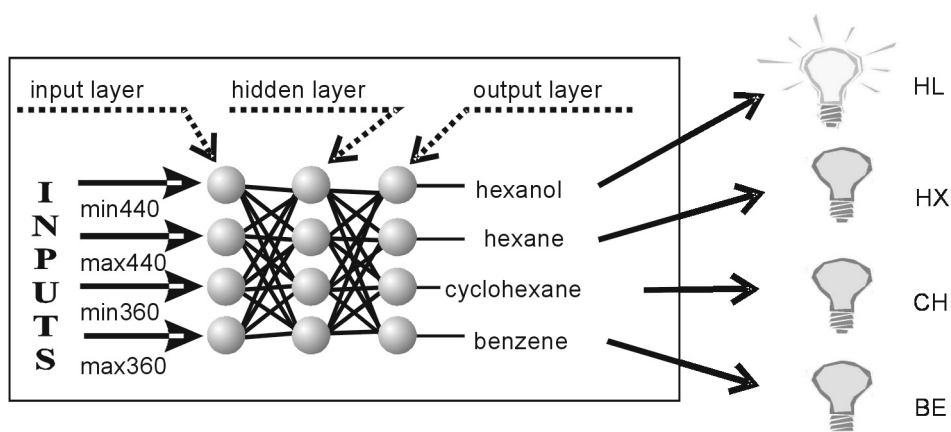

Fig. 2. Neural network structure

Table 1. Testing set – inputs and expected values (eBE, eCH, eHL, eHX)

min440	max440	min360	max360	eBE	eCH	eHL	eHX
16.6	36.7	1.23	2.84	**1**	0	0	0
15.5	36.3	1.23	2.84	**1**	0	0	0
10.4	59.7	1	3.2	0	**1**	0	0
10.4	63.8	1	2.9	0	**1**	0	0
11.5	67.2	1.4	30	0	0	**1**	0
11.4	83	1.4	30	0	0	**1**	0
8.2	108	1	49	0	0	0	**1**
8.3	107	0.3	34	0	0	0	**1**

Before the neural network processor can be used, it must be trained with the experimental data. The experimental data vectors were divided into 3 separate sets:

- training set (88 vectors),
- cross-validation set (12 vectors),
- testing set (8 vectors).

The final results for the 4-4-4 network are shown in Table 2. The results are almost perfect – no errors were found within the different testing sets. The network answers were stable and repeatable.

Table 2. Nnetwork outputs

BE	CH	HL	HX
0.99	0.00	0.00	0.01
0.99	0.01	0.01	0.00
0.01	**0.99**	0.01	0.00
0.01	**0.99**	0.01	0.01
0.01	0.00	**0.99**	0.00
0.01	0.00	**0.99**	0.01
-0.02	0.00	0.01	**0.98**
-0.03	0.01	0.01	**0.99**

As the topology of the network is fairly simple, it is possible to implement it in hardware as an embedded neural processor. The input signals are: $i(t)$, I, U, where $i(t)$ is gas sensor output current at 5 V, I, U – Pt heater power supply values. Knowing I and U, we can calculate both the power dissipated (P) and the resistance (R) of the heater. As R depends on the heater temperature, T can be measured directly on-sensor without additional components. By means of the MOSFET power transistor, the controller constantly controls the current (and power) dissipated in the sensor. As a result, we can maintain constant temperature on the sensor surface. The MOSFET transistor is also used to switch the heater on and off.

The bottom side of the sensor has a TiO_2 layer covering the gold electrodes. Given constant voltage supplied to the sensor (5 V), small current changes can be observed during temperature changes and for different organic vapours. The current is very low (0–100 nA), and it cannot be measured directly with the microcontroller ADC. As the time constant of the sensor is relatively high (over 180 s), a lock-in input amplifier can be used to achieve low noise, very small voltage and current offset, and high gain.

The Analog Devices AD8554 is a very good choice due to its offset voltage (V_{os}) of 1 μV, input offset drift of 5 nV/°C, input bias current (I_b) of 10 pA, single power supply and rail-to-rail inputs and outputs [10]. The controller hardware design is shown in Fig. 3. It consists of a power source, signal conditioners and an integrated data acquisition system based on the ADuC845 chip. The Analog Devices ADuC845 was chosen as it offers built-in precision analog-to-digital converters, digital-to-analog converters, and programmable gain amplifiers. 10 input channels can be configured either as single-ended or differential.
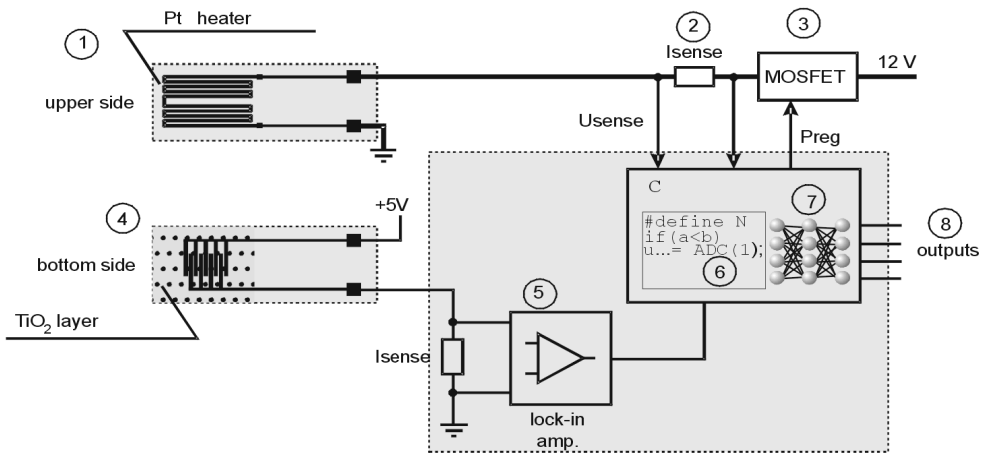
Fig. 3. Hardware design: 1 – Pt heater; 2 – series resistor for current sensing; 3 – MOSFET power
transistor control of the curren, 4 – sol-gel TiO_2 coating sensing layer, 5 – lock-in precision
amplifiers, 6 – control code power control, signal conditioning, 7 – ANN code, 8 – digital outputs

The device features are: two independent 24-bit ADCs, 10 analog input channels, 22-bit rms (19.5 bit p-p) effective resolution, offset drift 10 nV/°C, gain drift 0.5 ppm/°C (with chop enabled), 62-kbyte on-chip Flash/EE program memory, 12 MIPS @ 12 MHz, digital interfaces: UART, SPI®, and I2C® serial I/O, 34 GPIO pins, small outline dimensions (8×8 mm^2, Fig. 4).
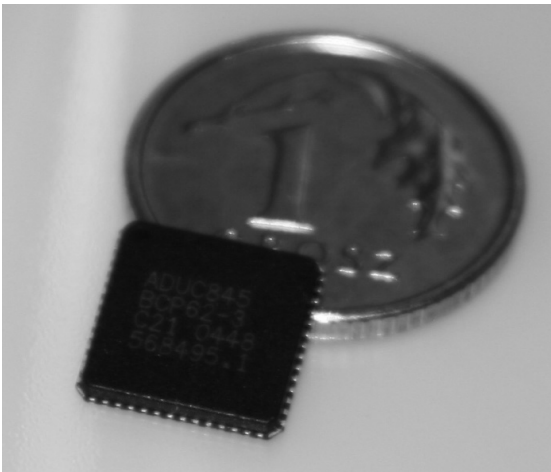

Fig. 4. Analog Devices' ADuC845
microcontroller

The combination of a gas sensor, a precision lock-in input amplifier, and 24-bit analog to digital converters provides a highly compact, accurate and cost-effective measurement system. The main advantage of using a microcontroller instead of pure ADCs is the ability to execute the code. The source code was written in C (both neural network and control code) [10].

The control code is responsible for time measurement, temperature stabilisation, and the preparation of input data for the neural network. After all data have been prepared, the second part of the code is executed. This part of the code is an implementation of a 3-layer perceptron consisting of 4-4-4 neurons. Within the code, the operation of the network is rather simple – each of the processing element is an adder with non-linear output function (tanh). The neurons are connected with synapses, represented by an array of floating-point numbers (neural network weights). As the ADuC845 does not provide a hardware implementation of a math co-processor, some of the calculations have to be software-emulated [10]. In our design, all of the network weights are calculated on a personal computer and hard-coded within the controller. The weights remain unchanged during the operation of the device.

The smart sensor design is very flexible – it can be used for different coatings, sensors and compounds [5]. The required changes can all be made in the software: the signal conditioner code and the weights (or topology) of the neural network. Each sensor-controller pair can be calibrated to achieve the best accuracy; long-term changes of the sensor properties can also be compensated.

The training time depends on the data sets and network structure; in our experiments, the range was between 3 and 10 seconds on an Intel Pentium 4 HT 3 GHz PC.

4. Conclusions

In modern sensors, especially organic gas sensors, there are often difficulties in interpreting output signals. In most cases, the raw output signal of the sensor depends on many factors and is not reproducible. The main goal is to obtain only meaningful results, while rejecting undesirable components.

This requires advanced data processing techniques, and an artificial neural network is a good choice. In practice, it is also very important for the sensor to be suitable for use outside of a laboratory environment. This can be achieved using a combination of a sensor, controller, and data processor.

We have presented a cost-effective, flexible design of a smart-sensor with an embedded artificial neural network. The effectiveness of the ANN in the classification of similar organic vapours is excellent, and the controller software can be easily adapted to other gas sensor designs and organic compounds.

References

[1] RUIZ A., CALLEJA A., ESPIELL F., CORNET A., MORANTE J.R., IEEE Sens. J., 3 (2003), 189.

[2] LI Y., WLODARSKI W., GALATSIS K., MOSLIH S.H., COLE J., RUSSO S., ROCKELMANN N., Sens. Actuators B, 83 (2002), 160.

[3] GALATSIS K., LI Y.X., WLODARSKI W., COMINI E., FAGLIA G., SBERVEGLIERI G., Sens. Actuators B, 77 (2003), 472.

[4] HUYBERECHTS G., SZECÓWKA P., ROGGEN J., LICZNERSKI B.W., Sens. Actuators B, 45 (1997), 123.

[5] BELING S., BLÄSER G., BOCK J., HEINERT L., TRAXLER M., KOHL D., Sens. Actuators B, 52 (1998), 15.

[6] CHEN J.C., LIU C.J., JU Y.H., Sens. Actuators B, 62 (2000), 143.

[7] DISLICH H., Thin films from the sol-gel process, [in:] L.C. Klein (Ed.) *Sol-gel Technology for Thin Films, Fibers, Performs, Electronics, Specialty Shapes*, Noyes Publications, Park Ridge, New Jersey, 1988, p. 54.

[8] LUKOWIAK A., MACIEJEWSKA M., SZCZUREK A., MARUSZEWSKI K., Thin Solid Films, 515 (2007), 7005.

[9] KOZŁOWSKA K., ŁUKOWIAK A., SZCZUREK A., DUDEK K., MARUSZEWSKI K., Opt. Appl., 35 (2005), 783.

[10] Analog Devices, ADuC845 & AD8554 datasheets, http://www.analog.com.

The internal friction background in PZT ceramics obtained by the sol-gel method

A. Zarycka, B. Bruś[*], J. Ilczuk, M. Czerwiec, M. Dukat

University of Silesia, Faculty of Computer Science and Materials Science,
Department of Materials Science, ul. Żeromskiego 3, 41-200 Sosnowiec, Poland

The results of internal friction background examined in fine-grained lead zirconate titanate PZT ceramics are presented. The aim of the study was to describe the influence of change in concentration of the lead titanate on the internal friction background. The internal friction examinations were performed using modern automatic frequency relaxator of the RAK-3 type at 293 K. PZT ceramics of the chemical composition $PbZrO_3$-$PbTiO_3$ with $PbTiO_3$ concentration ranging from 25% to 75% were the examined material. The nanopowders were prepared by the sol-gel method. PZT ceramics were obtained by the conventional sintering method. The influence of the changes in the structure of ceramic materials on the internal friction background was reported. SEM images of the domain structure were used to describe the obtained results.

Key words: *PZT; sol-gel method; internal friction; domain structure*

1. Introduction

In order to extend the applicability of ceramic materials it is necessary to learn about their physical, chemical and mechanical properties, their real structure and relaxation properties. Detailed studies of the dependences between the chemical composition, crystalline structure, elctrophysical properties and the domain structure will allow us to obtain ceramics with better properties, needed for the modern technology. Rapid development of modern investigation methods, and especially non-destructive methods, has been observed in the research on ceramic materials. Methods of mechanical spectroscopy, and the internal friction method in particular, have been used more and more frequently. A great interest in the method based on the measurement of internal friction in investigations of real structure of the ceramic material is caused by the fact that by observing macroscopic vibrations of a specimen, information about the behaviour of the material on atomic level can be obtained. This method is character-

---

[*]Corresponding autor, e-mail: bbeata2@poczta.onet.pl

ized by high sensitivity to changes in the concentration of point defects, to interaction between the defects, and changes in the real structure of materials [1–4].

Apart from the development of modern methods of investigation, a development of technologies of ceramics production can also observed. The PZT ceramics were obtained from PbO, ZrO_2, TiO_2 by the baking method at the temperature of 970–1200 K which caused significant deviations from stoichiometry as a result of loss of PbO. For that reason, conventional methods of synthesis of ceramic materials based on the reaction in the solid phase have been used less frequently in favour of chemical methods (reactions in the liquid phase) enabling us to obtain powders of high homogeneity of chemical composition and having grain size of the order of nanometers. The sol-gel method is one of the most widespread chemical methods. The method guarantees high purity of the materials obtained and enables one to conduct syntheses at a relatively low temperature, thus reducing the vaporization of components and favouring preservation of the stoichiometric composition. The possibility to conduct the synthesis at a lower temperature is of great importance, particularly in ceramics containing lead oxide. Ceramic grains of the size of 0.3–3 µm are made of crystallites of the size of 20–75 nm [5, 6]. The ceramics obtained from powders synthesized by this method have a high density, close to the theoretical value, which has a significant influence on its dielectric, piezoelectric, and mechanical parameters, allowing us to use it as piezoelectric and electro-acoustic transducers, pick-ups (vibration, pressure), servo-motors, filters, piezoelectric transformers, engines, parametric amplifiers, and ferroelectric memories [2, 6–8].

The aim of this paper was to examine the influence of changes in the lead titanate content on the phenomena of internal friction in the fine-grained PZT type ceramics obtained by the method of free sintering of powders synthesized by the sol-gel method.

2. Test material and test methods

The $Pb(Zr, Ti)O_3$ ceramics with various lead titanate contents from 25 mol % to 75 mol % was the test material. In order to obtain ceramic powders, a chemical synthesis method – the sol-gel method was used. Lead in the form of the lead acetate (II) – $Pb(COOCH_3)_2$, titanium and zirconium in the form of alcoholates: *n*-titanium propanolate $Ti(CH_3CH_2CH_2O)_4$ and *n*-zirconium propanolate $Zr(CH_3CH_2CH_2O)_4$ were added to the reaction medium. The synthesis reaction was carried out in argon atmosphere. The reaction product obtained was subject to distillation to remove propyl acetate. After cooling the solution to room temperature the solvent was added to obtain the solution of the concentration 0.8–1 mol/dm^3. In order to stabilize the alcoholate solution, acetylacetone was added and the solution was subjected to hydrolysis. Sol was obtained as a result of a series of hydrolysis reactions, and the sol, after transsofrming into gel, underwent the drying process at the temperature of 573 K. Then the obtained product was calcinated at 873 K for 4 h to remove organic residues.

The powder obtained was comminuted (grinding 2 h), and then after adding plasticizer (liquid paraffin) moldings were formed in a plate-like shape of the following dimensions: length – 40 mm, width – 10 mm, thickness – 3 mm. They were sintered by the free sintering method at the temperature of 1523 K for 5 h. The specimens obtained were ground, polished, and then they were coated with silver paste electrodes by the baking method.

The internal friction for all specimens in question was determined by an automatic relaxator of acoustic frequencies RAK-3, controlled by a computer [9]. This relaxator allowed us to determine internal friction (IF) by the measurement of damping of the specimen free vibrations.

3. Results and discussion

Dependences of the internal friction background on the lead titanate content in the tested specimens determined at 293 K are presented in Fig. 1.
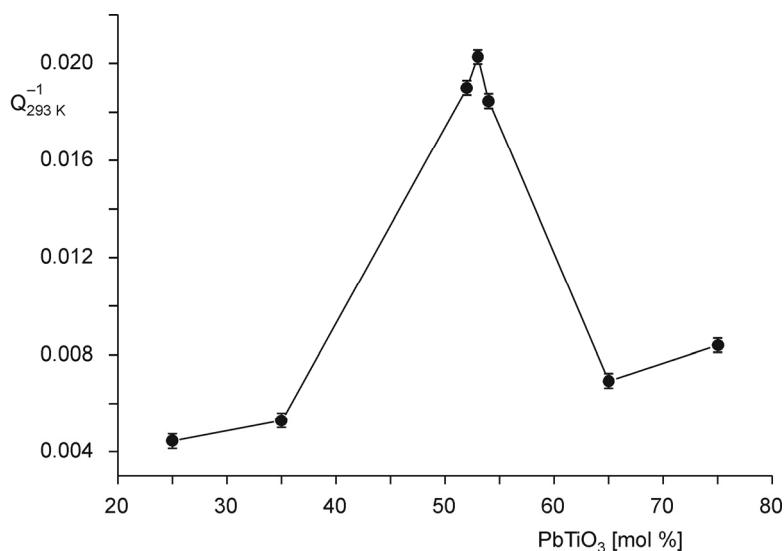

Fig. 1. Dependences of the internal friction background on the PbTiO$_3$ concentration in PZT ceramics obtained via the synthesis by the sol-gel method

The level of internal friction in the PZT ceramics depends, among others, on the type and number of domain walls and their mobility. However, the character of crystal fragmentation into ferroelectric domains depends on the presence of structural defects deformation, on electric conductivity and conditions involving a transformation into the ferroelectric phase, and the thermal and electric history of a material [3, 10].

The value of internal friction (*TW*) decreases with a decrease of the mobility of domain walls and a decrease in the number of domain walls. It is generally known that with a

change in the lead titanate concentration in the PZT ceramics there is a change in the mate-
rial structure from the antiferritic orthorhombic phase for low concentrations of the lead
titanate via the rhombohedral phase (25 and 35 mol % $PbTiO_3$), to the tetragonal phase
concentrations (65 and 75 mol % $PbTiO_3$). The morphotropic phase boundary represented
in the diagram by a line corresponds to the apparent equilibrium of the tetragonal (T) and
rhombohedral phases (R) [11]. However, real phase diagrams reveal most frequently
an area of coexistence of the phases and not the lines. In the range of the PZT composi-
tions from the dual phase morphotropic area, a great number of domain walls with high
mobility (Fig. 2) can be observed. Both 180° domain walls and 90°, 71°, 109° domain
walls were present [3, 4, 10].
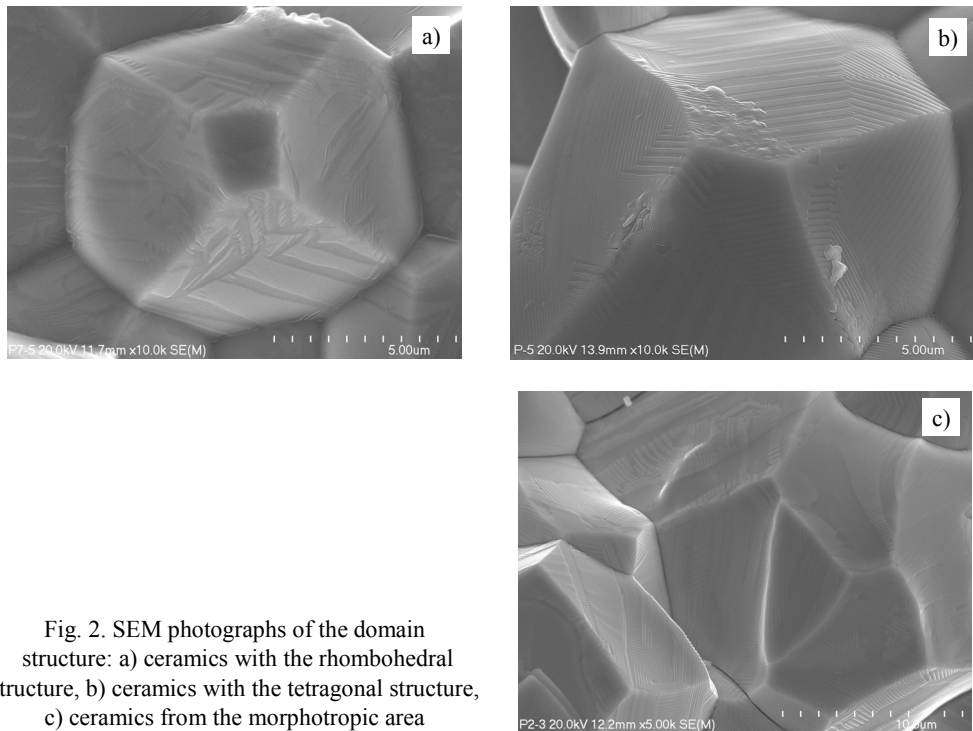
Fig. 2. SEM photographs of the domain structure: a) ceramics with the rhombohedral structure, b) ceramics with the tetragonal structure, c) ceramics from the morphotropic area

The presence of a great number of domain walls with high mobility is responsible
for the high value of internal friction for ceramics with the concentration of 53 mol %
$PbTiO_3$ belonging to the morphotropic area and slightly lower values for the ceramics
with the concentration of 52% i 54 mol % $PbTiO_3$ also belonging to the morphoropic
area. Moving away from the morphotropic area towards compositions with tetragonal
structure, a decrease in the internal friction value can be observed (Fig. 1). In the range
of higher $PbTiO_3$ concentrations corresponding to tetragonal structure (specimens with
65 mol % and 75 mol % of $PbTiO_3$) the configuration of domain structures must en-
sure the maximum compensation of mechanical stresses caused by an increase in the
deformation of a unit cell. For this reason, there is a complex structure with a great

number of 90° domain boundaries (Fig. 2) characterized by low mobility [12] in the tetragonal phase. Such a stabilized domain structure determines the ferroelectric hardness of ceramics, which causes an increase in mechanical quality factor, and therefore a decrease in internal friction. Moving toward the compositions with lower $PbTiO_3$ concentrations (25 mol % and 35 mol % of $PbTiO_3$), corresponding to a rhombohedral phase, an increase in the mechanical quality factor is also observed, thus a decrease in the internal friction background value (Fig. 1). This phenomenon is conditioned by a strong decrease in the number of domain walls for the ceramics with the rhombohedral phase structure. In this kind of ceramics, the 180° domain structure prevails (Fig. 2).

Values of internal friction background in the tested ceramics obtained from the synthesized powders by the sol-gel method are lower than the values of the internal friction background for ceramics obtained by a synthesis in the reaction method in the solid phase and sintering by the free sintering method. The value of internal friction depends on the domain width which in turn depends on the grain size in the ceramics. The domain width in the fine-grained ceramics obtained by the sol-gel method is much lower than the domain width in the coarse-grained ceramics [13–15]. This is why the values of the internal friction background are lower in these ceramics. An application of the sol-gel method to synthesize ceramic powders allows one to obtain PZT ceramics with high density and piezoelectric and dielectric parameters comparable with the parameters of the multi-component PZT type ceramics.

4. Conclusions

The value of internal friction background depends on the ceramics structure, grain size, type of domain structure. Ceramics belonging to the morphothropic area have the highest value of internal friction background. When moving from the $PbTiO_3$ concentration corresponding to the morphotropic area, both for the phase with the rhombohedral and tetragonal structure, a decrease in the value of internal friction background is observed, as a result of the presence of 90° domain structure with low mobility (the tetragonal phase) or a decrease in the number of domain walls (the rhombohedral phase). The characteristics of the dependence of $PbTiO_3$ concentration on internal friction background in PZT ceramics (obtained by the sol-gel method) are the same for ceramic materials sintered for different methods.

References

[1] BRUS B., ILCZUK J., Solid State Phen., 89 (2003), 309.
[2] XU H., *Ferroelectric Materials and Their Applications*, North Holland, New York, 1991.
[3] JAFFE B., COOK W.R., JAFFE H., *Piezoelectric Ceramics*, Academic Press, London, 1971.

[4] Fesenko E.G., Dancinger A.Ya., Razumovskaya O.N., *Novye piezokeramiczeskie materially*, RGU, Rostov-na-Donu, 1983 (in Russian).
[5] Surowiak Z., Kupriyanov M.F., Czekaj D., J. Eur. Cer. Soc., 21 (2001), 1377.
[6] Surowiak Z., Czekaj D., Mol. Quant. Acoust., 24 (2003), 183.
[7] Wallaschek J., J. Intell. Mat. Syst. Struct., 6 (1995), 71.
[8] Sun F.P., Chandhry Z., Liang C., Rogers C.A., J. Intell. Mat. Syst. Struct., 6 (1995), 134.
[9] Zachariasz R., Ilczuk J., Chrobak A., Ceramics, 66 (2001), 630.
[10] Tan Q., Viehland D., J. Am. Ceram. Soc., 81 (1998), 328.
[11] Zachariasz R., Zarycka A., Ilczuk J., Mater. Sci.-Poland, 25 (2007), 781.
[12] Bochenek D., Dudek J., Surowiak Z., Ceramics, 80 (2003), 445.
[13] Cheng B.L., Gabbay M., Fantozzi G., J. Mater. Sci., 31 (1996), 4141.
[14] Wang C., Fang Q.F., Zhu Z.G., J. Phys. D: Appl. Phys., 35 (2002), 1545.
[15] Bouzid A., Gabbay M., Fantozzi G., Mater. Sci. Eng., A 370 (2004), 123.

Synthesis and characterization of nanocrystalline $Ba_3Co_{0.9}Cu_{1.1}Fe_{24}O_{41}$ powder and its application in the reduction of radar cross-section

V. DA ROCHA CAFFARENA[1], T. OGASAWARA[2],
M. S. PINHO[3], J. L. LEIXAS CAPITANEO[2*]

[1]Centro Brasileiro de Pesquisas Físicas, Rua Xavier Sigaud 150, Urca, Rio de Janeiro, Brazil

[2]Dept. de Eng. Metalúrgica e de Materiais, Coppe-PEMM/UFRJ, Rio de Janeiro, Brazil

[3] Instituto de Pesquisas da Marinha (IPqM), Rio de Janeiro, Brazil

There has been a growing and widespread interest in the development of radar absorbing materials (RAM). Z-type hexaferrite is one of the most complex compounds in the family of hexaferrites that may be used in many applications. In this work, the citrate sol-gel process under an inert atmosphere was used to obtain the nanocrystalline $Ba_3Co_{0.9}Cu_{1.1}Fe_{24}O_{41}$ powder to be used as RAM. Cu^{2+} ions were incorporated into the structure of $Ba_3Co_2Fe_{24}O_{41}$ and, consequently, low temperature sintering and good magnetic properties were achieved. Composites of $Ba_3Co_2Fe_{24}O_{41}$ with polychloroprene (CR) were obtained for microwave absorption measurements by the transmission/reflection method, using a waveguide medium for the S- band and X-Ku bands. The 80:20 nanocomposite of $Ba_3Co_{0.9}Cu_{1.1}Fe_{24}O_{41}$:CR with 3.0 mm thickness exhibited the best performance as a RAM for the X-band, with 99.50% microwave absorption at 9.5 GHz.

Key words: *(Co–Cu)₂Z hexaferrite; hysteresis; inert atmosphere; citrate sol-gel process; nanocomposite; radar absorbing material; waveguide*

1. Introduction

Radar absorbing materials (RAM) play an important role in the stealth technology, which corresponds to the invisibility of military platforms to different systems of detection (radar, acoustic, infrared, etc), by suppressing microwaves reflected from metallic structures and reducing the radar cross section (RCS) of targets. Advanced ceramics (optical, electronic, structural, and magnetic ceramics) have been developed using a number of basic principles related to different structure levels, from the micro

---

* Corresponding author, e-mail: jeff@ima.ufrj.br

to macro level [1, 2]. Moreover, magnetic materials form the basis for numerous new devices, which rely on soft or hard (permanent) magnets [1].

As magnetic materials, barium hexaferrites are not generally replaced by any other magnetic material, because they are relatively inexpensive, stable, and have a wide range of technological applications. Barium hexaferrites have been classified, according to their structures, into five main classes: $BaFe_{12}O_{19}$ (M-type), $BaMe_2Fe_{16}O_{27}$ (W-type), $Ba_2Me_2Fe_{28}O_{46}$ (X-type), $Ba_2Me_2Fe_{12}O_{22}$ (Y-type), and $Ba_3Me_2Fe_{24}O_{41}$ (Z-type), where Me represents a divalent ion from the first transition series.

Z-type barium hexaferrite is a promising material for applications such as RAM at GHz frequencies, which requires high permeability, great resistivity, and good chemical and thermal stability. These ferrites absorb microwaves due to various interactive loss mechanisms related to the magnetization and electric polarization of the material. The values of relative complex permeability ($\mu' - j\mu''$) and permittivity ($\varepsilon' - j\varepsilon''$) affect the reflectivity of such materials, and therefore their performance as RAM.

(Co-Cu)$_2$Z barium hexaferrite is a new type of soft magnetic compound which presents these characteristics and a ferromagnetic resonance at GHz frequencies, being useful for inductor cores or in UHF communications in the microwave region [3, 4]. In conventional ceramic methods, a high sintering temperature is necessary to obtain this Z-type hexaferrite due to the complex crystalline structure shown in Fig. 1.

S   Spinel Blocks
H   Hexagonal Blocks
○   Cations in tetrahedral sites
●   Cations in octahedral sites

↕   Direction of magnetic momentum

○   O²⁻
◎   Ba²⁺
⊗   Hexagonal sites with five oxygen ions forming a byparamidal structure
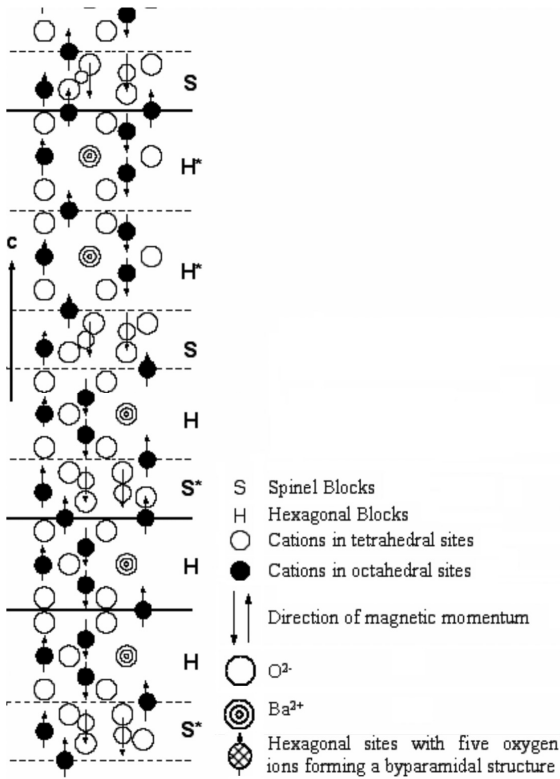
Fig. 1. Cross-section of one unit cell of the Z-type barium hexaferrite structure

By using chemical methods, this temperature can be reduced, which is necessary for modern cost-driven applications to produce electronic components, such as inductors, chips beads, beads arrays, LC filters, etc. [5].

In this work, the citrate sol-gel process under an inert atmosphere was used to obtain $Ba_3Co_{0.9}Cu_{1.1}Fe_{24}O_{41}$. The process permits the formation of the Z-type phase at lower sintering temperatures [6]. The introduction of Cu^{2+} ions in the structure of $Ba_3Co_2Fe_{24}O_{41}$ can also reduce the sintering temperature, because it can act as a flux due to its low melting point (1084.62 ºC). X-ray diffraction (XRD), X-ray fluorescence (XRF), thermal analysis (TGA/DTA), and atomic force microscopy (AFM) were used to characterize the synthesized material.

The relative complex permeability and permittivity parameters of ferrite-polymer composites may depend on the type, composition and concentration of ferrite, and the nature of the polymer besides the temperature and frequency of operation [6]. The way these magnetic and dielectric properties change with frequency is responsible for the performance of the RAM. In this way, composites of $Ba_3Co_{0.9}Cu_{1.1}Fe_{24}O_{41}$ and polychloroprene (CR) were obtained for microwave absorption measurements in the frequency ranges: 2.6–4.0 GHz (S-band), 8.0–12 GHz (X-band), and 12–16 GHz (Ku-band). The microwave measurements were based on the transmission/reflection method (T/R) using rectangular waveguides as the confining medium for the samples. The materials were analysed in the frequency ranges 2.6–4.0 GHz (S-band) and 8.0–16.0 GHz (X-Ku bands) [7]. The vibrating sample magnetometer (VSM) allowed the magnetic hysteresis loop to be determined.

2. Experimental

Each of several key-metal cations reacts with citric acid, under controlled pH conditions, to give the respective metal citrate, comprising a homogeneous joint metallic citrate precursor complex.

Nano-sized $(Co-Cu)_2Z$ structured powders were synthesized by the citrate precursor method using reagent grade $Fe(NO_3)_3.9H_2O$, $Ba(NO_3)_2$, monohydrate citric acid, $Co(NO_3)_2 \cdot 6H_2O$, and $Cu(NO_3)_2 \cdot 3H_2O$ in stoichiometric molar ratios to obtain $Ba_3Co_{0.9}Cu_{1.1}Fe_{24}O_{41}$ hexaferrite. The solids were weighed and then placed into appropriate closed vessels subject to a super dry nitrogen atmosphere to obtain the precursor solutions [8]. Distilled water was added under agitation, until the total dissolution of the solids.

The solutions were then transferred to a previously evacuated flask and mixed under super dry nitrogen operating as a reflux condenser, with intensive stirring. The resulting mixture was heated to 80 ºC to complete the reaction under reflux, in order to keep the inert atmosphere and to allow subsequent additions of ammonium hydroxide (NH_4OH) added drop-wise into the solution to render it neutral or slightly alkaline (pH 7.0–8.0) for the subsequent precipitation of the organometallic complex [8].

Pre-dried ethanol was previously added drop-wise under vigorous stirring into the reaction mixture, to promote the precipitation of a complex citrate gel of barium, iron, copper, and cobalt. While drying at 60 ºC, leaving behind the desired solid phase, the remaining aqueous solution was eliminated. The ideal temperature for citrate gel decomposition was determined by thermogravimetric analysis (TGA) and differential thermal analysis (DTA). Based on the results of the thermal analyses, the batch of dried solid was calcined inside a muffle furnace. TGA and DTA measurements were carried out on TA Instruments SDT-2960. The experiments were carried out in static air, using platinum crucibles between 20 and 1000 ºC, with a heating rate of 10 ºC/min.

The calcination was performed using the following heating schedule: 2 ºC/min up to 410 ºC, establishing a plateau for 1 hour, 10 ºC/min up to the final sintering temperature with a residence time of 4 hours at the sintering temperature. The material was then cooled to room temperature at the rate of 10 ºC/min.

X-ray fluorescence (XRF) measurements were carried out on a Philips model PW 2,400 sequential spectrometer. This quantitative method was used to determine the stoichiometry of the ferrite samples, which were analysed in the form of a fused bead, using a lithium tetraborate flux.

For the powder X-ray diffraction (XRD) analysis, the material was placed on a glass sample holder and spread out to form a thin layer. A Siemens AXS D5005 diffractometer was employed with a dwell time of 1 deg/min in the θ–2θ Bragg –Brentano geometry. Magnetic hysteresis loops were obtained using a vibrating sample magnetometer VSM 4,500 PAR. The morphological study was performed using a ZEISS DSM 940A scanning electron microscope and a Topometrix II® atomic force microscope.

In order to obtain composites for the measurements of microwave absorbing properties, the powders were mixed with polychloroprene (CR), resulting in a 80:20 composition (wt. %, ferrite:polychloroprene). The processing was carried out in a Berstorff two roll mill, at room temperature, with velocities of 22 and 25 rpm (back and forward). Vulcanised 8.0×4.0 cm^2 samples with variable thickness were obtained by compression moulding in a hydraulic press at 150 °C and 6.7 MPa. The vulcanisation times were determined by the data obtained in the Monsanto Rheometer TM100 [7]. The dispersion of the magnetic particles in CR was evaluated by SEM.

The microwave measurements conducted in this work were based on the transmission/reflection method (T/R) using rectangular waveguides as the confining medium for the samples. The microwave absorption of the sheet composites was illustrated by variations in reflectivity (dB) versus frequency (GHz), using a HP 8510B network analyser system. The HP 8510B was employed to determine the values of ε', ε'', μ', and μ'' at different frequencies, by measuring the reflected and transmitted scattering parameters, S_{11} and S_{21}. The materials were analysed in the frequency ranges 2.6–4.0 GHz (S band) and 8.0–16.0 GHz (X–Ku bands) [7, 9, 10].

3. Results and discussion

Results of the X-ray fluorescence analysis (Table 1) confirmed the elimination of the organic precursor and showed that the synthesized powders achieved the planned stoichiometry.

Table 1. Chemical composition of Ba$_3$Co$_{0.9}$Cu$_{1.1}$Fe$_{24}$O$_{41}$

Compound	Content (wt. %)
BaO	18.17
CoO	2.66
CuO	3.46
Fe$_2$O$_3$	75.71

Figure 2 shows TGA and DTA curves of the precursor gel. No significant weight loss occurred above 400 ºC, indicating that any remnant organic material had already been completely eliminated [9]. Based on this result, the gel was calcined at 410 ºC.
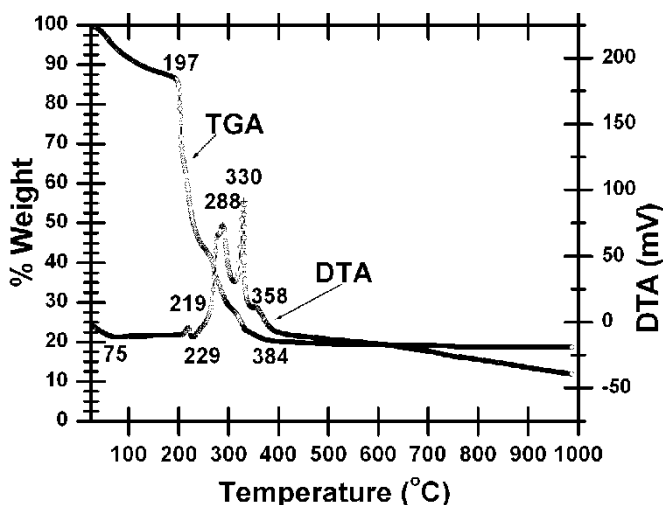
Fig. 2. TG-DTA curves for the Z-type precursor gel of Ba$_3$Co$_{0.9}$Cu$_{1.1}$Fe$_{24}$O$_{41}$ powder

XRD results presented in Fig. 3 indicate that at 950 ºC the Z-type phase was clearly the majority phase, according to JCPDS 19-0097. According to Pullar et al., however, this material contains small undetectable amounts of the Y-type phase (Ba$_2$Co$_2$Fe$_{12}$O$_{22}$), coexisting with the Z-type phase [11].

Atomic Force Microscopy (AFM) was used to characterize the Z-type ferrite powder and it is observed in Fig. 4 that the particles are sharply hexagonally plated with nanometric sizes (230×100 nm^2).
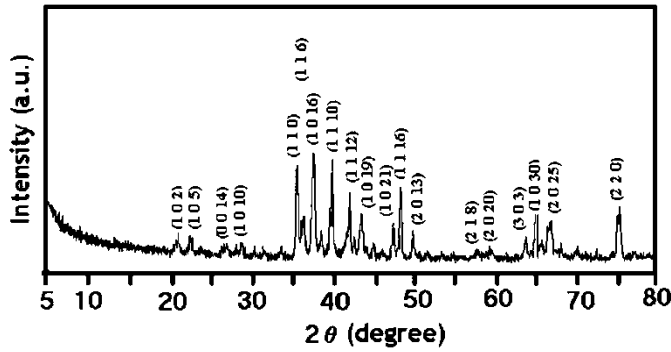
Fig. 3. X-Ray diffraction curve for the Z-type powder calcined at 950 ºC
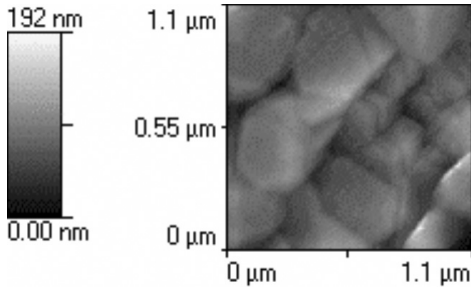
Fig. 4. AFM micrograph of $Ba_3Co_{0.9}Cu_{1.1}Fe_{24}O_{41}$ calcined at 950 ºC (100 000 X, 200 kV)

The hysteresis curves for Z-type barium hexaferrites fired at 950 °C are shown in Fig. 5. The magnetization curves show typical features of magnetically soft ferrites. The saturation magnetization M_s was obtained by extrapolating $M(1/H)$ curves to $1/H = 0$, resulting in values of 57.8 emu/g for $Ba_3Co_{0.9}Cu_{1.1}Fe_{24}O_{41}$ and 52.3 emu/g for Co_2Z ($Ba_3Co_2Fe_{24}O_{41}$).
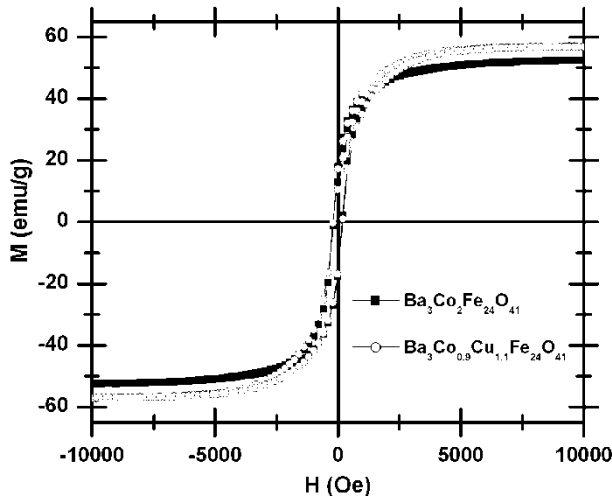
Fig. 5. Magnetic hysteresis curves of $Ba_3Co_2Fe_{24}O_{41}$ and $Ba_3Co_{0.9}Cu_{1.1}Fe_{24}O_{41}$ powders

The ionic radius of Cu^{2+} (0.085 nm) is very close to that of Co^{2+} (0.082 nm) and larger than that of Fe^{3+} (0.067 nm). The copper ions occupy the octahedral sites in the structure of Z-type hexaferrite and partially substitute cobalt ions. The Cu^{2+} ons distort the crystalline field due to their electronic configuration, and this behaviour results in an increase in M_s [5].
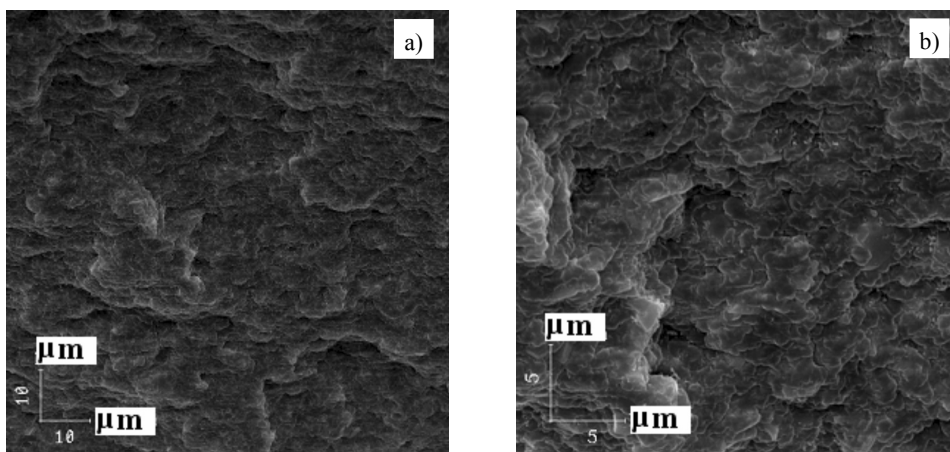

Fig. 6. SEM micrographs of Ba$_3$Co$_{0.9}$Cu$_{1.1}$Fe$_{24}$O$_{41}$:CR; magnification: a) 1000×, b) 3000×

Figures 6a and b show a good dispersion of Z-type hexaferrite magnetic particles in the polychloroprene matrix (80:20, wt. %). It can be seen from the SEM images (Fig. 6) that rubber mixing is a very good technique for the dispersion of Z-type hexaferrite particles, in spite of a high weight concentration used (80%) and the tendency of these particles to form magnetic agglomerates [7].
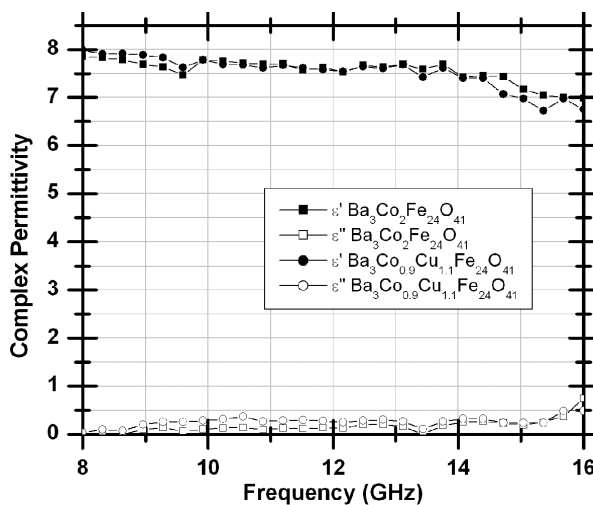

Fig. 7. Frequency dependences of the complex permittivity for the composites

Figure 7 indicates that the addition of Cu does not cause a significant variation in the permittivity measurements with frequency. Figure 8 shows the larger values of permeability for the $Ba_3Co_{0.9}Cu_{1.1}Fe_{24}O_{41}$:CR nanocomposite, which can be attributed to the addition of Cu.
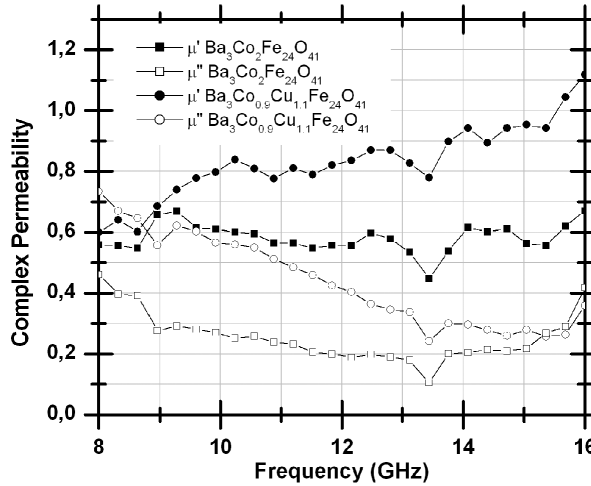

Fig. 8. Frequency dependences of the complex permeability for the composites

The microwave absorption spectra for the $Ba_3Co_{0.9}Cu_{1.1}Fe_{24}O_{41}$:CR nanocomposites of various thicknesses are illustrated by the reflectivity curves in Fig. 9, for the frequency ranges: (a) 2.6–4.0 GHz (S-band), (b) 8.0–16 GHz (X-Ku bands) [12, 13].
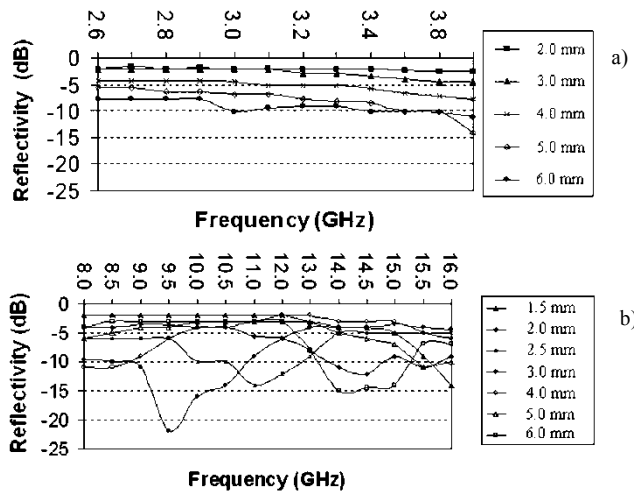

Fig. 9. Reflectivity curves for 80:20 (wt. %) $Ba_3Co_{0.9}Cu_{1.1}Fe_{24}O_{41}$:CR composites: (a) S-band and (b) X-Ku bands

As seen in Fig. 9b, the Ba$_3$Co$_{0.9}$Cu$_{1.1}$Fe$_{24}$O$_{41}$:CR nanocomposites (80:20) showed better performance as RAMs for the X-Ku bands (8–16 GHz), with smaller thickness. A microwave absorption of 90.00 % (a reflectivity of –10 dB) was observed in the frequency range 10.0–13.0 GHz for the thickness of 2.5 mm, with a maximum absorption of approximately 96.90 % (–15 dB) at 11.0 GHz. The effect of adding Cu on reflectivity measurements can be seen in Fig. 10.
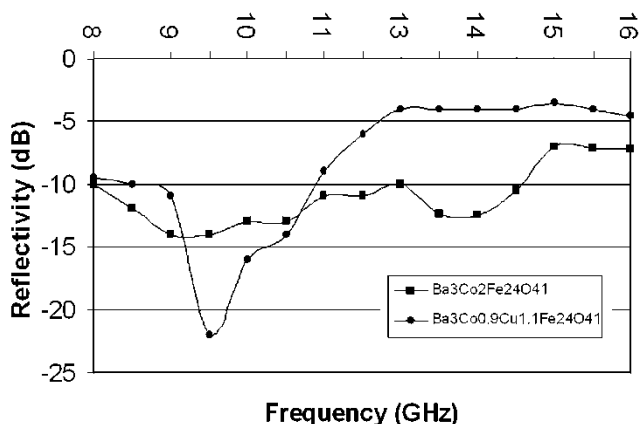

Fig. 10. The effect of adding Cu on the reflectivity measurements for 80:20 composites of Ba$_3$Co$_2$Fe$_{24}$O$_{41}$: CR and Ba$_3$Co$_{0.9}$Cu$_{1.1}$Fe$_{24}$O$_{41}$:CR, with thicknesses of 3.0 mm

The highest microwave absorption for the Ba$_3$Co$_{0.9}$Cu$_{1.1}$Fe$_{24}$O$_{41}$:CR nanocomposite ((99.50% at 9.5 GHz) with the thickness of 3.0 mm can be attributed to the addition of Cu, resulting in an increase of the magnetic properties.

4. Conclusions

The citrate method promoted the formation of nanocrystalline Z-type hexaferrite at a lower temperature (950 ºC) than that employed by the conventional methods (1200 –1300 ºC). The introduction of Cu^{2+} ions improved the magnetic properties of this ceramic, as illustrated by an increase of 5.5 emu/g in M_s and permeability. As a result, the 80:20 nanocomposite of Ba$_3$Co$_{0.9}$Cu$_{1.1}$Fe$_{24}$O$_{41}$:CR with the thickness of 3.0 mm showed the best performance as a RAM for the X-band, with a microwave absorption of 99.50% (–22.5 dB) at 9.5 GHz. This result allows its application by covering some strategic metallic parts of Brazilian Frigate superstructures, reducing the radar cross section of these targets.

References

[1] Cramer D.C., *Overview of Technical, Engineering, and Advanced Ceramics*, [in:] *Engineered Materials Handbook: Ceramics and Glasses*, ASM International, New York, USA, 1998, pp. 16–20.
[2] Deconihout B., Pareige C., Pareige P., Blavette D., Menand A., Microscopy Microanal., 5 (1999), 39.
[3] Zhang H., Zhou J., Yue Z., Wu P., Gui Z., Li L., Mater. Lett., 43 (2000), 62.
[4] Wang Z., Li L., Su S., Gui Z., Yue Z., Zhou J., J. Eur. Cer. Soc., 23 (2003), 715.
[5] Zhang H., Zhou J., Li L., Yue Z., Gui Z., Mater. Lett., 55 (2002), 351.
[6] Caffarena V.R., D. Sc. Thesis, *Study of the Magnetic and Microwave Absorber Properties of Z-Type Barium Hexaferrite Obtained by Citrate Precursor Method, PEMM-UFRJ*, Rio de Janeiro, Brazil, 2004.
[7] Pinho M.S., Gregori M.L., Nunes R.C.R., Soares B.G., Eur. Pol. J., 38 (2002), 2321.
[8] Ogasawara T., Oliveira M.A.S., J. Magn. Mag. Mater., 217 (2000), 147.
[9] Caffarena V.R., Ogasawara T., Capitaneo J.L., Pinho M.S., *Synthesis of (Co-Zn)-Z-Type Barium Hexaferrite for use as Microwave Absorber*, [in:] *Applied Mineralogy: Developments in Science and Technology*, M. Pechio, F.R.D. Andrade, L. Z. D'Agostino, H. Kahn, M. Sant'Agostino, M.M.M.L. Tassinari (Eds.), Fundação Biblioteca Nacional, São Paulo, Brazil, 2004, pp. 49–52.
[10] Austissier D., Podembski A., Jacquiod D.C., J. Phys. C, 4 (1997), 1409.
[11] Pullar R.C., J. Magn. Magn. Mat., 186 (1998), 313.
[12] Weir W.B., IEEE Trans., 62 (1974), 33.
[13] Weir W.B., IEEE Trans. Inst. Meas., IM 23 (1974), 140.

Computational study of the C–C interaction in the *bcc* Fe(001) inner plane containing a vacancy

S. SIMONETTI[1, 2*], A. JUAN[2], G. BRIZUELA[2]

[1]Departamento de Ingeniería Mecánica, Universidad Tecnológica Nacional,
11 de Abril 461, 8000 Bahía Blanca, Argentina

[2]Departamento de Física, Universidad Nacional del Sur,
av. Alem 1253, 8000 Bahía Blanca, Argentina

The C–Fe interaction in the (001) *bcc* Fe that contaning a vacancy was analyzed using a semi-empirical theoretical method. A cluster model containing 125 atoms was used to simulate the local environment of the Fe vacancy. Carbon atoms were positioned in their local energy minima configurations. The most stable positions for the C atoms in the (001) *bcc* Fe were found at about 1.2 Å from the vacancy centre and close to the first nearest-neighbour octahedral sites. Fe atoms surrounding the vacancy weaken their bond when C is present. This bond weakening is a consequence of the C–Fe bond formation. The Fe–C interactions occur mainly via Fe 4s orbitals with a lesser participation of Fe 4p and Fe 3d orbitals. The C–C interaction was also analyzed. For the C–C distance of 1.4 Å, there is a possible bonding between the C atoms in the (001) *bcc* iron. The Fe–C interactions are stronger than the C–C interaction.

Key words: *computer simulation; vacancy; iron; carbon*

1. Introduction

Desirable reactions include the formation of carbon nanotubes from gaseous hydrocarbons, making gasoline from synthesis gas, etc. [1–3]. On the other hand, coke formation on the catalyst surface is undesirable, as it poisons the catalyst [4]. It is therefore of interest to study how isolated carbon atoms bind with Fe surfaces, as the first step towards understanding further reactions involving carbon interaction with other carbon atoms on the surface or with substrate Fe atoms to form carbide. Carbon atoms occupy octahedral positions of the *bcc* Fe lattice causing distortion due to the size of its atomic radii [5]. Mc. Lellan et al. propose that diffusing C atoms occupy tetrahedral and octahedral sites successively [6]. Grabke investigates the C adsorption and reports that most probably it occurs in the interstitial sites on the surface, each embedded between four iron atoms [7]. Jiang and Carter find that carbon atoms bind strongly with Fe surfaces and prefer high coordination sites [8].

---

*Corresponding author, email: ssimonet@uns.edu.ar

The presence of carbon affects electronic structure of the bulk iron ions. Anderson studied the interaction of carbon with iron surfaces and found bond weakening and rehybridization of iron orbitals [9]. Gavriljuk et al. observed that the metal-impurity interaction was limited by the local environment. The electron states localized on the second Fe neighbour were weakly influenced by the impurity [10]. Carbon impurities have been observed to interact strongly with lattice defects. The study of foreign interstitial C atoms interacting with point defects in *bcc* Fe has been reported by Domain et al. The authors reported a strong binding energy of C with the vacancy [11].

The energy of a carbon and hydrogen atoms interacting with other iron crystalline defects was investigated by our group in previous works and reported in [12–14]. We have studied the electronic structure of C and H atoms simultaneously absorbed in an (111) edge dislocation core system in *bcc* iron [12], near a stacking fault zone in *fcc* iron [13] and in the region of a bivacancy [14]. The defect zone is the preferential region for the C localization. The C acts as an expeller of H and could reduce the detrimental effect of H on the Fe–Fe bonds. The C atom has also the possibility of making a bridge between Fe atoms of different layers that could provide an additional compensation effect to the Fe matrix.

The objective of the present work is to study the interaction between one and two C atoms with a monovacancy in the (001) *bcc* Fe, including the electronic structure and bonding considerations. The (001) *bcc* Fe plane was selected for the present study because it contains the metal vacancy and the nearest interstitial sites. The theory and model considered are described in the following sections.

2. Computational method

Our calculations were performed using the ASED-MO (atom superposition and electron delocalization molecular orbital) method which predicts molecular structures from atomic data (atomic wave functions and ionisation potentials) [15–18]. The modification of the extended Hückel molecular orbital method (EHMO) was implemented with the YAeHMOP program [19]. Double zeta expansions of metal d orbitals were employed. The parameters are listed in Table 1.

Table 1. Parameters for ASED-MO calculations

Atom	Orbital	Ionization potential [eV]	Slater exponent (au-1)	Linear coefficient	Electronegativity (Pauling)
Fe	3d	9.00	5.35	0.5366	1.8
			1.80	0.6678	
	4s	7.87	1.70		
	4p	4.10	1.40		
C	2s	16.59	1.55		
	2p	11.26	1.45		

The ASED-MO is a semi-empirical method which makes a reasonable prediction of the molecular and electronic structure [20]. The ASED theory is based on a physical model of molecular and solid electronic charge density distribution functions [18–21]. The adiabatic total energy values were computed as the difference between the electronic energy (E) of the system when the impurity atom/fragment was at a finite distance within the bulk and the same energy when that atom/fragment was far away from the solid surface. There are many types of energies concerning electronic structure calculations.

The sequential carbon absorption energy can be expressed as:

$$\Delta E_{\text{total}} = E\left(Fe_m - C_n\right) - E\left(Fe_m - C_{n-1}\right) - E\left(C\right) + E_{\text{repulsion}} \tag{1}$$

where m is the size of the cluster and n is the number of carbon atoms.

The stability of the agglomeration of carbon in Fe, that is the energy difference between the agglomeration of n carbon and n single carbon atoms in Fe vacancy, was also computed as:

$$\Delta E_{\text{aggl,total}} = E\left(Fe_m C_n\right) - E\left(Fe_m\right) - n\left[E\left(Fe_m C_1\right) - E\left(Fe_m\right)\right] + E_{\text{repulsion}} \tag{2}$$

where again m is the size of the cluster and n is the number of carbon atoms.

The binding energy is the difference between the minimum adsorption energy of C impurity in the vacancy, $\Delta E(C_{\text{def}})$, and the adsorption energy of C impurity on a tetrahedral or octahedral interstitial site of the perfect Fe matrix, $\Delta E(C_{\text{int}})$. Then, it was calculated as:

$$\Delta E_{\text{binding}} = \Delta E(C_{\text{def}}) - \Delta E(C_{\text{int}}) \tag{3}$$

The repulsive energy was computed taking into account all atom–atom interactions.

To understand the interactions between the atoms, we used the concept of DOS (density of states) and COOP (crystal orbital overlap population) curves. The DOS curve is a plot of the number of orbitals per unit volume per unit energy. The COOP curve is a plot of the overlap population weighted DOS vs. energy. The integration of the COOP curve up to the Fermi level (E_f) gives the total overlap population of the bond specified and it is a measure of the bond strength.

A comment follows about the methods used in this paper. The (EH) based methods supply useful information about different aspects of the electronic structure and the chemical reactivity. The method has been successfully employed for the analysis of experimental information and their correlation with atomic data. It is a methodology that reveals the basic interactions that are responsible for chemical bonding and allows one to examine the relationship between systems with similar geometrical and compositional distributions. Another advantage of the method (and its modification) is that it allows working with systems that include hundred atoms of transition metals per unit cell. Our group has recently used this method in similar systems, computing under the ASED approximation the C and H trajectories in defects of α-Fe and γ-Fe matrices

[12–14]. Our results match qualitatively those of ab-initio calculations. The structure and properties of iron bulk and Fe alloys were calculated in order to establish the reliability of the method employed, as well as to determine suitable converged values of computational parameters to be used in the subsequent determination of the impurity position. When we compare our results obtained from the ASED method with those obtained from other theoretical methods, we can see that the results are in a good agreement. The method allows us to determine the contribution of each orbital of Fe and C atoms to the bonding. Using extended Hückel calculations we have tried to build a bridge between chemical intuition and computational theory. We are interested in understanding, trends, and occasionally predictions. The key strength of the ASED (or EH) method consists in its transparency and the main objective of the present work is to provide a qualitative picture of C atoms binding within the Fe matrix.

3. The Fe-vacancy cluster model

BCC iron has a *bcc* structure with a lattice parameter *a* of 2.861 Å and the nearest neighbour distance of 2.47 Å [22]. The cluster used to simulated solid *bcc* Fe has 125
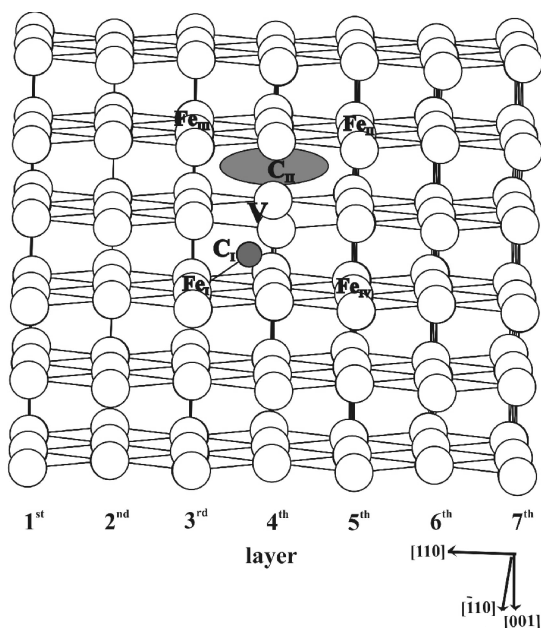
Fig. 1. Schematic view of the impurity adsorption in the (001) *bcc* Fe containing the vacancy (V). The C_I location and the favourable zone for C_{II} adsorption are indicated

atoms of Fe distributed in seven layers stacking (110) planes. The vacancy is set in the fourth layer (Fig. 1). The thickness of this slab is sufficient to approximate the electronic structure of 3D bulk Fe in the innermost layer.

We have computed the adiabatic total energy of the system absorbing up to one and two carbon atoms in the vacancy region. The impurities were located, one by one, in their positions of minimum energy. We have computed the minimum energy position for the impurities covering the entire (001) plane which contains the metal vacancy, and the nearest octahedral and tetrahedral sites. Having determined the most stable position for the impurities in the zone near the vacancy, we studied the Fe_{matrix} –C and the impurity–impurity interactions.

4. Results and discussion

4.1 The Fe_{125}–C_I system

4.1.1. Location of a carbon atom near the vacancy zone

First of all, we performed calculations for a single carbon atom (C_I) inside the cluster, finding a minimum of −13.55 eV, indicating its most stable localization in the (001) *bcc* Fe. The minimum was found at 1.72 Å of its first Fe neighbour (Fe_I). The contour lines corresponding to the energy surface for C absorbed on the region mentioned in the previous paragraph are shown in Fig. 2.
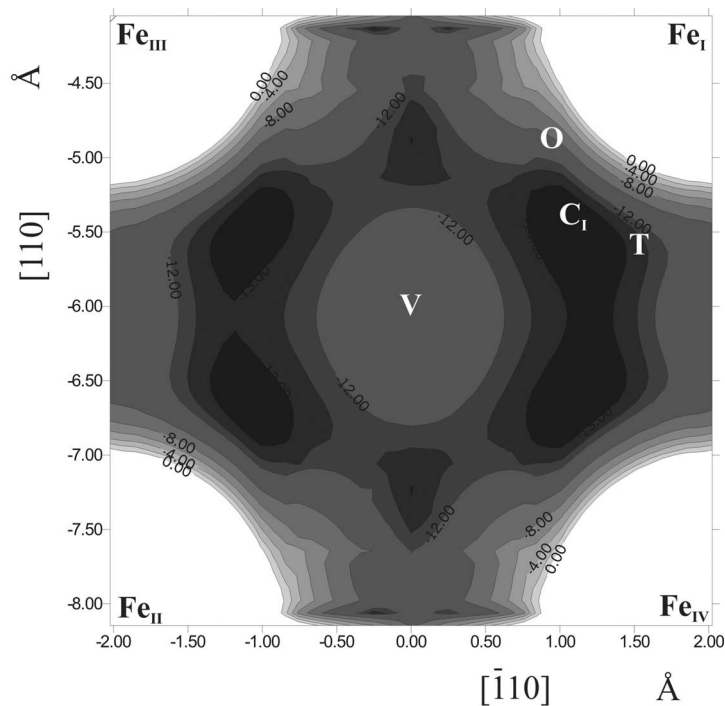
Fig. 2. Contour lines corresponding to the energy (eV) for the Fe_{125}–C_I system in the (001) plane containing the vacancy (V). The tetrahedral (T) and octahedral (O) interstitial sites are indicated

In an ab initio high level investigation of the diatomic iron carbide molecule, FeC, Tzeli and Mauridis report the C–Fe distance of 1.581 Å which agrees with the corresponding experimental one [23]. Niu et al. report the Fe–C distance near the dislocation core of 1.84 Å, using first principles methods including atomic relaxation [24]. Wu et al., while investigating the effect of C on Fe-grain boundary cohesion by first principles, found the C–Fe distance on (111) surface of 1.80 Å and 4% shorter than this value in the grain boundary environment [25]. Anderson, studying diatomic iron carbides, reported the Fe–C bond length of 1.77 Å which compares well with the Fe–C bond length of 1.82 Å in $[Fe_6C(CO)_{16}]^{2-}$ [21]. Jiang and Carter reported Fe–C distances of 1.98 Å on Fe (100) and 2.37 Å on Fe(110) [8]. On the other hand, the C minimum energy position in the vacancy region was found at 1.19 Å from the vacancy centre. Hautojärvi et al. established that during vacancy migration at 220 K, an asymmetric vacancy–carbon pair was formed, where the carbon atom was located 1.042 Å off the centre of the vacancy [26]. Domain et al. reported the vacancy–C distance of 1.142 Å from the vacancy centre [11]. Johnson and Damask reported that the carbon atom was positioned at 0.73 half-lattice constants from the vacancy centre along the <100> line, not far from the neighbouring octahedral position at the distance of one half-lattice constant [27]. In our case, the C atom was positioned at 0.389 Å and 0.508 Å from the nearest octahedral and tetrahedral sites, respectively. We also computed the binding energy (section 2) and discovered that the C minimum energy position in the zone of the monovacancy was 1.577 eV and 3.017 eV more stable than the C location on the tetrahedral and octahedral site of the perfect Fe matrix, respectively. These results showed an additional effect of trapping of the vacancy zone on the C atom.

4.1.2 Electronic structure

In Figure 3, an interaction diagram is shown. The metal d states form a band starting at −12 eV and with a bandwidth of 5 eV. A substantial number of s and p states penetrate the d band. The dispersion of s and p bands is much larger than the d band, reflecting the higher overlap between s and p orbitals and the more contracted nature of d orbitals. If we compare both the total DOS shown in Figs. 3a, b we can see that they are similar. The DOS of the Fe_{125}–C_I system is dominated by many bulk and surface Fe atoms. However, some changes could be observed in the region below the d metal band and it consists of peaks corresponding to C_I-based states. The impurity-based peaks are centred at lower energies, which represent an additional energetic stabilization in the vicinity of the vacancy. The small contribution of the impurity to DOS is due to its low concentration. Figure 3c shows the projected DOS for the C_I impurity. The value of the Fermi energy (E_f) is −8.138 eV. As expected, we found no significant change in the E_f. The total DOS is dominated by the Fe matrix, so that the changes are small.

Carbon affects the states of its nearest neighbour metallic bonds. The number of Fe atoms involved in the Fe–Fe bond closer to C_I. Fe_I–Fe_{nn} OP decreases to about 62%

when the C_I atom is present (Table 2). This bond weakening is a consequence of a strong C_I–Fe_I interaction. The COOP curves in Fig. 4, corresponding to the C_I–Fe_I interaction, represent bonding and antibonding peaks and the integration up to the E_f gives the total OP for the C–Fe bonding. Then, the C_I–Fe_I bonding is formed with an OP of 0.633.
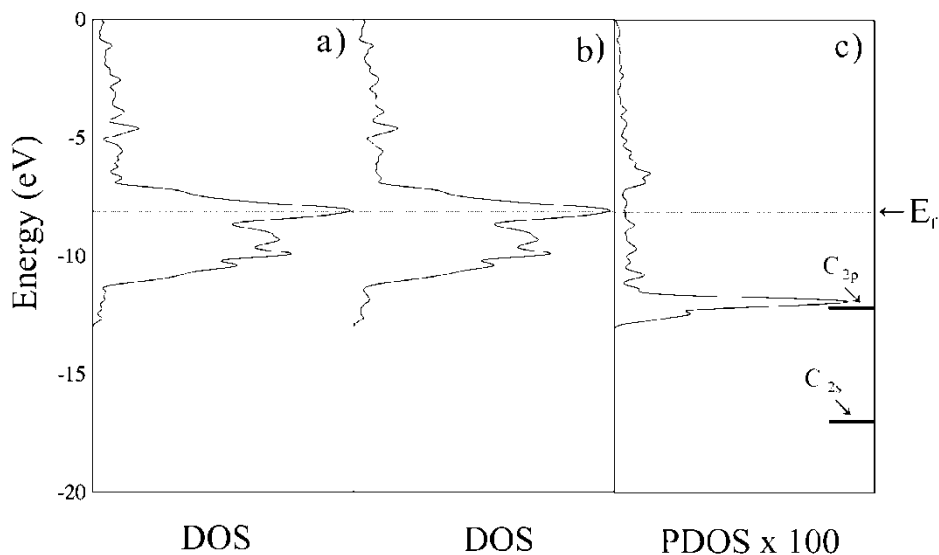

Fig. 3. Total DOS for the isolated Fe cluster (a), total DOS for the Fe_{125}–C_I cluster (b) and projected DOS for the C_I atom in the Fe_{125}–C_I cluster (c)

Table 2. Atomic orbital occupations and net charges for the C atoms and their neighbouring Fe atoms as well as the corresponding OP values for these atoms

Atom	s	p	d	Charge	Bond	OP
C_I	1.550	3.779[a]		−1.329[a]	C_I–Fe_I	0.633[a]
	1.546	3.702[b]		−1.248[b]		0.636[b]
C_{II}	1.543	3.704[b]		−1.247[b]	C_{II}–Fe_{II}	0.683[b]
Fe_I	0.606	0.272	5.616[a]	1.507[a]	C_I–C_{II}	0.050[b, c]
	0.605	0.273	5.641[b]	1.480[b]		0.021[b, d]
	0.709	0.280	5.854[e]	1.157[e]	Fe_I–Fe_{Inn}	0.116[a]
						0.115[b]
Fe_{II}	0.694	0.293	5.730[a]	1.283[a]		0.302[e]
	0.587	0.281	5.420[b]	1.711[b]		
	0.694	0.292	5.718[e]	1.297[e]	Fe_{II}–Fe_{IInn}	0.102[b]
						0.298[e]

[a]In the Fe_{125}–C_I system.
[b]In the Fe_{125}–C_I–C_{II} system.
[c]Corresponding to the C–C distance of 1.40 Å.
[d]Corresponding to the C–C distance of 2.40 Å.
[e]In the isolated Fe_{125} system.

The Fe_I 4s population decreases to about 14% when the C_I impurity is present. This indicates a participation of Fe_I 4s orbitals in the C_I–Fe_I bondings. The contribution of Fe_I 4p and Fe_I 3d populations decrease to about 3% and 4%, respectively. Some Fe–Fe bonding states are pushed up to just below the E_f. There is an electron transfer of $0.35e^-$ to the impurity from its nearest Fe neighbours. Domain et al. report that the only charge transfer clearly visible is between the C atom and its first neighbours [11].
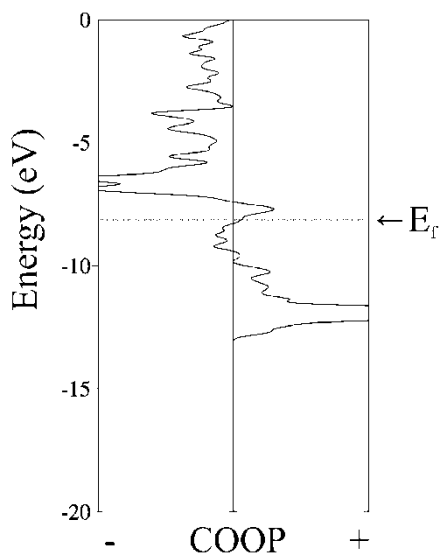
Fig. 4. COOP curves for C_I–Fe_I in the Fe_{125}–C_I system

A charge of about $0.53e^-$ was reported for interstitial C in Fe clusters located at octahedral sites of the lattice [33]. Ellis et al., studying the diffusion properties in the interstitial Cu–C solid solutions with embedded cluster density functional calculations, determined that the C acts as an acceptor of electrons in Cu, when an isolated interstitial C is placed at different sites in the lattice. The charge transfer comes from its nearest neighbours [34]. Niu et al. studying the electronic effect in dislocation core system with the presence of a C atom in the *bcc* Fe found that there were charge transfers of 0.68 e⁻ from the adjacent Fe atoms to the C atom and strong hybridizations occured between the C 2s, 2p orbitals and the Fe 4s, 4p orbitals [24]. In the present study, the impurity develops a negative charge while the closest Fe atoms obtain more positive charge. The additional electron from the carbon atom occupies an Fe–Fe antibonding level near E_f. So, the Fe–Fe antibonding states are now populated and it is due to the increase in E_f with respect to the clean cluster. There is less bonding due to greater participation of the Fe 4s orbital in the Fe-impurity bondings. The charge and the electron densities of the atoms involved in the interactions are summarized in Table 2.

4.2. The Fe$_{125}$–C$_I$–C$_{II}$ system

4.2.1. Location of the second carbon atom near the vacancy zone

In the second stage, we performed calculations for an additional C atom (C$_{II}$) in the (001) *bcc* Fe that contains a vacancy. The fixed first C atom (C$_I$) resides in its minimum position (as described above), while C$_{II}$ is moved along the vacancy region. Figure 5 shows the energy contour plot for the Fe$_{125}$–C$_I$–C$_{II}$ system. We can see that there is a region of minimum energy for C$_{II}$ adsorption. The vacancy offers much more room to accommodate the interstitial C atoms. Considering this zone, the shorter distances of the equilibrium C$_I$–C$_{II}$ interactions are within the typical covalent bond length for C (1.38–1.48 Å for sp^2 bonds [30]). On the other hand, the minimum energy for C$_{II}$ location corresponds to –13.17 eV at a longer C$_I$–C$_{II}$ distance of 2.42 Å.
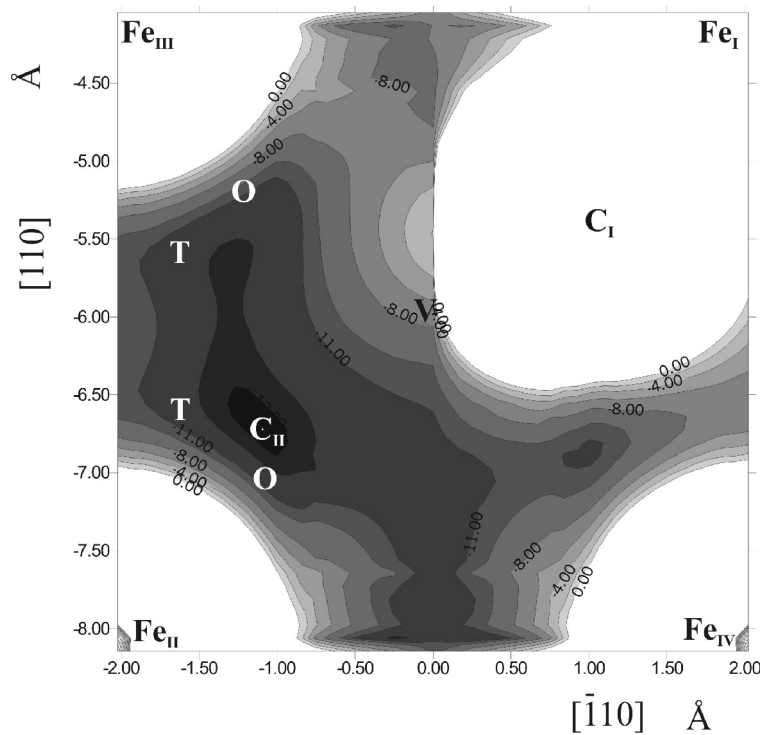
Fig. 5. Contour lines corresponding to the energy (eV) for the Fe$_{125}$–C$_I$–C$_{II}$ system in the (001) plane containing the vacancy (V). The region for C$_{II}$ location is shown in dark. The tetrahedral (T) and octahedral (O) interstitial sites are indicated

The minimum C$_{II}$–Fe$_{II}$ distance for this configuration is 1.68 Å. Similarly to C$_I$, the C$_{II}$ atom was also finally located at 0.523 Å and 0.335 Å from the nearest tetrahedral and octahedral sites, respectively; and the distance of 1.23 Å from the vacancy centre. The most stable configuration in the plane (001) corresponds to both C atoms

occupying the vacancy zone near the first nearest-neighbour octahedral sites. The agglomeration energy (section 2) was also analyzed. According to our calculations, the energy of two C atoms associated with one vacancy is close to the energy of one C atom with a vacancy. This result indicates that for C there exists, with a high probability, a competition between the formation of another C–V pair and the formation of a V–C_2 complex. Takaki et al. found that monovacancies are nuclei for small clusters containing a limited amount of C atoms [31]. Domain et al. found that a vacancy can bind to up to two C atoms only, in a configuration where both C atoms occupy first nearest-neighbour octahedral sites whose shortest distances are perpendicular to each other [11]. Other results show that the kinetics are clearly bimolecular, indicating that only one carbon atom associates with each vacancy [32]. Under normal conditions and even under irradiation, the vacancy concentration in Fe is smaller than the C atom concentration (for pure Fe or Fe alloys), and a large proportion of the vacancies may be associated with one or two C atoms, with strong binding energies.
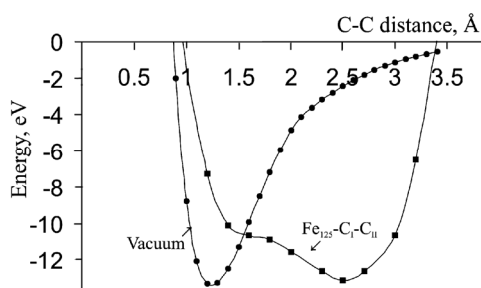
Fig. 6. Adiabatic total energy vs. C–C distance in the (001) plane containing the vacancy and under vacuum

The energy of the system was also computed as a function of the C–C distance. The C_{II} atom was moved along a line as path connecting to the C_I in order to check the stability of the system (Fig. 6). The system was more stable for C–C distances between 1.0 Å and 3.3 Å. The curve represents two relative minimums near 1.4 Å and 2.4 Å, respectively, that belong to the minimum energy region for C_{II} location previously analyzed. The region of minimum energy for C_{II} adsorption shown in Fig. 5 corresponds to C–C distances between 1.3 and 3.1 Å in Fig. 6. As a comparison, we have also obtained the adiabatic total energy curve corresponding to the C–C interaction in the vacuum (Fig. 6). The equilibrium C–C distance in the vacuum (within the ASED-MO approximation) is 1.20 Å with an energetic minimum of –13.32 eV. System stability in the Fe cluster is similar to the corresponding under vacuum.

4.2.2. Electronic structure

When two C atoms are considered, again the total DOS curves are similar to those obtained for the free cluster, as can be observed in the comparison of Fig. 7a, b. Two peaks emerge below the d metal band and this corresponds to a density of states coming from C atom states, as can be seen in Figs. 7c, d. The value of E_f is –8.134 eV.
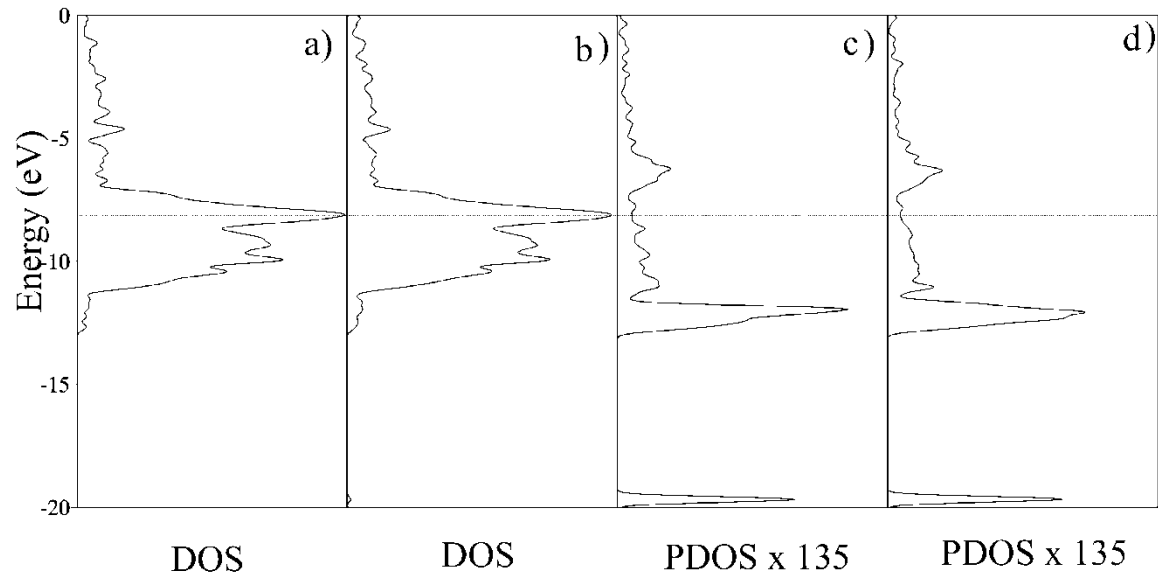
Fig. 7. Total DOS for the isolated Fe cluster (a), total DOS for the Fe_{125}–C_I–C_{II} cluster (b), projected DOS for the C_I atom in the Fe_{125}–C_I–C_{II} cluster (c) and projected DOS for the C_{II} atom in the Fe_{125}–C_I–C_{II} cluster (d)

Again, a C–Fe bonding is achieved at the expense of the Fe–Fe nearest neighbours bond. COOP curves in Figs. 8a, b show this behaviour. The interaction is almost bonding except for a region close to E_f. The OP for the C_{II}–Fe_{II} bond is 0.683 (Table 2). The interstitial C_{II} atom affects the electronic states of its surrounding Fe atoms causing a rearrangement of the electronic densities. The Fe_{II} s population decreases to about 15% while the Fe_{II} p and d populations decreases to about 4% and 5%, respectively. There is an electron transfer of about $0.43e^-$ to the C_{II} atom from the Fe_{II}. From the charge density, one can obtain a direct understanding of the interatomic bonding characteristics. The charge distribution characteristics indicate strong interactions between C and their Fe nearest neighbour atoms as well as the covalent-like bonds formed therein. As a consequence, the OP between the iron atoms near the C atom decreases. The OP for the closer Fe_{II}–Fe_{IInn} bond decreases by nearly 66%. The metal–metal bonds are then weakened.
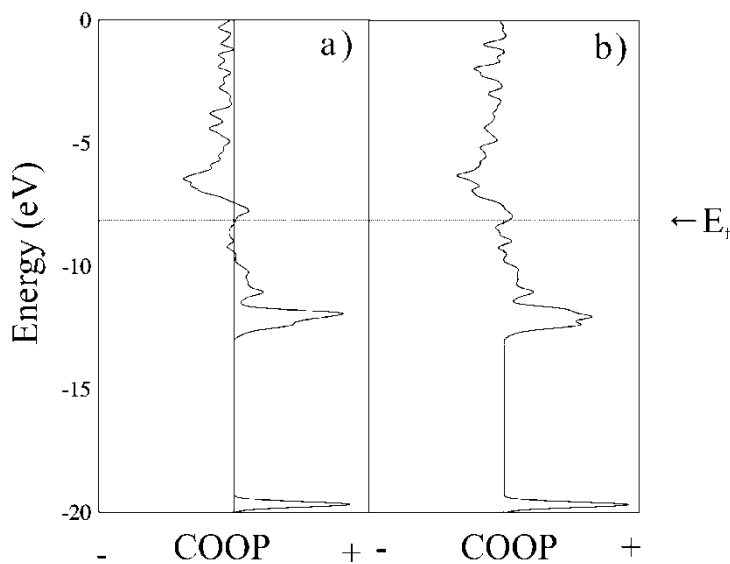
Fig. 8. COOP curve in the Fe_{125}–C_I–C_{II} system for:
a) C_I–Fe_I interaction, b) C_{II}–Fe_{II} interaction

When C_{II} is located in the Fe_{125}–C_I cluster, it practically does not affect the C_I electronic states. The addition of the C_{II} atom has a minor effect on the C_I–Fe_I bond. The C_I–Fe_I OP remains almost unchanged while the second carbon atom bonds to its closest Fe atom. The C_I becomes a bit more strongly bonded to Fe_I. The C_I–Fe_I OP increases to about 0.5% (see Table 2). In the same way, the bond strength between Fe pairs next to C_I almost does not decrease any further by the introduction of a second C. Instead, the Fe–Fe bonds close to C_{II} weaken in a similar way Fe_I–Fe_{Inn} had upon introduction of the first C atom. Then, no additional decohesion is observed in the Fe–Fe bonds when the second C atom is present but in this case more Fe–Fe bonds are af-

fected. It is observed that the charge and electronic structure of more distant iron atoms are almost unaffected by the C atoms. We thus believe their influence is limited to their first neighbours.

Considering the region of minimum energy for C_{II} location, there is a set of possible C–C associations. As we mentioned before, the minimum distances between the C atoms are around the typical covalent bond length for C and the impurity–impurity interactions are feasible. We found a small bonding between the C atoms in the (001) plane. Considering the two relative minima shown in Fig. 6, the C–C OP value is 0.050 at a C–C distance of 1.4 Å, while for a diatomic C–C in vacuum it is 0.50 and the C–C OP value is 0.021 at a C–C distance of 2.4 Å with an OP of 0.31 in the vacuum. Very low C–C OPs are a direct consequence of the metal matrix that populates antibonding C–C states at energies closer to E_f. Then, the C–C interaction on the vacancy region is small. At the same time, each C atom prefers to be bonded to the neighbouring Fe atoms. Subsequently, the Fe–C interactions are stronger than the C–C interaction.

5. Conclusions

The electronic structure of carbon in the (001) *bcc* iron with a vacancy has been studied by the ASED-MO cluster calculations. First, we included a C atom near the vacancy and then, the addition of a second C atom was analyzed.

The minimum energy positions of C atoms in the (001) *bcc* Fe were found at ca. 1.2 Å from the vacancy centre. The most stable configurations correspond to both C atoms occupying the vacancy zone near the first nearest-neighbour octahedral sites.

The addition of a C atom in the Fe matrix that contains a vacancy diminishes the strength of the local Fe–Fe bond to about 62% of its original bulk value, and by further 4% when the second C is located. This bond weakening is a consequence of a strong C–Fe interaction. The Fe–C bonds are formed at the expense of the Fe–Fe neighbour bonds. There is an electron transfer to C atoms from their Fe nearest neighbours. The Fe–C interactions occur mainly via Fe 4s orbitals with a lesser participation of Fe 4p and Fe 3d orbitals.

When two C atoms are located near the vacancy, the results are qualitatively similar to that obtained for only one C atom, that is, each C atom bonds to the surrounding Fe. No additional decohesion is observed in the Fe–Fe bonds, however in this case more Fe–Fe bonds could be affected. The C–Fe interaction is much stronger than the C–C interaction. Our results indicate that for C there exists, with a high probability, a competition between the formation of another C–V pair and the formation of a V–C_2 complex.

References

[1] Nishimura K., Okazaki N., Pan L., Nakayama Y., Jpn. J. Appl. Phys. Part 2, 43 (2004), L471.

[2] Schaper A., Hou H., Greiner A., Phillipp F., J. Catal., 222 (2004), 250.

[3] Anderson R., *The Fischer–Tropsch Synthesis*, Academic Press, Orlando FL, 1984.

[4] Meima G., Menon P., Appl. Catal. A, 212 (2001), 239.

[5] Fromm E., Hörz G., Inter. Met. Rev., 256 (1980), 5.

[6] Mc Lellan R., Ishibachi I., Trans. AIM., 233 (1985), 1938.

[7] Grabke H., Mater. Sci. Eng., 42 (1980), 91.

[8] Jiang D. E., Carter E. A., Phys. Rev. B, 71 (2005), 045402.

[9] Anderson A., Phys. Chem., 99 (1977), 696.

[10] Gavriljuk V.G., Kucherenko Yu N., Moravetki V.I., Nadutov V.N., Sheludchenko L.M., J. Phys. Chem. Solids, 55 (1994),1181.

[11] Domain C., Becquart C.S., Foct J., Phys. Rev. B, 69 (2004), 144112.

[12] Simonetti S., Pronsato E., Brizuela G., Juan A., Appl. Surf. Sci., 217 (2003), 56.

[13] Simonetti S., Moro L., Gonzalez E., Brizuela G., Juan A., Int. J. Hydrogen Energy, 29 (2004), 649.

[14] Simonetti S., Moro L., Brizuela G., Juan A., Int. J. Hydrogen Energ., 31 (2006), 1318.

[15] Hoffmann R., Lipscom W., J. Chem. Phys., 36 (1962), 2179.

[16] Hoffmann R., J. Chem. Phys., 39 (1963), 1397.

[17] Whangbo M., J. Amer. Chem. Soc., 100 (1978), 6093.

[18] Anderson A., J. Chem. Phys., 62 (1975), 1187.

[19] Landrum G., Glassey W., *Yet Another extended Hückel Molecular Orbital Package (YAeHMOP)*, Cornell University, 2004.

[20] Anderson A., Hoffmann R., J. Chem. Phys., 60 (1974), 4271.

[21] Anderson A., J. Electroanal. Chem. Interf. Electrochem, 280 (1990), 37.

[22] Wyckoff R., *Crystal Structures*, 2nd Ed., Interscience, New York, 1963.

[23] Tzeli D., Mavridis A., J. Chem. Phys., 116 (2001), 4901.

[24] Niu Y., Wang S., Zhao D., Wang C., J. Phys.: Condens. Matter, 13 (2001), 4267.

[25] Wu R., Freeman A., Olson G., Phys. Rev. B, 53 (1996), 7504.

[26] Hautojärvi P., Johansson J., Vehanen A., Yli-Kauppila J., Moser P., Phys. Rev. Lett., 44 (1980), 1326.

[27] Johnson R. A., Damask A. C., Acta Metall., 12 (1964), 443.

[28] Rosato V., Acta Metall., 37 (1989), 2759.

[29] Ruda M., Farkas D., Abriata J., Scr. Mater., 46 (2002), 349.

[30] March J., *Advanced Organic Chemistry*, Wiley, New York, 1985.

[31] Takaki S., Fuss J., Kugler H., Dedek U., Schults H., Radiat. Eff., 79 (1983), 87.

[32] Arndt R.A., Damask A.C., Acta Metall., 12 (1964), 341.

[33] Gong X., Zeng Z., Zheng Q., J. Phys.: Cond. Matter. J. Phys.: Condens. Matter, 1 (1989), 7577.

[34] Ellis D.E., Mundim K.C., Fuks D., Dorfman S., Berner A., Philos. Mag. B, 79 (1999), 1615.

Polarization spectra analysis for the investigation of space charge in dielectric nanocomposites

B. MAZUREK[1, 2], L. MORON[1*]

[1]Electrotechnical Institute, Wrocław Division, ul. M. Skłodowskiej-Curie 55/61, 50-369 Wrocław, Poland

[2]Wrocław University of Technology, Faculty of Electrical Engineering,
Wybrzeże Wyspiańskiego 27, 50-371 Wrocław, Poland

The aim of the study was to examine the influence of the dimension of matrix–filler interface on properties of epoxy nanocomposites. Using traditional investigation methods: dielectric spectroscopy, transient currents and thermally stimulated depolarization, as well as measurements of space charge distribution by the electroacoustic method, it was possible to evaluate the types of polarization and capability of accumulation and decay of space charge. The measurements performed made it possible to compare properties of a nanocomposite, microcomposite and pure resin. It was confirmed that the size of interface area plays a crucial role in the phenomena occurring in composites under the influence of electric fields.

Key words: *nanocomposite; interface; dielectric spectroscopy; thermally stimulated depolarization; TSD; pulse electroacoustic analysis; PEA*

1. Introduction

Dielectric composites made of polymers with inorganic fillers have been successfully used in electrical engineering for many years. The advantage of such materials, compared to pure resins, is the improvement of their mechanical and thermomechanical properties, lower shrinkage, and – not less important – reduction of their price. Using different fillers one can control the composite properties, e.g. conductivity, electric permittivity, thermal conductivity, etc. However, the use of traditional fillers of macro- or micro-sizes, such as SiO_2 in epoxy resins leads to a worsening (to an acceptable degree though) of dielectric properties, such as resistivity, dielectric strength or tanδ [1]. It should be indicated, however, that in spite of many years of research our knowledge of mechanisms responsible for these changes is still insufficient. In par-

---

*Corresponding author, e-mail: moron@iel.wroc.pl

ticular, very few works deal with the influence of composite microstructure on phenomena occurring in an electric field.

Introduction of a granular filler into resin matrix results in creation of interface boundaries influencing the composite properties. The influence of interface in macro scale is well known and utilised in the so called multilayer insulation, used in manufacturing of transformers, cables or capacitors. In an insulation containing components with different electric conductivities, ions can be adsorbed on boundary surfaces, thus creating dipoles. This process continues until the flow of current is settled. In this way a new distribution of electric field is established, and in consequence the electric permittivity ε, loss tangent $\tan\delta$ and resistivity ρ are changed as well. Binding of free carriers within material structure, from the point of view of dielectric properties, should be regarded as a positive effect, because, particularly in weak fields, it should lead to a decrease of conductivity and hence to lower dielectric losses. However, when local limiting values of the electric field at a phase boundary are exceeded, the collected charges can be released with all consequences, and thus they can enable easy discharging, decrease of electric strength, increase of loss tangent, etc. That is why new experimental methods have been sought which would make it possible to evaluate the distribution of space charge in a dielectric, changes of this distribution under the influence of electric field or temperature. Similarly to numerous previous works [2–5], also in this paper the use is made of the possibilities presented by measurements of dielectric spectroscopy in wide frequency range, measurements of thermo-stimulated depolarization (TSD), distribution of space charge using pulse electroacoustic (PEA) method, as well as measurements of absorption and resorption transient currents. In order to describe the samples with different contents of matrix-filler interface, standard tests of mechanical and electric properties were performed. The authors are aware of the shortcomings of the methods used, it is, however, essential to check their usefulness for evaluation of the influence of nanofillers on the phenomena occurring in nanocomposites in electric fields.

2. Experimental

2.1. Samples

The experiments were performed on samples made of epoxy composition without any filler, and composition filled with quartz meal of average grain size from 4 μm to 20 μm and silica gel of grain size from 7 nm to 40 nm. Quartz meal of 20 μm grain is the most popular filler in epoxy composites used for manufacturing of high and medium voltage insulators. 60 wt. % content of the meal in a composite is considered the optimum [1]. The maximum content of silica gel in a nanocomposite amounts to ca. 3.4 wt. %. This limitation results from the need to preserve the viscosity required in the process of casting (250 mPa at 343 K). In the samples used in the experiments

described in this paper, the composite matrix was the dian epoxy resin Epidian 5, with epoxy content 4.7–5.4 Eq/kg, cross-linked with anhydride hardener Ciba HY 905, with addition of amine accelerator K-54. The mass proportion used was 100 parts of resin, 90 parts of the hardener and 0.2 part of the accelerator. A half of the filler was added to the liquid epoxy resin at 343 K. Both components were mixed for 15 min, with a "Cowel" stirrer of 25 mm diameter, at 10 000 rpm. In the same way, the second part of the composition was prepared, and then both parts were mixed together for another 15 min and degassed in vacuum. The samples were cast and hardened in vertical open moulds. The process of hardening proceeded in two stages. In the first stage, the samples were hardened at 343 K for 5 h. The second stage consisted in after-baking at 403 K for 12 h.

Measurements of electric properties were performed using samples with dimensions $100\times100\times1$ mm^3, using a three-electrode set with a protective ring. The measuring electrode had a diameter of 50 mm, and the diameter of the voltage electrode was 75 mm. The electrodes were made of vacuum-evaporated silver. Measurements of mechanical properties were done on samples with dimensions $120\times10\times4$ mm^3. The interface areas contained in 1 cm^3 of the composites, in function of the filler share and grain diameter, are given in Table 1.

Table 1. Surface of interface matrix-filler in 1cm^3 of the composite

Composite	Filler	Weight share of the filler [%]	Average size of the filler grain [nm]	Interface area matrix–filler [m^2/cm^3]
1	Aerosil 380	3.4	7	18.6
2	Aerosil 200	3.4	12	8.2
3	Aerosil 0X50	3.4	40	2,1
4	SF 500	44	4000	1.1
5	W-12	60	20000	1.0

Table 2 presents the specific surface area of fillers used for fabricating the composites.

Table 2. Specific surface areas of nanofillers

Nanofiller	Specific surface area [m^2/g]
Aerosil 380	380
Aerosil 200	200
Aerosil 0X50	50
SF 500	3.9
W-12	0.9

The specific surface areas were calculated from the equation

$$S_{int} = \gamma A S_w \qquad (1)$$

where S_{int} is the interface area in 1 cm^3 of the composite, A – weight share of the filler, γ – mass of 1cm^3 of the composite, and S_w – specific surface area of the filler [m^2/g].

Scanning microscope (SEM) was used to visualise plane surfaces of fractures of the epoxy composite samples 2–4 (Figs. 1–3).
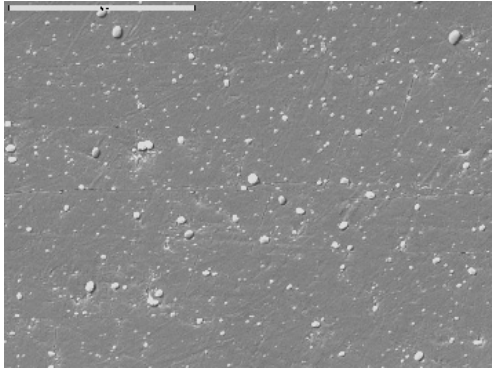

Fig. 1. Scanning photograph of the fracture surface of the epoxy nanocomposite with silica gel of 12 nm grains
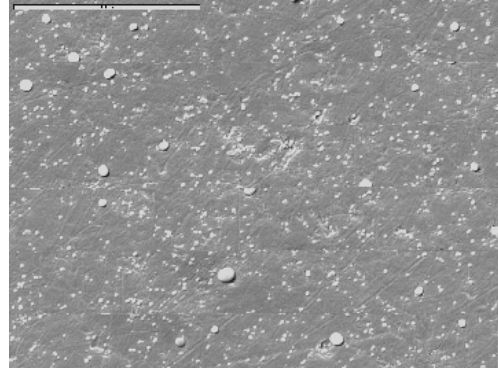
Fig. 2. Scanning photograph of the fracture surface of the epoxy nanocomposite with silica gel of 40 nm grains
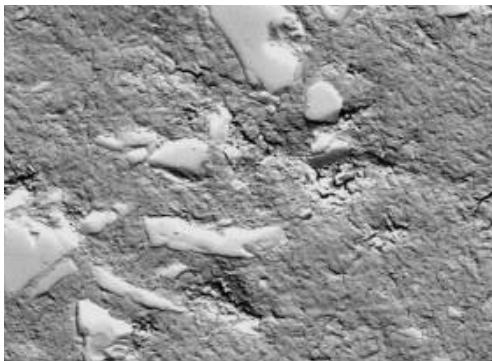
Fig. 3. Scanning photograph of the fracture surface of the epoxy microcomposite with quartz meal of 4 μm grains

Quartz meal SF-500 and W-12 produced by Quartzwerke used in the composites is a ground quartz sand with irregular grain shapes (Fig. 3). Nanosilica gels Aerosil 380, Aerosil 200 and Aerosil OX50, produced by Degussa with use of the flame method have ball-shaped grains. The contents of SiO$_2$ amounted to over 99% in quartz meals, and above 99.8% in silica gels.

During preparation of the samples much attention was paid to a proper dispergation of filler grains in epoxy matrix. The results of this treatment are shown in Figs. 1–3 as scanning electron microscope pictures of plane surfaces of fractures of the epoxy composite

samples. Beside grains of diameters of 20 nm there are agglomerates of diameters from 100 to 500 nm.

Based on these microscopic photographs, it can be concluded that the smaller the grains of a filler, the easier the agglomerates are created and the more difficult is their dispergation.

2.2. Measuring equipment

In order to establish the influence of the size of the interface area on the properties of epoxy composite, basic standard measurements of mechanical properties (impact resistance, flexural strength) as well as of electric properties (volume resistivity, electric strength and permittivity ε and loss tangent tanδ at the frequency 50 Hz) were performed.

The measurements of $\varepsilon''(f,T)$, measurements of currents of thermally stimulated depolarization (TSD), transient currents and distributions of space charges using pulse electroacoustic analysis (PEA) were applied to investigate the space charge. The measurements of ε'' in the range from 10^{-4} Hz to 10^2 Hz were performed using a General Electric IDA 200 analyzer. The measurements were taken at ambient temperature and at 373 K. For the frequencies from 10^2 Hz to 2×10^5 Hz, the measurements were made in the temperature range from 293 K to 373 K with use of an HP 4284 A impedance analyzer.

The activation energy was calculated from the $\varepsilon''(f,T)$ characteristics (Eq. (2)) [6]. For the TSD measurements an 6517 A (Keithley) electrometer was used. After evaporation of silver electrodes, the samples were polarized with constant voltages of 100 V and 200 V at 403 K. The TSD measurements were made at a constant heating rate equal to 5.5 K/min.

The measurements of isothermal transient currents (absorption and resorption) were made at 293 K and 373 K.

The measurements of space charge with use of pulse electroacoustic analysis (PEA) were made as described in [7–9].

3. Results and discussion

3.1. The influence of interface area on nanocomposite properties

Solid dielectrics designed for manufacturing of electric insulators have to possess good mechanical properties. In nanocomposites with a thermoplastic matrix, these properties depend considerably on the size of the interface area [10, 11]. The results obtained in our research for an epoxy resin matrix are shown in Fig. 4 as a dependence of flexural strength on the interface area. Figure 5 shows this dependence for the impact resistance.
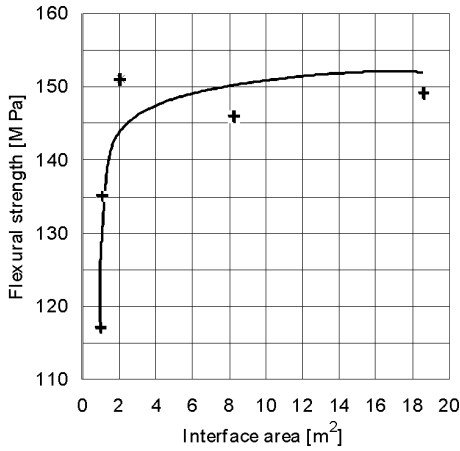
Fig. 4. Interface area dependence of the flexural
strength in the epoxy composites 1–5
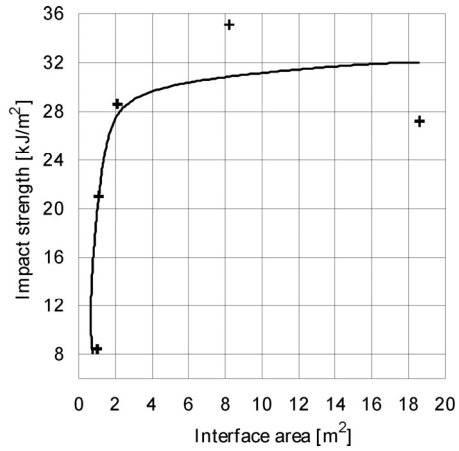
Fig. 5. Interface area dependence of the impact
strength in the epoxy composites 1–5

Upon increase of the interface area from zero to ca. 2 m^2, the flexural strength and impact resistance grow considerably from ca. 120 MPa to 150 MPa and from ca. 10 kJ/m^2 to 30 kJ/m^2, respectively. These values are much higher than those for microcomposites and pure resins. It should be stressed that we obtained these very good mechanical properties with practically unchanged specific weight related to pure resin. Electrical properties – resistivity ρ, loss tangent tanδ, permittivity ε and electric strength E_s are essential features characteristic of electroinsulating materials. These properties in function of the interface area are shown in Figs. 6–9.
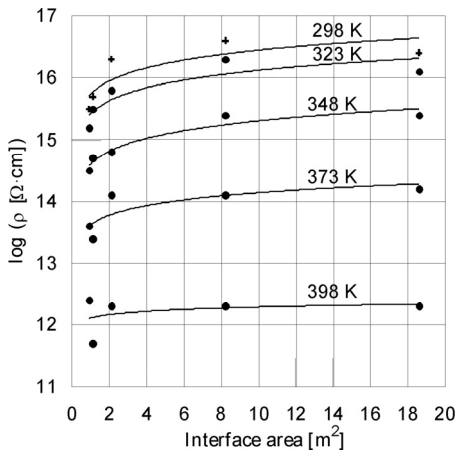
Fig. 6. Interface area dependence
of the volume resistivity ρ in the epoxy
composites 1–5
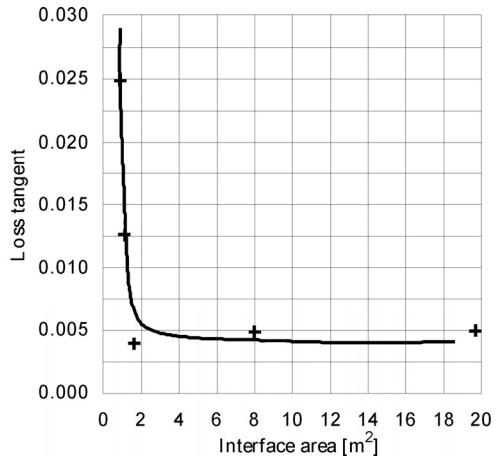
Fig. 7. Interface area dependence of the dielectric
loss tangent tanδ in the epoxy composites
1–5; temperature 296 K, voltage 1000 V, 50 Hz
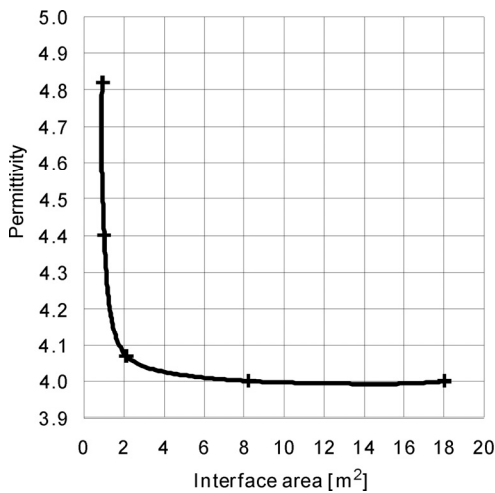
Fig. 8. Interface area dependence of the permittivity ε of the epoxy composites 1–5. Temperature 296 K, voltage 1000 V, 50 Hz
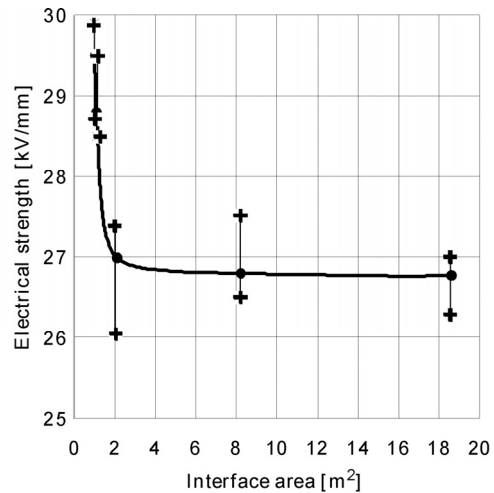
Fig. 9. Interface area dependence of the electric strength of the epoxy composites 1–5. Temperature 296 K, alternative voltage 50 Hz

The volume resistivity increases with the increase of the interface area, particularly for measurements performed at temperatures lower than 373 K (Fig. 6). A stronger influence of the interface is visible in the case of loss tangent and dielectric permittivity (Figs. 7 and 8). Introduction of nanofiller and increase of interfacial area lead to a lowering of the electric strength (Fig. 9).

Essential information about the space charge in a dielectric can be obtained from measurements of absorption and resorption transient currents. The lack of a mirror reflection of both time-dependent curves is an evidence that space charge is accumulated in the material [12]. Such a situation was also noted in our investigation.
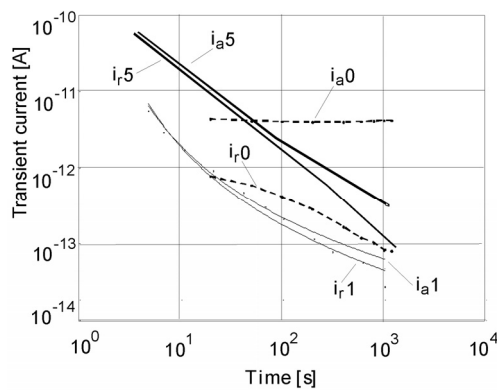
Fig. 10. Time dependences of transient currents of absorption i_a and resorption i_r of epoxy composites 0, 1, 5

Figures 11 and 12 show dispersional curves of the imaginary part of permittivity ε'' determined at 293 K and 373 K, in the frequency range from 10^{-4} Hz to 2×10^{5} Hz.
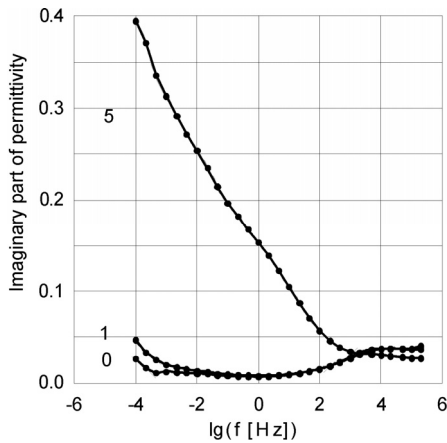
Fig. 11. Dependence of the imaginary part
of permittivity ε on the frequency f in epoxy
composites 0, 1, 5. Measurements at 296 K
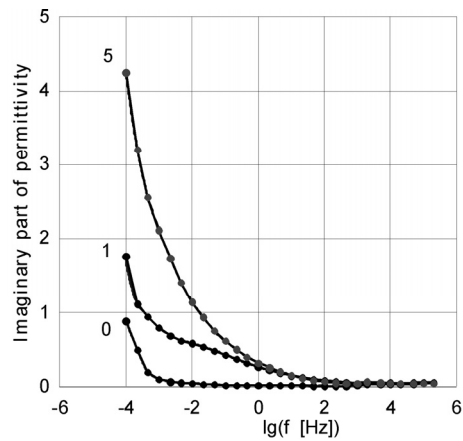
Fig. 12. Dependence of the imaginary part
of permittivity ε on the frequency f in epoxy
composites 0, 1, 5. Measurements at 373 K

At ambient temperature, the highest values of ε'' were obtained for the frequency 10^{-4} Hz for the composite 5 with microfiller of interfacial area 1 m^2, whereas pure resin and the resin with nanofiller (18.6 m^2) had similar, visibly lower values, slightly changing with frequency. At 373 K, the curves visibly vary, again the highest values obtained for the composite 5 and the lowest ones with the pure resin. When the temperature is raised, the values of ε'' are by one order of magnitude higher than those at ambient temperature. From the characteristics $\varepsilon''(f,T)$, activation energies were determined using the equation [6]:

$$\Delta W = \frac{0.198}{\Delta\left(\dfrac{T}{1000}\right)} \quad [\text{eV}] \tag{2}$$

where: $\Delta(T/1000)$ is an increment $T/1000$ for one frequency decade. The results are presented in Table 3.

Table 3. Activation energy ΔW of epoxy composites 0, 1, 5 [eV]

Composite	$T < 403$ K	$403 < T < 413$ K	$T > 413$ K
0	3.30	3.30	2.44
1	3.80	3.04	2.34
5	2.87	2.87	2.55

At the investigated temperature ranges, three polarization processes are visible with three different activation energies. Below 403 K a process of group polarization γ takes place, at temperature range 403–413 K group polarization β, and above 413 K, a process of segmented polarization α is likely to occur [13, 14]. Taking into account

that for each composite tested the same epoxy matrix7 was used, the reasons for different values of activation energies can be attributed to different resisting forces during charge relocation. The smallest activation energy is characteristic of composite 5, with micro-size quartz meal, and the highest one of composite 1. These differences disappear at higher temperatures. Dipole polarization processes induced by space charges can be determined from the TSD current curves which are shown in Figs. 13–16.
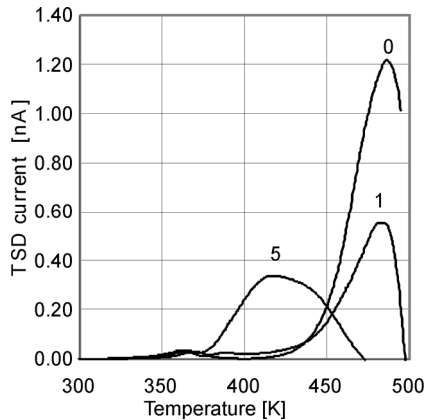
Fig. 13. Temperature dependences of the TSD currents in composites 0, 1, 5. Polarization in the electric field 100 kV/m, temperature 403 K
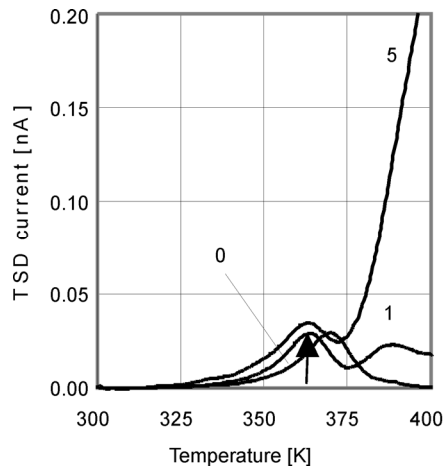
Fig. 14. Temperature dependences of the TSD currents in composites 0, 1, 5. Polarization in the electric field 100 kV/m, temperature 403 K. A detail from Fig. 13
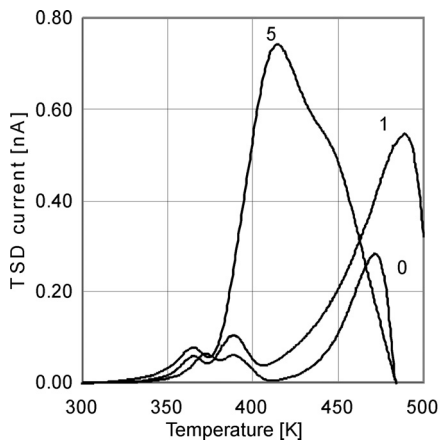
Fig. 15. Temperature dependences of the TSD currents in composites 0, 1, 5. Polarization in the electric field 200 kV/m, temperature 403 K
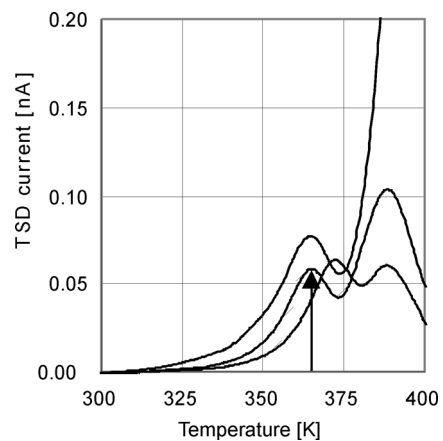
Fig. 16. Temperature dependences of the TSD currents in composites 0, 1, 5. Polarization in the electric field 200 kV/m, temperature 403 K A detail from Fig. 15

The dipole feature of the local maximum is confirmed by a change of TSD current value, proportional to the polarizing voltage, at a given temperature [15, 16]. For instance, for composite 0, the dipolar character of the peak at temperature 370 K is confirmed by the doubled increase of this value for a doubled polarizing voltage (cf. Figs. 14 and 16). A complete analysis of the presented TSD spectra requires additional measurements with other parameters of sample polarization.

The investigation of the role of interface area in accumulation and decay of the space charge in the tested epoxy composites 0, 1, 5 was performed using the pulse electroacoustic analysis (PEA). The results are shown in Figs. 17–22.
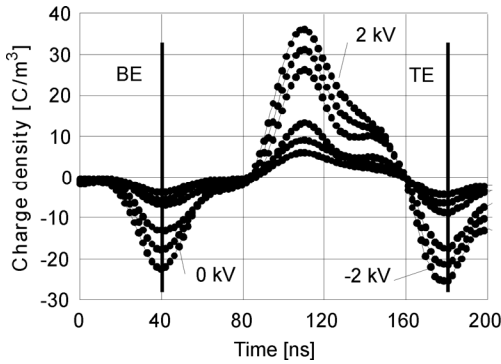
Fig. 17. Charge density distribution in composite 0 obtained with PEA. Polarizing voltage from – 2 kV to 2 kV. BE – lower electrode, TE – upper electrode
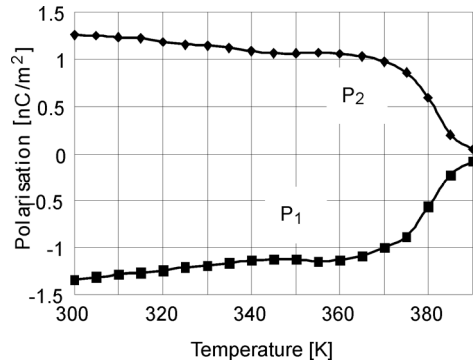
Fig. 18. Charge decay in composite 0 measured with PEA
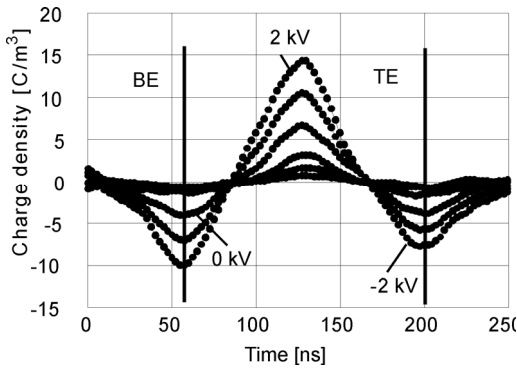
Fig. 19. Charge density distribution in nanocomposite 1 obtained with PEA. Polarizing voltage from –2 kV to 2 kV; BE – lower electrode, TE – upper electrode
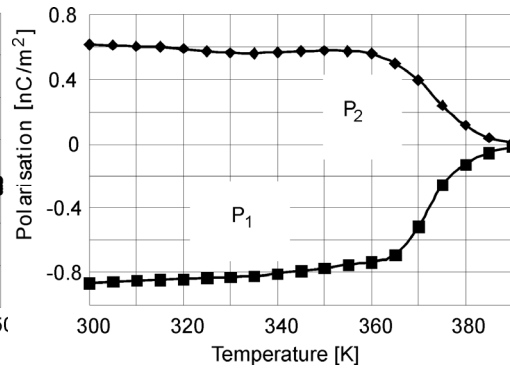
Fig. 20. Charge decay in nanocomposite 1 measured with PEA

The results of measurements point to an essential role of interface in the accumulation and distribution of the space charge in the tested composites, affecting new dis-

tribution of electric field. Free charge is adsorbed on the interface. Free charge on electrodes is compensated by polarization charges. The highest amount of charge is gathered in composite 0 (without filler), twice lower amount in nanocomposite 1 (interfacial area 18.6 m^2), and six-fold lower in composite 5 with micro-filler with interfacial area 1 m^2, (Figs. 17, 19 and 21).
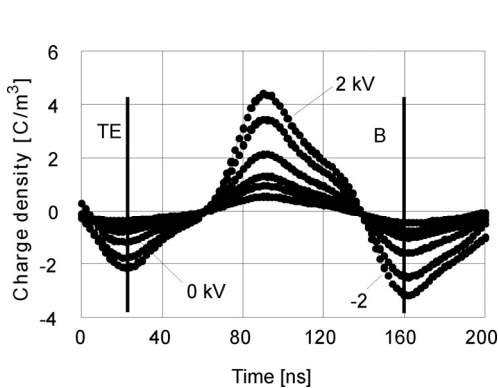

Fig. 21. Charge density distribution in microcomposite 5 obtained with PEA. Polarizing voltage from –2 kV to 2 kV; BE – lower electrode, TE – upper electrode
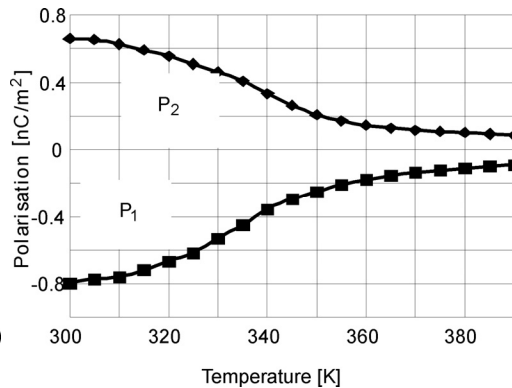
Fig. 22. Charge decay in microcomposite 5 measured with PEA

On increasing temperature, the charges on the interface disappear, what is confirmed by the polarization curves P_1 and P_2 (Figs. 18, 20 i 22). In composite 0, a visible dropout of the polarization begins at the highest temperature (ca. 375 K) and is the fastest one (Fig. 18). In sample 1 with the nanofiller, the dropout begins at ca. 365 K and proceeds somewhat slower (Fig. 20). At the lowest temperature (ca. 325 K) the polarization begins to vanish in composite 5 with a micro-filler (Fig. 22).

4. Conclusions

In the process of nanocomposite production a particular attention should be paid to a proper dispergation of nanoparticles in a polymer matrix, so as to avoid creation of agglomerates.

The investigation of mechanical properties showed a visible increase of impact and flexural strength in comparison to micro-composites. This means that the insulators made of such material will be lighter and much stronger.

With the increase of the interfacial area, the dielectric properties are improved, as are resistivity, loss tangent and permittivity. Only a slight worsening of electric strength could be observed. This effect could result from an increase of a local electric field caused by gathering of charges near the interface boundary.

The measurements of transient currents show that a space charge gathers in the tested material what is confirmed by the lack of a mirror reflection in the curves of absorption and resorption currents.

The role of interface is also visible in the measurements of the imaginary part of the permittivity (ε'') in function of frequency. A microcomposite is characterized by a much higher imaginary permittivity, particularly at lower frequencies, in comparison to a pure resin, and the introduction of a nanofiller practically makes dielectric losses independent of the frequency at room temperature, forcing them to remain at a level characteristic of a pure resin. Similarly, at higher temperatures the nanocomposite loss is visibly lower than that of a micro-composite. This considerable increase of dielectric loss in a micro-filled composite can be explained by the occurrence of the Maxwell–Wagner polarization on micro-grains absent in nanocomposites. This was confirmed by the observations described in [17].

The activation energy calculated for the pure resin (composite 0), microcomposite (5) and nanocomposite (1) based on measurements of ε'' in function of frequency and temperature (Eq. (2)), at temperature ranges slightly higher than glass transition temperature was found to be the lowest for a microcomposite. At higher temperatures (above 413 K), the activation energies of the tested samples are very similar. This finding is essentially different from the results reported in [2] where TiO_2 was used as a filler.

The comparison of TSD current curves for three investigated materials (composites 0, 1 and 5) showed that in the pure resin and in composite 1 both the dipole polarization and the polarization due to the space charge are present. For microcomposite 5, however, the size of the TSD current peak varies proportionally to the change of the polarization voltage what suggests that it is related to dipole polarization only. Asymmetrical shape of this peak (Fig. 15) may be an effect of overlapping with a component due to the space charge.

PEA tests showed that the ability to collect the charge generated by corona discharge is the highest for pure resin, twice lower for a nanocomposite and six time lower for a microcomposite. Charge decay for pure resin begins at the highest temperature 375 K and its duration is the shortest. Introduction of a micro-filler lowers this temperature to ca. 325 K and visibly prolongs the time. A nanocomposite compared to a microcomposite is characterized by a higher loss temperature and shorter loss time.

Constantly growing number of papers concerning this issue indicates that introducing nanofillers into a polymer matrix essentially influences the properties of nanocomposites due to the increase of a boundary surface area filler–matrix. The mechanism of this phenomenon has not been fully clarified, nonetheless in the investigation of dielectrics, dielectric spectroscopy, measurements of transient currents, TSD currents and analysis of charge distribution with acoustic methods are commonly used. The weakness of these methods consists in the fact that the results obtained are usually quantities averaged from local signals, generated in numerous electrically active weak places which decide about electric strength, partial discharges or dielectric losses. It should also be stressed that the investigation methods mentioned above are applied at

different voltages and different local field intensities and therefore the results obtained cannot be directly compared. Thus it is necessary to investigate and develop new methods and measurement techniques. Nonetheless, making use of the classical tests permits a better evaluation of application potentials of new materials and can be useful in drawing conclusions on the mechanisms of phenomena occurring in dielectrics exposed to electric fields.

Acknowledgements

References

[1] CZUB P., *Napełniacze* [in:] P. Czub, Z. Bończa, P. Penczek, J. Pielichowski (Eds.), *Chemia i Technologia Żywic Epoksydowych*, WNT, Warszawa, 2002 (in Polish).

[2] NELSON J.K., HU Y., J. Phys. D: Appl. Phys., 38 (2005), 213.

[3] ROY M., NELSON J.K., IEEE Trans. Diel. El. Insul., 12 (2005), 629.

[4] BUR A.J., LEE YU-HSIN, STEVEN C., Annual Technical Conference ANTEC 2004 Plastics, Chicago, Vol. 1. *Processing*, p. 1284.

[5] DAVIS R.D., BUR A.J., MCBREARTY M., Polymer, 45 (2004), 6487.

[6] JONSCHER A.K., *Dielectric Relaxation in Solids*, Chelsea Dielectrics Press, London, 1983, p.108.

[7] TAKADA T., IEEE Trans. Diel. El. Insul., 6 (1999), 519.

[8] MOTYL E., J. Electrostatics, 40–41 (1997), 469.

[9] MOTYL E., Zesz. Nauk. Polit. Śl., Ser. Mat. Fiz., 87 (1999), 95.

[10] MONTANARI G.C., FABIANI D., PALMIERI F., IEEE Trans. Diel. El. Insul., 11 (2004),754.

[11] REICHERT P., NITZ H., KLINKE S., Macromol. Mater. Eng., 275 (2000), 8.

[12] DAS-GUPTA D.K., IEEE Trans. Diel. El. Insul., 4 (1997), 149.

[13] SCHONHALS A.D., *Molecular Dynamics in Polymer Model Systems*,[in:] F. Kramer, A. Schonhals (Eds.), *Broadband Dielectric Spectroscopy*, Springer, Berlin, 2003.

[14] SAZIN B.J., *Elektricheskyie Svoystwa Polimerov*, Khimia, Moscow, 1997 (in Russian).

[15] VANDERSCHUEREN J., GASIOT J., *Field-Induced Thermally Stimulated Currents*, [in:] P. Bräunlich, *Thermally Stimulated Relaxation in Solids*, Springer, New York, 1979.

[16] LAVERGNE C., LACABANNE C., IEEE El. Insul. Mag., 9 (1993), 5.

[17] NELSON J.K., HU Y., Ann. Rep. Conf. El. Insul. and Diel. Phen., IEEE Plenary Meeting, Albuquerque, NM, USA, 2003, p. 719.